Interstellar catalysts and the PAH universe

Campisi, D.

Citation

Campisi, D. (2021, September 14). *Interstellar catalysts and the PAH universe*. Retrieved from https://hdl.handle.net/1887/3210124

Cover Page

Universiteit Leiden

Author: Campisi, D.
Title: Interstellar catalysts and the PAH universe
Issue Date: 2021-09-14

Interstellar Catalysts and the PAH universe

Proefschrift

ter verkrijging van
de graad van doctor aan de Universiteit Leiden,
op gezag van rector magnificus prof.dr.ir. H. Bijl,
volgens besluit van het college voor promoties
te verdedigen op dinsdag 14 september 2021
klokke 11:15 uur

door

Dario Campisi

geboren te Palermo, Italië
in 1986

Promotiecommissie

Promotor: Prof. Dr. Alexander G. G. M. Tielens
Co-Promotores: Dr. Inge Loes ten Kate (Universiteit Utrecht)
Dr. Thanja Lamberts

Overige leden: Prof. Dr. Huub Röttgering
Prof. Dr. Serena Viti
Prof. Dr. Herma M. Cuppen (Radboud Universiteit)
Prof. Dr. Liv Hornekær (Universiteit van Aarhus)
Dr. Albert Rimola (Universitat Autònoma de Barcelona)
Dr. Timothy Lee (NASA Ames Research Center)
Dr. Mariëtte Wolthers (Universiteit Utrecht)

With great power
comes great
responsibility.

Stan Lee's Spider Man

To myself,
look how far you've come.

CONTENTS

I

CHAPTER 1

INTRODUCTION

Chemistry is a scientific discipline that has the aim to study how elements combine to form "complex systems". Citing the Britannica encyclopedia, "chemistry is the science that deals with the properties, composition, and structure of substances".[1] Astrochemistry is the discipline that studies the interaction of atoms and molecules as well as their chemical and physical properties in space. Astrochemistry is a field that bridges astronomy and chemistry, and is also called molecular astrophysics. Although astrochemistry studies the chemistry of the medium between the stars (interstellar medium, called ISM), cosmochemistry is the study of molecular formation in solar system objects such as asteroids, comets, and planets.[2]

The key questions of astrochemistry are: What is the role of molecules in the evolution of the universe? How can molecules be used to probe the universe? What is the organic inventory of regions of star and planet formation? Are interstellar molecules related to the molecular inventory of the Earth and the terrestrial planets in the solar system? Hence the aim of astrochemistry is to study how molecules regulate the chemical and physical conditions that lead to galaxy and planet formations. This entails the formation and processing of molecules in the ISM and their delivery to solar system objects. Finally, one of the current hot topics revolves around the formation of the building blocks of life, such as glycine.[2]

Almost 14 billion years ago, after the Big Bang explosion, subatomic particles such as quarks and electrons started to build up the first hydrogen and helium nucleus in the range of 3 minutes. Only after about 300.000 years, they formed the first atomic hydrogen and helium. Once the first atomic and molecular species are formed the timescale required to form complex molecular entities such as us increases manifold. However,
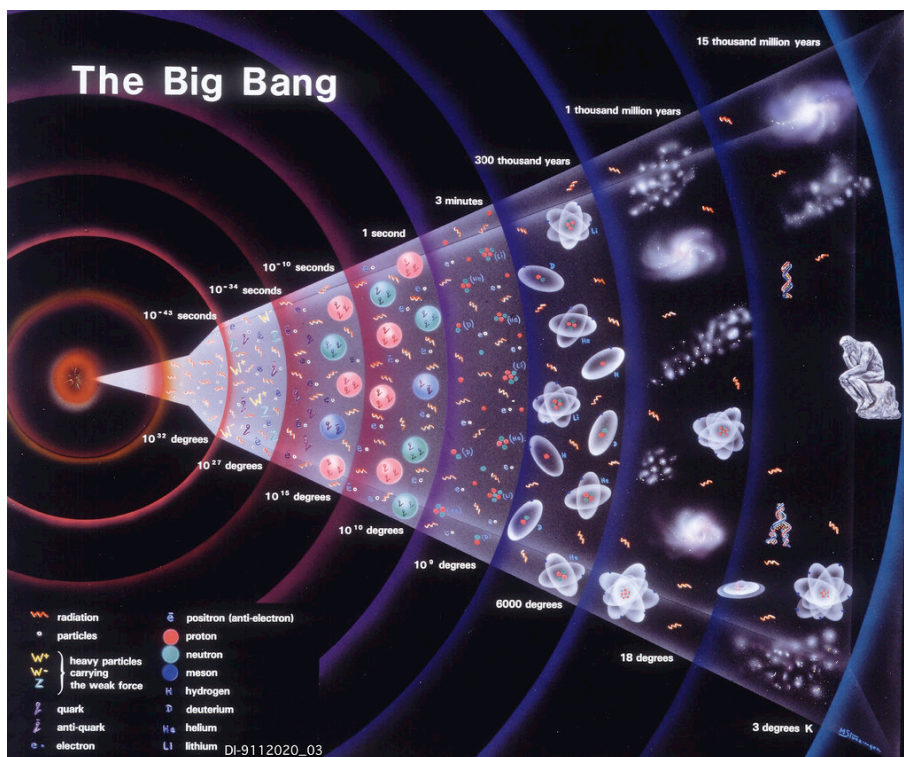
Figure 1.1: The timescale of subatomic, atomic, molecular and supramolecular formation from the big bang until today.[4]

molecules have all the time of the universe to meet, collide and react.[3]

Every substance on Earth and in space undergoes a transformation that releases or absorbs energy. This energy is converted into many forms and one of the most important is thermal energy.[5] The latter is a consequence of molecular and/or atomic collisions that cause the formation and the breaking of bonds. Hence, atomic and molecular collisions are responsible to build the so-called complex organic molecules.

Besides the chemical reactivity in space, the identification of molecular composition in objects far from Earth is an important consequence of the light interaction from a nearby star.[6,7] The light interaction with a molecular entity promotes electronic excitation which is partially converted into vibrational modes. After a relaxation process, the molecule emits to a precise and detectable wavelength in space. Hence, astronomical observations play an important role in the identification and characterization of molecular composition in space as a consequence of their rotational, vibrational, and electronic excitations.[6]

Over 200 species have been detected in space by astronomical obser-

vations. The diversity of molecular species in space varies from the most simple one such as H_2 to more complex ones such as fullerenes, C_{60}, C_{70} and, no less important, polycyclic aromatic hydrocarbons (PAHs).[8] The latter locks up about 20% of the carbon in the universe and, hence, makes up a considerable fraction of the organic inventory of the universe.[8] Could this PAH reservoir be related to the molecular inventory of the Earth and the terrestrial planets is our solar system? For example, could the PAHs be altered and the carbon used in the formation of complex molecular species?

The aim of this thesis is, using quantum chemistry methods, to shed light on the chemical reactivity and catalysis involving the most abundant and observed molecular species in the universe such as PAHs. Specifically, the studied PAH samples of this thesis are, pentacene, pyrene, naphthalene, anthracene, fluoranthene, pyrene, coronene, and benzocoronene.

1.1. Modeling Interstellar Catalysts

Before discussing in detail the role of PAHs in the universe, a short explanation of chemical modeling and interstellar catalysts must be introduced. These are the keys to understanding the molecular complexity of our universe and, hence, the study of bond formation and destruction routes at the atomistic level. This will be followed by a detailed section (*Chemical Processes in the Universe*) on the role of molecules in the ISM and solar system and the theoretical methods to study the complexity of our universe (*The Basis of Quantum Chemistry Methods*).

1.1.1. Chemical Modeling

The prediction of molecular abundances that evolve in time is investigated through astronomical models that make use of kinetic rate equations with parameters derived from astronomical observations (*i.e.*, column density, density, temperature) and quantum chemistry calculations (*i.e.*, binding and activation energy).[9] Astronomical modeling aims to study the kinetics and reactivity of molecular species in the interstellar environment[9] with input parameters obtained from concomitant chemical modeling (this includes classical and quantum approaches).[10] The latter, more generically, aims to study the kinetics and reactivity of molecular species in every environment. These two approaches to modeling are complementary and both are needed for a proper characterization of the chemical routes driving molecular complexity in space.

Within the chemical modeling, the energy of atomic species as a function of their position, named "Potential Energy Surface" (PES), explains how atomic and molecular species are interconnected. When two species come close to the equilibrium of the electronic repulsion and the electronic
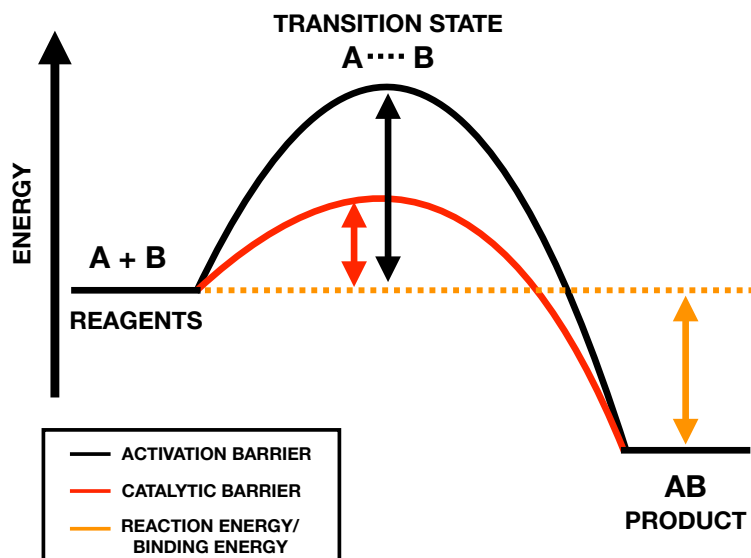
Figure 1.2: Schematic representation of a transition state and a catalytic process of connecting two generic atoms, A and B, forming a molecule, AB.

attraction, they form an imaginary species located in the maximum of a PES called transition state (TS), shown in Fig. 1.2. The TS is a molecular configuration that corresponds to the bottle-neck in potential energy along the reaction coordinate. A TS cannot be detected in lab or in space since it is purely a transitory state. However, the TS allows estimating the energy barrier or activation energy (the difference in energy between the TS and the reagent). Hence, the energy that the system needs to overcome to form the products. On the contrary, the reaction energy (the difference in energy between the product and the reagent) tells us how favorable is the reaction based on the quantity of energy released (exoergic process) and/or required (endoergic process).[11] The binding energy is a measure of how much energy we need to provide to dissociate the molecule or to desorb a molecule from a surface or another molecule.[12] Hence, the binding energy is the inverse of reaction energy (energy difference between the reagent and the product shown in Fig. 1.2). Transition state theory (TST)[13] provides a good explanation of chemical processes at thermodynamic equilibrium and allows to derive the kinetic rate of a process. The harsh environment of space does not allow molecules to reach thermodynamic equilibrium, and generally, kinetics is the dominant factor.[14]

1.1.2. Catalysis

Catalysis is a way to increase the rate of a chemical process. A catalyst can be anything, including a radical, a molecule, or a surface that reduces the large energy barrier associated with the formation of the product. Usually, the efficiency of a catalyst is expressed in terms of the turn over number or frequency, the number of cycles in which the catalyst takes part in the reaction (undergoing chemical transformation) and regenerates in a loop. However, not all catalysts are regenerated during the process and some of them might lose their catalytic activity due to the degradation of the active site of the catalyst (the site that binds the reagent).[10]

The investigation of the transition state and the reaction pathways requires sophisticated quantum chemical methods such as density functional theory (DFT), see subsection 1.3.1, the most common quantum chemistry method to model organic molecules and solid surfaces.[11,12] In space, grains,[15] radical hydrogens[16] and PAHs[16–18] are mainly responsible for catalytic processes.

1.2. Chemical Processes in the Universe

The known pathways to the hypothesized formation of molecular complexity go through the bottom-up, from small to big (from Fig. 1.3 (a) to (d)), and top-down, from big to small (from Fig. 1.3 (e) to (d)) approach.[8] Although the focus of this thesis is related only to the processes reported in Fig. 1.3 (f) and (d), (a) summary of all hypothesized chemical processes that occur in space will clarify the general aim of this study and, therefore, the big picture (building the organic inventory of solar system). Hence, subsections from 2.1 to 2.6 will provide detailed explanations of the chemical processes occurring in space.

1.2.1. Bottom-Up Approach

The bottom-up approach starts in so-called dark molecular clouds (Fig. 1.3 (a)), cold and dense regions of the ISM.[8] Here, atomic carbon is locked up in the CO molecule, a stable and less-reactive molecule. Catalysts such as silicate grains and water ice can gather these CO molecules on their surfaces and activate them.[19,20] During the hydrogenation of CO molecule, formaldehyde (H_2CO) and methanol (CH_3OH) can be produced (Fig. 1.3 (b)).[21] In regions of ISM surrounding a new protostar (hot core regions), cosmic rays and UV photons can promote further radical attachment and loss to form more complex molecular species, whereas thermal processes might favor the formation of large size molecules (Fig. 1.3 (c)).[8] Shocks and the heating of the ice sputter the molecules in the gas phase where they can collide and react via ion-neutral and neutral-neutral reactions.[8]
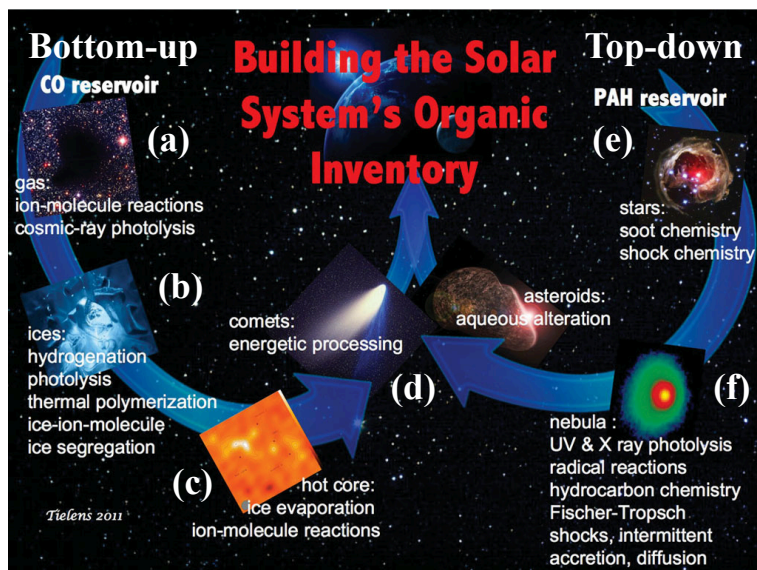
Figure 1.3: Modified scheme of molecular formation from CO and PAHs (bottom-up and top-down approaches, respectively) reported by Tielens.[8]

1.2.2. Top-Down Approach

The top-down approach builds molecular complexity by dismantling big molecules into small ones that can react with other species with heteroatoms, such as nitrogen (N) and oxygen (O) atoms, forming more complex molecules, *e.g.*, amino acids.[8,22] This approach starts with the formation of large PAHs[23] (from 50 to 200 atoms) in the envelope of AGB stars (Fig. 1.3 (e)).[24] PAHs are formed in the gas phase soot chemistry, and further processed by energetic photons such as X-ray and UV. In hot core regions, PAHs can be attacked by H and OH radicals formed during the warming phase of a new protostar (Fig. 1.3 (f)).[25]

Finally, all the products from the top-down and bottom-up chemistry will be collected and further processed by cometesimals and planetesimals (Fig. 1.3 (d)).[8] Specifically, PAHs can be gathered by grains in the solar nebula. These grains coagulate to bigger and bigger particles that form the building blocks from which asteroids are formed. Part of the parent body (asteroids) may be broken up into meteorites that fall on Earth. In the parent body, further chemical processes may occur such as the aqueous alteration (alteration of the mineral composition promoted by water). Water present in the asteroid will start to react with the dominant mineral phase made by olivine structure $((Mg,Fe)_2SiO_4)$, in a temperature range between 20 and 140°, to form a mineral called serpentine $(Mg_2Si_2O_5(OH)_4)$. During the conversion from olivine to clay, it has been hypothesized that the proton
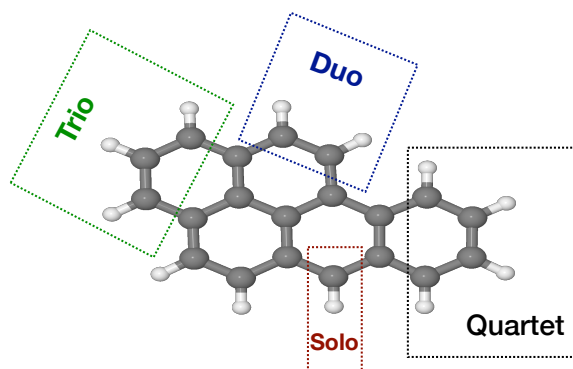
Figure 1.4: Astronomical classification of the hydrogens of a PAH.

exchange between PAHs and olivine might break them down into small aliphatic units. The formed fragments might react with CO_2 and NH_3, via the so-called Strecker reaction, forming amino acids such as glycine.[22]

1.2.3. Polycyclic Aromatic Hydrocarbons

Polycyclic Aromatic Hydrocarbons (PAHs) are organic molecules present everywhere on our planet and in the universe. They are the main focus of this thesis. Here, I give a short introduction on PAHs in the universe, building up from their formation and detection to the rationale for their importance for the research described in this thesis.

PAHs are conjugated compounds with perfect planar sp^2 carbons that provide them with distinct stability and resistance to the reactivity of other species and high temperatures.[2,26] PAHs are observed everywhere in the interstellar medium.[2] Depending on the temperature and radiation, they are present in their neutral, cationic and anionic forms.[26] Their carbon skeleton structures (Fig. 1.4) have been classified by the astronomers based on the IR signature of specific vibrational modes of the C-H and C-C bond (Fig. 1.5).[27] However, none of the single whole structures of PAHs has been yet identified in space. Brett McGuire recently characterized the first spectroscopic signature of benzonitrile (C_6H_5CN) that has been thought to be a possible precursor of PAHs, as the first step to identify the chemical pathway that leads to PAH formation in the ISM.[28]

When PAHs absorb a UV photon, they are electronically excited, this process is very infrequently (depending on the physical condition of the region, this occurs from 1 day to 1 year). Due to their limited heating capacity, they become very hot (about 1000 K) but they rapidly relax, cooling down, in the order of seconds, and emitting in the IR. In contrast, for grains with sizes larger than 10 nm, the heating and cooling timescales are
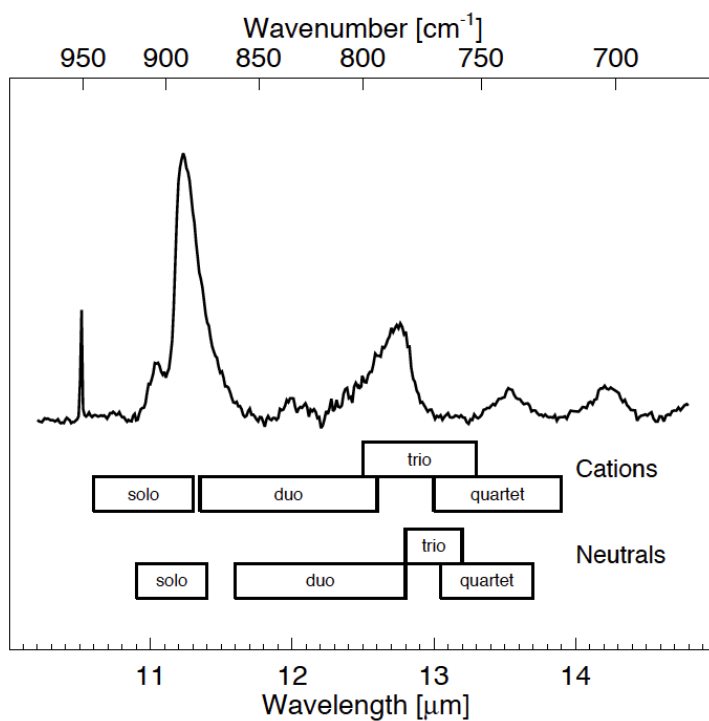
Figure 1.5: The average IR spectrum of out of plane C-H bending modes of PAHs and the associate range of solo, duo, trio, and quartet hydrogens (see Fig. 1.4) reported by Hony *et al.*[29]

a) Buckyball   **b) Soccer ball**
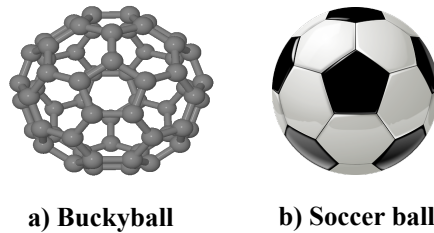
Figure 1.6: Fullerene structure (a) compared to the soccer ball structure (b).

comparable and these species are in radiative equilibrium, resulting in low temperatures.[2] However for PAHs, the IR emission is in competition with the H-loss. With a typical binding energy of 4.5 eV, this is energetically feasible. For high UV photon fluxes, more than one H might be lost forming a graphene-like structure that can isomerize resulting in the so-called buckyball fullerene (C_{60}), shown in Fig. 1.6 (a).[30]

Observationally, astronomers identified a direct correlation between PAH destruction and fullerene formation as a function of the distance from the star.[31]

PAHs in the ISM might be found as isolated molecules in the gas phase or they can be part of the dust composition. Due to the electronic delocalization of the π ring, they can form van der Waals complexes with each other.[32] However, the stability of these complexes decreases with the increasing radiation field leading to a single PAH cation in the gas phase.[2,32] Due to their photo-electric heating properties, they regulate the phase structure of galaxies and star formations.[26] PAHs, due to their chemical properties, might be great catalysts. For instance, they are thought to be responsible for molecular hydrogen formation in photo-dissociation regions (see subsection 2.4).[17]

1.2.4. Molecular Hydrogen Formation

The most abundant molecule in the universe is molecular hydrogen (H_2). The latter has been observed abundantly in dense molecular clouds, but also in high UV radiation field environments such as the so called photo-dissociation regions (PDR).[33] The UV radiation field is so strong that H_2 is rapidly photo dissociated. As H_2 is observed to be very abundant, this requires a rapid reformation process.[34]

In diffuse clouds, small (0.01-0.1 µm) solid dust grains made by carbonaceous materials or minerals, are thought to provide surfaces on which radical hydrogen can diffuse, gather and react. Hence, grains offer surfaces in which atoms have all the time of the universe to form molecular species, *e.g.*, molecular hydrogen, and more complex ones.[35–37] However,

a) LH mechanism   **b) ER mechanism**
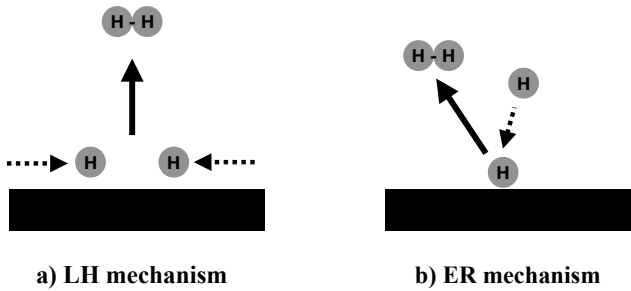
Figure 1.7: Schematic representation of molecular hydrogen formation through Langmuir–Hinshelwood (LH) and Eley–Rideal (ER) mechanism on a solid surface.

in a PDR, due to the high temperature of the dust, hydrogen cannot bind with the surface, and H_2 formation on grain surfaces would be very inefficient.[38] If PAHs are present, hot hydrogen radicals bind strongly with the PAH surface, unable to be released.[16,39,40]

For the case of silicate grains, the most favorable mechanism for molecular hydrogen formation is the diffusion of one or two hydrogen radicals followed by a desorption process (Langmuir–Hinshelwood, LH, mechanism shown in Fig. 1.7 (a)).[33] On PAHs, the desorption process of two atomic hydrogens, forming the molecular one, is not favorable and requires overcoming a barrier of about 4.8 eV.[16] However, the addition of more than two hydrogens on the PAHs might promote the H_2 formation. Ideally, PAHs might fully host as many hydrogen radicals as many carbon sites are available, becoming superhydrogenated PAHs.[39,41] However, this is not always the case. In fact for the case of coronene, in the PDRs, the hydrogenation will not exceed three extra hydrogen atoms chemisorbed on the carbon sites due to the competition between H-loss and H-gain.[41]

The most favorable mechanism is the Eley–Rideal (ER, shown in Fig. 1.7 (b)) in which upon the chemisorption of hydrogen, on a carbon site, it can be extracted, through barrierless reaction, from radical hydrogen that chemisorbs on top of it.[17] Hence, PAHs act as efficient catalysts for molecular hydrogen formation.

1.2.5. From ISM to Solar System: The Organic Inventory

Silicate dust grains are formed in the envelope of the red giant branch (RGB) and the asymptotic giant branch (AGB).[42] About 15% of the dust has the composition of crystalline olivine and pyroxene such as forsterite (Mg_2SiO_4) and enstatite ($MgSiO_3$). Forsterite condenses in the dust at high temperatures (about 1400K) and partially transforms to enstatite at somewhat lower temperatures.[42] At high temperatures, silicates can adjust to

their most stable form, the crystalline structure. But at temperatures be-
low the glass temperature, amorphous materials, without long range or-
der, result.[43,44] Dust propagates in the ISM processed by shocks and only
submicron-size, or smaller, silicate grains survive sputtering, thermal ero-
sion, and grain-grain collisions.[45] Grains can have also carbonaceous na-
ture including silicon carbide (SiC), which was recognized by astronomers
through the strong Si-C stretching mode at 11.3 µm.[42,43] Furthermore,
about 10% of the dust composition is composed of hydrocarbons, both
aliphatic and aromatic, observed at 3-15 µm.[42]

During the collapse of a molecular cloud core resulting in the forma-
tion of a spinning disk, materials start to accrete and, therefore, organics
and silicate dust will be incorporated forming planetesimals and cometesi-
mals, and ultimately planets.[46] During the accretion period, carbonaceous
chondrite materials are formed, called chondrites due to the presence of
chondrules, mm-sized inorganic mineral grains, and carbonaceous due to
their organic composition. Carbonaceous chondrites are considered prim-
itive because they did not suffer from major transformation and, therefore,
they contain a record of the organic and inorganic composition of the early
solar system. About five tons of meteorites that fall on earth every year are
of the family of carbonaceous chondrites.[47]

The organic composition of carbonaceous chondrites can be divided into
soluble (SOM) and insoluble (IOM) organic matter. However, almost 95% of
the carbon in carbonaceous chondrites are composed by IOM. The analy-
sis of these materials requires usually high mass spectroscopy resolution.
Almost 140000 molecules have been identified in carbonaceous chondrites
meteorites.[47]

Table 1.1 show the families of extraterrestrial organic molecules found
in Murchinson meteorites and their abundance. It is still unclear how
those molecules were formed, however, it has been suggested that the pres-
ence of molecules formed in the circumstellar environment (*i.e.*, formalde-
hyde and PAHs) might have played an important role during the aqueous
alteration of the parent body.[48]

The IOM composition of Murchinson (*i.e.*, macromolecular materials)
is very difficult to characterize with spectroscopy, whereas the SOM char-
acterization (the rest of compounds in Table 1.1) helped to identify im-
portant building block's of life such as amino acids. Here, the large abun-
dance of L-amino acids (with respect to the usual D-amino acids abundant
in terrestrial environments) helped to identify the extraterrestrial nature
of these compounds.[49] However, possible formation routes of complex or-
ganic molecules are still to be clarified. It is quite possible that multiple
pathways and catalytic processes are involved. In particular, it is unclear
whether these species have already been formed in the solar nebula and
incorporated in the asteroid body or that they have been formed after the
incorporation, inside the parent body, due to the catalytic activity of the
minerals.

Composition	Concentration ($\mu g{*}g^{-1}$)
Alyphatic hydrocarbons	12–35
Aromatic hydrocarbons	15–28
Alcohols	11
Aldehydes	11
Amino acids	60
Ketones	16
Carbon dioxide	106
Carbon monoxide	0.06
Methane	0.14
Monocarboxylic Acids	332
Dicarboxylic Acids	25.7
α-hydroxycarboxylic Acids	14.6
Sugars	60
Ammonia	19
Amines	8
Urea	25
Basic N-heterocycles (pyridines, quinolines)	0.05–0.5
Pyridinecarboxylic acids	>7
Dicarboximides	>50
Pyrimidines (uracil and thymine)	0.06
Purines	1.2
Benzothiophenes	0.3
Sulfonic acids	67
Phosphonic acids	1.5
Macromolecular material	1.45 (%)

Table 1.1: Composition and concentration of organic species found in Murchison meteorites reported and studied by Sephton. [47]

a) Corannulene   **b) Fluoranthene**
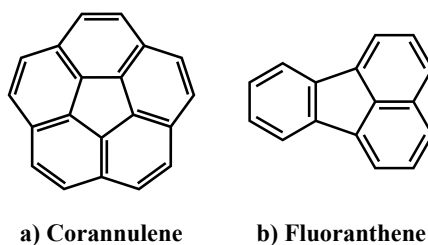
Figure 1.8: Skeletal structure of corannulene (a) and fluoranthene (b).

During the aqueous alteration, PAHs might breakdown and form fragments that can react with other molecular species helping to build up complex organic molecules listed in Table 1.1. The migration of water from the interior of the parent body to the surface helps to transport and concentrate PAHs in the parent body.[50] For instance, the large abundance of alkylated PAHs, detected in Murchison and Mukundpura meteorites, might be the result of aqueous alteration of the parent body.[51,52] However, it is not yet clear why large PAHs (more than five aromatic ring units) have not been detected in these meteorites and, thus, this is still under investigation.[53]

1.2.6.   Defects

Defects in solid materials might have great importance in astrochemistry and cosmochemistry since their reactivity might contribute to promote the chemical complexity of our universe.[12,16] In this section, I provide an overview of several types of defects that might be formed in PAHs and minerals.

PAHs are commonly known as perfect planar structures with six-membered rings. However, sometimes they might have different ring arrangements, similar to fullerene (*e.g.*, pentagons), in which other types of ring shapes are present. For instance, corannulene and fluoranthene are two examples of PAHs with a five-membered ring, shown in Fig. 1.8 (a) and (b), respectively. Different ring arrangements, doping with a metal or hetero-atom, and the lack of one or more atoms in the PAH lattice are called defects. Since PAHs might be considered small graphene-like structures, they can have graphene-like defects.[54] Defects might be promoted by radiation or chemical reactions, which might occur in the harsh space environment even though only a few studies addressed the defect formations and stabilities in PAHs.[16,55,56] Fig. 1.9 (a), (b), and (c) show three examples of defects such as Stone-Wales (two seven- and five-membered ring modification), mono and divacancy (removal of one or more atoms) in a graphene-like structure.[54] The Stone-Wales defect[57] is particularly

a) Stone-Wales

b) Monovacancy   **c) Divacancy**
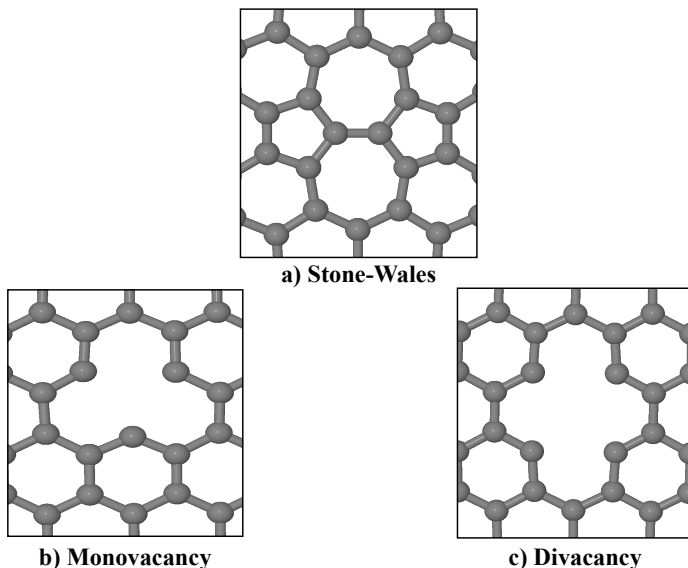
Figure 1.9: Stone-Wales (a), mono (b) and di (c) vacancy defects on a graphene-like structure.

interesting in astrophysics since it has characteristic infrared absorption features that can explain the undefined infrared bands observed at 6.9 and 6.14 μm in the ISM.[58]

Besides PAHs, defects are ubiquitous also in crystalline materials such as minerals. These defects break the periodicity of the crystal lattice. In particular, defects can be located around a single atom, therefore a point, namely point defects.[59] For instance vacancies (Fig. 1.10 (c) and (d)) as well as the substitution of an atom with another one (doping, such as in Fig. 1.10 (b)) are two example of point defects. Other types of defects can be present in the bulk of the crystal (bulk defects) and/or along a specific direction of the lattice structure (line and planar defects).[59]

In this thesis, we focus on the point defects since those are able to locally modify the chemical reactivity of the system making them catalytic.[16,60] When a solid system is ionic and formed by the same number of cation (A^+) and an anion (B^-) maintaining the neutrality of the system, several types of point defects might occur (Fig. 1.10).[61] Besides the doping and the single vacancy, another type of vacancy, named Schottky vacancy, takes place when two opposite charged ions leave the crystal lattice.[61] In this way, the system maintain its neutral charge. There are two types of Schottky defects, one might occur when a cation and anion leave from two distant sites (Fig. 1.10 (e)) and the other one from adjacent sites (Fig. 1.10 (f)). The latter constitutes a neutral divacancy.[61]

a) System A$^+$B$^-$ b) C-doped A$^+$B$^-$ c) V$_A$-A$^+$B$^-$ d) V$_B$-A$^+$B$^-$

e) Schottky V$_{AB}$-A$^+$B$^-$ f) Schottky V$_{AB}$-A$^+$B$^-$
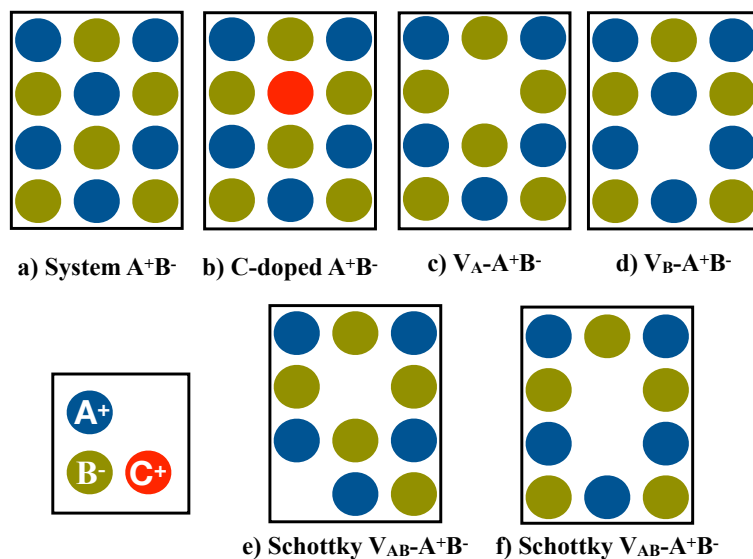
Figure 1.10: Example of point defects in a ionic lattice A$^+$B$^-$: (a) Non-defective lattice (pristine), (b) doped lattice, (c),(d),(e) and (f) vacancy (V) lattice.

On forsterite, Schottky defects might be formed due to the reaction of the mineral with water, even in a small amount.[62] This defect, thus, might have great relevance in asteroidal settings.[63]

1.3.   The Basis of Quantum Chemistry Methods

In order to study the reactivity of molecular species, in space, quantum chemistry[2] can provide meaningful insights describing the so-called potential energy surface (PES) landscape. Fig. 1.2 shown an example of a two-dimensional potential energy curve. As discussed in subsection 1.1, a PES provides meaningful information such as minima (reagents, intermediates, and products) and so-called saddle points, which are associated to transition states. The difference in energy between minima or minimum and saddle point provides the binding energies, reaction energies, and energy barriers, as shown in Fig. 1.2.[11]

The so-called Born-Oppenheimer approximation states that the nuclear and electronic wave functions can be treated separately, because of the large difference between the electron mass and the masses of atomic nuclei, and, therefore, the time scales on which they move. Thus, we can approximately solve the non-relativistic time-independent electronic Schrödinger equation:

$$\hat{H}\Psi = E\Psi \tag{1.1}$$

$\hat{H}$ is the Hamiltonian operator that includes the kinetic energy of the electrons, the potential energy of the electrons and nuclei, the potential energy of each nucleus-electron interaction, electron-electron interaction, and nucleus-nucleus interaction as well as dispersion energy (electronic long-range interactions). E is the electronic energy and Ψ is the electronic wave function that is often approximated by a linear combination of basis functions.[11] Obtaining a good estimation of the electronic interactions (correlation) is the main problem of solving the Schrödinger equation due to the many electronic contributions (many-body problem).[11]

Several methods, in quantum chemistry, have been developed to solve the Schrödinger equation. For instance, the Hartree-Fock (HF) method can approximate the Ψ as a single Slater determinant of N one-electron spin orbitals (product of a spatial orbital and its spin functions):

$$\Psi_{HF} = \frac{1}{\sqrt{N!}} \begin{vmatrix} \Psi_1(\vec{r}_1) & \dots & \Psi_N(\vec{r}_1) \\ \vdots & \vdots & \vdots \\ \Psi_1(\vec{r}_N) & \dots & \Psi_N(\vec{r}_N) \end{vmatrix} \tag{1.2}$$

N is the number of electrons, $\vec{r}$ is the coordinate, Ψ_N is the N one-electron spin-orbital. The Slater determinant in equation (1.2) makes sure that the wave function is antisymmetric, on exchanging two-electrons with respect to their position, and using the spin-orbitals as an orthonormal basis.[11] The baseline of this method is that the electrons move independently with respect to each other considering their average position. The electrons feel the Coulomb repulsion and a exchanging interaction (they exchange their positions) due to the antisymmetrization. For all these reasons, the HF method is known as mean-field theory and, also, self-consistent field (SCF) since the Schrödinger equation is solved iteratively starting from a guessed spin-orbital.[11] The consequence of using an approximated wave function to solve the Schrödinger equation is that the electronic energy will be always higher than the true energy (variational problem).[11]

In order to improve on the major shortcoming of HF theory, namely electronic correlation, so-called post-Hartree Fock methods have been developed. One of these methods, coupled-cluster characterized by iterative inclusion of single and double excitations with perturbative inclusion of triple excitations, CCSD(T), is nowadays often seen as the gold standard of computational chemistry.[11]

1.3.1. Density Functional Theory

One way to calculate the ground state energy of a molecule or collection of molecules is to make use of Density Functional Theory (DFT) developed by Walter Kohn and co-workers[64] who received the nobel prize for this in

1998. DFT is a cheap and accurate way based on a single Slater Determinant that replaces the N-dimensional wave function by a 3-dimensional electron distribution function. Hence, this method is a convenient alternative to wave function-based methods to model large systems with a computational cost similar to Hartree Fock and accuracy similar or lower to Post-Hartree-Fock methods. [11,64]

DFT is based on the two Hohenberg-Kohn (HK) theorems. [65] *The ground state energy ($E[\rho]$) can be expressed as integral ($\int$) of the sum of an external potential $v(r)$ of an interacting electron gas in the ground state and a universal functional $F[\rho(r)]$ of the density (i.e., a function of another function) of a multielectron system*:

$$E[\rho] = \int v(r)\rho(r)dr + F[\rho(r)] \tag{1.3}$$

This is the first Hohenberg-Kohn theorem [65] that announces the existence of a functional. The latter cannot be identified exactly which is one of the main problems of DFT. The $F[\rho(r)]$ can be expressed as sum of functional contributions:

$$F[\rho(r)] = T[\rho(r)] + Q[\rho(r)] + E_{ee}[\rho(r)] \tag{1.4}$$

$T[\rho(r)]$ is the kinetic energy, $Q[\rho(r)]$ is the known classical Coulomb interaction, and $E_{ee}[\rho(r)]$ is the energy of a quantum contribution of the electron-electron repulsion.

$T[\rho(r)]$ has two contributions, one is the known contribution of electron interactions ($T_{known}[\rho(r)]$) and a second contribution, describing the Pauli exclusion principle, that is unknown ($T_{unknown}[\rho(r)]$). The unknown contribution and $E_{ee}[\rho(r)]$ can be written as:

$$E_{xc}[\rho(r)] = E_{ee}[\rho(r)] + T_{unknown}[\rho(r)] \tag{1.5}$$

$E_{xc}[\rho(r)]$ is a new functional that is named exchange-correlation functional that includes the unknown contribution of the ground state energy.

Therefore, the energy of a ground state system ($E[\rho(r)]$) can be written as:

$$E[\rho(r)] = E_{known}[\rho(r)] + E_{xc}[\rho(r)] \tag{1.6}$$

the $E_{known}[\rho(r)]$ includes the electron kinetic energy and the Coulomb interactions between the nuclei and the electrons, electron pairs, and nuclei pairs.

The second Hohenberg-Kohn theorem, following in the footsteps of the variational problem, [11] defines that *the ground state energy will be higher or equal than the true ground-state energy when a trial electron density [ρ'] function is used to solve the Schrödinger equation*:

$$E[\rho'(r)] \geq E[\rho(r)] \tag{1.7}$$

$E[\rho(r)]$ is also defined as electronic energy and its accuracy is related to the used exchange-correlation functionals (Eq. 1.5). [11]

Kohn and Sham overcame the difficulties of modeling a many-body system of interactive electrons, using an alternative method to solve the Schrödinger equation. The so-called Kohn Sham (KS) equation is based on one single Slater determinant of spin-orbitals with a local effective potential:

$$\left[\frac{-\hbar^2}{2m}\Delta^2 + V(\rho(r)) + V_H(\rho(r)) + V_{xc}(\rho(r))\right]\rho_i(r) = E[\rho_i(r)]\rho_i(r) \qquad (1.8)$$

$\hbar$ is the reduced Planck constant ($h/2\pi$), m is the mass of the electron, $V(\rho(r))$ is the potential of the electron and the nuclei, $V_H(\rho(r))$ is the Hartree potential (the electrostatic potential of the electron charge density), whereas $V_{xc}(\rho(r))$ is the functional derivative of the exchange-correlation energy:

$$V_{xc}(\rho(r)) = \frac{\delta E_{xc}(\rho(r))}{\delta\rho(r)} \qquad (1.9)$$

This approximation overcomes the issue to define the $T_{unknown}[\rho(r)]$ of the functional and introduces a one-electron interactive system. [11] In this way the energy of a system, with non-interactive electrons, can be described as the single contribution of multiple terms (electronic kinetic energy, Coulomb interactions, and exchange-correlation energy). In this way, the approximated system has the same density as a real system of interacting electrons with a low computational cost. [11]

In order to solve the Kohn-Sham equation, we need to know $\rho(r)$, but in order to know $\rho(r)$, we need to solve the Kohn-Sham equation. A way to overcome this difficulty is to use the self-consistent field[66] (SCF) method. SCF method consists of using a trial electron density ($\rho'(r)$) to solve the Kohn-Sham equation and then compare the calculated electron density distribution to the initial one. The electron density distribution function is updated and used for the following iteration cycle and this process is continued until a specified accuracy is achieved. [11]

1.3.2. **Exchange-Correlation Functionals**

Over the years, several classes of exchange-correlation functionals have been developed: Local-density approximation (LDA), local spin-density approximation (LSDA), generalized gradient approximation (GGA), meta GGA, hybrid GGA and hybrid meta GGA. [11] These classes are schematized in Fig. 1.11.
LDA and LSDA uses a uniform electron gas to define the E_{xc}, however, this ignores that the electron density is not uniform. To overcome the

CLASS   **FUNCTIONALS**

Hybrid meta GGA ————————— M06, M06-2X, M06-HF

Hybrid GGA ————————— B3LYP, PBE0, HSE

Meta GGA ————————— M06L

vdW-DF2 ————————— LMKLL

vdW-DF1 ————————— DRSLL, KBM

GGA ————————— PBE, revPBE, PW91, BLYP

LDA, LSDA ————————— PW92

Accuracy
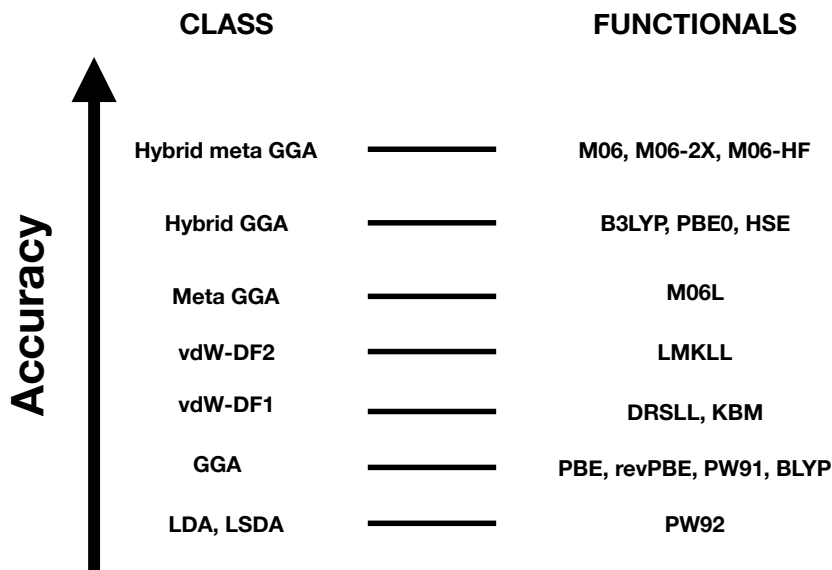
Figure 1.11: Jacob's ladder scheme of seven classes of exchange-correlation functions, including Van der Waals functionals, according to Perdew *et al.*[67] For each class, some of the commonly used functionals are reported.[68–77]

non-homogeneity of the electron density, one can use GGA functionals, such as PBE and PW91,[69] that make use of the first derivative of the electron density. However, both functionals are far from being perfect and accurate especially for highly correlated systems and van der Waals complexes.[78] More accurate than GGA is the meta-GGA that makes use of the Laplacian, *i.e.*, the second derivative of the electron density.[11] Meta-GGAs widely used are the so-called "Minnesota Functionals" such as M06-L.[77] In order to increase the accuracy of DFT functionals, the integration of the exact exchange part using a wave function-based method, such as Hartree Fock, can be included in the exchange-correlation functional. Such type of functionals are called hybrid functionals.[11] In astrochemistry, the Becke three parameters Lee-Yang-Parr functional (B3LYP)[74] is one of the most used and employed hybrid GGA to compute both spectra and studying reaction pathways.[79] However, hybrid functionals such as B3LYP poorly describe all systems in which the dispersion energy (non-covalent interactions) plays an important role.[80] To overcome this issue, Donald Truhlar developed also the hybrid version of the meta-GGA functionals, such as M06 and M06-2X, that include a certain percent of the exact Hartree Fock exchange.[77]

However, it is not always possible to employ hybrid functionals and

meta-GGA functionals. This is particularly the case for computational demanding periodic systems (solid-state). [12]

Commonly, DFT functionals do not take into account the dispersion forces that are long-distance interactions between two molecules or an atom and a molecule. [81] Therefore, in order to accurately describe non-covalent interactions such as Van der Waals and London dispersion forces, the use of van der Waals functionals (vdW-DF) based on the electron density is needed. [82] VdW-DFs describe the exchange-correlation energy (E_{xc}^{vdW-DF}) as:

$$E_{xc}^{vdW-DF} = E_{xc} + E_c^{nl} \tag{1.10}$$

E_{xc} is the exchange energy of the functional that lies at the basis of the particular vdW-DF used, for instance revPBE. [70] E_c^{nl} is the non-local dispersion energy and also contributes to the correlation of interacting electrons at a short distance. The original vdW-DF is DRSLL that takes its name from the developers Dion, Rydberg, Schröder, Langreth, Lundqvist. [72] The advantage of this vdW-DF [82] and its upgraded version vdW-DF2 [83,84] is that the dispersion energy is self-consistely included via the charge density. Another way to estimate the dispersion energy is to employ empirical corrections called DFT-D ("DFT-Dispersion") developed by Prof. Grimme's groups. [81] Sometimes DFT-D method uses damping functions, such as that one developed by Becke-Johnson [85] (BJ damping), to avoid overcounting the correlation at intermediate distances. [81]

1.3.3. Basis Sets, Periodic Approach and Electronic Structure

In order to overcome the mathematical complexity of solving the Schrodinger equation, we need to use a finite set of basis functions, named basis sets. [11] In this way, the orbitals can be expressed as a linear combination of basis functions. The most commonly used basis sets employed for gas-phase calculations are localized atomic orbitals (LCAO) that are centered on the atomic positions. When there are multiple basis functions (single, double, triple,etc.) for a single valence orbital, we define single zeta basis set (SZ), double zeta basis set (DZ), and so on. [11] Sometimes basis sets might include one of more polarization functions and diffusive functions. These extra functions include the polarization of the electron density and the flexibility of the atomic orbitals to enlarge and change shape to account for dipole moments or anions, respectively. [11] It is commonly mandatory to use polarization functions to obtain publishable results. LCAO basis sets are commonly implemented in DFT codes for gas phase calculations such as Gaussian, [86] NWChem [87] and PSI4. [88] For solid systems, periodic boundary conditions (PBC) must be applied to the model that is placed in a box called unit cell. The unit cell is defined by three lattice vectors and by
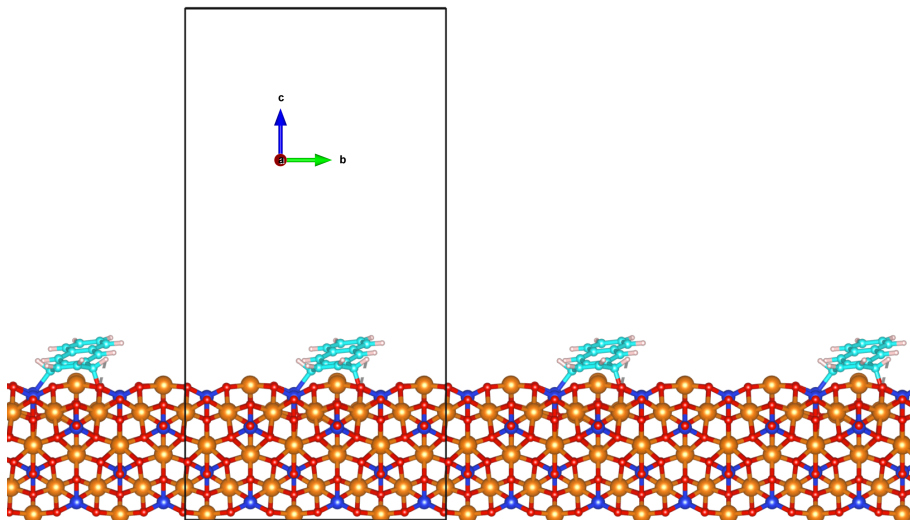
Figure 1.12: Translation symmetry along the axis (a) of a naphthalene unit chemisorbed on a forsterite (Mg_2SiO_4) surface. The box is the unit cell defined by the vector (a), (b) and (c).

repeating in the three corresponding spatial directions, the translational symmetry of a crystalline structure is obtained, as shown in Fig. 1.12.[89] In order to solve the Schrödinger equation for a periodic system, it is more convenient for the wave function (Ψ) to take the form of a plane-wave in a periodic potential, mathematically, described by Bloch's theorem:[89]

$$\Psi(r) = e^{ik*r} p(r) \tag{1.11}$$

r is the atomic position, e is the Euler's number, i is the imaginary unit, k is the set of reciprocal lattice vectors (Brillouin's zone) and p is a periodic expansion in r space directions. Plane waves basis sets (PW) are the most commonly used basis sets for periodic structures. PWs are not centered in the nuclei and they fill uniformly the region of space occupied by the system inside the unit cell. The number of plane waves are defined by a cutoff energy.[89] To obtain accurate results, a higher cutoff energy must be carefully selected which carries high computational cost. A way to avoid the use of large basis sets is to fix the core electrons of each atoms using pseudopotentials.[89] Core electrons are not that important to describe the chemical bond which is the reason why several pseudopotentials have been implemented for PW codes such as the ultrasoft pseudopotentials and projector augmented-wave (PAW).[90,91] Therefore, PWs are the most common basis sets used for solid systems implemented in codes such as VASP,[92] Quantum Expresso,[93] Abinit[94] and GPAW.[95]

LCAO can also be employed in periodic systems multiplying them for the phase e^{ik*r} using the Bloch's theorem.[96,97] Widely used periodic DFT codes with LCAO are SIESTA[98] and Crystal.[99] LCAO is less commonly used, with respect to PWs, due to the basis set superposition error[100] (BSSE). BSSE is an error of the basis sets that overestimates the energy of a system composed of any two closely interacting entities, *e.g.*, a dimer or an adsorbed molecule. This is caused by the electron density described by functions centered on other nuclei.[12] A widely used procedure to overcome the BSSE, for an adsorbed atomic or molecular species (A) onto another one (B), adduct AB, is to use the counterpoise method[101] (CP):

$$\Delta E_{cp} = (E_{A[ghost]B} + E_{AB[ghost]}) - (E_{A^*} + E_{B^*}) \tag{1.12}$$

ΔE_{cp} is the counterpoise energy correction that will be added to the binding energy to obtain the CP corrected energy. E_{A^*} is the energy of a single point calculation of the adduct AB deprived by B. E_{B^*} is energy of a single point calculation of the adduct AB deprived by A. $E_{A[ghost]B}$ is the energy of a single point calculation of the adduct AB in which the basis sets of A has been deprived of the A nuclei (ghost atoms) and $E_{AB[ghost]}$ is vice-versa. PW basis sets do not suffer from the BSSE since they uniformly fill the space occupied by the system and, therefore, they are considered the standard for periodic calculations. However, they can be orders of magnitude more computationally expensive than LCAO basis sets when surfaces are modeled.[12] This is caused by the filling nature of PWs that uniformly occupies the vacuum region in the unit cell, the empty space facing the surface as shown in Fig. 1.12. On the contrary, LCAOs are only centered in the atomic positions. This is the reason why we need to account for a large number of PWs to obtain accurate results, which in turn are computationally demanding. Therefore, LCAOs even though less accurate than PWs are widely used for large systems. On top of this, the CP correction reduces the binding energy obtaining results comparable with PWs methods.[12]

The bands, namely the periodic orbitals, defined by Bloch's electrons can be estimated for each k-points.[89] The k-points can be easily sampled for a calculation using the Monkhorst Pack[102] scheme and they are inversely proportional to the unit cell.[89] The interpolation of the eigenvalue for each k-point defines the band structure in which, for a specific energy range, the projection of the single atomic orbital on the total crystal orbital defines the Projected Density of State (PDOS, the contribution of an atomic orbital to the total electronic structure).[89]

1.4.   This Thesis

This thesis is a quantum chemical study of important catalytic processes that occur in the ISM and solar system involving PAHs. The content of this thesis is as follows:

Chapter 2, Superhydrogenation of Pentacene: the Reactivity of Zigzag-Edges. This chapter is a combined theoretical and experimental effort between Leiden Observatory, Milan University, and Aarhus University. The aim of this study is to understand the hydrogen sequence that leads to superhydrogenated pentacene molecule (a pentacene completely hydrogenated) and explains the so-called magic numbers shown in the mass spectra peaking at a pentacene molecule with 2, 4, 6, 10, 16, and 22 extra hydrogens attached. Study the hydrogenation sequence of PAHs and therefore their hydrogenated intermediates that range from a single hydrogenation to a full hydrogenation is important to understand their potential catalytic role for molecular hydrogen formation.

In this study we clarified the role of binding energy with respect to barrier energy in the hydrogenation sequence of pentacene. Specifically, the binding energy tells us about the stability of hydrogenated species, whereas the barrier energy allows us to identify species with longer lifetimes, that control the magic numbers. Moreover, the hydrogen sequence revealed a possible route for nanotubular formation. Based on the DFT calculations, linear PAHs such as pentacene are more reactive with respect to pericondensed PAHs such coronene and, therefore, they might play important roles in catalyzing H_2 in the PDRs.

Chapter 3, Do Defects in PAHs Promote Catalytic Activity in Space? Stone–Wales Pyrene as a Test Case. In line with chapter 2, the hydrogenation of PAHs might open up new chemical reactivity. The aim of this work is to identify possible catalytic routes for the formation of the Stone-Wales defect and molecular hydrogen formation catalyzed by this defect. Using DFT methods, we found that the hydrogen radical is able to catalyze Stone-Wales formation in a prototype PAH such as pyrene reducing the barrier by about 2 eV. Once the SW defect is formed, it is stable due to the large barrier in the backward reaction. The defect also increases the reactivity of the PAH toward hydrogen chemisorption and reduces the barrier for molecular hydrogen extraction. Hence, catalysts such as H and PAHs may play an important role for isomerization and catalytic conversion of H to H_2 in the ISM.

Chapter 4, Interaction of Aromatic Molecules with Forsterite: Accuracy of the Periodic DFT-D4 Method. Prior to studying the interaction of PAHs on silicates, specifically the forsterite mineral (chapter 5), an accurate DFT method to compute surface phenomena at the inorganic

interface of the mineral needed to be idenitfied. We tested DFT methods, using both LCAO and PW, for the adsorption of benzene, naphthalene and benzocoronene on the [010] forsterite surface and transition metal-doped surfaces (Fe and Ni). We tested the empirical dispersion corrected PBE (PBE-D4) functional and a van der Waals functional (DRSLL), comparing their results with PW methods. Furthermore, we clarified the role of BSSE which is indispensable to accurately predict binding energies, comparable to those obtained by PW methods. In order to evaluate the accuracy of PBE-D4 and DRSLL, when transition metals are employed, we modeled a small system, benzene-transition metal cation complexes, as a reference for big-scale systems, and we compared the results with post-HF methods. PBE-D4 with LCAO provided a good description of the binding energy of PAHs on forsterite surfaces, agreeing well with PW and post-HF methods.

Chapter 5, Adsorption of PAHs and C_{60} onto Forsterite: C-H Bond Activation by the Schottky Vacancy. Using the PBE-D4 approach benchmarked in chapter 4, we study the adsorption of a sample of PAHs (naphthalene, anthracene, fluoranthene, pyrene, coronene, and benzocoronene), along with fullerene, on [010]-forsterite and its defective surfaces (Fe, Ni-doping and MgO Schottky vacancy). The aim is to study the interaction of PAHs and C_{60} onto (010) forsterite surfaces and the C-H activation (bond breaking) of PAHs catalyzed by the Schottky defect. This has important implications for studying the chemical evolution of these molecules in the ISM and the solar system.

PAHs and C_{60} adsorbs with high stability on the Fe and pristine (010) forsterite surfaces with respect to Ni one. The adsorption of these species is driven by the number of atomic interactions with the surface and the surface area of the molecule. The Schottky vacancy surface showed different reactivity with respect to pristine and transition metal surfaces. This is due to the orientation of the PAHs adsorbing onto the surface. The parallel adsorption with respect to the surface leads to strong adsorption and chemisorption of naphthalene, anthracene, fluoranthene, benzocoronene, and fullerene with the formation of stable C-O and C-Si covalent bonds. Pyrene and coronene prefer to be only physisorbed forcing the vacancy to reconstruct (local bond formation between the atoms) their Si and O atoms, whereas the fullerene cage is stabilized by the formation of covalent bonds.

The perpendicular adsorption of PAHs onto the Schottky vacancy surface leads to the breaking of the C-H bond of PAHs through an exoergic and barrierless process. This effect is promoted by the formation of Frustrated Lewis Pairs (FLP) in the vacancy. These FLPs are localized Lewis acids and bases that cannot bind due to geometrical hindrance and, hence, this causes the strong catalytic activity of the vacancy surface.

The Schottky vacancy has shown great catalytic potential that might trigger the breakdown reaction of PAHs in asteroidal settings. This, thus, has great implications for understanding the organic inventory formation

of the solar system.

1.5.   Future Perspectives

This study carried out during the four years of this PhD contributes to identifying the role of linear and defective PAHs in molecular hydrogen production and partially answers the question: What is the role of interstellar molecules in the evolution of the Universe?

The employing of accurate computational methods to study the organic evolution of PAHs on minerals is the starting point that can be used as guidance for future studies. This will contribute to answering the question: How are PAHs related to the molecular inventory of the Earth and the terrestrial planets in the solar system? Future experimental studies using sophisticated techniques such as scanning electron, tunneling microscopy, and atomic force microscopy (SEM, STM, and AFM respectively), will help to obtain images of the local density of state of those PAHs on the mineral surface, whereas temperature-programmed desorption (TPD) will estimate their binding energy to the surface.[2] This will help to further verify and confirm the accuracy of the periodic DFT-D4 method employed in this thesis.

Future quantum chemistry development, which I will personally carry out during my post-doc at Chicago University, of multi-reference methods on periodic systems will open a new future frontier for astrochemistry. Specifically, further development of density matrix embedding theory[103] for periodic systems will allow the inclusion of multi-reference methods to accurately model strongly correlated systems such as the adsorption and reaction of PAHs on minerals containing transition metals. On top of this, future studies on surrogated machine learning methods[104] will contribute to correctly predict the structure of defects in solid materials, such as forsterite, that are not in thermodynamic equilibrium (*e.g.*, in the ISM environment). This cannot be predicted using only chemical intuition such as the case of amorphous materials and the formation of reconstructions of the atoms in the defect.[104]

On the astronomical side, the launch of the James Webb Space Telescope (JSWT) with its high spatial and spectral resolution and its high sensitivity will allow us to characterize PAHs in protoplanetary disks. As the PAH emission is sensitive to the local physical conditions (*e.g.*, temperature and pressure), this will contribute to answering the key question: how can molecules be used to probe the Universe?[23,105,106] Moreover, combining computational, experimental, and observational studies will shed light on the formation, diffusion, and chemical activation of PAHs from the ISM to the solar system. Thus, this will clarify the link between interstellar PAHs and the organic inventory of meteorites. Future studies will need to address the IR characterization of PAHs with defects (*e.g.*, Stone-Wales) in

support of future JSWT observations.

Studies on the hydrogenation sequence of mineral-supported PAHs might further explain the formation of complex organic molecules in interstellar environment. Moreover, data from NASA's missions (OSIRIS-REx[107] and Lucy[108]) will further support future theoretical studies on shedding light on the catalysis of PAHs during the aqueous alteration of asteroids, specifically their role in catalyzing the proton exchange with the mineral as well as their role as precursors of complex organic molecules. In particular, the OSIRIS-REx mission – launched by NASA in 2016 – will return about 60 grams of asteroid material (asteroid 101955 Bennu) to Earth in September of 2023. Detailed analysis of its mineral and carbonaceous content may shed further light on the organic composition of primitive objects in the solar system.

CHAPTER 2

SUPERHYDROGENATION OF PENTACENE: THE REACTIVITY OF ZIGZAG-EDGES

D. Campisi, F. D. S. Simonsen, J. D. Thrower, R. Jaganathan, L. Hornekær, R. Martinazzo and A. G. G. M. Tielens, *Phys. Chem. Chem. Phys.*, **2020**, *22*, 1557-1565

Abstract. Investigating the hydrogenation of carbonaceous materials is of interest in a wide range of research areas including electronic device development, hydrogen storage, and, in particular, astrocatalytic formation of molecular hydrogen in the universe. Polycyclic Aromatic Hydrocarbons (PAHs) are ubiquitous in space, locking up close to 15% of the elementary carbon. We have used thermal desorption measurements to study the hydrogenation sequence of pentacene from adding one additional H to the fully hydrogenated pentacene species. The experiments reveal that hydrogenated species with an even number of excess H atoms are highly preferred over hydrogenated species with an odd number of H atoms. In addition, the experiments show that specific hydrogenation states of pentacene with 2, 4, 6, 10, 16 and 22 extra H atoms are preferred over other even numbers. We have investigated the structural stability and activation energy barriers for the superhydrogenation of pentacene using Density Functional Theory. The results reveal a preferential hydrogenation pattern set by the activation energy barriers of the hydrogenation steps. Based on these studies, we formulate simple concepts governing the hydrogenation that apply equally well for different PAHs.

2.1. Introduction

Polycyclic aromatic hydrocarbons (PAHs) are an important class of carbon bearing molecules which are ubiquitous in the universe and lock up close to 15% of the cosmic carbon.[105] PAHs also play an important role in the chemistry of space.[8] The role of PAHs in the formation of H_2, the most abundant molecule in the universe, in the interstellar medium (ISM)

has been studied extensively. [17,41,109–112] PAHs are of general interest to the scientific community due to their pollutant and carcinogenic properties in terrestrial environments. [113] In this context, the reduction (hydrogenation) sequence that leads to the formation of aliphatic compounds [114] and the reduction of PAHs by metal free catalysts [115] have been studied, showing that the hydrogenation of these compounds leads to a less toxic mixture of saturated and unsaturated species. Owing to their photo-physical and structural properties, PAHs are also of interest for applications in hydrogen storage [116] and in optoelectronic devices. [117–120]

In this work, we focus, specifically, on one specific kind of linear catacondensed PAH, pentacene ($C_{22}H_{14}$), representative of a class called acenes. These compounds, consisting of a linear row of condensed six membered rings, [121] are characterized by zig-zag edges and they are representative of the smallest graphene nanoribbon. Zig-zag edges are a structural repetition of carbon atoms already bound to a single hydrogen atom, well known in the literature as "solo sites", [26] and bridge carbon atoms that are not bound to any hydrogen atoms. The zig-zag edges are important in astrophysics since they have strong infrared signatures that have been clearly detected in astronomical spectra. [122]

In contrast to catacondensed PAHs such as the acenes, some pericondensed PAHs (*e.g.* coronene) have no zigzag edges and their structure is characterized by duo carbons (two adjacent hydrogenated carbon sites) with strong CH modes in the 12-13 μm range. [29,123] Both catacondensed and pericondensed PAHs are susceptible to hydrogenation by hydrogen atoms under interstellar conditions, but the hydrogenation sequence differs due to their different structures. [18,40] For instance, a recent study demonstrated that the hydrogenation sequence of coronene, a pericondensed PAH, starts from the duo carbons [40] with delayed hydrogenation of the other carbon sites. For catacondensed species, the hydrogenation sequence begins from the central aromatic ring, saturating both inner and edge carbons. [18,124]

Superhydrogenated PAHs are important since they might be responsible for the formation of molecular hydrogen in Photodissociation Regions (PDRs). [125] PDRs are regions where the ultraviolet radiation from nearby bright stars influences the chemical and physical properties of the present molecular structures. [34] It is well appreciated that, because of the high UV flux, molecular hydrogen has to be rapidly reformed and that the normal routes considered for H_2 formation in the ISM do not suffice to account for its observed abundance. [33,126] As astronomical observations have revealed a spatial correlation between the H_2 formation rate and interstellar PAHs emission in these regions, PAHs have been suggested as possible catalysts for H_2 formation. [126,127] Different mechanisms have been studied in order to understand the formation of molecular hydrogen on PAHs, including reactions between two chemisorbed atomic hydrogen atoms through Langmuir-Hinshelwood (LH) and Eley-Rideal (ER)

mechanisms. These mechanisms have been studied for pyrene[128] and for coronene,[17,110] demonstrating that Eley-Rideal abstraction is a viable pathway for PAH catalyzed molecular hydrogen formation. Moreover, Rasmussen[124] studied the correlation of the increase in hydrogen binding energy with increasing zigzag edge length, using several acenes with different length as models. Therefore, it is crucial to study the aromatic–aliphatic character of PAHs when they are in a hydrogen rich environment in order to shed light on the sequence that leads to the so called "Magic Numbers" in the hydrogenation sequence of these species.[129]

This study aims to determine and understand the hydrogenation sequence of pentacene that leads to complete superhydrogenation of the molecule, using a combination of experimental and theoretical techniques. Specifically, temperature programmed desorption (TPD) is employed to directly determine the sequence of products of hydrogen addition to pentacene while density functional theory (DFT) calculations are used to investigate the hydrogenation sequence. This also serves as a test of simple concepts that may be applicable to other aromatic species featuring a bipartite lattice (*e.g.* carbon sp^2 structured as a graphene lattice).

2.2. Experimental and Theoretical Methods

2.2.1. Thermal Desorption Measurements

Experimental investigations of superhydrogenation of pentacene were conducted using temperature programmed desorption (TPD) measurements under ultra high vacuum (UHV) conditions; p < 10^{-9} mbar. A few multilayers of commercially available pentacene ($C_{22}H_{14}$; Sigma-Aldrich; triple-sublimed grade, ≥99.995%) were deposited onto highly oriented pyrolytic graphite (HOPG), held at 290 K, using a home-built Knudsen-type effusion cell. The HOPG substrate was cleaved in air prior to mounting and then annealed in UHV to 1100 K before each measurement. Typically 2-3 pentacene multilayers were obtained after 2 minutes deposition with the molecular doser at 135 °C (408 K). A monolayer could then be consistently produced by annealing the sample to 330 K for 5 minutes, removing the multilayers.

The monolayer of pentacene on HOPG was then exposed to a beam of atomic hydrogen (H) using a hydrogen atom beam source (HABS).[130] The HABS was operated at ≈ 2200 K, producing a hot atomic H beam which was subsequently cooled collisionally, through a quartz nozzle, to an estimated temperature of ≈ 1400 K.

TPD measurements were performed with a linear ramp of β =1 K s^{-1} until reaching 1100 K. To mass-selectively detect the species that leave the surface a quadrupole mass spectrometer (QMS) (Extrel CMS LLC) was used, scanning the range 258-340 atomic mass units (amu)/charge. The

TPD spectra within the given mass range are integrated and averaged over the relevant desorption temperature range to give the presented mass spectra.

2.2.2.   Density Functional Theory Calculations

Theoretical investigations were conducted using density functional theory (DFT) as implemented in the Gaussian 16 software suite.[131] In order for our calculations to have sufficiently high accuracy, we used the exchange correlation functional M06-2X.[77] This functional has been proven to provide an accurate description of PAHs hydrogenation since it has been found to be in close agreement with coupled-cluster calculations.[40] All calculations were carried out using the unrestricted (UHF) formalism. We employed the new pcseg-1[132] basis set, a segmented polarization consistent double zeta basis set optimized for DFT. All geometries were optimized using the Berny algorithm[133] and, in order to characterize the minima and saddle points, normal modes were analyzed within the harmonic approximation. All energies were corrected in order to reduce the basis set superposition error (BSSE) using the counterpoise scheme[100,134] implemented in Gaussian 16. We employed the molden[135,136] software package to visualize molecular structures and normal modes.

The theoretical part of this work is divided into two sections: the first describes the sequence of H addition that leads to fully hydrogenated pentacene while the second describes the hydrogenation sequence of superhydrogenated species based on a binding energy and energy barrier analysis.

The binding energies are defined as:

$$E_{bind} = [(E_{\mathrm{H}} + E_{\mathrm{reagent}}) - E_{n\mathrm{H–pentacene}}] \tag{2.1}$$

E_{bind} is the binding energy, E_{H} is the energy of atomic hydrogen in gas phase, E_{reagent} is the energy of the reactant that is interacting with the atomic hydrogen. Positive values of binding energies indicate exoergic processes, while negative values indicate endoergic ones.

The energy barriers are defined as:

$$E_{bar} = [E_{\mathrm{TS}} - (E_{\mathrm{H}} + E_{\mathrm{reagent}})] \tag{2.2}$$

E_{bar} is the energy barrier, E_{TS} is the energy of the transition state structure calculated as a first order saddle point, while E_{H} and E_{reagent} are the energy of the minima for the hydrogen atom and reactant, respectively. For the definition of transition state, the energy barrier is always positive.

Finally, the formation energy is defined as:

$$E_f = [E_{\mathrm{product}} - (E_H + E_{reagent})] \tag{2.3}$$

E_{f} is the formation energy, E_{product} is the energy of the product, while E_{H} and E_{reagent} are the energies of the hydrogen atom and reactant, respectively. In the case of the formation energy, negative values indicate exoergic

processes, whereas positive values indicate endoergic ones. For simplicity, we label the hydrogenated species of pentacene as nH-pentacene where n is a whole number (*e.g.* 3H-pentacene, is pentacene with 3 extra hydrogen atoms attached, namely $C_{22}H_{17}$). We use the term *syn* (*cis* position) when the extra hydrogen are chemisorbed on the same side of the molecule, while, we use the term *anti* for the hydrogens chemisorbed on opposite sides (*trans* position).

In order to gain broader insights into the hydrogenation process, the sequence of hydrogenation was rationalized with simple concepts derived from a tight-binding model where the most reactive site is related to the smallest π-coordination number (number of carbon atoms connected to a carbon center) and the highest hypercoordination number (number of second carbon atom neighbours that have the same coordination number) for closed-shell systems. [137] Attaching a hydrogen on a closed-shell system (*i.e.* all odd extra hydrogens chemisorbed) generates an unpaired electron (mid-gap state) that localizes preferentially in the *ortho-* or *para*-positions respect to the already extra hydrogen attached. Therefore, the odd hydrogenations were predicted using the coordination and hyper-coordination rule, whereas the even hydrogenations were predicted using the *ortho–para* localization. Finally, these simple rules were confirmed through the binding energy and energy barrier analysis. The latter are correlated by the Bell–Evans–Polanyi principle according to which larger energy barriers are associated with lower binding energies. [138,139]

2.3.   **Experimental Results**

In Fig. 2.1, mass spectra for pentacene monolayers exposed to increasing H atom fluences are displayed. The initial mass spectrum before hydrogenation can be seen in Fig. 2.1(a). In the mass spectrum prominent peaks are seen at masses: 278 amu (the pentacene molecule, $C_{22}H_{14}$), 280 amu (6,13-dihydropentacene (DHP), $C_{22}H_{16}$), 294 amu (6-hydroxypentacene $C_{22}H_{14}O$), and 308 amu (pentacenequinone (PQ), $C_{22}H_{12}O_2$). Mass 279 contains contributions from both the fragmentation of DHP during the ionization step in the QMS and from pentacene with the naturally occurring ring isotope ^{13}C (^{13}C is also seen in DHP as mass 281 in Fig. 2.1(a)). All masses detected below 278 amu, *e.g.* 276 amu, are ascribed to fragmentation in the QMS. The commercially available pentacene batches are known to have the oxidized species PQ as a main contaminant, [140] and more oxidised and/or superhydrogenated species are known to form when pentacene is exposed to air and light. [141] DHP is also present in commercially available pentacene and is known to be a byproduct of sublimation. [142]

Fig. 2.1(b)-(e) show the mass distribution of superhydrogenated pentacene after hydrogenation times of b) 180 s, c) 900 s, d) 1800 s and e) 54000 s (17 hours). Fig. 2.1(b) shows a small degree of hydrogenation
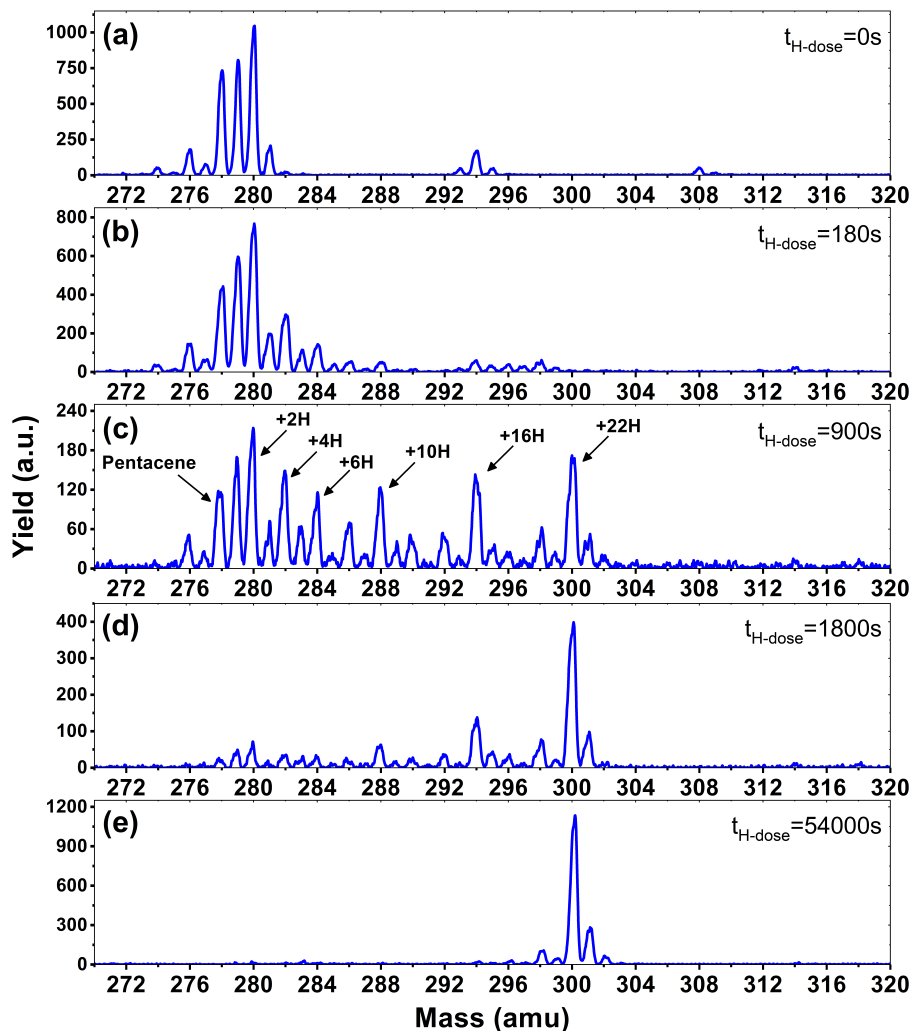
Figure 2.1: Mass spectra showing the mass distribution of a pentacene monolayer after different H-atom exposure times presented in the figure. (a) Mass distribution of a monolayer of pentacene (mass 278) with the prominent contaminants dihydropentacene (mass 280) and 6-hydroxypentacene (mass 294). (b)-(e) Mass distributions shifting towards higher masses with increasing H atom fluences, eventually reaching mass 300 corresponding to fully superhydrogenated pentacene.

for both the pentacene and the oxidized species. The species with even masses such as 280, 282 and 284 are seen to be more prominent than the odd. This is consistent with the fact that superhydrogenated pentacene

molecules with an odd mass will be open-shell, and hence exhibit a radical behaviour and therefore be more reactive towards the addition of a subsequent H atom. By contrast, the even mass species are less prone to further hydrogenation. The odd-even oscillation is clearly visible in Fig. 2.1(c) where the mass distribution covers the entire range from pristine pentacene, mass 278, to fully superhydrogenated pentacene, $C_{22}H_{36}$, with mass 300. While the odd-even oscillation is clearly visible, it is also evident that some specific species (with specific superhydrogenation degrees) appear more prominently than others. The most prominent species are: 280 (+2H), 282 (+4H), 284 (+6H), 288 (+10H), 294 (+16H) and 300 (+22H), also indicated in Fig. 2.1(c).

After extended H atom exposure, see Fig. 2.1(d)-(e), the mass distribution is pushed towards mass 300, corresponding to fully superhydrogenated pentacene $C_{22}H_{36}$. In Fig. 2.1(e) the peak at mass 300 completely dominates the spectrum. The smaller peaks seen at masses 301-302 and 298-299 are ascribed to the ^{13}C isotope and fragmentation in the QMS, respectively. Hence, the fact that it is possible to drive the entire mass distribution to fully superhydrogenated pentacene for long H deposition times (see Fig. 2.1(e)) reveals that H atom addition reactions dominate over H atom abstraction for superhydrogenated pentacene.

2.4.   Theoretical Results

2.4.1.   Hydrogenation Sequence

The hydrogenation sequence found for pentacene is schematically shown in Fig. 2.2. At the first hydrogenation, the carbon sites more inclined to be hydrogenated are C1 and C6 (Fig. 2.3(a)) with the highest hyper-coordination. The least inclined carbon atoms to be hydrogenated are the inner carbons C5 and C14 (Fig. 2.3(a)) since they have the highest coordination numbers. The carbon atoms C13 and C12, have intermediate propensity to be hydrogenated (a detailed description of the sequence is reported in the Appendix). The first hydrogenation and all odd hydrogenation steps are the single addition of a hydrogen atom to a closed-shell species and are, therefore, associated with the formation of a mid-gap state (singly occupied molecular orbital) which is represented schematically in Fig. 2.3(b). The mid-gap state generated is in a radical open-shell system and will react readily with a radical species such as a further hydrogen atom. The mid-gap state formation increases the electron affinity of the carbon sites where an unpaired electron is localized, but this affinity decreases as the distance from the hydrogenated carbon sites increases.[137] For instance, the highest probability that an atomic hydrogen will be chemisorbed are those carbon sites nearby the already extra hydrogen chemisorbed. This tendency is illustrated in Fig. 2.3(b). Hence,
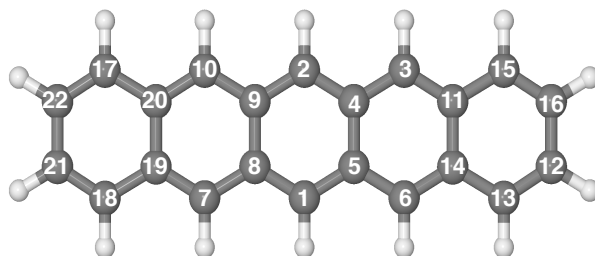
Figure 2.2: Optimized molecular structure of pentacene in balls and sticks. The numerical labels reported indicate the full hydrogenation sequence of pentacene.
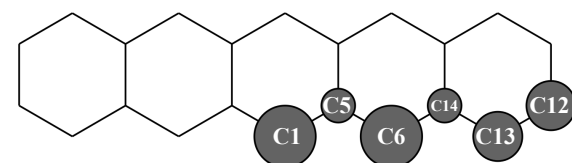
(a)
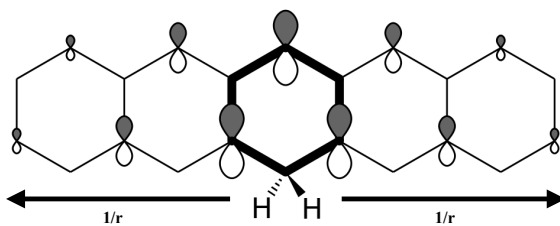
(b)

Figure 2.3: (a) Schematical representation of the affinity of the carbon atoms to be chemisorbed by the first hydrogen atom. Larger balls indicates higher hydrogenation affinity. (b) Graphical representation of localized mid-gap states for the second hydrogenation. The arrows show decreasing effect of mid-gap state with increasing distance from the first hydrogenated carbon site.

for even hydrogenation reactions, the sequence is led by *ortho-para* local-ization of the unpaired electron by the mesomeric effect with respect to the already chemisorbed extra hydrogen. Therefore, the mid-gap state drives the reactivity to specific carbon sites in the molecule. The second atomic hydrogen might chemisorb in *ortho* or in *para* with respect to the already chemisorbed extra hydrogen (Fig. 2.3(b)).

The hydrogenation sequence follows a simple rule: first hydrogenation of the carbon in the solo position (CH bonded H where adjacent C atoms do not have a H), followed by hydrogenation of the neighboring inner carbons (bridge carbons). The latter step reflects that an inner carbon is under-coordinated upon hydrogenation of a neighbour carbon site. This is in line with the study carried out by Klærke *et al.*[143] and Bonfanti *et al.*[137] confirming that it is easier to hydrogenate edge carbons than bridge ones.

The highest binding energy found is associated with the chemisorption of the extra hydrogen in position 2 (Fig. 2.2), which is *para* with respect to carbon 1. Once carbons 1 and 2 are hydrogenated, two topologically disconnected systems are generated. The molecule now consists of two naphthalene units, bound to the hydrogenated non-aromatic ring, out-lined in bold in Fig. 2.4(a). These two naphthalene units are equivalent

(a)

(b)
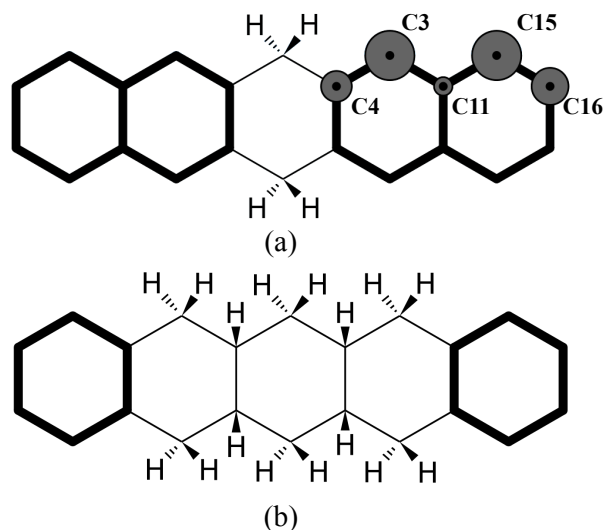
Figure 2.4: (a) Graphical representation of disconnected naphthalene units and their propensity to be hydrogenated. (b) Graphical representation of disconnected benzene units.

and therefore, we considered the chemisorption of the third hydrogen atom on C3 (Fig. 2.4(a)) which has the highest hyper-coordination. Fig. 2.4(a) also reports graphically the propensity of the carbon atoms to be hydro-genated (details reported in the Appendix) where it is clearly shown that

C3 and C15 have higher affinity (high hyper-coordination) compered to the inner carbon site C11 as the latter has the highest coordination number, while, C16 and C4 have lower propensity to be hydrogenated since these carbon sites have lower hyper-coordination. The fourth hydrogen atom, then, chemisorbs on the least coordinated carbon site (labeled C4 in Fig. 2.4(a)) that is a bridge carbon one. The sequence, schematically shown in Fig. 2.2, continues with the system tending to preserve the aromaticity of individual rings as long as possible. Moreover, during the hydrogenation, disconnected systems are created, as naphthalene and benzene rings (shown in bold in Fig. 2.4(b)), and the hydrogenation sequence might change accordingly. A complete overview of the sequence is reported in the Appendix.
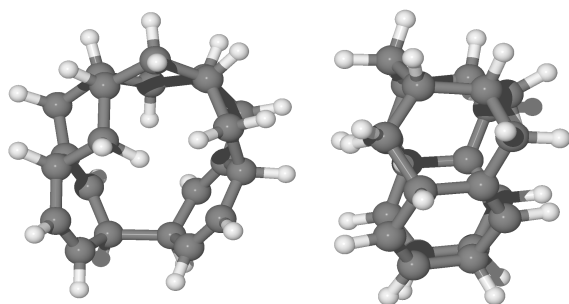
Figure 2.5: Front view and side view, respectively, of the optimized molecular structure in balls and sticks of quasi-nanotube formed by the chemisorption of 12th hydrogen on a less reactive carbon site of *syn*-11H-pentacene (see section 12th Hydrogenation in the Appendix).

2.4.2.   *Syn* and *Anti* Conformation

In our experiments, a pentacene molecule is exposed to a flux of hydrogen atoms on only one side as the monolayer is deposited on a graphite surface. Therefore, one could argue, from a geometric perspective, that superhydrogenation only occurs on one side. Initially, we studied the reaction sequence by chemisorbing hydrogen atoms on single side of the molecule (*syn* path). The complete hydrogenation of pentacene leads to the formation of a bent structure as reported in Fig. 2.7. As it may be relevant for the hydrogenation of gaseous pentacene, we also considered binding the hydrogen atoms to the bridging carbon atoms of the molecule on alternat-
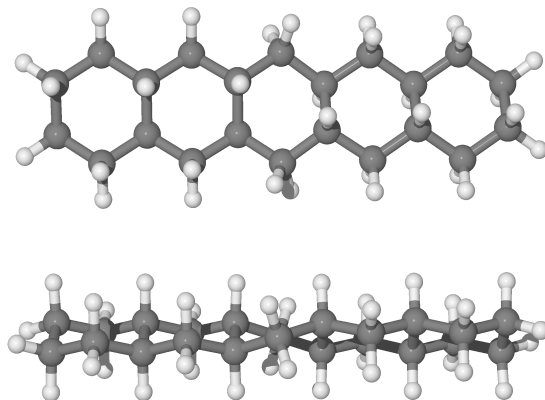
Figure 2.6: Side view and top view of optimized molecular structure of *anti*-22H-pentacene in balls and sticks.

ing sides of the molecular plane (*trans*-hydrogenation), referred to here as "*anti* position", and shown in Fig. 2.6. The *anti* conformation in the case of pentacene is relevant only in carbon sites where no hydrogen atoms are already bound. In fact, in the case of edge carbons where two hydrogen atoms are attached, the hydrogen atoms are topologically equivalent.

The hydrogenation sequence for the *anti* path begins with the 4th hydrogenation since the hydrogen atoms already chemisorbed are topologically equivalent. Specifically, the hydrogen atom may chemisorb on carbon 4 (Fig. 2.2) from the bottom side with respect to the plane of the molecule. The addition of the next hydrogen atom to carbon 5, proceeds from the top of the molecule with respect to the molecular plane. Hence, if the hydrogen atom chemisorbs on the bottom side of the molecule, specifically on carbon atoms 4, 8, 11 and 20, we can observe a more linear structure with all rings in arm-chair conformation. A complete description of why those hydrogenated species are formed, based on the analysis of binding energies and energy barriers, is reported in the next section and a more complete description of the sequence is reported in the Appendix.

2.4.3. Quasi-Nanotubular Formation

Furthermore, the formation of these topologically disconnected systems may cause an intramolecular homo-coupling (*i.e.* formation of C-C bond inside the same molecule). Specifically, we found that for radical species, *syn*-9H-pentacene, *syn*-11H-pentacene, *syn*-13H-pentacene and *syn*-15H-pentacene (see Appendix), further hydrogenation takes place in the ring disconnected from the already present unpaired electron and an

intramolecular radical-radical reaction will occur leading to the formation of a nanotubular structure during the chemisorption of the 12th hydrogen radical (*e.g.* that shown in Fig. 2.5). The disconnected systems do not allow the localization of the unpaired electron within the same molecule and thus results in the formation of such a nanotubular structure. As discussed in the Appendix, several nanotubular structures could be formed during the hydrogenation process.

Table 2.1: Formation energy (ΔE_f) of quasi-nanotubes from pentacene with n numbers of extra H atoms chemisorbed on the same side.

Hn	ΔE_f (eV)
10	-2.39
12	-1.20
14	-2.50
16	-2.70

Table 2.1 provides the exoergic formation energies, indicating that the formation of quasi-nanotubular structures is thermodynamically favourable, especially during the addition of the 16th hydrogen atom in a less reactive carbon site (more details are reported in the Appendix). Moreover, the formation of these nanotubular structures occurs only in the gas-phase and involves an intramolecular homo-coupling (formation of a carbon bond within a molecule). In a similar study, the formation of intermolecular homo-coupling (formation of a carbon bond between two molecules) between two pentacene molecules on Au(111), resulting from superhydrogenation, has been investigated.[144] In this case, intermolecular homo-coupling dominates on a surface. This process is not important in the gas phase as collisions are rare. Instead, in the gas phase, intramolecular nanotubular formation dominates.

2.4.4. Analysis of Superhydrogenated Species

Fig. 2.8 shows the trend of energy barrier for the *syn* and *anti* path. We do not expect energy barriers of activation for odd to even hydrogenation since 1H-pentacene is an open-shell radical ready to react through a barrier-less reaction with another radical (atomic hydrogen), which is in line with the studies conducted on coronene and pyrene.[17,40,128] From chemical principles, we expect that this is a general rule and we have focused our calculations on determining energy barriers involved in the formation of odd hydrogenated species.

Syn Path. Pentacene is particularly reactive for the first two hydrogenation reactions, as indicated by the presence of 6,13-dihydropentacene (*syn*-2H-pentacene) as a contaminant in the experiments. Once *syn*-2H-pentacene is formed, hydrogenation proceeds until larger energy barriers
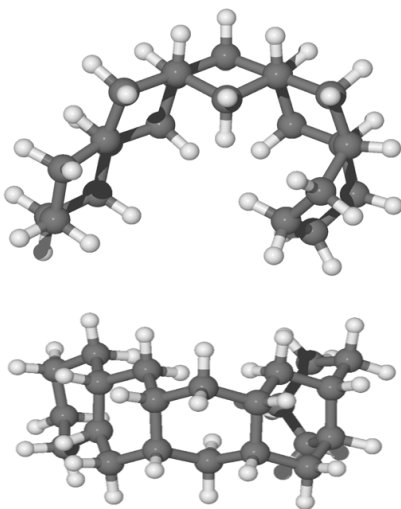
Figure 2.7: Side view and top view of the optimized molecular structure of *syn*-22H-pentacene in balls and sticks.
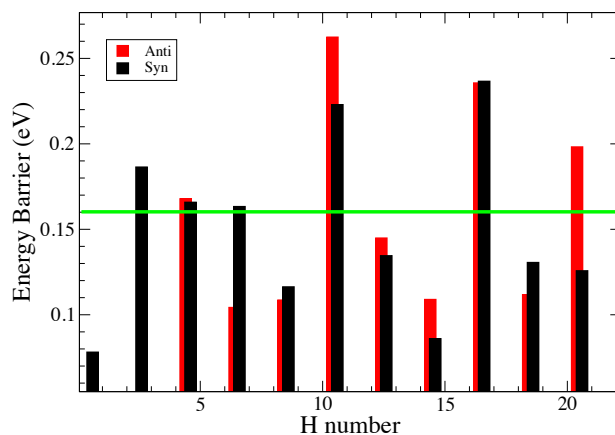
Figure 2.8: Calculated energy barriers in the hydrogenation from an even to an odd number of H's on pentacene. H number indicates the number of extra hydrogens chemisorbed on pentacene. The green line represents energy barrier relevant under our experimental conditions. Note that there is no energy barrier for the hydrogenation from an odd to an even number of H atoms.

are difficult to overcome at the experimental conditions. Specifically, energy barriers higher than 0.16 eV (green line in Fig. 2.8) are less accessible in our experiment with a 1400 K atomic hydrogen beam. In fact, the peaks related to +2H, +4H, +6H, +10H, +16H are observed in the mass spectra reflect the difficulty to overcome barrier heights for further hydrogenation processes.

Syn-21H-pentacene can react through a barrierless reaction with another radical to produce the fully hydrogenated pentacene with a mass of 300 amu. The peak corresponding to mass 300 amu becomes prominent as exposure times to atomic hydrogen increases. The presence of magic numbers in the hydrogenation of pentacene reflects that the energy barriers are particularly high whenever a new aromatic ring has to be attacked.
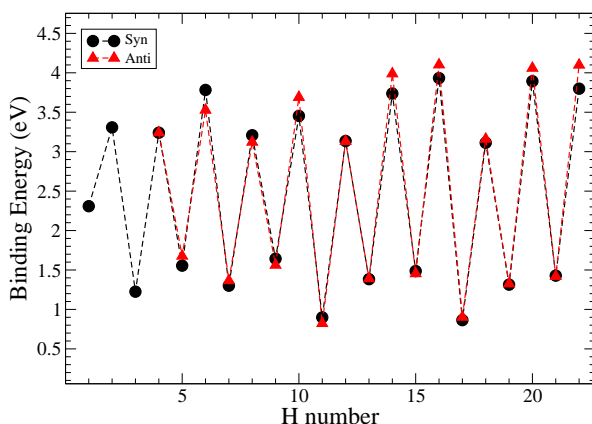
Figure 2.9: Trend of binding energies for the hydrogenation of pentacene for two different paths: *syn* and *anti*. H number indicates the number of extra hydrogens chemisorbed on pentacene.

The values of binding energies reported in Fig. 2.9 suggest that all even hydrogenated species are more favourable than the odd hydrogenated species and have binding energies between 3 and 4.5 eV. The species with an odd number of extra hydrogen atoms attached display smaller binding energies between 2.5 eV and 1 eV. This trend was studied and confirmed on several neutral PAHs, [17,124,128] while for the cation the opposite is found as expected for an open shell species. [129,145] Within the odd and even sequences there are small variations in binding energy which are due to high electron affinity of these carbon sites toward the hydrogenation. However, these differences are small and, at the temperature of the experiment, these are unlikely to be relevant for the discussion of the magic numbers.

Our study of the binding energies reveals that superhydrogenation is energetically favorable for all species. The odd-even pattern and the presence of magic numbers in the even sequence reflects the pattern of activation barriers in the production of odd species from even ones. The lowest energy barriers found in this work are related to the chemisorption of the hydrogen on aliphatic carbon and, in particular, for the case of the formation of *syn*-9H, *syn*-13H, *syn*-15H and *syn*-19H-pentacene.

Anti Path. The hydrogenation sequence in gas phase space environments may reflect the fact that both sides of the pentacene molecule can be attacked by radical hydrogen atoms. Therefore, we investigated an alternative path where the hydrogen atoms chemisorbed on the bridge carbons are in *anti* conformation respect to the plane of the molecule, as shown in Fig. 2.6. The energy barriers for the addition of hydrogen atoms to the *anti* hydrogenated pentacene follow the same trend as that of the *syn* path with some significant exceptions. Table 2.2 reports the difference in en-

Table 2.2: Difference of energy barriers between the *anti* and *syn* hydrogenation ($\Delta E^{anti}_{bar} - \Delta E^{syn}_{bar}$). H$n$ indicates the number of extra hydrogens chemisorbed on pentacene.

Hn	$\Delta E^{anti}_{bar} - \Delta E^{syn}_{bar}$ (eV)
7	-0.070
11	0.039
13	0.010
15	0.019
21	-0.072

ergy barrier between *anti* and *syn*. The trend revels significant differences between *syn* and *anti* that cannot explain the magic numbers found in our experiment. Specifically, based on this trend we should not expect the presence of *anti*-6H-pentacene due to the lower barrier respect to the *syn* counterpart, whereas we might expect the *anti*-20H-pentacene due to the difficulties to a further hydrogenation. For a complete overview, see Fig. 2.8.

The *anti* path has the same trend in binding energies as the *syn* path. We show that *anti*-6H, *anti*-10H, *anti*-12H, *anti*-14H, *anti*-16H and *anti*-20H-pentacene have large binding energies (larger than 3.4 eV), while *anti*-11H and *anti*-17H have lower binding energy by 1 eV. Table 2.3 shows the difference of binding energies between *syn* and *anti* hydrogenation, indicating that the *anti* chemisorption of hydrogen atoms might be more favourable for some hydrogenations.

Some hydrogenation steps are not included in Table 2.3 as the energy differences are small (~0.007 - 0.09 eV). The observed pattern of magic numbers in the hydrogenation of pentacene adsorbed on graphite is fully consistent with our expectation that, because of steric reasons, hydrogenation will occur following the *syn* sequence. Specifically, we observed

Table 2.3: Difference of binding energies between the *syn* and *anti* hydrogenation of pentacene ($\Delta E^{anti}_{bind} - \Delta E^{syn}_{bind}$). H$n$ indicates the number of extra hydrogens chemisorbed on pentacene.

Hn	$\Delta E^{anti}_{bind} - \Delta E^{syn}_{bind}$ (eV)
5	0.12
10	0.24
14	0.25
16	0.17
20	0.16
22	0.30

a dominant peak at the mass of 6H-pentacene and only a minor peak corresponding to 20H-pentacene in accordance with the *syn*-sequence, but not the *anti*-sequence.

2.5.   **Astrophysical Implications**

Massive stars have a profound influence on their nascent clouds. Specifically, far-ultraviolet photons with energies in the range 6 to 13.6 eV do not have enough energy to ionize atomic hydrogen but can photodissociate molecules and heat the gas in the surrounding molecular cloud.[146] Hydrogen is atomic in the surface layers of these so-called photodissociation regions (PDRs) while carbon is singly ionized (C$^+$). Going into the PDR, the dissociating and ionizing far-UV photons are attenuated by small dust grains and atomic hydrogen is converted into H$_2$ and, eventually, C$^+$ into CO. Gas temperatures in the atomic H and molecular H$_2$ zones of PDRs range from 200-500 K depending on star involved, while the dust is 30-75 K. Deeper in, where CO has formed, the gas cools down to 40 K. Observationally, PDRs shine brightly in the vibrational transitions of UV-pumped PAH molecules, the far-infrared fine-structure transitions of abundant atoms (C$^+$, O), the ro-vibrational transitions of H$_2$, and molecular rotational lines of *e.g.*, CO.[146]

Analysis of this data has revealed that H$_2$ must be very efficiently made in these surface layers.[126] This is not understood as the dust in PDRs is too warm to allow efficient H$_2$ formation.[33] This observed efficient H$_2$ formation in PDR surfaces has been ascribed to the catalytic activity of PAHs and detailed studies have appeared in the astronomical literature.[41,147–149] The present study is geared towards elucidating the interaction of atomic H with PAHs and quantitative measuring of the molecular parameters involved that are needed for these astronomical models. Our results show that addition of the first two hydrogens will be very efficient as the energy barriers involved are small and the kinetic temperature of the gas is quite high. However, adding the third hydrogen has a prohibitive energy barrier

(Fig 8) even at gas temperatures relevant for PDRs (200-500 K). To estimate the importance of quantum mechanical tunneling, we have evaluated the cross-over temperatures for the reactions involved and these are reported in the Appendix. Typically these vary from 136 to 213 K and hence, quantum mechanical tunneling is not expected to play a role in the warm gas of PDRs but it may play more of a role in cold molecular cloud. We note also that the binding energies of these extra H's are relatively low and these are readily lost in strong radiation field of a PDR.[41,148] Detailed astronomical modeling will be required to assess the balance of reactions of atomic H with PAHs and the UV photolysis in a PDR environment as well as the importance of hydrogenation of PAHs in PDRs for the formation of H_2. The experimental and theoretical results reported here will form the basis for such a modeling effort. We defer this to a follow up study that will be reported in an appropriate journal.

2.6.   Discussion and Conclusion

The experimental and theoretical study conducted here has elucidated the steps that will be relevant for the hydrogenation of pentacene. We do stress that the goal of this study is to provide fundamental parameters, as energy barriers and binding energies, useful for astronomical modeling such as Andrews *et al.* addressed for coronene's family.[41] In fact, in space, superhydrogenation of PAHs is a balance between H addition and UV photolysis, energy barriers and binding energies will each play their role in setting the hydrogenation pattern of PAHs in space.

Specifically, we found that even hydrogenated species of pentacene are more preferred than the odd hydrogenated species since chemisorbing odd hydrogens on pentacene leads to the formation of reactive open-shell radicals. These extremely reactive species interact with further hydrogen atoms forming preferred species (species with magic numbers seen to dominate in mass spectra). The analysis of binding energies and energy barriers carried out in this study have confirmed the validity of the hypercoordination and coordination rule (discussed in detail in the Appendix), demonstrating that these simple concepts are applicable to small condensed and linear systems. These concepts are validated for systems formed by hexagonal aromatic rings and are applicable during the hydrogenation sequence for all benzene-like structures that still present bipartite lattices. However, we emphasize that these simple concepts are useful tools and can guide the choice of hydrogenation sites, but they cannot replace a deeper analysis of binding energies and energy barriers. Specifically, energy barriers calculation provide insights into the hydrogenation sequence, showing which species are more likely to form. We found that the energy barrier required for hydrogenating an aliphatic carbon is lower (<0.13 eV) than the energy required for hydrogenating aromatic carbons

(up to 0.15 eV). Hence, the presence of magic numbers in the mass spectra are explained by the energy barriers rather than the binding energies. In fact, the absence in the mass spectra of the peaks corresponding to the masses of 12H, 14H, 18H and 20H-pentacene was confirmed by our theoretical calculations since a further hydrogenation (11H, 13H, 17H and 19H-pentacene) requires the highest energy barrier, up to 0.16 eV. Our theoretical results also suggest that both *anti* and *syn* confirmations are possible in the gas phase. The sequence found for the syn-path in our calculation matches the magic numbers found in the mass spectra for the hydrogenation of pentacene, whereas the *anti*-path might be more relevant for the hydrogenation sequence that will occur in the gas phase.

Furthermore, we noticed differences in the hydrogenation sequence that occurs in pentacene with respect to pericondensed PAHs such as coronene.[40] The hydrogenation scheme tends at first, in these aromatic molecules, to break the aromaticity of the central aromatic ring of pentacene through addition to solo sites. In contrast in coronene, where such sites are not present, this occurs for the aromatic rings located at the edges. Moreover, pentacene is more reactive at the first hydrogenation with a barrier of only 109 meV with respect to coronene.[40] As a last difference, coronene has a barrierless reaction for the addition of the last odd hydrogen. Therefore, zig-zag edges are significantly more reactive for the first hydrogen addition reaction with respect to pericondensed PAHs.

We also discovered a pathway that leads to the formation of quasi-nanotubular structures during the hydrogenation of pentacene in the gas phase. This is due to the formation of two topologically separated structures in the molecule. The two unpaired electrons located in two different systems cannot be shared any longer. Therefore, a spontaneous curling up of the structure occurs with the formation of a quasi-nanotube.

We discovered that the flexibility of the molecule provides extra structural stability with respect to more rigid molecules as coronene or graphene. Zigzag edges present on linear and flexible molecules may provide extra reactivity that may correlate the presence of H_2 with the formation of superhydrogenated species.

2.7. Appendix

In this appendix, we explain in detail the hydrogenation sequence that leads to the formation of *syn*-full-hydrogenated pentacene. We adopted the *syn* reaction sequence for the *anti*-path to enable direct comparison between two different routes. We assume that any variation in the sequence is due to the variation of the electronic structure when other positions are hydrogenated and that sequence does not change due to the orientation of the hydrogen on the molecule with respect to the molecular plane. For simplicity, we did not correct binding energies for ZPE and BSSE since

these binding energies are required only for justifying the selection rules for each hydrogenation step. The energy barriers are corrected at ZPE, but not for the BSSE, since frequency analysis is necessary in order to characterize saddle points.

Hydrogenation Sequence

1st Hydrogenation

Pentacene is a symmetric molecule ($C_{22}H_{14}$, D_{2h} point group) as shown in Fig. 2.10. Initially, due to the high symmetry of the molecule, there are six possible positions where the first additional hydrogen might chemisorb as shown by C(1a-1f) in (Fig. 2.10). We can distinguish between carbon atoms that are bound to a single hydrogen atom (edge carbons) and those at inner edge sites not bound to a hydrogen atom (bridge carbons). All edge carbons have a high coordination of 2 with C(1a), C(1b) and C(1d) having hyper-coordination values of 2. C(1c) is less hyper-coordinated with a value of one. The binding energies reported in Table 2.4 shows that C(1a) and C(1b) are the most reactive and exoergic sites and are thus preferred for the first hydrogen addition, in line with the hyper-coordination rule. The calculated binding energies are in agreement with those calculated by Rasmussen using PBE. [124] We note that the C(1a) site on pentacene is significantly more reactive than the edge sites of coronene which have a binding energy of 1.16 eV. [17]

Our results are in line with the study carried out by Bonfanti *et al.*[137] since a hydrogen atom prefers to bind in a site with a high hyper-coordination number as consequence of electronic localization in a re-normalized lattice. The difference in binding energy between C(1a) and C(1b) is 0.17 eV, while the energy barriers for chemisorbing hydrogen atoms on C(1a) and C(1b) are 0.078 eV and 0.097 eV, respectively. This means that both C(1a) and C(1b) are possible sites for the first additional hydrogen atom, but C(1a) site is preferred. The hydrogenated species through this addition is referred to as 1H-pentacene in the subsequent sequence.

2nd Hydrogenation

It is well known that the chemisorption of the first additional hydrogen atom results in a favourable addition for a second hydrogen atom through a barrierless reaction resulting in a high binding energy. This has been demonstrated previously for a range of neutral and cationic PAHs. [17,128,145] 1H-pentacene is an open shell radical with singlet multiplicity. The system is characterized by a mid-gap state generated by a singly occupied molecular orbital that will react readily through a barrierless radical-radical reac-

Figure 2.10: Side view and top view of the optimized molecular structure of pentacene. The alpha-numerical labels show the sequences of the possible carbon sites where an atomic hydrogen might chemisorb.

Table 2.4: Binding energies (ΔE_{bind}) for the hydrogenation of different carbon sites of pentacene. Binding energies (*) calculated by Rasmussen[124] are reported for comparison.

C site	ΔE_{bind} (eV)	Rasmussen[124]
C(1a)	2.61	2.40*
C(1b)	2.44	2.29*
C(1c)	1.81	1.79*
C(1d)	1.71	1.70*
C(1e)	0.93	0.86*
C(1f)	0.54	0.53*

tion with another radical species, such as a hydrogen atom. The mid-gap state generated is localized in the *ortho* and *para* positions with respect to the first added hydrogen atom, through Lewis resonance. This is confirmed by the trend in the calculated binding energies as shown in Table 2.5. We also considered addition to the meta positions. In this case, during the geometry optimization, the meta site hydrogen atoms were transferred from the bridge carbon to the neighbouring singly hydrogenated carbon site as shown by the red arrows in Fig. 2.11.

The calculated binding energy decreases for second addition sites far from the first hydrogenated carbon atom since the influence of the mid-gap state decreases with $1/r$. The calculations reveal that C(2a), in the *para* position, is most favourable site for the addition of a second hydro-

Figure 2.11: Side view and top view of the optimized molecular structure of 1H-pentacene. The alpha-numerical labels show the sequences of the possible carbon sites where a further atomic hydrogen might chemisorb.

Table 2.5: Binding energies (ΔE_{bind}) for the addition of a second extra hydrogen considering different carbon sites of 1H-pentacene.

C site	ΔE_{bind} (eV)
C(2a)	3.67
C(2b)	2.98
C(2c)	2.04
C(2d)	1.94
C(2e)	0.29

gen atom. The resulting product is 6,13-dihydropentacene (2H-pentacene) with two additional hydrogen atoms, a *para* configuration across the central hexagonal ring in a quasi-planar structure as shown in Fig. 2.12.

3rd Hydrogenation

The chemisorption of two extra hydrogen on the pentacene molecule results in a species consisting of two naphthalene units that are topologically disconnected in the same lattice. Since these two intramolecular napthalenes are equivalent and symmetric, we considered just five carbon sites for the chemisorption of the third additional hydrogen atom. C(3a) and C(3b) both present a hyper-coordination number of 2 and essentially equal binding energies (Table 2.6). Hydrogen chemisorption on either car-

bon site would be a valuable pathway to follow. Hence, we have selected to study the pathway initiated by hydrogen chemisorption on C(3a), but we expect that hydrogen chemisorption on C(3b) leads to comparable results. Sites (3d) and C(3c) have a hyper-coordination number of 1 and are, therefore, favourable for further addition. The calculated binding energies reported in Table 2.6, confirm the prediction of the hyper-coordination rule. The resulting structure of 3H-pentacene is a curved aromatic-aliphatic molecule, as shown in Fig. 2.13.
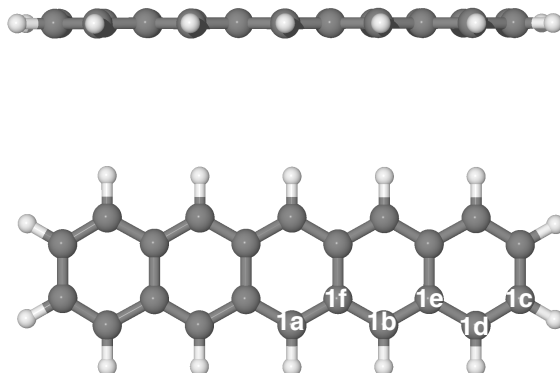

Figure 2.12: Side view and top view of the optimized molecular structure 2H-pentacene. The alpha-numerical labels show the sequences of the possible carbon sites where a further atomic hydrogen might chemisorb.

Table 2.6: Binding energies (ΔE_{bind}) for the addition of a third extra hydrogenation in different carbon sites of 2H-pentacene.

C site	ΔE_{bind} (eV)
C(3a)	1.47
C(3b)	1.43
C(3c)	1.20
C(3d)	1.03
C(3e)	0.35

4th Hydrogenation

With the formation of 3H-pentacene, a mid-gap state is again generated and localized in the associated *ortho* and *para* positions, highlighted in Fig.

2.13, as C(4a) and C(4b) sites, respectively. The difference in binding energy ($E_b\{4a\}$ - $E_b\{4b\}$) is 0.04 eV, as shown in Table 2.7. We considered also the binding of a hydrogen atom to the bridge carbon adjacent to C(4a). During the geometry optimization process the additional hydrogen atom was transferred to the C(4b) site, as shown by the red arrow in Fig. 2.13. We can, therefore, state that the C(4a) and C(4b) sites are most favourable for the addition of the fourth hydrogen atom, but we selected to follow the pathway initiated by hydrogen attachment on C(4a). Also in this case, we expect that hydrogen attachment on C(4b) leads to comparable results. Less reactive sites considered are C(4d) and C(4e), characterized by planar structures associated with low binding energies since the mid-gap state decreases with distance. The geometry optimization following a addition to site C(4c) results in the formation, of a five membered-ring and three membered-ring in a curved structure shown in Fig. 2.14 and labeled in yellow in order to indicate that the chemisorption of the hydrogen in this carbon site leads to the formation a different structure. This ring arrangement has a formation energy of -1.22 eV and it is unlikely to form and will therefore not be considered for further addition.
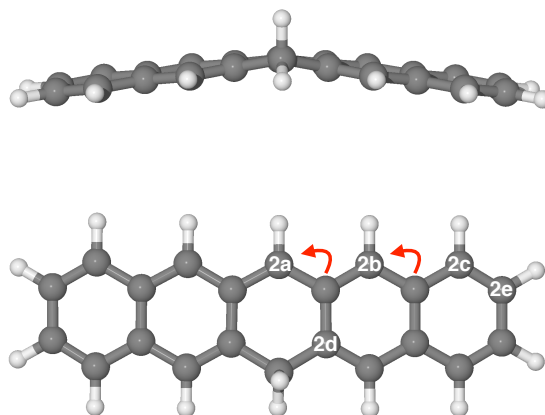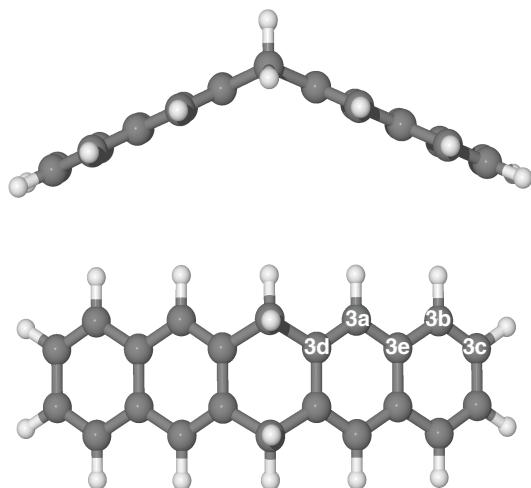

Figure 2.13: Side view and top view of the optimized molecular structure of 3H-pentacene. The alpha-numerical labels show the sequences of the possible carbon sites where a further atomic hydrogen might chemisorb.

5th Hydrogenation

In the case of 4H-pentacene the coordination rule dominates with respect to the hyper-coordination rule since the addition of the 4th hydro-

Table 2.7: Binding energies ΔE_{bind} for the addition of a fourth extra hydrogenation in different carbon sites of 3H-pentacene.

C site	ΔE_{bind} (eV)
C(4a)	3.62
C(4b)	3.58
C(4d)	0.72
C(4e)	0.24
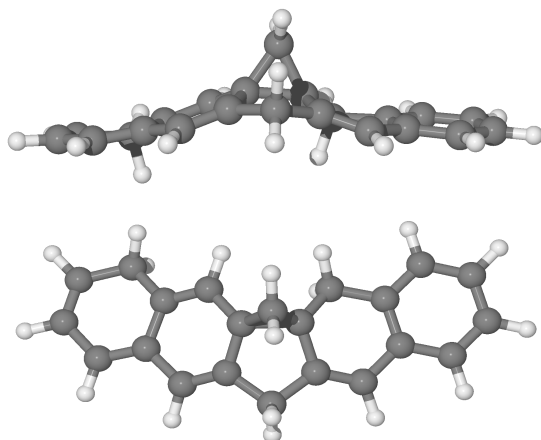
Figure 2.14: Optimized molecular structure of 4H-pentacene with a structure formed by the presence of five and three membered-rings.

gen atom results in a reduction in the coordination of the adjacent bridge carbon site, labeled 5a in Fig. 2.15, hence the fifth additional hydrogen atom prefers to bind on C(5a). This prediction is confirmed by the calculated binding energy trend shown in Table 2.8. This system presents two topologically disconnected structures, not counting the carbon atoms with two hydrogen atoms chemisorbed. We can see a naphthalene-like structure and a benzene ring-like structure, along with an aliphatic chain-like structure in the same carbon network. The hydrogen atom prefers to bind to an aliphatic rather than aromatic carbon with C(5b) being the second most favourable site. Finally, the less favourable sites belongs to the naphthalene-like structure C(5d), with a hyper-coordination number of 1. While in the benzene like structure C(5e) and C(5c) present low energy barrier respect to C(5b) and C(5a). The latter leads to the formation of the 5H-pentacene structure shown in Fig. 2.16.

Figure 2.15: Side view and top view of the optimized structure of 4H-pentacene. The alpha-numerical labels show the sequence of the possible carbon sites where a further atomic hydrogen might chemisorb.

Table 2.8: Binding energies (ΔE_{bind}) for the fifth hydrogenation of pentacene considering different carbon sites.

C site	ΔE_{bind} (eV)
C(5a)	1.83
C(5b)	1.57
C(5c)	1.44
C(5d)	1.29
C(5e)	0.78

6th Hydrogenation

The mid-gap state generated due to the addition of the fifth atomic hydrogen leads to the chemisorption of the sixth hydrogen atom on C(6a) as shown in Fig. 2.16 with a high binding energy of 4.16 eV. While, site C(6b) shows a lower binding energy (2.82 eV). Since the system consists of two topologically disconnected structures, the trend of binding energies reported in Table 2.9 shows that the mid-gap state cannot be localized on the naphthalene-like structure. Of all sites in this region of the molecule, C(6c) has the largest binding energy as a result of having a hyper-coordination number of 2, whereas the other carbon sites have close to zero or even, in some cases such as C(6f), negative binding energies.
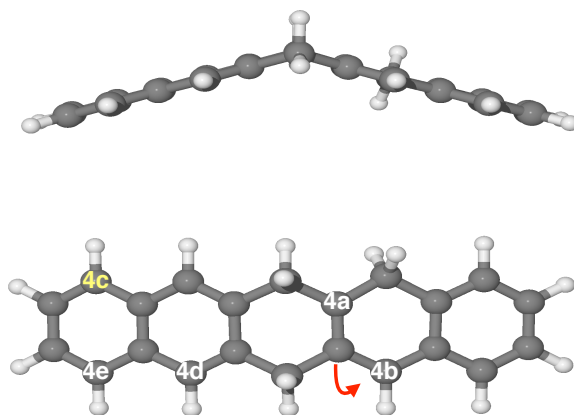
Figure 2.16: Side view and top view of the optimized structure of 5H-pentacene. The alpha-numerical labels show the sequences of the possible carbon sites where a further atomic hydrogen might chemisorb.

Table 2.9: Binding energies (ΔE_{bind}) for the sixth hydrogenation of pentacene considering different carbon sites.

C site	ΔE_{bind} (eV)
C(6a)	4.16
C(6b)	2.82
C(6c)	2.58
C(6d)	0.22
C(6e)	0.13
C(6f)	-0.14

7th Hydrogenation

We can again view the system as a structure formed by a naphthalene-like and a benzene-like ring (see Fig. 2.17). The values reported in Table 2.10 show that C(7e), C(7h), C(7f) and C(7g) are associated with the lowest binding energies and are those having a hyper-coordination number of 1. Instead, the carbons with the highest hyper-coordination number, *i.e.* 2, are, in order of decreasing binding energy, C(7a), C(7b), C(7c) and C(7d). With the formation of 7H-pentacene, the structure begins to twist on itself as shown in Fig. 2.18 where the preferred hydrogenation sites are located on the planar naphthalene unit.

Figure 2.17: Side view and top view of the optimized structure of 6H-pentacene. The alpha-numerical labels shows the sequences of the possible carbon sites where a further atomic hydrogen might chemisorb.

Table 2.10: Binding energies (ΔE_{bind}) for the seventh hydrogenation of pentacene considering different carbon sites.

C site	ΔE_{bind} (eV)
C(7a)	1.55
C(7b)	1.54
C(7c)	1.45
C(7d)	1.45
C(7e)	1.27
C(7f)	1.22
C(7g)	1.22
C(7h)	1.06

8th Hydrogenation

Binding energies for the addition of the eighth hydrogen atom are reported in Table 2.11. The mid-gap state is localized preferentially on C(8a) or C(8b) within the naphthalene-like structure. This reactivity is also evidenced in Fig. 2.18 where the red arrows show the transfer of the added hydrogen atom to the *ortho* or *para* sites during the geometry optimization if the atom is initially placed at the adjacent bridge (meta) sites. If the eighth hydrogen is, instead, added to C(8h) and C(8i) a negative binding energy results, indicating an unfavourable endoergic chemisorption process.
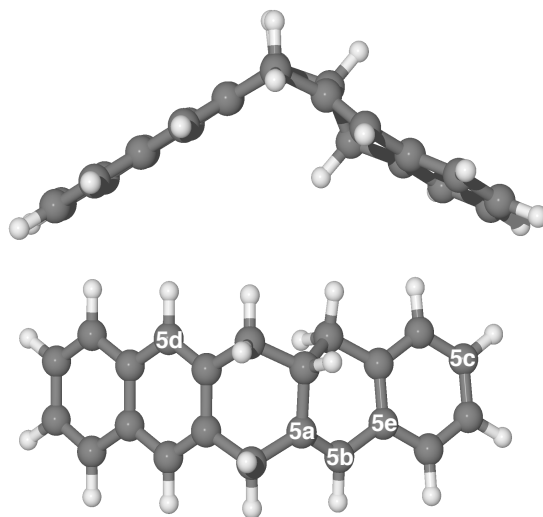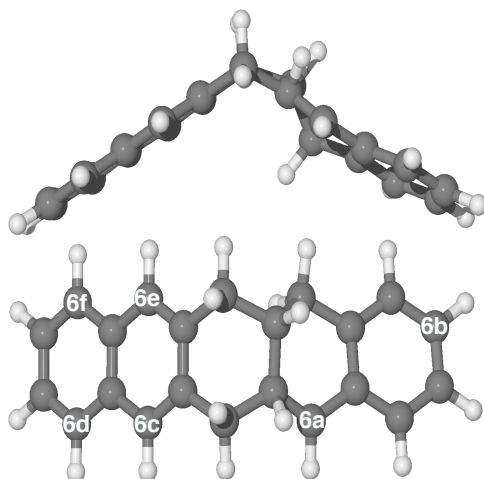
Figure 2.18: Side view and top view of the optimized structure of 7H-pentacene. The alpha-numerical labels shows the sequences of the possible carbon sites where a further atomic hydrogen might chemisorb.

Table 2.11: Binding energies (ΔE_{bind}) for the eighth hydrogenation of pentacene considering different carbon sites.

C site	ΔE_{bind} (eV)
C(8a)	3.60
C(8b)	3.58
C(8c)	2.43
C(8d)	2.31
C(8e)	2.30
C(8f)	1.14
C(8g)	0.14
C(8h)	-0.18
C(8i)	-0.19

9th Hydrogenation

In the case of addition to 8H-pentacene (see Fig. 2.19), we can view the system as a benzene ring with a carbon chain-like structure consisting of C(9b) and C(9a). These two carbons are the most reactive sites, for the chemisorption of the hydrogen, since C(9a) is the least coordinated carbon with coordination 1 (this carbon is the least coordinated carbon because it is bonded with just one sp^2 carbon, we do not consider the coordination with sp^3 carbons since they do not belong to the chain-like structure) and C(9b) is the second favourite site due to Lewis resonance. For the ben-

zene ring formed by C(9h), C(9d), C(9g), C(9c), C(9f) and C(9e), we cannot consider the hyper-coordination rule since a benzene ring is not a bipartite lattice. The largest binding energy is associated with chemisorption on C(9c), C(9d), C(9e), while the remaining carbon sites have the lowest binding energies (i.e 9f, 9g, 9h). These values are reported in Table 2.12.
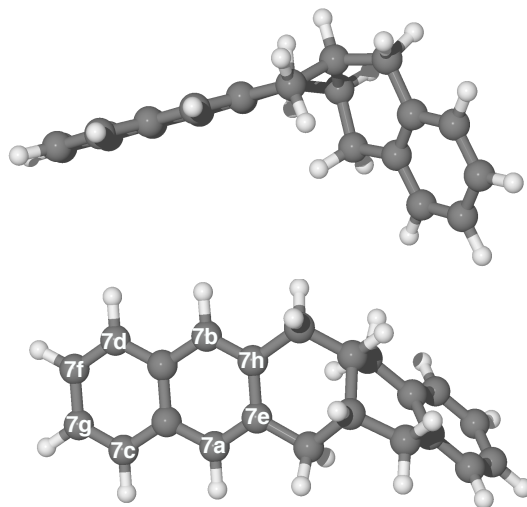

Figure 2.19: Side view and top view of the optimized molecular structure of 8H-pentacene. The alpha-numerical labels shows the sequences of the possible carbon sites where a further atomic hydrogen might chemisorb.

Table 2.12: Binding energies (ΔE_{bind}) for the ninth hydrogenation of pentacene considering different carbon sites.

C site	ΔE_{bind} (eV)
C(9a)	1.92
C(9b)	1.58
C(9c)	1.29
C(9d)	1.26
C(9e)	1.18
C(9f)	1.06
C(9g)	1.05
C(9h)	0.63

10th Hydrogenation

In the case of addition to 9H-pentacene, the mid-gap state is localized on the less coordinated C(10a), although it can also be localized on

C(10b), C(10d) and C(10c) by resonance. We noticed a further intramolec-
ular transfer, during the geometry optimization, caused by the bent struc-
ture of the molecule (see the long arrow that connects two carbon sites on
opposite ends of the molecule in Fig. 2.20). The bending of the molecule
brings the two aromatic rings together, promoting a hydrogen transfer,
intramolecularly, from one ring to another. The reactivity of C(10a) and
C(10d) is also evidenced by the observed transfer of chemisorbed hydro-
gen atoms to these sites when they are attached in neighbouring bridge
carbon sites as shown in Fig. 2.20. When the hydrogen atom is attached
to C(10g) the chemisorption process is endoergic with a negative binding
energy (Table 2.13), whereas chemisorption on C(10e) results in the for-
mation of an intramolecular C(10g)-C(10f) bond (Fig. 2.21), with a length
of 1.50 Å, during the geometry optimization. The formation of this in-
tramolecular bond leads to the formation of an unsaturated nanotubular
structure with a formation energy of -1.20 eV. Chemisorbing an atomic
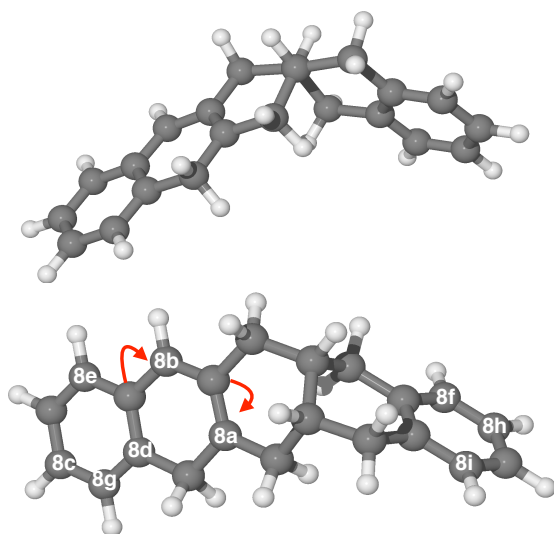hydrogen on C(10a) leads to the formation of 10H-pentacene.
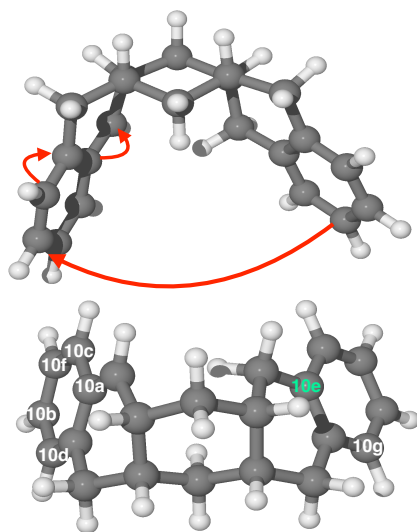
Figure 2.20: Side view and top view of the optimized structure of 9H-pentacene.
The alpha-numerical labels shows the sequences of the possible carbon sites where
a further atomic hydrogen might chemisorb.

11th Hydrogenation

The 10H-pentacene (see Fig.   2.22) has a structure formed by
two topologically disconnected and equivalent benzene-like rings formed
by C(11a)-C(11b)-C(11j)-C(11i)-C(11c)-C(11k) and C(11d)-C(11e)-C(11h)-
C(11f)-C(11g)-C(11l). The two benzene rings topologically have equivalent

Table 2.13: Binding energies (ΔE_{bind}) values of the tenth hydrogenation of pentacene considering different carbon sites.

C site	ΔE_{bind} (eV)
C(10a)	3.84
C(10b)	2.79
C(10c)	2.65
C(10d)	2.45
C(10f)	0.15
C(10g)	-0.39
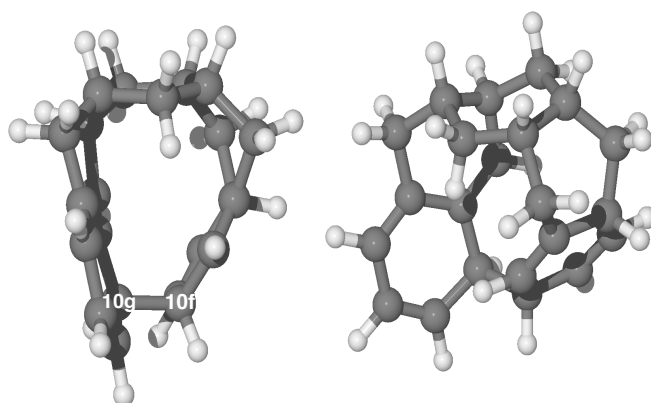
Figure 2.21: Optimized molecular structure of the quasi-nanotube 10H-pentacene formed when the 10th additional hydrogen chemisorbs on C(10e).

sites. In particular, as reported in Table 2.14, the binding energies are equal for C(11a) and C(11b), while the equivalent most reactive sites C(11e) and C(11d), in the opposite benzene-like ring, present small differences of binding energies. Instead, C(11c) and C(11i) are the second most reactive sites, or equivalently C(11f) and C(11g), since they are mirror images for symmetry. The less reactive sites are C(11k), C(11J), C(11l) and C(11h), respectively. Therefore due to the presence of carbon sites with the same binding energy, we also considered the calculated energy barriers, as reported in Table 2.15. Specifically, this shows that C(11a) has the lower energy barrier. C(11d) shows the same energy barrier as C(11a), especially in the geometrical structure of the transition state. The same applies to C(11b) and C(11c), while, C(11f) has the higher energy barrier. Therefore, we chose to proceed with the sequence from the structure obtained by chemisorbing the hydrogen on C(11a). At this stage of the sequence, it is impossible to predict further hydrogenation using the hyper-coordination

rule since the two benzene rings are not bipartite lattices. The coordination and Lewis resonance rules, however, remain valid.
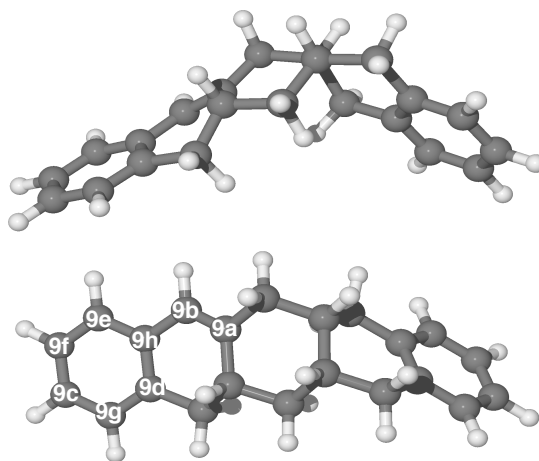

Figure 2.22: Side view and top view of the optimized structure of 10H-pentacene. The alpha-numerical labels show the sequences of the possible carbon sites where a further atomic hydrogen might chemisorb.

Table 2.14: Binding energies (ΔE_{bind}) for the eleventh hydrogenation of pentacene considering different carbon sites.

C site	ΔE_{bind} (eV)
C(11a)	1.15
C(11b)	1.15
C(11c)	1.14
C(11d)	1.12
C(11e)	1.10
C(11f)	1.08
C(11g)	1.07
C(11h)	1.05
C(11i)	1.05
C(11j)	0.99
C(11k)	0.91
C(11l)	0.99

Table 2.15: Energy barriers (ΔE_{bar}) for the eleventh hydrogenation of pentacene considering different carbon sites.

C site	ΔE_{bar} (eV)
C(11a)	0.22
C(11b)	0.23
C(11c)	0.23
C(11d)	0.22
C(11f)	0.28

12th Hydrogenation

The hydrogenation sequence continues with the attachment of the 12th additional hydrogen at the *ortho* position C(12a) as shown in Fig. 2.23. The carbon sites labeled in green indicate hydrogenation sites that lead to the formation of a quasi-nanotube, while the yellow one indicates the formation of a three-membered ring. The binding energies for the *ortho* [C(12b), C(12c)] and *para* [C(12a)] positions are shown in Table 2.16. Chemisorbing a hydrogen on the carbon located between 12b and 12a leads to the transfer of the hydrogen to C(12a) since this is the most reactive site (see short red arrow in Fig. 2.23). Hydrogen chemisorption in the carbon sites labeled in Table 2.17 leads to the formation of a biradical system that forms an intramolecular C-C bond with the creation of a nanotubular structure (see Fig. 2.24).

Table 2.16: Binding energies (ΔE_{bind}) for the 12th hydrogenation of pentacene in different carbon sites.

C site	ΔE_{bind} (eV)
C(12a)	3.49
C(12b)	3.46
C(12c)	3.44

Table 2.17: Formation energy (ΔE_f) of quasi-nanotubes (from 12d to 12h) and pentacene with a three membered-ring (12i).

| C site	ΔE_f (eV)
C(12d)	2.39
C(12e)	2.38
C(12f)	2.33
C(12g)	2.01
C(12h)	1.83
C(12i)	1.62

Figure 2.23: Side view and top view of the optimized molecular structure of 11H-pentacene. The alpha-numerical labels show the sequence of the possible carbon sites where a further atomic hydrogen might chemisorb.
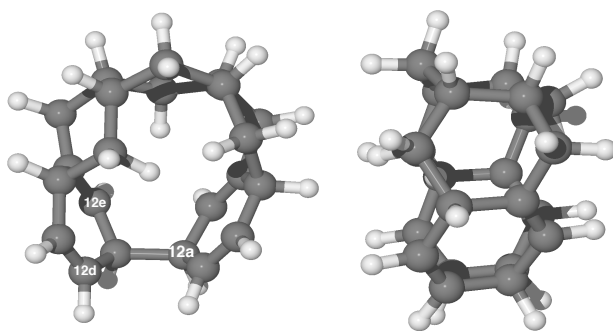
Figure 2.24: Front view and side view, respectively, of the optimized molecular structure of quasi-nanotube formed due to the chemisorption of an extra hydrogen on C(12d).

13th Hydrogenation

12H-pentacene is characterized by a bent structure with a single aromatic ring and an aliphatic diene-like ring, as shown in Fig. 2.25. Con-

sidering the calculated binding energies in Table 2.18, we observe that the hydrogen atoms prefer to bind on the aliphatic carbon sites rather than breaking the remaining aromaticity. This is demonstrated by fact that the binding energies are lower when we consider chemisorption to carbons belonging to the aromatic ring.
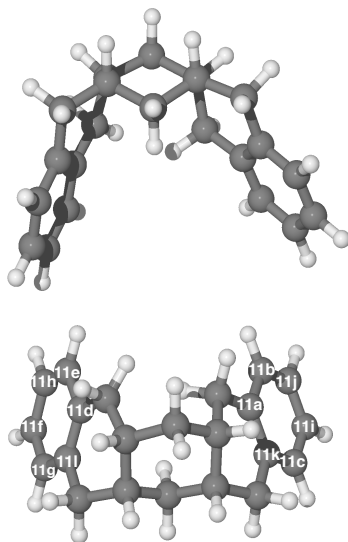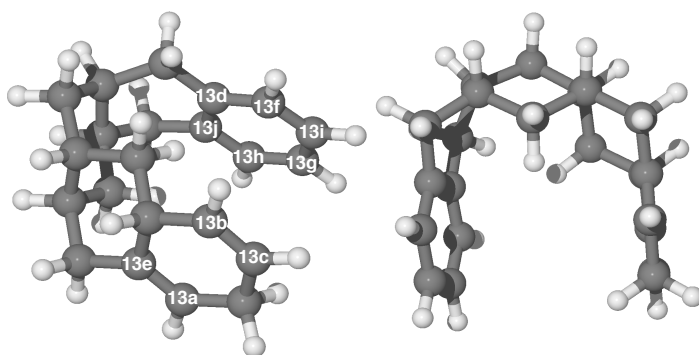

Figure 2.25: Side view and top view of the optimized molecular structure of 12H-pentacene. The alpha-numerical labels show the sequence of the possible carbon sites where a further atomic hydrogen might chemisorb.

Table 2.18: Binding energies (ΔE_{bind}) for the 13th hydrogenation of pentacene in different carbon sites.

C site	ΔE_{bind} (eV)
C(13a)	1.65
C(13b)	1.63
C(13c)	1.61
C(13d)	1.57
C(13e)	1.14
C(13f)	1.11
C(13g)	1.07
C(13h)	1.07
C(13i)	1.06
C(13j)	1.02

C(13a) is the most reactive, exhibiting a binding energy 0.02 eV larger than C(13b), and 0.04 eV larger than C(13c). The differences in energy are so small that in principle all three carbons are favourable sites for

hydrogen addition. Therefore, we calculated the energy barriers for the carbon sites associated with highest binding energies, as reported in Table 2.19. These calculations confirm that C(13a) is the most reactive carbon site with the highest binding energy and lowest energy barrier. Although, C(13b), C(13c) and C(13d) show energy barriers close to the lowest value (0.13 eV), we chose to proceed with the sequence that presents the minimal energetic path. Therefore, the 13th atomic hydrogen chemisorbs on C(13a) forming 13H-pentacene.

Table 2.19: Energy barriers (ΔE_{bar}) for the 13th hydrogenation of pentacene in different carbon sites.

C site	ΔE_{bar} (eV)
C(13a)	0.13
C(13b)	0.16
C(13c)	0.17
C(13d)	0.16

14th Hydrogenation

In the case of 13H-pentacene, the only possible carbon site in which a hydrogen might bind is C(14a) since it is the least coordinated site (see Fig. 2.26). Attaching the hydrogen atom to the aromatic ring leads to negative binding energies (Table 2.20) and results in a nanotubular structure due to the formation of intramolecular biradical systems. Formation energies for such structures range from -2.50 to -2.04 eV as reported in Table 2.21. Adding a hydrogen atom to C(14b) leads to the formation of the structure shown in Fig. 2.27 which is characterized by two four membered-rings and has a formation energy of -3.07 eV. Attaching the hydrogen to the most preferred site, C(14a), thus leads to the formation of 14H-pentacene.

Table 2.20: Binding energies (ΔE_{bind}) for the 14th hydrogenation of pentacene in different carbon sites.

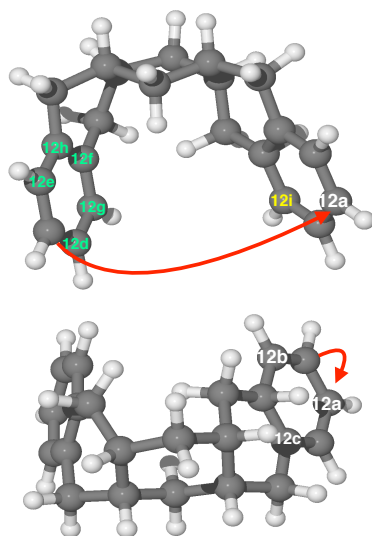| C site	ΔE_{bind} (eV)
C(14a)	4.15
C(14f)	0.47
C(14g)	-0.48
C(14h)	-0.56
C(14i)	-0.53

Figure 2.26: Side view and top view of the optimized molecular structure of 13H-pentacene. The alpha-numerical labels shows the sequences of the possible carbon sites where a further atomic hydrogen might chemisorb.

Table 2.21: Formation energies (ΔE_f) of quasi-nanotube (from 14c to 14e) and pentacene with two four membered-ring (14b) from 14H-pentacene.

C site	ΔE_f (eV)
C(14b)	-3.07
C(14c)	-2.50
C(14d)	-2.28
C(14e)	-2.04

15th Hydrogenation

Consistent with the previous cases, the hydrogen atom prefers to bind to the remaining two aliphatic carbons that are topologically disconnected from the aromatic ring (Fig. 2.29). This is also supported by the trend of binding energies reported in Table 2.22. It is reasonable that the system acts in this way in order to preserve the aromaticity. Attaching the hydrogen to C(15a) leads to the formation of 15H-pentacene where the remaining aliphatic rings have armchair conformation structures. Attaching an hydrogen atom on C(15b) does not change significantly the sequence since it generates a mid-gap state that is localized on C(15a). Therefore, the chemisorption of the atomic hydrogen to C(15a) or C(15b) leads to the same path of the sequence. Furthermore, the most reactive site is C(15a) with a binding energy 0.05 eV larger than C(15b). Accordingly, we proceed with the chemisorption of an extra hydrogen on C(15a) that leads to the
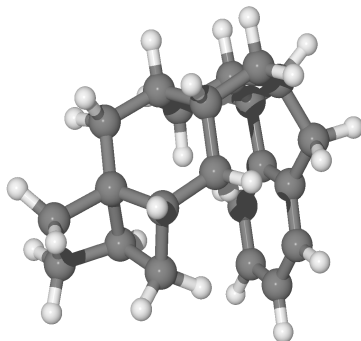
Figure 2.27: Optimized molecular structure of 14H-pentacene where the chemisorption of an extra hydrogen on C(14b) leads to the formation of two four-membered-rings.
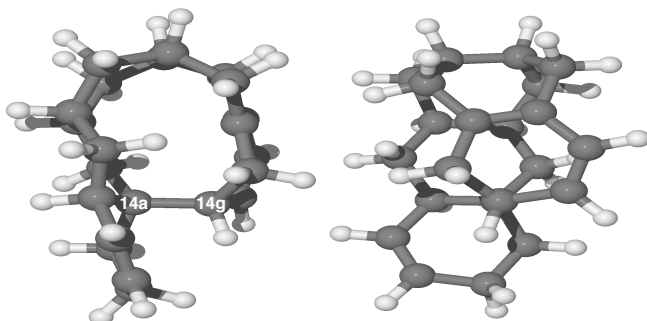
Figure 2.28: Optimized structure of the quasi-nanotube structure of 14H-pentacene formed when the 14th additional hydrogen chemisorbs on C(14c).

formation of 15H-pentacene.

16th Hydrogenation

Adding an extra hydrogen to the most favourable site of 15H-pentacene, C(16a), results in a binding energy of 4.34 eV. Binding a hydrogen atom

Figure 2.29: Side view and top view of the optimized molecular structure of 14H-pentacene. The alpha-numerical labels show the sequences of the possible carbon sites where a further atomic hydrogen might chemisorb.

Table 2.22: Binding energies (ΔE_{bind}) for the 15th hydrogenation of pentacene in different carbon sites.

C site	ΔE_{bind} (eV)
C(15a)	1.72
C(15b)	1.67
C(15c)	1.12
C(15d)	1.08
C(15e)	1.07
C(15f)	1.07
C(15g)	1.06
C(15h)	0.91

on one of the aromatic carbon sites, labeled in green in Fig. 2.30, leads to a singly occupied molecular orbital that results in the formation of an intramolecular C-C bond generating nanotubular structures (see Fig. 2.31) with formation energies ranging from -2.79 to -2.18 eV (see Table 2.23). Consistent with the previous case, adding hydrogen to the most reactive site C(16a) leads to the formation of 16H-pentacene.
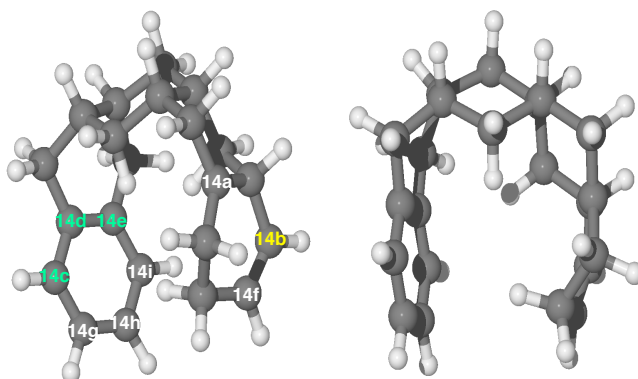
Figure 2.30: Side view and top view of the optimized molecular structure of 15H-pentacene. The alpha-numerical labels shows the sequences of the possible carbon sites where a further atomic hydrogen might chemisorb.

Table 2.23: Formation energies (ΔE_f) of quasi-nanotube.

C site	ΔE_f (eV)
C(16b)	-2.70
C(16c)	-2.54
C(16d)	-2.52
C(16e)	-2.47
C(16f)	-2.18

17th Hydrogenation

Once the pentacene molecule has reacted with 16 extra hydrogen, a single aromatic ring-like structure remains to be hydrogenated. C(17a), C(17b) and C(17c) are the most favourable sites for the 17th addition with a small difference in binding energy of 0.02 eV between C(17a) and C(17b) or C(7c). C(17b) and C(17c) are energetically equivalent. The trend in calculated binding energies is reported in Table 2.24, while, the addition sites are reported in Fig. 2.32. We continue the sequence by chemisorbing the hydrogen on C(17a) forming 17H-pentacene structure (Fig. 2.33), but we expect that hydrogen chemisorption on C(17b) or C(17c) leads to comparable results.
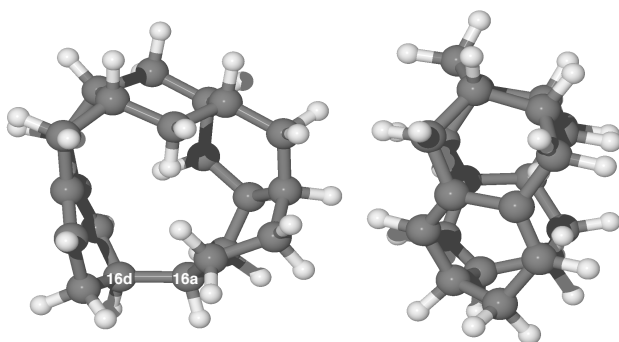
Figure 2.31: Optimized molecular structure of the quasi-nanotube structure of 16H-pentacene formed when the 16th extra hydrogen chemisorbs on C(16b).

Figure 2.32: Side view and top view of the optimized molecular structure of 16H-pentacene. The alpha-numerical labels show the sequences of the possible carbon sites where a further atomic hydrogen might chemisorb.

18th Hydrogenation

The 17H-pentacene molecule has mid-gap state localized in the *ortho* and *para* positions, as shown in Fig. 2.33. Calculated binding energies

Table 2.24: Binding energies (ΔE_{bind}) for the 17th hydrogen addition to pentacene.

C site	ΔE_{bind} (eV)
C(17a)	1.10
C(17b)	1.08
C(17c)	1.08
C(17d)	1.07
C(17e)	1.05
C(17f)	0.89

are shown in Table 2.25. Similar to other cases with such a mid-gap state, the addition at the meta positions leads to the transfer of the hydrogen atom during the geometry optimization process. This confirms that C(18c) is one of the reactive sites. Attaching an hydrogen on the highlighted yellow C(18d), instead, leads to the formation of a triangle and pentagon in the same conformation structure (see Fig. 2.34) with a formation energy of -3.02 eV. The structures formed by adding a hydrogen atom to C(18a) and C(18b) have essentially equal binding energies, but we considered to chemisorb the hydrogen on C(18a). We expect that hydrogen chemisorption on either carbon site would be a valuable pathway to follow leading to comparable results.
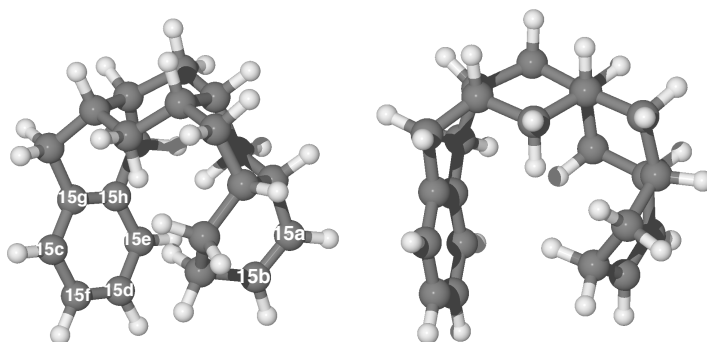

Figure 2.33: Side view and top view of the optimized molecular structure of 17H-pentacene. The alpha-numerical labels shows the sequences of the possible carbon sites where a further atomic hydrogen might chemisorb.

Table 2.25: Binding energies (ΔE_{bind}) for the 18th hydrogen on pentacene.

C site	ΔE_{bind} (eV)
C(18a)	3.48
C(18b)	3.44
C(18c)	3.36
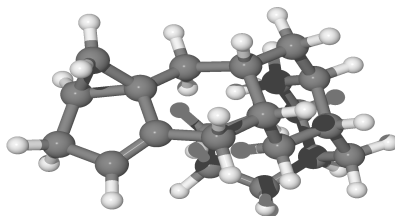
Figure 2.34: Optimized molecular structure of 18H-pentacene with a three and five membered-ring formed by the chemisorption of the hydrogen on C(18d).

19th Hydrogenation

The resulting 18H-pentacene molecule (Fig. 2.35) has four remaining aliphatic carbons which have similar values of binding energies for the addition of the 19th additional hydrogen atom, as reported in Table 2.26. Therefore, we have calculated the energy barriers as reported in Table 2.27, in order to determine the most reactive carbon site.

Based on the energy barriers, C(19d) and C(19c) have similar reactivity and so adding a hydrogen to C(19d) or C(19c) does not significantly change the sequence. If a hydrogen atom is chemisorbed on C(19c), a further hydrogen will chemisorb on C(19d) since it is then the least coordinated carbon site. Similarly, adding first to C(19d) results in the subsequent addition to C(19c). Therefore, we continue the sequence by chemisorbing the hydrogen atom on C(19c) in order to form 20H-pentacene.

Table 2.26: Binding energies (ΔE_{bind}) for the 19th hydrogen on pentacene.

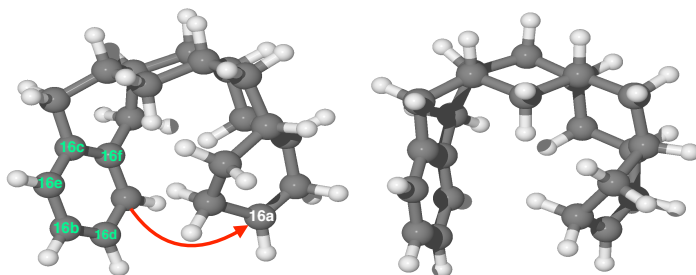| C site	ΔE_{bind} (eV)
C(19a)	1.62
C(19b)	1.60
C(19c)	1.60
C(19d)	1.56
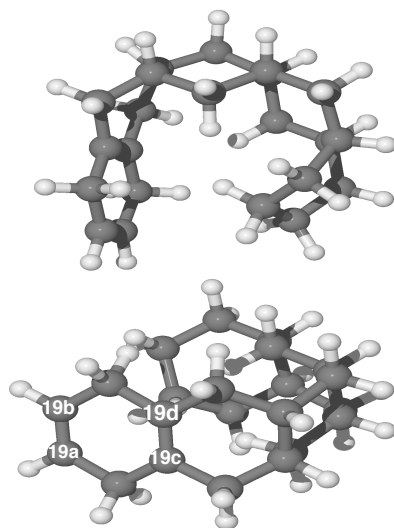
Figure 2.35: Side view and top view of the optimized molecular structure of 18H-pentacene. The alpha-numerical labels shows the sequences of the possible carbon sites where a further atomic hydrogen might chemisorb.

Table 2.27: Energy barriers (ΔE_{bar}) for the 19th hydrogen on pentacene.

C site	ΔE_{bar} (eV)
C(19a)	0.17
C(19b)	0.18
C(19c)	0.13
C(19d)	0.13

20th Hydrogenation

Fig. 2.36 shows the sites in which the 20th extra hydrogen could be added. For molecules from 19H-pentacene and beyond, the mid-gap state cannot be localized since the molecule is no longer aromatic. The most reactive carbon site is C(20a) with a binding energy of 4.27 eV. While, chemisorbing a hydrogen atom on C(20b) leads to the transfer of the already chemisorbed hydrogen on the carbon bridge between C(20c) and C(20a), to C(20c) as the arrow shows in Fig. 2.36. Adding the hydrogen to directly to C(20c) leads to a open chain structure with a exoergic formation energy of -3.39 eV, as shown in Fig. 2.37. This occurs due to the breaking of the C-C bond, formed by the CH_2 groups between C(20b) and C(20a), caused by the impossibility to localize two unpaired electrons in the same ring.
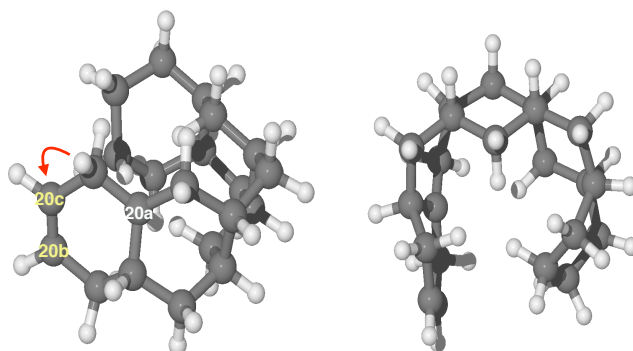
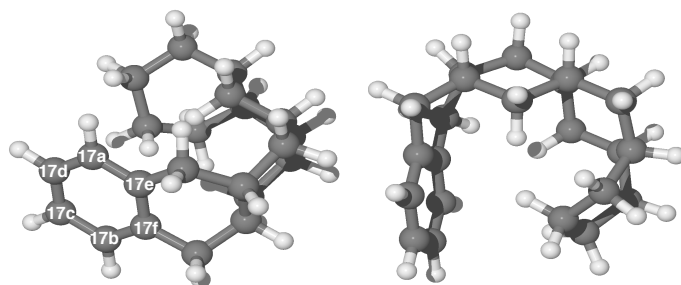**Figure 2.36:** Side view and top view of the optimized structure of 19H-pentacene. The alpha-numerical labels show the sequence of the possible carbon sites where a further atomic hydrogen might chemisorb.
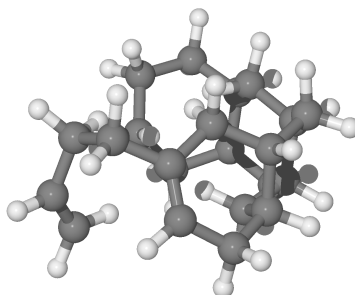
Figure 2.37: Optimized molecular structure characterized by a open aliphatic ring.

21th Hydrogenation

For the 20-H-pentacene molecule, two positions remain unhydrogenated (see Fig. 2.38). Specifically, C(21a) with a binding energy of 1.67 eV and C(21b) with a binding energy of 1.65 eV. Since the binding energies are similar, we calculated the energy barriers in order to establish the more reactive position. Specifically, adding a hydrogen on C(21a) requires overcoming an energy barrier of 0.09 eV, whereas for C(21b) the barrier is

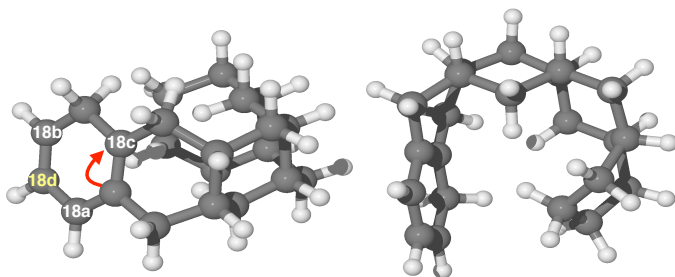0.16 eV indicating that the most reactive site is C(21a).
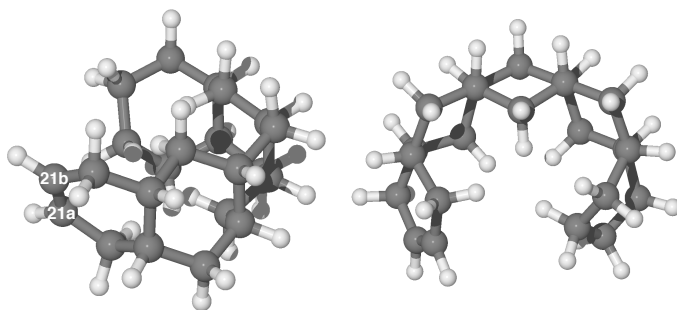
Figure 2.38: Side view and top view of the optimized molecular structure of 20H-pentacene. The alpha-numerical labels show the sequences of the possible carbon sites where a further atomic hydrogen might chemisorb.

22th Hydrogenation

After the chemisorption of the 21st hydrogen the reaming carbon available is C(21b), shown in Fig. 2.38. A hydrogen adsorbed in this final position has a binding energy of 4.20 eV forming the full hydrogenated pentacene, 22H-pentacene ($C_{22}H_{36}$).

Crossover Temperatures

In Table 3.5 are reported the values of crossover temperature (temperature below which quantum tunneling effects are important) calculated using the following expression: $Tc = (\hbar * freq)/k_b$. $\hbar$ is the reduced Planck's constant ($\hbar = h/2\pi$), freq is the module of the imaginary frequency of the transition state and k_b is the Boltzmann's constant.

Table 2.28: Values of crossover temperatures (Tc), classical TST rates (*Kc*) and the Gibbs free energies difference between the TS and the reactant at the crossover temperature (ΔG^{Tc}) for each odd hydrogenation (H*n*) of pentacene.

H*n*	Tc (K)	*Kc* (s^{-1})	ΔG^{Tc} (eV)
1	136.59	16712120.68	0.14
3	199.26	136556.81	0.29
5	184.94	193213.29	0.27
7	191.13	344328.39	0.27
9	136.16	881983.68	0.17
11	213.12	10245.73	0.36
13	166.33	887483.50	0.22
15	145.71	3734276.02	0.17
17	210.82	17974.56	0.35
19	180.88	525659.29	0.25
21	167.41	941511.59	0.22

While the classical TST rate (*Kc*) has been calculated as following: *Kc* = (k_b*Tc/h)exp(-ΔG^{Tc}/R*Tc). ΔG^{Tc} is the Gibbs free energies difference between the TS and the reactant at the crossover temperature and R is the gas constant.

CHAPTER 3

DO DEFECTS IN PAHS PROMOTE CATALYTIC ACTIVITY IN SPACE? STONE–WALES PYRENE AS A TEST CASE

Abstract. Using density functional theory (DFT), we studied the formation of Stone–Wales defects in pyrene, as a prototype PAH molecule. In addition, we studied the reactivity of the defective and pristine pyrenes toward hydrogenation, a process that can occur in some regions of the interstellar medium. We found that the formation of the defect requires overcoming energies of the order of 8.4 eV, but the defective structure is stable due to the high reverse reaction barrier (approx. 6 eV). We also found that the presence of the defect decreases the sticking barrier for the first hydrogenation and promotes more stable singly and doubly hydrogenated intermediates with respect to that of the pristine pyrene. Finally, our results show that both Stone–Wales pyrene and pristine pyrenes can lead to the formation of H_2 through an extraction mechanism involving H atoms attached on distal carbon atoms with energy barriers below 2 eV.

3.1. Introduction

Among the different type of sp^2 carbon nanomaterials, Polycyclic Aromatic Hydrocarbon (PAH) molecules are of particular interest in astrophysics since they are responsible for a family of infrared emission bands in the 3-20 μm range, the so-called aromatic infrared bands (AIBs), which are observed everywhere in our galaxy and beyond.[27,105,150] PAHs are ubiquitous in space and, thus, they should participate in the chemistry of the interstellar medium (ISM). Indeed, they have been proposed as sources of small carbon chains[151] and even fullerenes.[31] PAHs act as catalytic surfaces where H_2, the most abundant interstellar molecule, can be formed.[33] It has been proposed that both neutral and cationic PAH molecules can first react with atomic hydrogen with little (few meV) to no barrier becoming superhydrogenated and, then, promote barrierless H_2 abstraction through the Eley–Rideal mechanism.[17,152] Since detailed photochemical evolution models of PAHs in the ISM have questioned the efficiency of the Eley–Rideal H_2 abstraction,[41] more recently other mechanisms have been invoked, such as photodissociation of H_2 from normally hydrogenated PAHs.[153]

Stone Wales (SW) defects are topological changes in the structure ubiquitous in sp^2 carbon materials such as fullerene, graphene, nanoribbons, and carbon nanotubes.[154–156] They are also studied in material that have graphene-like structures but different compositions, *e.g.* boron nitrides.[60] The defect is produced upon a 90° rotation of a C-C bond located in a hexagonal carbon ring, creating two seven-membered and two five-membered rings. The generation of SW defects can cause a curvature of the material that hosts it, but in the case of graphene or other planar hexagonal materials this defect results in a planar structure. Ma *et al.*[157] proved that, in 2D materials, the formation of SW defects is inducted in non-equilibrium conditions by irradiation or the effect of mechanical strain. Experimental and theoretical studies conducted on fullerene and PAHs have shown that an extra hydrogen or carbon atom, chemisorbed on the molecule, induces a structure promoting the formation of the SW defect with a lower energy barrier than the formation of the defect in the pristine material.[58,158] Defects are known to change the physical and chemical properties; for example, they can open band gaps and exhibit increased reactivity toward oxygen and hydrogen atoms.[159–161] Theoretical studies have shown that PAH containing 5,7-membered rings are stable enough to survive interstellar conditions and they might be responsible for two of the AIBs, at 6.9 and 16.4 μm.[162,163]

In this study, we used density functional theory (DFT) to determine the mechanism leading to the formation of Stone–Wales defects in a prototypical PAH molecule, pyrene. We investigated the effect of the SW defect on the reactivity of pyrene toward hydrogenation (single and double) and its ability to catalyse the formation of molecular hydrogen in an interstellar environment.

3.2. Theoretical Methods

We employed density functional theory (DFT) implemented in the Gaussian 16,[131] to estimate barrier, binding and reaction energies. We used the hybrid meta exchange-correlation functional M06-2X developed by Truhlar and coworkers,[77] with the segmented polarization-consistent double zeta basis set pcseg-1 optimized for DFT and developed by Jensen.[132] M06-2X proved to be accurate when compared with CCSD(T) calculations for the investigation of hydrogen chemisorption on graphene-like structures such as PAHs.[40] We corrected all calculated energies for zero point vibrational energy and for basis-set superposition error, using the counterpoise method.[100,134]

The geometry optimization of minima and transition states (TSs) in the potential energy surface (PES) were calculated using the Berny algorithm[133] and their nature in the PES were characterized by analyzing the normal modes (*i.e.* one imaginary frequency for the TS and no imaginary frequencies for the minima). All calculations were carried out using the unrestricted approach (UHF) and in order to produce a correct UHF wavefunction for blue singlet open-shell biradical systems in the case of TSs, we mixed the HOMO and LUMO destroying α-β orbitals and spatial symmetries (see Appendix).[164]

The vibrational frequencies, molecular structures, and intra- and intermolecular distances were analyzed with Molden.[135,136] Binding energy, energy barrier and reaction energy were calculated according to the following equations:

$$\Delta E_{bind} = [(E_\text{H} + E_\text{reagent}) - E_{n\text{H–pyrene}}] \tag{3.1}$$

$$\Delta E_{bar} = [E_\text{TS} - (E_\text{H} + E_\text{reagent})] \tag{3.2}$$

$$\Delta E_r = [E_\text{product} - (E_H + E_{reagent})] \tag{3.3}$$

ΔE_{bind} is the binding energy, ΔE_{bar} is the energy barrier and ΔE_r is the reaction energy. E_H is the energy of the isolated hydrogen, $E_{reagent}$ is the energy of the isolated pyrene, $E_{nH\text{-}pyrene}$ is the energy of pyrene with one or two atomic hydrogens chemisorbed, E_{TS} is the energy of the transition state structure and $E_{product}$ is the energy of pyrene with two atomic hydrogen atoms chemisorbed. The binding energies are considered exoergic when they are positive as opposed to the reaction energies that are negative for exoergic processes. Barrier energies are always positive for the definition of transition state.

3.3. Results

3.3.1. Formation of PAHs with Stone-Wales Defect

Pyrene ($C_{16}H_{10}$) is an organic molecule belonging to the D_{2h} point group (Fig. 3.1). The system can undergo a Stone-Wales transformation,[57] through the in-plane 90° rotation of the bond formed by C(2) and C(4) to a Stone–Wales defect in the structure, characterized by the presence of two seven-membered rings and two five-membered rings.

Pyrene   **SW-Pyrene**
(Pristine)   **(Defect)**
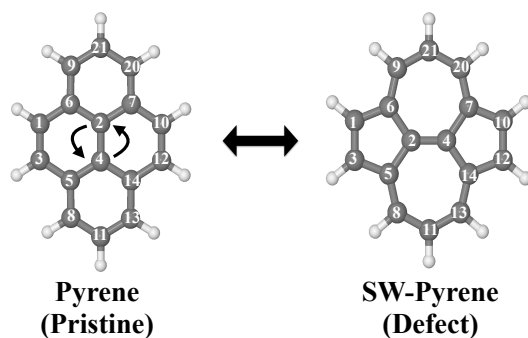
Figure 3.1: Labeled optimized structures of pyrene and SW–pyrene. The arrows show the Stone–Wales formation.

The formation of a SW defect in the neutral pyrene molecule features two concerted transition states (Fig. 3.2) of the first order, connected by a shallow minimum. A similar mechanism was proposed in a previous study using a modified G4(MP2) method,[163] but in that case only transition states of the second order were obtained. The first transition state (TS 1) is a non-planar structure characterized by the partial breaking of two carbon-carbon bonds C(2)-C(7) and C(5)-C(4) (now 2.42 Å apart) and an energy barrier of 8.26 eV, slightly higher than that calculated before.[163] The mechanism, then, proceeds with the formation of a high-energetic intermediate (8.17 eV) with a bicyclic structure of two ten-membered rings. Once this intermediate is formed, 0.25 eV is required to overcome a second barrier associated with a second non-planar transition state (TS 2) featuring the partial formation of bonds C(2)-C(5) and C(4)-C(7) with elongation of 2.32 Å. Overcoming the second energy barrier leads to the production of SW–pyrene, which lies 2.35 eV above the pristine structure. Thus the formation of pyrene is an endoergic process, requiring 8.42 eV. Nevertheless, once the defective structure is created, 6.07 eV is needed to revert to the pristine structure. During the formation of the defect, all equivalent carbon–carbon distances are contracted down to 1.38 Å with respect to pristine pyrene where these carbon–carbon distances are 1.43 Å, similar to what is observed in graphene.[165]

Figure 3.2: Potential energy surface for the formation of a Stone–Wales defect starting from pristine pyrene, illustrated with optimised molecular structures. Energies are calculated with respect to pristine pyrene.

It has been proposed that the presence of additional H chemisorbed on carbonaceous material can catalyze the formation of a SW defect.[158] As we are interested here in defective PAHs and their reactivity, we investigated this mechanism for pyrene. We started with a molecular structure where a hydrogen atom is chemisorbed on one of the inner carbon atoms (C(2) or C(4)) involved in the SW transformation (Fig. 3.3). Starting from this structure, the reaction goes through a transition state (TS 1h) lying 2.20 eV above the reactant. For comparison, an energy barrier of 6.8 eV was found to break a central carbon–carbon bond in a graphene nanoflake with a chemisorbed H atom.[161] In our system the TS is characterised by the partial breaking of a carbon–carbon bond, where the carbons are 2.33 Å apart. After TS 1h, intermediate Int 1h is formed at 2.14 eV, featuring a ten-membered ring structure. From there, an additional 4.05 eV is needed to break a second carbon–carbon bond and form intermediate Int 2h, a shallow minimum with a bicyclic structure. After overcoming 0.46 eV (TS 3h) a new carbon–carbon bond is created, leading to the formation of a pentagonal ring. In the end, we have the formation of a more stable intermediate (Int 3h) geometrically structured by a five membered-ring, a seven membered-ring and a ten membered-ring. The process ends with the barrierless formation of the SW–pyrene with a hydrogen chemisorbed

on the inner carbon (1H–SW–pyrene).

To summarize, the creation of a Stone–Wales defect in neutral pyrene requires an energy of 8.42 eV and the overcoming of two transition states. Once the shallow intermediate structure is formed, due to the small difference in barriers, the rate of the forward (creation of SW–pyrene) and backward reaction (creation of pyrene) should be comparable. The addition of a chemisorbed H atom catalyzes the process, which requires a total energy of 6.60 eV. However due to symmetry breaking, the process requires several additional steps. In particular, after the formation of Int 1h, the energy difference between TS 1h (0.06 eV) and TS 2h (4.05 eV) indicates that the former is more likely to happen, thus making the formation of 1H–SW–pyrene unlikely.

Table 3.1: Binding energies (ΔE_{bind}) and energy barriers (ΔE_{bar}) for the hydrogenation of different carbon sites of Stone-Wales and pristine pyrene.

C site	SW pyrene		Pristine pyrene	
	ΔE_{bind} (eV)	ΔE_{bar} (eV)	ΔE_{bind} (eV)	ΔE_{bar} (eV)
C(12)	1.55	0.18	1.23	0.23
C(8)	1.45	0.19	1.24	0.22
C(5)	1.14	0.27	-	-
C(11)	1.10	0.25	-	-
C(2)	1.04	0.21	0.26	0.43

3.3.2. Hydrogenation Process

First Hydrogen Attachment. Due to the symmetry of the SW–pyrene, there are five non-equivalent carbon sites, C(2), C(5), C(8), C(11) and C(12) available for interaction with a radical hydrogen atom; we calculated the binding and barrier energies for H chemisorbed on these sites. The most reactive carbon sites are the one possessing the highest binding energies and the lowest energy barriers. Table 3.1 reports the values for the different sites for SW–pyrene and pristine pyrene for comparison. In both structures, edge carbons C(12) and C(8) are the most reactive sites with binding energies of 1.55 and 1.45 eV and energy barriers of 0.18 and 0.19 eV, respectively. To follow, C(5), C(11) and C(2) have lower binding energies and slightly higher energy barriers, up to 0.27 eV in the case of C(5). Thus, the addition of the H atom to edge carbons C(8) and C(12) produces the most stable isomers, in line with previous studies.[17,109,137,166] In any case, all the energies calculated are exoergic and favorable.

The energetics for H adsorption on three different sites (2 edge and 1 graphene-like carbon) of pristine pyrene were also calculated, to evaluate the effect of the SW defect on reactivity. The values reported for the binding energies (Table 3.1) are consistently lower by 0.25 eV with respect to previous calculations,[128] while the barrier energies are consistently higher
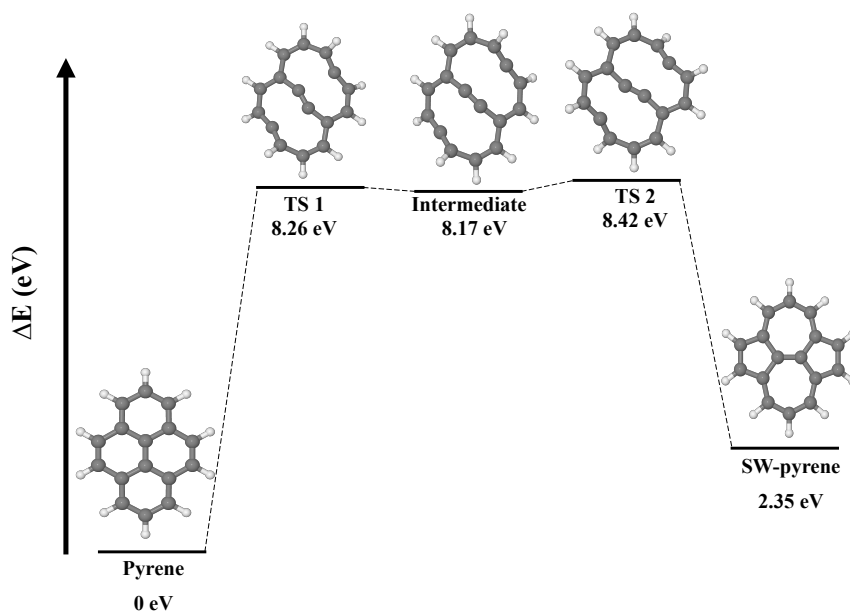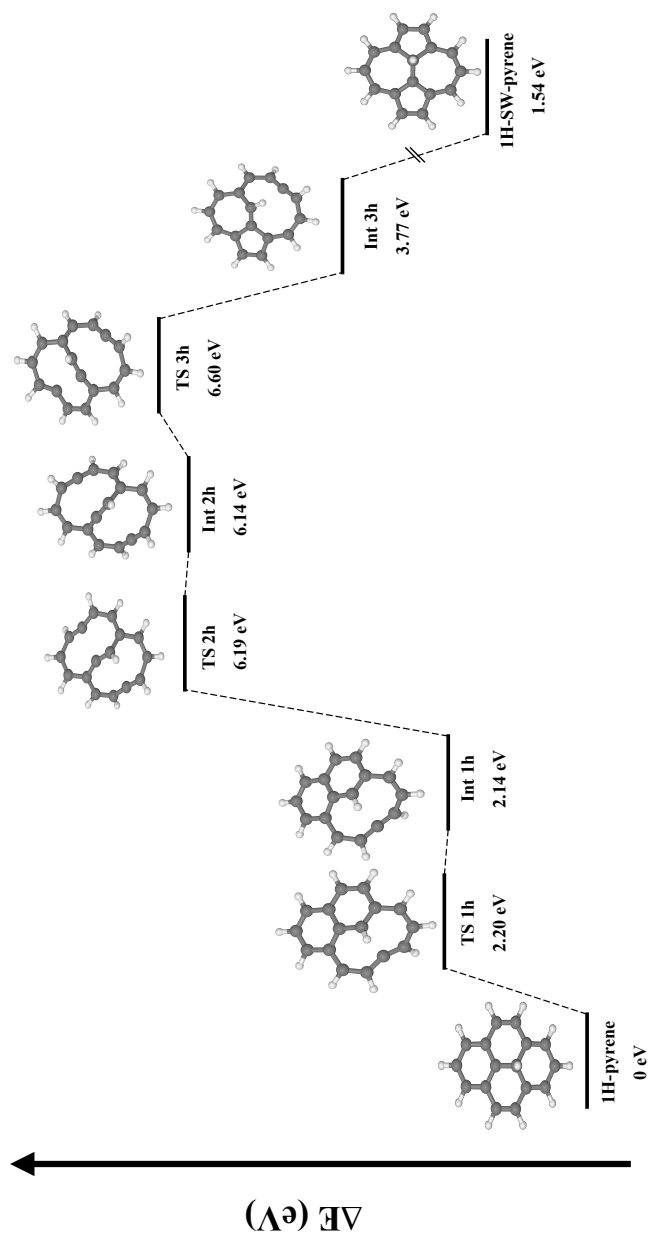
Figure 3.3: Potential energy surface for the formation of a Stone–Wales defect starting from hydrogenated pyrene illustrated with optimised molecular structures. The symbol (//) indicates the absence of energy barriers.

by 0.16 eV. This is expected since the previous work used a different functional (PBE) and in our work a correction for zero-point vibrational energy is also included. Binding energies for singly hydrogenated SW–pyrene are always larger than those in the pristine molecules and energy barriers are smaller in accordance with the general Brønsted-Evans-Polayni rule [138,139] that in a reaction lower energy barriers are connected to larger exoergicity. In particular, when C(2) is hydrogenated in the SW–pyrene the binding energy is 1.04 eV compared to only 0.26 eV in the pristine molecule, and the energy barrier is halved, 0.21 *versus* 0.43 eV. To understand the origin of this difference we looked at the structural differences in the two molecules. Indeed, in a PAH molecule the addition of a H atom changes the hybridization of the C atom where it is bonded from sp^2 to sp^3, leading to a tetrahedral puckering of the carbon skeleton. This structure relaxation is fundamental as it creates the correct condition for the binding to happen. Both the defect and pristine pyrene are planar and hydrogenation triggers the creation of a much rippled structure for SW–pyrene. The hydrogenation of C(2) generates a puckering of 0.40 Å in the SW structure *versus* 0.46 Å in the pristine pyrene. In addition, in the SW-structure, edge carbon atoms forming the pentagons, C(1), C(3), C(10) and C(12), experience a downward motion of 0.29 Å, while for the pristine pyrene C(21) and C(11) move downward by 0.21 Å, and C(9) and C(20) by 0.10 Å. The larger puckering of C(2) in the pristine pyrene is likely responsible for the higher energy barrier. [128] As for the larger binding energy, we hypothesize that the flexibility of SW–pyrene permits the downward motion of the five-membered rings, thus, releasing part of the strain caused by the H-addition in the molecule. Thus, this results in more stable hydrogenated intermediates, with the extreme case of C(2), in the SW molecule. Our calculations confirm that introducing a Stone–Wales defect increases consistently the reactivity of a PAH as it happens for graphene. [167]
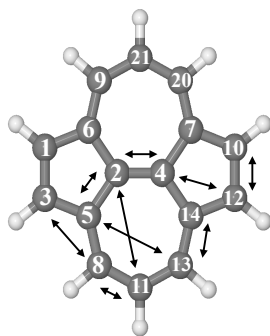
Figure 3.4: Optimized molecular structure of SW–pyrene with arrows indicating the different carbon pairs considered in this study.

a) 1H-C8-SW   **b) 1H-C12-SW**

c) 1H-C2-SW
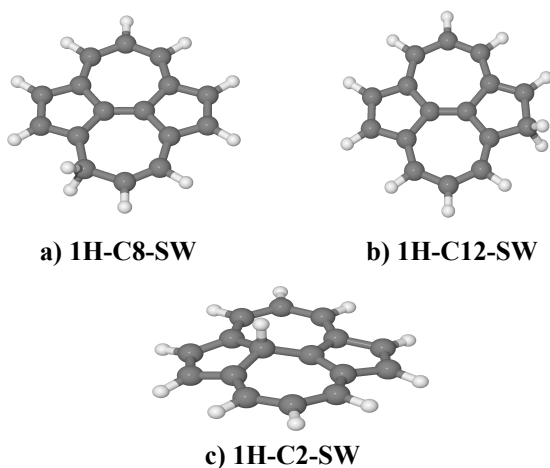
Figure 3.5: Optimized molecular model of different isomers of hydrogenated SW–pyrene with an atomic hydrogen bonded on C(8) (a), C(12) (b) and C(2) (c). All belong to the C_s point group.

Second Hydrogen Attachment. The attachment of a H atom to SW–pyrene generates an open-shell doublet structure with an unpaired electron that is susceptible to the attack of another H atom. As we are interested in the ability of SW–PAHs to catalyse H_2, we considered both adjacent and non-adjacent carbon sites, which are illustrated in Fig. 3.4.

A spin population analysis (values are reported in the Appendix) based on Mulliken partitioning scheme for the single hydrogenated species of SW-pyrene and pristine pyrene (Fig. 3.7 and 3.8) shows a population of spin-up and spin-down electrons on the carbon framework. Specifically, for 1H–C2–SW–pyrene and 1H–C5–SW–pyrene a larger population of spin-up is localized in the carbons adjacent to the hydrogenated site (Fig. 3.7a and b, respectively); this is also true for 1H-C12-pyrene (Fig. 3.8b). These are the sites where we expect that the second hydrogen will most likely chemisorb as seen for coronene and pentacene molecules.[39,40] The other isomers analysed have the population of spin-up electrons distributed more uniformly over the entire carbon framework.

We first attempted to calculate the energy barrier for the attachment of the second H atom to a different site. Due to the computational issues of dealing with bi-radical systems in a singlet spin state, not all the calculations reached convergence (see Appendix). In isomer 1H-C12-SW (Fig. 3.5) the attachment of a second H atom on C(14) has an energy barrier of 0.033 eV, while there is no barrier when, on 1H–C2–SW, the second H atom attaches on C(4). If the second H is attached to an edge C atom that was hydrogenated previously, the reaction is found to be barrierless. In pristine pyrene it is found that in 1H–C(2)–pristine, the energy barrier to

a) **2H-C5C13-SW**   b) **2H-C12C10-SW**

c) **2H-C2C4-SW**
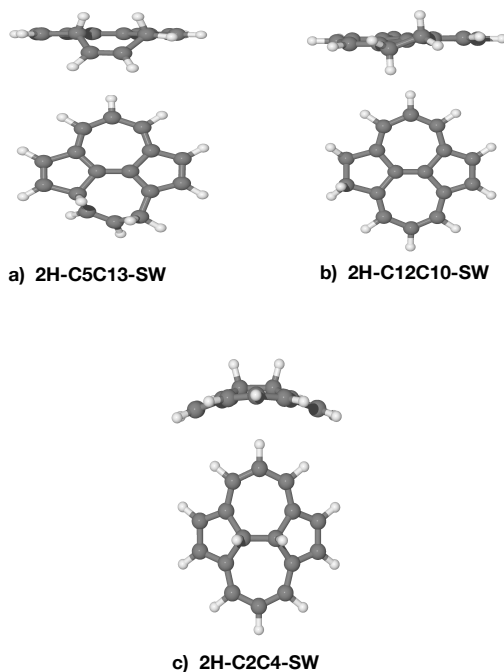
Figure 3.6: (a) Side and top views of optimized molecular structures for different isomers of hydrogenated SW–pyrene with two extra atomic hydrogens bonded on C(5) and C(13) (a), C(12) and C(10) (b) and C(2) and C(4) (c).

attach the second H to C(4) is calculated to be 0.19 eV, whereas we do not find transition state structures for the edge carbons of the pristine pyrene due to convergence issues. A previous study[128] found that all the second H-addition reactions to singly-hydrogenated pyrene are barrierless, while for our study this is true only when the reaction involves edge carbons. The difference is likely due to the different methods used and the lack of zero-point correction in the previous study. Incidentally, we note that the observed small barriers of 5 and 33 meV (Table 3.2) are below the barrier heights error of M06-2X (0.06 eV) estimated by Mardirossian *et al.*[168] with the hydrogen transfer barrier heights database (HTBH38) and, therefore, these small energy barrier values obtained here can be approximated to 0 eV.

The stability of the doubly-hydrogenated defective species in terms of binding energy is summarised in Table 3.2 together with the carbon-carbon distance. There is no correlation between the stability of the intermediates and the carbon–carbon distances. All the double hydro-
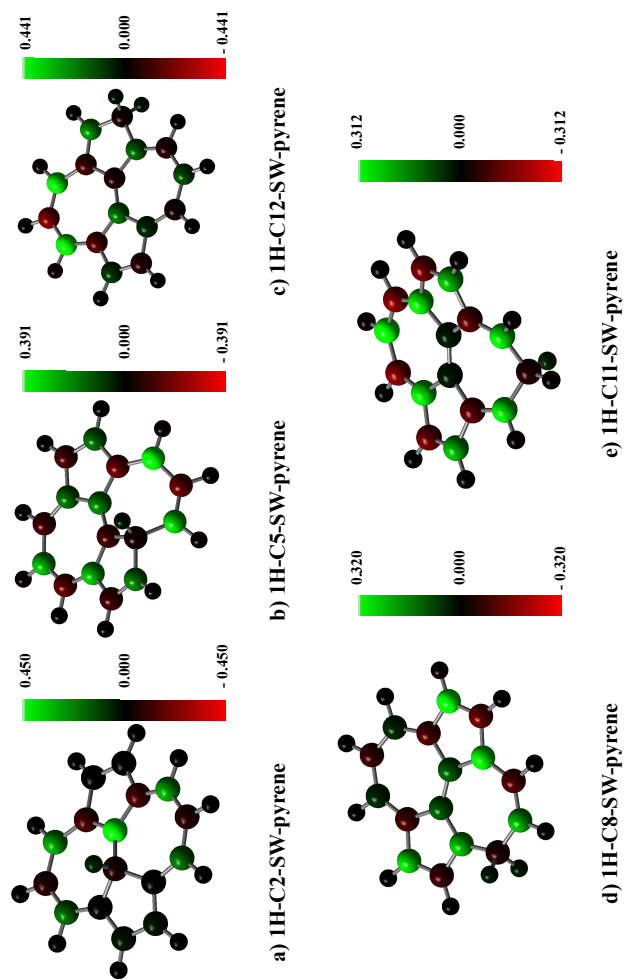
Figure 3.7: Spin population analysis for each optimized geometry of single hydrogenated species of SW–pyrene. The colour scale shows the distribution of spin-up (green) and spin-down (red) for each atom.
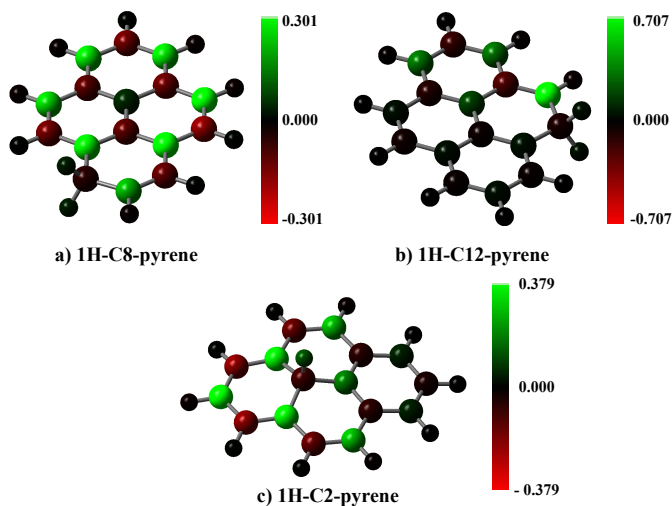
Figure 3.8: As in Fig. 3.7, but for each optimized geometry of single hydrogenated species of pristine pyrene.

Table 3.2: Energy barrier (ΔE_{bar}), binding energy (ΔE_{bind}) and carbon-carbon distance (d) values for distal (|) and adjacent (-) carbon pairs of SW-pyrene hydrogenated with two extra hydrogen atoms.

C pairs	ΔE_{bar} (eV)	ΔE_{bind} (eV)	d (Å)
C(12)|C(4)	0.033*	2.00	2.49
C(5)-C(2)	a	2.21	1.56
C(8)|C(3)	a	2.41	2.66
C(11)|C(2)	a	2.49	3.27
C(2)-C(4)	0.005*	2.59	1.55
C(8)-C(11)	0.005*	3.00	1.53
C(5)|C(13)	0.005*	3.02	2.91
C(12)-C(10)	0.005*	3.18	1.52

a Denotes calculations that did not converge.

* Values to be considered 0 eV (see main article text).

genated isomers have non-planar structures (Fig.3.6 for some examples). As to be expected,[17,128] the most stable species are 2H–C12C10–SW and 2H–C8C11–SW, where the dihydrogenation occurs at the edge.[169] The isomer 2H–C5C13–SW has a similar binding energy even if the 2 H atoms are attached to distal carbons. The dihydrogenation of the C(2)–C(4) junction follows at 2.59 eV. The presence of the SW defect significantly decreases the energy barrier in the C(2)-C(4), thus, increases the reactivity of the molecule. Calculations on equivalent carbon sites in pristine pyrene reveals that the dihydrogenation on C(5)|C(13) has a binding energy of 2.21

eV, C(8)-C(11) of 2.70 eV and C(2)-C(4) of 1.72 eV, hence, showing less stability than the same positions calculated on SW–pyrene. Surprisingly, the binding energy for the 2H–C12C10 isomer is 3.59 eV, 0.41 eV more stable than the equivalent isomer of SW–pyrene. In this last case, the inversion of reactivity might be attributed to the added strain on the already perturbed pentagonal ring in the SW–pyrene. The high binding energy of 2H–C5C13–SW (Fig. 3.6) suggests that the heptagonal ring can provide additional flexibility and, hence, a larger stability for the isomer. Indeed in this isomer the part of the hydrogenated heptagon that deviates significantly from planar has bond angles C(5)-C(8)-C(11) = 121.19° and C(13)-C(11)-C(8) = 121.77°, closer to the internal angles of an hexagon (120°) than those of a heptagon. We thus confirm that the most stable species are formed due to the largest electronic affinity of the atomic hydrogen for the carbons located on the edges. [137] Furthermore, in the case of the second hydrogenation, introducing a Stone–Wales defect appears to increase the reactivity and in most cases the stability of the dihydrogenated species.

3.3.3.   Molecular Hydrogen Formation

To follow, we investigated the formation of molecular hydrogen from the dihydrogenated intermediates discussed in the previous section. The formation of H_2 in these molecules can occur through two different mechanisms. The first type of mechanism is the extraction process that can in-

a) Extraction Mechanism

b) Transposition-Extraction Mechanism
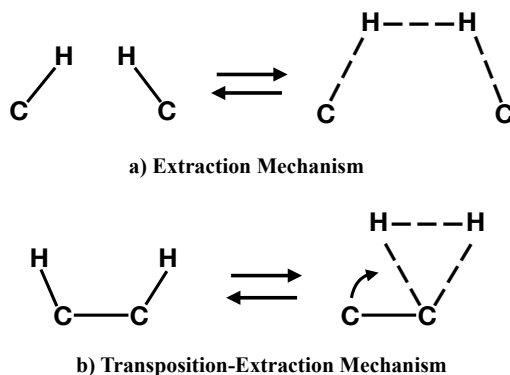
Figure 3.9: Schematic representation of the process that leads to the formation of transition state for the molecular hydrogen formation: the extraction (a) and the transposition-extraction (b) mechanisms.

volve H atoms attached either to neighbour or distal carbons. This mechanism is characterized by a concerted transition state formed by the partial formation of a H–H bond and the partial break of C–H bonds (Fig. 3.9,

top panel). The second type of mechanism occurs only for adjacent carbon pairs, in particular on C(2)–C(4), C(5)–C(8) and C(8)–C(11), and can be defined as a transposition-extraction (Fig. 3.9, bottom panel). In the transition state of this mechanism one H atom is transposed to the adjacent carbon where there is the partial formation of a H–H bond and the partial rupture of a C–H bond. This eventually leads to the extraction of H_2.

Table 3.3: Values of energy barrier (ΔE_{bar}), reaction energy (ΔE_r) for the extraction of H_2 in different isomers of doubly hydrogenated SW–pyrene. Also reported are distances between the two carbon atoms where the extra hydrogen atoms are attached (d) in the transition state and the type of mechanism involved in the formation (see Fig. 3.9). The symbols - and | identify adjacent and distal carbons, respectively.

STONE-WALES				
C pairs	ΔE_{bar} (eV)	ΔE_r (eV)	d (Å)	type
C(12)-C(10)	4.87	0.28	1.44	a)
C(8)-C(11)	4.60	0.10	1.48	a)
C(5)-C(8)	3.46	0.03	1.51	b)
C(2)-C(4)	2.94	-0.72	1.51	b)
C(5)-C(2)	2.42	-1.00	1.55	a)
C(8)|C(3)	2.58	-0.49	2.42	a)
C(12)|C(4)	2.07	-0.80	2.28	a)
C(5)|C(13)	1.84	-0.21	2.83	a)
C(11)|C(2)	1.96	-0.77	2.85	a)

Table 3.4: Values of energy barrier (ΔE_{bar}), reaction energy (ΔE_r) and carbon-carbon distance (d) in the transition state for the extraction of molecular hydrogen in pristine pyrene.

PRISTINE				
C pairs	ΔE_{bar} (eV)	ΔE_r (eV)	d (Å)	type
C(12)'-C(10)'	4.89	0.48	1.45	a)
C(8)'-C(11)'	4.21	-0.28	1.50	b)
C(2)'-C(4)'	2.71	-2.33	1.57	b)
C(5)'| C(13)'	1.67	-0.77	2.61	a)

Table 3.3 shows the values for energy barriers and reaction energies (*i.e.* the difference in energy between the products and the reagents) together with the carbon–carbon distances in the transition state and the type of reaction. The extraction of H_2 from adjacent carbons in the edge — as in the case for C(12)–C(10) and C(8)–C(11) — is the most energetically expensive, with energy barriers of almost 5 eV and slightly endoergic products. On adjacent, internal carbon atoms, the extraction of H_2 requires almost 3 eV and the reaction is quite exoergic, with the products being almost 1 eV

more stable than the reactants. This is to be expected, since the release of H_2 would remove the strain in the molecules caused by the sp^3 hybridisation at the single hydrogenation site. Interestingly, we found that distal carbon atoms promote the formation of H_2, with barrier lower than 2 eV and exoergic reactions.

We evaluated energy barriers and reaction energies for selected dihydrogenated isomers in the pristine pyrene for comparison (Table 3.4). Energy barriers for H_2 extraction are slightly lower than the values found for the same process in defective pyrene, with a maximum difference of 0.39 eV when considering the C pair C(8)-C(11). The reaction is also more exoergic; in particular for the same reaction type (a) and bond length, the extraction of H_2 from the C-pair C(2)–C(4) has a reaction energy of -0.72 eV in the defective pyrene and of -2.33 eV in the pristine molecule. This is the result of the high stability of the pristine pyrene with respect to its hydrogenated counterparts. The energy barriers for the H_2 formation found on pristine pyrene are slightly higher than what was found previously on graphene;[170,171] this confirms that small graphene-nanoflakes like pyrene behave like graphene when H_2 formation is considered.

Fig. 3.10 shows the potential energy surface for the formation of H_2 on defective and pristine pyrene, considering hydrogenation on the same ring (left) and on the SW junction C(2)–C(4). In the case of SW–pyrene, the energy barrier for the first hydrogenation, namely 0.2 eV, is the limiting barrier for the formation of H_2 independently, if we consider carbons belonging to the same ring or the SW junction. For pristine pyrene, on the other side, the limiting barrier is 0.7 eV, represented by the transition state for the formation of H_2 on the hydrogenated intermediates. If distal carbon atoms are considered, H_2 formation has a submerged barrier, with a value comparable to what is seen in SW–pyrene. As seen in Section 3.3.2, the addition of H atoms on the reactive SW–pyrene results in stable isomers and the subsequent formation of H_2 has a submerged barrier.

3.3.4. Astrophysical Implications

Observed infrared spectra of astronomical objects have been interpreted as revealing the presence of SW–PAHs.[162,172] We calculated the infrared spectra of pristine and Stone–Wales pyrene (see Appendix) and their spectra can be identified apart, thanks to the presence of a strong mode around 1375 cm^{-1} in pristine pyrene (see also ref.[163]). The same is true for 1H–C2–SW pyrene that shows strong activity in the 1300-1600 cm^{-1} region, while 1H-C2 pristine pyrene as little to no activity there. Hopefully the James Webb Space Telescope that will observe the AIB spectrum in the full 3-20 μm region at high spectral resolution (R>1550) will allow astronomers to confirm the presence of SW-PAHs. Defective PAHs as pristine PAH molecules should take part in the chemistry happening in space. Astrochemical models based on combustion chemistry[173] suggest
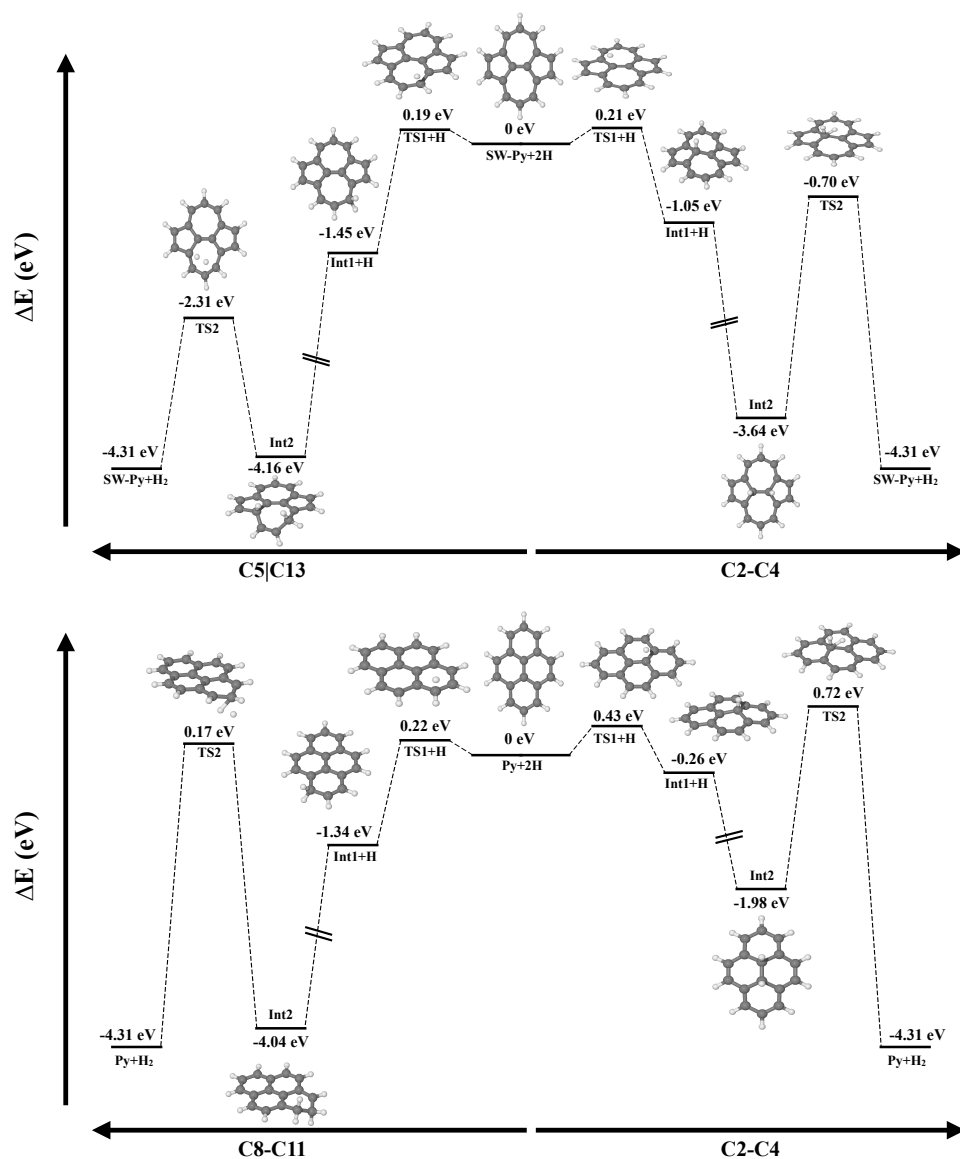
Figure 3.10: Comparison between the potential energy surfaces for the formation of molecular hydrogen from SW (top) and pristine pyrene (bottom).

that PAHs and carbon soot should be efficiently formed in the inner regions of carbon-rich giant stars.[174] Defective PAHs can be created starting from 6-membered ring species through a process requiring energies of the order of ≈8 eV (Fig. 3.2). To evaluate the stability of the mechanism, we
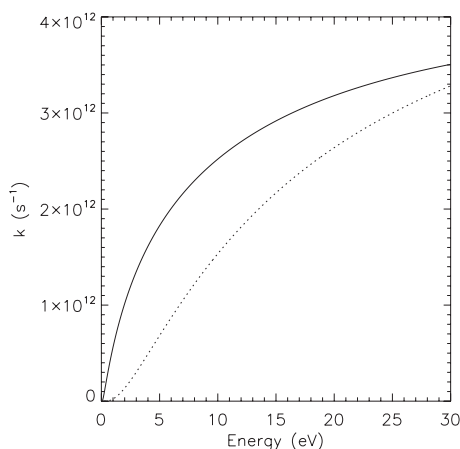
Figure 3.11: Comparison between reaction rates for the forward reaction toward SW–pyrene (solid line) and for the reverse reaction toward pristine pyrene (dashed line) as a function of internal energies. Rates were calculated using the RRKM formalism [147,175] starting from energies and vibrational analysis performed in this paper at M06-2X/pcseg-1 level.

calculated the Rice-Ramsperger-Kassel-Marcus (RRKM) rates [175] as functions of internal energy for the backward and forward reactions when the system is in the inter- mediate state (Fig. 3.2). Once the intermediate is formed and possess enough internal energy, roughly a third of the time the mechanism will go forward and a defective structure will be created. The timescale needed for the intermediate to revert back to pristine pyrene is comparable with the timescales to share the excess energy among the other modes of the molecule, few tens of picoseconds. [176] At internal energies above 30 eV the process is even more frequent. On graphene the energy needed to perform a Stone–Wales transformation is calculated to be 5 eV [157] and this might hint at the size dependence of the energy involved in the SW rearrangement. Nevertheless, the high barrier derived here makes it unlikely that SW–PAHs are formed in the interstellar medium itself. An alternative route could be the formation through energetic processing of 6-membered ring species. Indeed, molecular dynamics simulations show that interaction of PAHs with a sub-keV ion can break C–C bonds without perturbing the rest of the structure [177] and can promote the formation of the 5- and 7-membered rings. [178] Clearly more studies are needed to identify a precise pathway for the formation of SW–PAHs through energetic processes. Once SW–PAHs are formed, they can survive for a long time due to the higher barrier required for the conversion to the unaltered 6-membered PAHs and, thus, take part in the AstroPAH populations (Fig. 3.11).

Both neutral and cationic PAHs have been put forward as catalytic surfaces where H_2 can be efficiently formed *via* an Eley–Rideal mechanism after initial hydrogenation (see the recent review by Wakelam et al.[33]). The key resides in the very low sticking barrier when the H is on the edge, calculated to be a few tens of meV, and the barrierless abstraction of H_2, as seen from both experiments and theory. Photochemical evolution models of PAHs in photodissociation regions show that the Eley–Rideal mechanism is effective only when the gas temperature is enough to overcome addition and extraction barriers.[41] Accurate DFT calculations including zero point vibrational energy correction, like the one presented here and also elsewhere[40] give sticking barriers one order of magnitude higher (few hundreds of meV) than what were used in photochemical models in the past.[41,112,148] This means that even higher gas temperatures are needed for the process to happen. Also, the efficiency of the Eley–Rideal mechanism depends on the incident direction of the H that impinges on the superhydrogenated PAH molecule. If the molecule is heavily superhydrogenated, this is not much of an issue. However, astronomical observations of PAHs and the aforementioned photochemical models show that PAHs are scarcely superhydrogenated, with up to 4 additional hydrogen atoms in the shielded region ($A_v > 4$). Thus, while the energetics of Eley-Rideal H_2 formation are very favourable, its efficiency is below 1%.[41]

Other mechanisms, such as H_2-loss from photodissociation of normally hydrogenated PAHs[153] and protonated PAHs[179,180] have been invoked to explain the enhanced H_2 formation rates in some photodissociation regions.[126] In addition, PAH molecules can exist in the form of aggregates or clusters in the denser part of the photodissociation regions[32,181] and they might catalyse the formation of H_2. The study of the specific reactions involved and the interplay with competing channels is interesting and could have important implications for H_2 formation; however it is beyond the scope of the present work and should be addressed in a separate publication.

Here we have shown that Stone–Wales defects in PAHs can facilitate the catalytic formation of H_2. First, the presence of the defect lowers the difference in the H addition barrier between internal and edge carbons, which is 0.05 eV compared to pristine pyrene where the difference is 0.2 eV. Second, singly and doubly hydrogenated intermediates in SW–pyrene are located in a deeper well of the PES than in the case of pristine pyrene. The largest differences are seen for the 1H–C2–SW and 2H–C2C4–SW, where the H atoms are attached on the Stone–Wales rotated C2–C4 bond (Fig. 3.10, upper right). Moreover, the 2H-C2C4-SW intermediates needs slightly higher energies, in the order of 0.2 eV, to either lose a H atom or form H_2 than in the same isomer for the pristine case. This may imply that superhydrogenated Stone–Wales PAH species may have a longer lifetime against dehydrogenation than superhydrogenated pristine PAH in the interstellar medium and that they can be a sink for additional hydrogen atoms also in the case of

diffusion. [169] Finally, in SW-pyrene the catalytic formation of H_2 is limited only by the barrier for first hydrogen attachment, which is of the order of 0.2 eV. H_2 formation from 2H-C2C4-SW pyrene requires 2.9 eV, comparable to the energy needed to photodissociate H_2 from a PAH cation. [147] An additional favourable channel for catalytic H_2 formation was found in both SW and pristine pyrenes, in the case where hydrogenation occurs on distal carbon atoms (2H-SW-C5C13 and 2H-SW-C11C2, see Table 3.3 and 3.4). The energy barrier for this reaction, that proceeds through an extraction mechanism, is typically below 2 eV with the lowest for pristine pyrene at 1.67 eV. This type of reaction might help to increase the amount of H_2 formed in the interstellar region where superhydrogenated PAHs are present.

There are other processes that can compete with the formation of H_2 on hydrogenated SW-PAHs. Specifically, H-loss and H-roaming might be important reactions to be considered. [147,182,183] For SW-pyrene, H-loss can be a competitive channel when H_2 is formed on the C2–C4 junction, as the difference between the two reactions is 0.35 eV, which favours the H-loss. This is not the case for the formation of H_2 on distal carbons, where the energy difference is 0.88 eV, favouring the H_2 formation (Fig. 3.10). Calculations of energy barriers and reaction energies for H-roaming from C4 to C7 on 2H–SW–C2C4 are 0.92 and 0.40 eV, while for the reverse reaction they are 0.52 and -0.40 eV, respectively. This means that H will move rapidly to the nearby tertiary carbon position but likely go back to position C4. This will slow down the formation of molecular hydrogen. Calculations for H roaming along the edge in 2H–SW–C5C13 gives higher values, 1.65 eV for the energy barrier and 1.00 eV for the reaction energy. The reverse reaction has a barrier of 0.65 eV and a reaction energy of -1.00 eV. The difference in energy barrier between H-roaming and H_2 formation is only 0.2 eV and thus competition might be less important. We defer a detailed modelling of the kinetics of the processes involved to a future study.

Finally, we want to note that in this study we provided binding and barrier energies for H_2 extraction that can be useful for astrochemical modelling. We note that cross-over quantum mechanical temperature ranges between 397 and 534 K for SW–pyrene and between 400 and 571 K for pristine pyrene (see Appendix). For lower temperatures a proper evaluation of the reaction rate coefficient has to take tunneling effects into account.

3.4. Conclusions

We studied, using computational chemistry, the formation mechanism and catalytic properties of a prototype PAH with a Stone–Wales defect, pyrene. We calculated binding energies and barrier energies indispensable for subsequent astronomical modelling studies. We found:

- The creation of a SW defect requires 8.42 eV. Moreover, the addition of one atomic hydrogen on the inner carbon of pristine pyrene reduces the energy barrier for the creation of the SW defect by 1.82 eV.

- The C–C bond involved in the creation of the SW defect has enhanced reactivity, which translates to a lower H addition barrier for the first hydrogenation (the second is barrierless) and more stable singly hydrogenated SW–pyrene with respect to the pristine molecule. Thus, the SW defect "normalises" the differences in sticking barriers and stability seen between edge and central carbon atoms in pristine PAHs.

- Catalytic formation of H_2 in SW–pyrene is limited only by the barrier of the first hydrogen addition, in the order of 0.2 eV.

- An additional mechanism for H_2 formation involves hydrogenation of distal carbon atoms and has an energy below 2 eV, both in pristine and SW–pyrenes.

In the interstellar medium, due to their enhanced reactivity towards hydrogenation and stability, SW-containing PAHs can act as H sinks in regions of moderate irradiation. In this region, together with pristine PAHs, they can promote the catalytic formation of H_2 in addition to the Eley–Rideal mechanism.

3.5. Appendix

Dealing with Biradical Systems

In order to produce a correct UHF wavefunction for singlet states open-shell biradical systems, we mixed HOMO and LUMO in order to destroy α-β orbitals and spatial symmetries (keyword guess=mix implemented in Gaussian16) doing a constrained optimization of the geometry when the hydrogen is distant more than 3 Å from the carbon site taken in exam. We verified the correctness of the calculation for singlet closed shell bi-radicals analyzing the eigenvalue S^2 (*i.e.* close to 1) and verifying that the molecular orbitals (MOs) and, specifically, alpha orbital and beta orbital are distinguishable and separated upper the Fermi level (*i.e.* the MOs of pyrene are separated by the MO of the radical hydrogen upper the Fermi level). We optimized the geometry of TS controlling the initial guess with the correct wave function (using the keyword guess=read implemented in gaussian16 after having recorded the correct wave function in a appropriate chk format from the constrained optimization done in the precedent step).

Table 3.5: Crossover temperatures (Tc) and imaginary frequencies (*ifreq*) of the transition state for the extraction of molecular hydrogen promoted by the carbon pairs located in the Stone-Wales and pristine pyrene.

STONE-WALES		
C pairs	Tc (K)	*ifreq* (cm^{-1})
C(12)-C(10)	502	i2192.9714
C(8)-C(11)	488	i2132.8003
C(5)-C(8)	421	i1838.1007
C(2)-C(4)	400	i1747.8361
C(5)-C(2)	511	i2230.0669
C(8)|C(3)	534	i2330.1100
C(12)|C(4)	427	i1863.5223
C(5)|C(13)	397	i1733.7670
C(11)|C(2)	444	i1940.0362
PRISTINE		
C(12)'-C(10)'	506	i2210.3011
C(8)'-C(11)'	571	i2494.1826
C(2)'-C(4)'	481	i2100.1131
C(5)'|C(13)'	401	i1750.1005

Mulliken Spin analysis

Mulliken Spin partitioning scheme, employing the M06-2X/pcseg-1 theory level, for each atoms of the minima optimized structures of single extra hydrogenated species of SW-pyrene and pristine pyrene are reported (Fig. 3.12 and 3.13)

Crossover Temperature

We report in Table 3.5 the values of crossover temperatures along with the imaginary frequencies (*ifreq*) of the transition states, for each carbon pairs, of the process related to the molecular hydrogen extraction by Stone-Wales and pristine pyrene.

The crossover temperature (Tc) has been calculated with the following equation:

$$Tc = (\hbar * \text{freq})/k_b \tag{3.4}$$

$\hbar$=h/2π is the reduced Planck's constant, $ifreq$ is the module of the imaginary frequency of the transition state and k_b is the Boltzmann's constant.

(a) 1H-C2-SW-pyrene

(b) 1H-C5-SW-pyrene

(d) 1H-C8-SW-pyrene

(c) 1H-C12-SW-pyrene

(e) 1H-C11-SW-pyrene
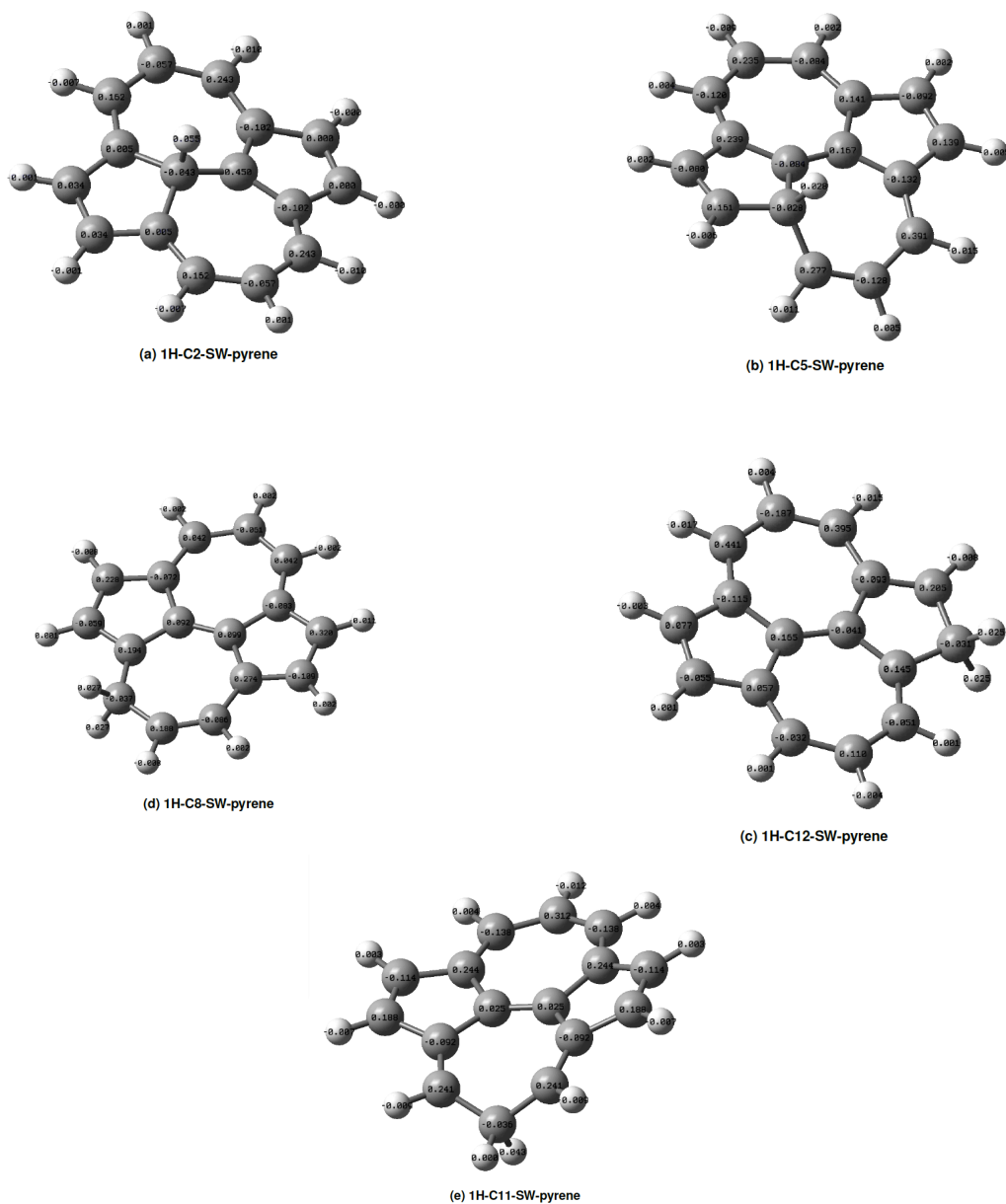
Figure 3.12: Mulliken Spin partitioning scheme of several species of SW-pyrene with one hydrogen chemisorbed.

(a) 1H-C8-pyrene

(b) 1H-C12-pyrene

(c) 1H-C1-pyrene
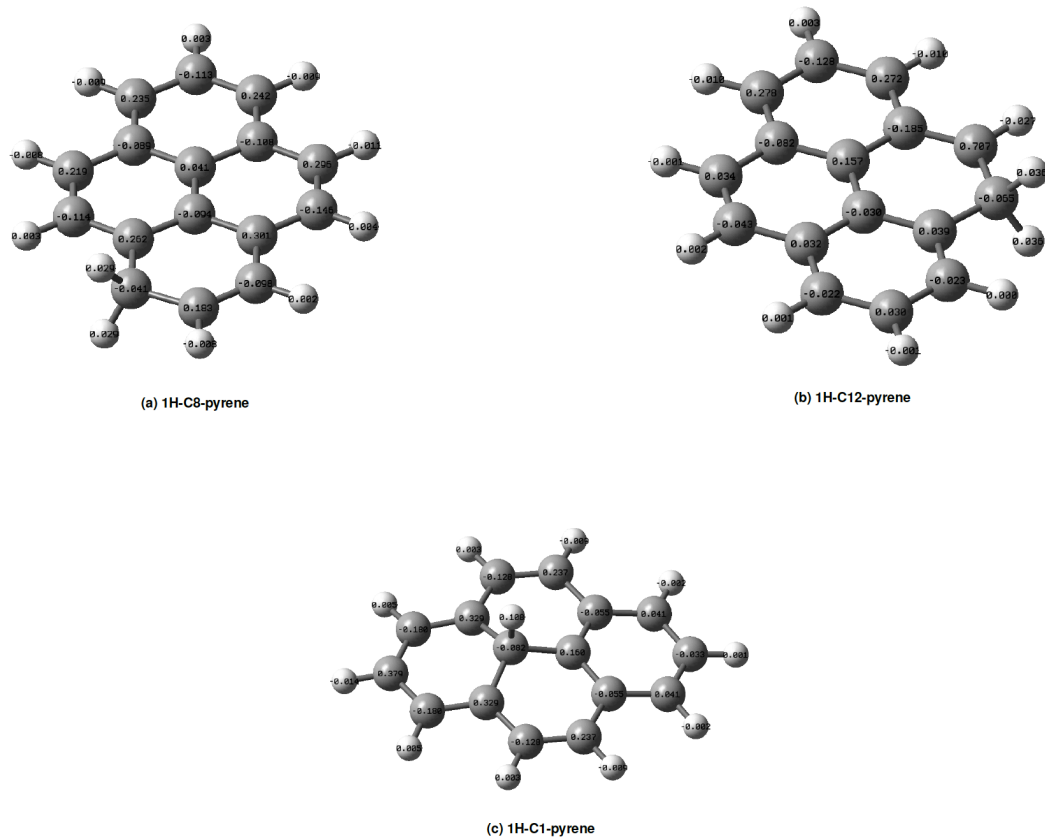
Figure 3.13: Mulliken Spin partitioning scheme of several species of pyrene with one hydrogen chemisorbed.
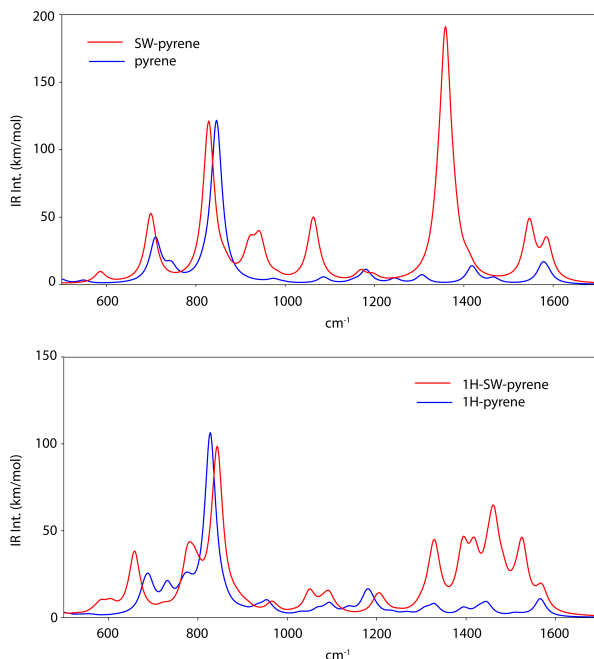
Figure 3.14: Top panel. Comparison between the infrared spectrum obtained at B3LYP/4-31G level of Stone-wales pyrene (red) an pristine pyrene (blue). Bottom panel. Comparison between 1H-C2-SW pyrene and its pristine isomer.

Infrared Spectroscopy of Pristine and Stone-Wales Pyrene

The harmonic infrared spectra of pristine, Stone-Wales pyrene and their singly hydrogenated isomers were calculated with B3LYP/4-31G and a triple scaling factor scheme developed especially for PAH molecules.[184] The spectra were convoluted with a Gaussian line shape with a Full Width Half Maximum of 30 cm^{-1} and are represented in Fig. 3.14. Stone-Wales pyrene possesses a very strong C-C mode at 1357 cm^{-1} and other less strong modes at 1062 cm^{-1} (C-H in plane) and 940 cm^{-1} (C-C skeleton mode) which are not present in pristine pyrene and can help distinguishing between the two structures. As for the singly hydrogenated molecules, 1H-C2-SW pyrene shows strong infrared activity in the 1300-1600 cm^{-1}, with a combination of C-C stretch and C-H in plane modes.

CHAPTER 4

INTERACTION OF AROMATIC MOLECULES WITH FORSTERITE: ACCURACY OF THE PERIODIC DFT-D4 METHOD

D. Campisi, T. Lamberts, N. Y. Dzade, R. Martinazzo, I. L. ten Kate, and A. G. G. M. Tielens, *J. Phys. Chem. A*, **2021**, *125*, 13, 2770–2781

Abstract. Density functional theory (DFT) has provided deep atomic-level insights into the adsorption behavior of aromatic molecules on solid surfaces. However, modeling the surface phenomena of large molecules on mineral surfaces with accurate plane wave methods (PW) can be orders of magnitude more computationally expensive than localized atomic orbitals (LCAO) methods. In the present work, we propose a less costly approach based on the DFT-D4 method (PBE-D4), using LCAO, to study the interactions of aromatic molecules with the {010} forsterite (Mg_2SiO_4) surface for their relevance in astrochemistry. We studied the interaction of benzene with the pristine {010} forsterite surface and with transition-metal cations (Fe^{2+} and Ni^{2+}) using PBE-D4 and a vdW-inclusive density functional (Dion, Rydberg, Schröder, Langreth, and Lundqvist (DRSLL)) with LCAO methods. PBE-D4 shows good agreement with coupled-cluster methods (CCSD(T)) for the binding energy trend of cation complexes and with PW methods for the binding energy of benzene on the forsterite surface with a difference of about 0.03 eV. The basis set superposition error (BSSE) correction is shown to be essential to ensure a correct estimation of the binding energies even when large basis sets are employed for single-point calculations of the optimized structures with smaller basis sets. We also studied the interaction of naphthalene and benzocoronene on pristine and transition-metal-doped {010} forsterite surfaces as a test case for PBE-D4. Yielding results that are in good agreement with the plane wave methods with a difference of about 0.02-0.17 eV, the PBE-D4 method is demonstrated to be effective in unraveling the binding structures and the energetic trends of aromatic molecules on pristine and transition-metal-doped forsterite mineral surfaces. Furthermore, PBE-D4 results are in good agreement with its predecessor PBE-D3(BJM) and with the vdW-

inclusive density functionals, as long as transition metals are not involved. Hence, PBE-D4/CP-DZP has been proven to be a robust theory level to study the interaction of aromatic molecules on mineral surfaces.

4.1. Introduction

Astronomical observations have revealed a rich and diverse inventory of molecules in interstellar space. The observed different species range from simple molecules such as H_2, H_2O and NH_3, identified in the birthplace of stars (molecular clouds), to ions and radicals detected in regions with high UV radiations as well as complex and stable aromatic molecules.[8] Furthermore, complex aromatic molecules along with prebiotic building blocks of life, *e.g.*, amino acids and sugars, have been detected in asteroids and meteorites.[185] Polycyclic aromatic hydrocarbons (PAHs) are a class of abundant aromatic molecules in our galaxy and beyond. They have been identified through their vibrational signature in infrared spectra and thought to be involved in many important processes that regulate the physical conditions of star-forming regions.[26] Specifically, PAHs have been extensively studied as catalysts for interstellar H_2 formation.[16–18,39,40,129,186] They may also play a role as reagents in many reactions involving atoms, ions, and molecules that contribute to the rich organic inventory of space.[187] Finally, it has been suggested that PAHs may be more directly involved in the origin of life by providing a convenient assemblage structure for RNA.[188]

The coexistence and high abundance of both simple and complex species in space are indicative of the presence of at least two and potentially more chemical routes toward molecular complexity.[8] One chemical route is a bottom-up approach, where atoms and small molecules react to form larger species, one or a few atoms at a time. As densities and temperatures are low, this buildup is slow, and only relatively small molecules are formed this way. Much of this chemistry is thought to take place on submicron-sized grains, where CO can be hydrogenated on icy surfaces by H atoms to form H_2CO and CH_3OH.[189] The latter can be the feedstock for further complex chemistry.[190–193] The other chemical route starts in the high-density and -temperature regimes associated with stellar outflow. The stellar conditions will lead to soot formation, and large molecules such as PAHs are formed and injected into the interstellar medium (ISM).[194–196] Exposed to harsh environments, these molecules can fragment or isomerize due to interaction with UV photons and/or energetic ions.[31] PAHs and their daughter products can also interact with simple species on ice surfaces in space.[197,198] Eventually, the products of both bottom-up and top-down chemistry as well as the prevalent mineral grains can become part of planetesimals in planet-forming disks. During the early stages of their evolution, planetesimals will go through a warm (~500 K), aqueous phase, and large-scale transport within these bodies will allow direct interaction

of PAHs with mineral surfaces, opening up new reaction channels. Eventually, these planetesimals will contribute to the organic inventory of terrestrial planets in the habitable zone of new planetary systems.[8]

Chemistry on mineral surfaces may thus be of great relevance to molecular astrophysics. However, studies on astronomically relevant mineral surfaces are sorely lacking.[9] Specifically, while quantum chemistry and in particular density functional theory (DFT) are well established as important tools in assessing the relevance of gas-phase reactions of PAHs to space,[16,39,40,79] studies on the interaction of molecular species with mineral species have lagged due to the prohibitive computational costs and the challenges in employing hybrid functionals that correct the self-interaction error of standard (semilocal) DFT methods.[199] In material sciences, plane wave (PW) codes such as VASP have been widely employed as they ensure robust and accurate results.[92,200–202] However, plane wave codes allow modeling of molecules of limited size due to their computational cost.[203] Codes such as SIESTA[98] make profitable use of localized atomic orbitals (LCAO) basis sets that allow the study of larger systems than plane wave by employing periodic DFT. Unfortunately, LCAO methods suffer from the so-called basis set superposition error (BSSE), which leads to an overestimation of the binding and adsorption energy.[204] This is the "price to be paid" for computational efficiency. This issue can be overcome using the counterpoise method developed by Boys *et al.*,[100] which is a pragmatic solution to the problem. Another challenge is that DFT methods describe bond formation well, thanks to a good description of the electronic correlation in the region of orbital overlapping between atoms to form the bond, but their weak spot is the lack of an accurate description of the London dispersion, *i.e.*, density transfer between two long-distance orbitals.[81] One of the approaches to overcome this issue is to compute an interatomic potential named the DFT-D method.[205,206] This method is a posteriori empirical correction to the KohnSham (KS) energy. Hence, the dispersion energy is calculated independently and is summed up to the KS energy ($E_{KS} + E_D$).[81] An alternative method to take the London dispersion into account is through the use of nonlocal correlation functionals such as vdW-DF[82] and vdW-DF2,[207] which depend directly on the electron density. However, this method results in significant BSSE issues when calculating the binding energy of organics on metal surfaces.[208]

Few studies have benchmarked DFT functionals that model the interactions of molecules on forsterite surfaces.[209] Here, we test an accurate, yet cheap method based on LCAO that employs the Perdew, Becke, and Ernzerho (PBE)[210] exchangecorrelation functional and the DFT-D4 method developed by Grimme *et al.*[206] (PBE-D4). The aim of this work is to compute accurate binding energies that can be used in astronomical grain surface models[9,211] to predict the abundance of large aromatic molecules such as PAHs interacting with a mineral surface under interstellar conditions, specifically the {010} forsterite surface, because of its relevance in astro-

physics.[37,212,213] The proposed theoretical approach is focused on systems of interest in astronomy, but its validity applies equally well to systems of interest in planetary science and material science. In fact, PAHs were detected in martian and carbonaceous chondrite meteorites,[214] and in the terrestrial environment; they are relevant because of their carcinogenic properties as well as their pollution properties.[113] The general problem in removing PAHs from contaminated soils makes materials such as minerals worthy of investigations.

4.2.   Theoretical Methods and Models

In the present work, we model a 4 × 3 {010} forsterite surface ({010}-fo) with the molecular formula $Mg_{96}O_{192}Si_{48}$ (Fig. 4.1), which is the most studied and stable forsterite surface under dry conditions[215–217] as well as the most studied one for the interaction of organic compounds.[218,219] Along with the pure {010}-fo (Fig. 4.1(a) and 4.1(c)), we study its defective surfaces with a single doped Fe^{2+} (Fe-{010}-fo) and single doped Ni^{2+} (Ni-{010}-fo), as shown in Fig. 4.1(b) and 4.1(d). The defective surfaces are generated by the substitution of a transition-metal atom, Fe or Ni in this case, for a Mg atom on the surface of 4 × 3 {010}-fo.

The non-polar {010}-fo is generated by cutting the fully optimized bulk with the METADISE code, which ensures a zero dipole moment along the z-axis.[220] The generated surface has a thickness of 9.28 Å to preserve the bulk properties and a vacuum region of 25 Å to avoid the interactions between the slab images. Finally, we create a 4 × 3 supercell of the nonpolar {010}-fo, which is large enough (18.996 Å x 17.938 Å) to minimize lateral interactions between adsorbed molecules in neighboring image cells.

In view of the large computational cost involved in modeling the interaction of large aromatic molecules with the supercell of {010}-fo, we employ SIESTA as the LCAO code[98] with core pseudopotentials. We use PBE[210] as the generalized-gradient approximation (GGA) exchangecorrelation functional and the Dion, Rydberg, Schröder, Langreth and Lundqvist[72] (DRSLL) vdW-DF exchangecorrelation functional along with a polarized double-zeta (DZP) basis set. We set the radii for the split-valence type of the basis of hydrogen atoms to 0.50. Furthermore, the PBE/DZP method was already tested to reproduce correctly the adsorption properties of small molecules on {010}-fo.[209] To have comparable results, we use the same pseudopotentials for both the PBE and DRSLL functionals. For the case of DRSLL, we set the maximum angular momentum of the KleinmanBylander projectors for the H atoms to zero to avoid ghost states for high values of angular momentum. We employ the MonkhorstPack[102] scheme to sample the Brillouin zone using 7 × 3 × 7 K-points for the bulk and 2 × 2 × 1 for the {010}-fo supercell along with the spin-unrestricted formalism for all calculations. The structures are considered optimized when the Hellman-

(a) {010}-fo (Top View)

(c) {010}-fo (Side View)

(b) (M=Fe/Ni)-{010}-fo (Top View)

(d) (M=Fe/Ni)-{010}-fo (Side View)
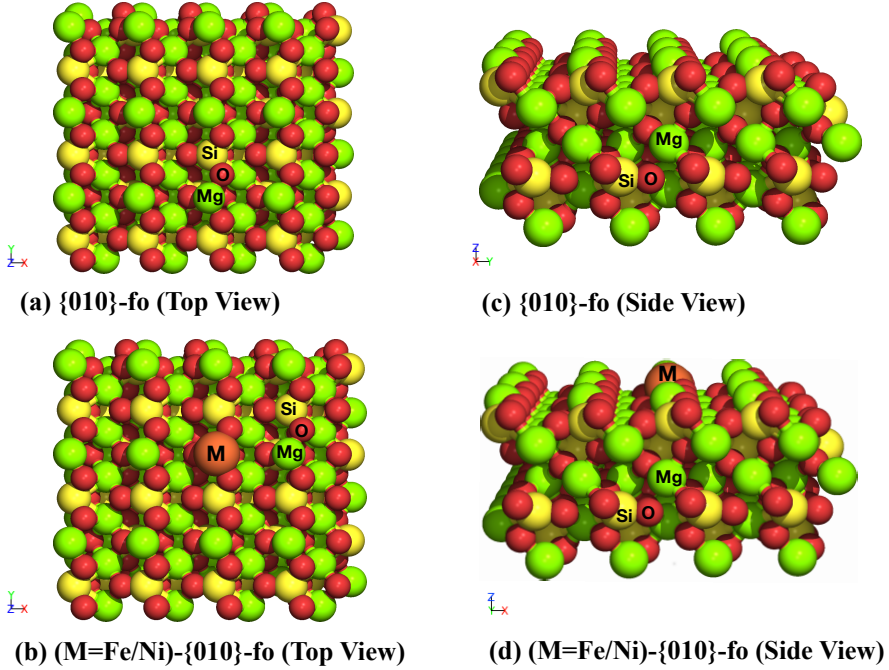
Figure 4.1: Top view (a) and (b) and lateral view (c) and (d) of the optimized structure of the 4×3 {010} forsterite surface with the corresponding atomic labels (Mg, O, Si, and M = Fe or Ni). The vacuum region is located along the z-axis.

nFeynman forces are less than 10^{-3} eV Å^{-1}. The mesh cutoff grid density converges to 200 Ry (convergence test reported in the Appendix). We apply the counterpoise scheme to correct the total energy for the BSSE.[100,101]

When a non-vdW-inclusive functional such as PBE is employed, the London dispersion energy (E_D) is calculated a posteriori with DFT-D4[206,221,222] and DFT-D3[205] codes due to the lack of implementation of these methods in SIESTA code. Therefore, the E_D is computed separately and summed up to the E_{KS} estimated at PBE level. We use the revised Becke-Johnson damping (BJM)[223,224] for the DFT-D3 method for a fair comparison with DFT-D4 that uses the same damping function[206] and the nonadditive AxilrodTellerMuto three- body dispersion correction for both methods.[225]

The electronic structure of bulk forsterite is characterized by the projected density of states (PDOS) generated with the LDAU + U method as implemented in SIESTA.[226] The Hubbard U value is set to 15.3 eV to include the strong on-site Coulombic interaction of the 2p orbitals of oxygen atoms and reproduce the experimental band gap[227] of 8.4 eV with a tolerance population of 4×10^{-4} and a threshold tolerance of 10^{-2}. The PDOS

is generated by a single-point calculation from the optimized structure of PBE/DZP employing a polarized triple-zeta (TZP) basis set. We set the radii for the split-valence type of basis to 0.30 for all atoms besides the hydrogen, in which we use the same setup as for the case of DZP (see Appendix). This approach is necessitated by the need to converge correctly the empty states that require expensive and larger basis sets. An extra grid of 4 × 4 × 1 K-points of MonkhorstPack[102] is employed for all PDOS calculations. The peak width is generated using 5000 points and a broadening eigenvalue of 0.05 in the energy window between -60 and 200 eV.

To accurately compute the binding energy, the Hubbard U value needs to be retro-corrected based on experimental data but these are currently lacking in the literature. Our adopted approach allows us to compute the electronic structure without interfering with the binding energy trend while avoiding computational expensive calculations.

For all calculations involving the organics on the {010} forsterite surfaces, an electric field is applied to compensate for the dipole moment at the vacuum region on every self-consistent field (SCF) cycle. The structure and reference energy of the gas-phase molecules are obtained in a cubic cell of dimensions (15 Å x 15 Å x 15 Å) using a 1×1×1 MonkhorstPack K-point mesh.[102]

In this study, we refer to binding energy (E_b) as the difference between the energy of the reagents (the slab or the transition-metal cation, and the molecule in the gas phase) and the energy of the product (the molecule adsorbed on the slab or complexes with a transition-metal cation). A positive value of binding energy indicates an exoergic process. The adsorption energies reported in other studies are converted, for simplicity, into binding energies that are the opposite of the adsorption energy by definition.

4.3. Results and Discussions

Forsterite Bulk Properties. The bulk of forsterite (Mg_2SiO_4) has an orthorhombic structure and Pbnm as the space group,[228] see insert of Fig. 4.2. The forsterite structure is characterized by octahedral Mg atoms bound with six O atoms and tetrahedral Si atoms bound with four O atoms. This ionic system is formed by cations (Mg^{2+}) and an equivalent number of anions (SiO_4^{2-}) that maintain the system's electroneutrality.

From a geometry optimization using the PBE/DZP functional, the unit cell parameters are predicted at a = 4.80 Å, b = 10.28 Å, c = 6.01 Å and $\alpha = \beta = \gamma = 90°$, which compared closely with known experimental values and plane wave code results (Table 4.1). Including dispersion corrections using a vdW-inclusive functional such as DRSLL or an empirical method such as DFT-D3 does not change significantly the unit cell parameters of the bulk structure of forsterite. Also, the unit cell parameters obtained using PBE/ DZP are in close agreement with the hybrid functional B3LYP.
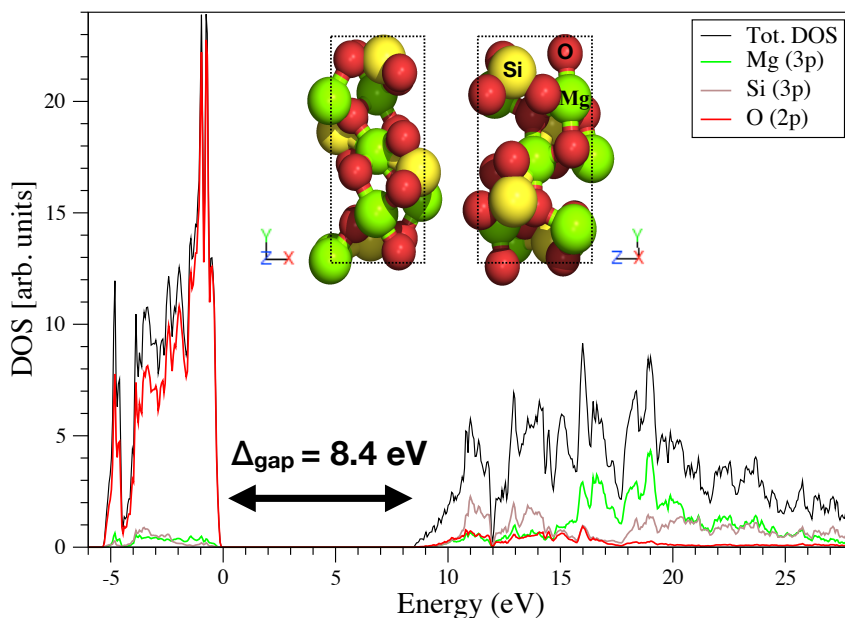
Figure 4.2: Hubbard-corrected total and projected density of states, PDOS, and optimized structure of the bulk (PBE/DZP) of forsterite with atomic labels reported on the corresponding atoms.

Table 4.1 also reports the elapsed time for the two different methods employed in this work, *i.e.*, PW and LCAO methods. PBE seems slightly faster than DRSLL, but both methods are about 1519 s (Table 4.1) faster than plane wave methods for the optimization of the bulk of forsterite.

Perusing the projected density of states (PDOS) spectra, shown in Fig. 4.2, the insulating behaviour of Mg_2SiO_4 is also well reproduced with a band gap of 8.4 eV in accordance with commonly reported band gaps of 7.59.5 eV.[227,229,230] The valence band is dominated by electrons of the 2p orbitals of O atoms, whereas the conduction band is dominated by electrons of 3p orbitals of Mg and Si atoms in conformity with theoretical studies making use of plane wave methods.[231] The electron density is centered around MgO and SiO bonds with average bond distances of 2.09 and 1.69 Å, respectively, in agreement with the previous experimental[232] and theoretical calculations.[213,233] Therefore, PBE/DZP can reproduce the bulk properties of forsterite.

Benzene Adsorption on Mg_2SiO_4 {010} Surface. The {010}-fo surface is characterized by an external layer, the interface between the mineral and vacuum region, of undercoordinated Mg atoms with a square pyra-

Table 4.1: Optimized unit cell of the bulk of forsterite at different levels of theory along with the experimental values and the elapsed time per SCF cycle (E.T.^{scf}) where applicable.

Methods	a (Å)	b (Å)	c (Å)	E.T.^{scf} (sec)
PBE/DZP*	4.80	10.28	6.01	23.068
PBE-D3/PW**	4.77	10.25	6.01	41.993
DRSLL/DZP*	4.83	10.34	6.04	27.318
PBE/PW[234]	4.76	10.24	6.00	
PBE/DZP[235]	4.80	10.28	6.02	
B3LYP/GTO[213]	4.80	10.25	6.01	
Experiments[228]	4.76	10.21	5.98	
Experiments[232]	4.75	10.19	5.98	

*This work employing SIESTA.

** This work employing VASP (see Appendix).

midal geometry above the inner layer of fully coordinated atoms in accordance with previous studies.[213] Here, we focus on the level of theory for the adsorption of a small aromatic molecule, benzene, on {010}-fo.[218,219] The binding energies of benzene interaction on the {010} forsterite (Fig.

Table 4.2: Binding energy (E$_b$), at various levels of theory, of benzene on the {010} forsterite surface. d$_{cm}$ is the distance between the center of the ring and the near Mg atom on the surface. .../TZP//.../DZP indicates a single-point calculation of the optimized geometry at the DZP level, whereas CP indicates a counterpoise-corrected basis set. Elapsed time per SCF cycle (E.T.^{scf}), only for the adsorbate on the surface, is reported for the corresponding theoretical level.

Level of Theory	E$_b$ (eV)	d$_{cm}$ (Å)	E.T.^{scf}
DRSLL/CP-DZP^a	0.75	3.17	
DRSLL/DZP^a	1.80	3.17	78.711
PBE-D4/CP-DZP^a	0.84	2.45	
PBE-D4/DZP^b	1.81	2.45	66.304^c (1381.018^d)
PBE-D4/CP-TZP//PBE-D4/DZP^a	0.70	2.45	
PBE-D4/TZP//PBE-D4/DZP^b	1.70	2.45	
PBE-D2/PW[219]	0.87		
B3LYP-D2/TZP//B3LYP-D2/DZP[218]	1.29	2.42	

^{a}This work.

^{b}As a without CP correction.

^{c} Elapsed time per SCF cycle without D4 correction.

^{d} Elapsed time at PBE/PW (VASP).

4.3) are reported in Table 4.2 for different levels of theory. PBE-D4 is consistent with the PW method using PBE-D2.[219] The interatomic distances, calculated with PBE-D4, between the center of the ring and the Mg atom are in good agreement with the B3LYP-D2 calculation.[218] However, the binding energy calculated at the PBE-D4/CP-DZP level differs from B3LYP-D2/TZP//B3LYP-D2/DZP[218] by 0.45 eV. The difference between the two
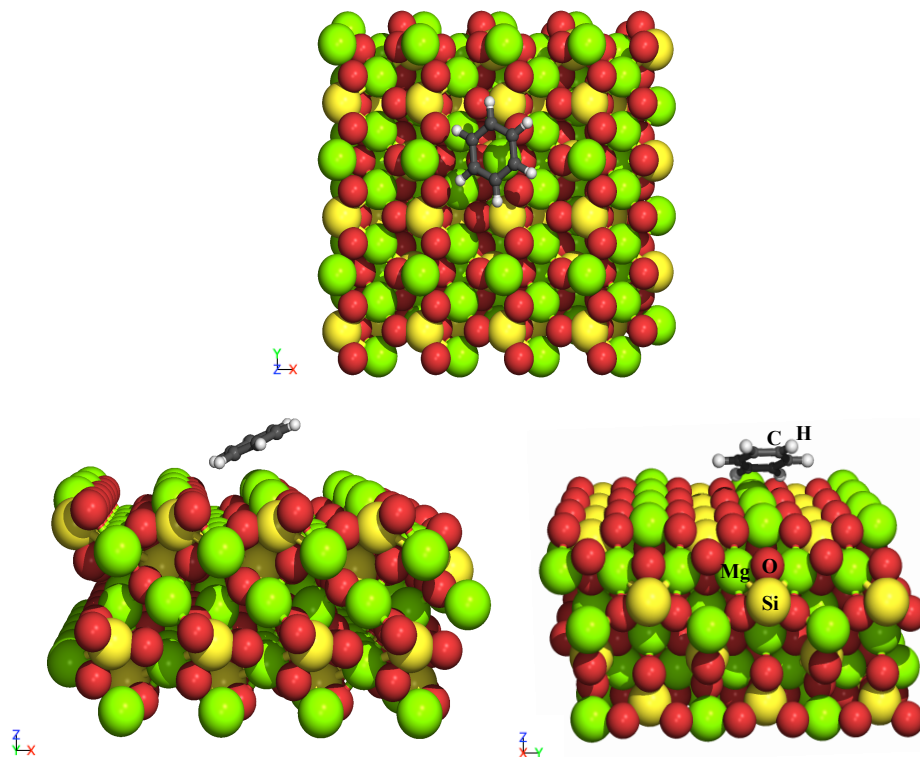
Figure 4.3: Optimized structure (PBE/DZP) of benzene adsorbed on the {010} forsterite surface. The colored balls correspond to the following atoms: hydrogen (white), carbon (gray), magnesium (green), silicon (yellow), and oxygen (red). Atomic labels are reported on the corresponding atoms.

methods (PBE-D4 and B3LYP-D2) can be attributed to the lack of BSSE correction in the B3LYP-D2 calculation.

For a fair comparison, we calculated the binding energy for the adsorption of benzene on {010}-fo, using a TZP basis set as a single-point calculation on the optimized geometry of PBE-D4/CP-DZP, in line with the calculation carried out by Rimola *et al.*[218] at the B3LYP-D2/TZP//B3LYP-D2/DZP level of theory. The binding energies are reported in Table 4.2, with (*e.g.*, CP-TZP//DZP) and without (*e.g.*, TZP//DZP) BSSE correction. The estimated BSSE error is about 1 eV for both PBE-D4/DZP and the PBE-D4/TZP//PBE-D4/DZP. In other words, a TZP single-point calculation on the optimized geometry of DZP does not reduce the BSSE since a full optimization with a TZP basis set would be required.

The vdW-inclusive density functional DRSLL shows a slightly lower

binding energy than PBE-D4/CP-DZP and PBE-D2/PW. Without account-
ing for the counterpoise correction, DRSLL/DZP is in agreement with PBE-
D4/DZP. However, DRSLL underestimates the distance between the Mg
atom and the center of the benzene ring by 0.72 Å compared to the other
methods. Moreover, as shown in Table 4.2, both DRSLL and PBE-D4 in
the LCAO approach are faster by about a factor of 20 with respect to plane
wave methods.

   Benzene Complexes of Transition Metal Cations. Forsteritic olivine
grains in meteorites contain a low amount, about 1%, of transition metals
as point defects.[236,237] Specifically, Rimola *et al.*[213] already studied the
structure of forsterite with Fe^{2+} atoms, showing that Fe is more stable on
the surface when it is undercoordinated and in its most stable electronic
configuration (quintet state). Atomic Ni has chemical properties similar to
those of atomic Fe and it has been detected in chondrite meteorites with
an abundance of about 1% and in olivinic grains analyzed by NASA's Star-
dust mission.[238,239] Therefore, in preparation for studies of metal-doped
forsterite surfaces and in view of their astronomical relevance, we have
studied the effect of Fe^{2+}, in quintet state, and Ni^{2+}, in triplet state, on the
adsorption geometry and energetics of benzene, Benz-Fe^{2+} and Benz-Ni^{2+}
respectively, as shown in Fig. 4.4.

Table 4.3: Binding energy (E_b), distances between the center of the aromatic ring
and the transition metal (d_{cm}), and the carbon-carbon distance (d_{C-C}) of benzene
coordinated with Fe^{2+} (Benz-Fe^{2+}), in quintet state, and Ni^{2+} (Benz-Ni^{2+}), in triplet
state.

System (Level of Theory)	E_b (eV)	d_{cm} (Å)	d_{C-C} (Å)
Benz-Fe^{2+} (PBE-D4/CP-DZP)[a]	6.80	1.77	1.44
Benz-Fe^{2+} (DRSLL/CP-DZP)[a]	7.01	2.74	1.43
Benz-Fe^{2+} (CCSD(T)/6-311++G(2d,2p))[240]	5.61		
Benz-Fe^{2+} (MP2/6-311++G(2d,2p))[240]	5.55	1.85	1.41
Benz-Fe^{2+} (B3LYP-D2/6-311++G(2d,2p))[240]	6.71		
Benz-Fe^{2+} (B3LYP-D2/6-31G**)[241]	6.78	1.80	
Benz-Fe^{2+} (ωB97X-D/6-311++G(2d,2p))[240]	6.38		
Benz-Ni^{2+} (PBE-D4/CP-DZP)[a]	9.19	1.61	1.44
Benz-Ni^{2+} (DRSLL/CP-DZP)[a]	7.52	2.63	1.44
Benz-Ni^{2+} (CCSD(T)/6-311++G(2d,2p))[240]	8.14		
Benz-Ni^{2+} (MP2/6-311++G(2d,2p))[240]	8.39	1.69	1.42
Benz-Ni^{2+} (B3LYP-D2/6-311++G(2d,2p))[240]	9.68		
Benz-Ni^{2+} (ωB97X-D/6-311++G(2d,2p))[240]	9.53		

[a]This work.

   Table 4.3 reports the interaction energy of benzene coordinated with
Fe^{2+} and Ni^{+2} at different levels of theory. The interatomic distances at
PBE-D4 are consistent with MP2 calculations.[240] The obtained results
suggest that all DFT methods overbind by about 1 eV compared to more

(a) **(b)**
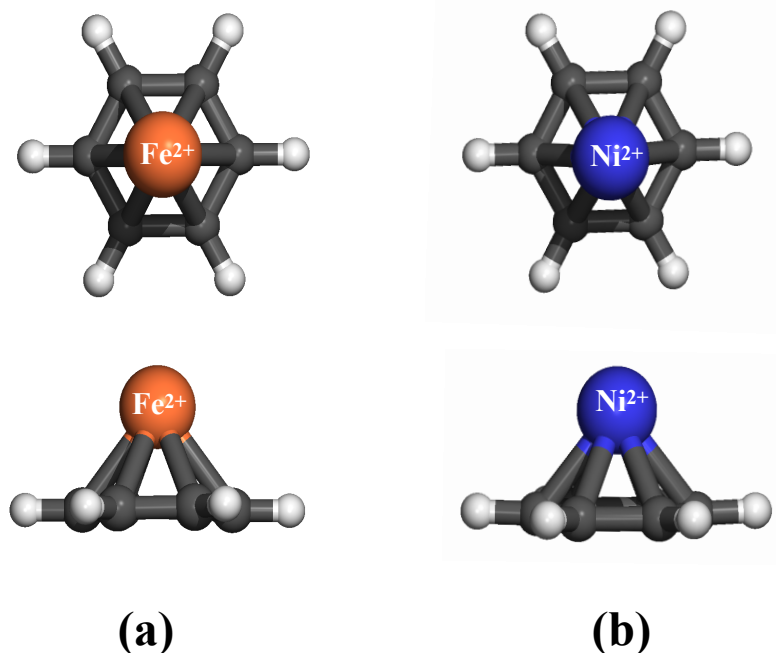
Figure 4.4: Top view and side view of the optimized geometry (PBE/DZP) of benzene coordinated with (a) Fe^{2+} (Benz-Fe^{2+}) in quintet state and (b) Ni^{2+} (Benz-Ni^{2+}) in triplet state.

accurate PostHartreeFock methods (MP2 and CCSD(T)). The overbinding nature of DFT methods might be caused by the lack of an accurate description of the electronic localization over delocalization, *e.g.*, describing the localization of the electrons of the d and f orbitals of transition metals as electronically delocalized and vice versa. In fact, hybrid functionals, even though energetically and geometrically more accurate than pure GGA ones, have problems in accurately describing the electronic localization of metalcarbon bonds.[242]

PBE-D4 provides results in good agreement with B3LYP-D2 and ωB97X-D, for Benz-Fe^{2+}. For Benz-Ni^{2+}, PBE-D4 is about 0.4 eV lower in energy than the other DFT methods. For clarity, we report the B3LYP-D2 binding energy calculated using both double-zeta (6-311++G(2d,2p)) and triple-zeta (6-31G**) basis sets as well as DRSLL/CP-DZP. Note that the basis set does not significantly change the adsorption energy trend. For the case of DRSLL/CP-DZP, the binding energies are in agreement with the general trend, with only slight overbinding for the Fe^{2+} complex and underbinding for the Ni^{2+} one with respect to the other DFT methods. As for the benzene on the forsterite surface, the distance between the center of the ring and

the transition-metal cations is larger by about 1 Å compared to PBE-D4
and MP2 calculations.

Table 4.4: Binding energy trend (E_b^{Ni2+} - E_b^{Fe2+}), using different levels of theory,
of benzene coordinated with Fe^{2+} and Ni^{2+}.

Level of Theory	E_b^{Ni2+} - E_b^{Fe2+} (eV)
B3LYP-D2/6-311++G(2d,2p)[240]	2.97
ωB97X-D/6-311++G(2d,2p)[240]	2.82
MP2/6-311++G(2d,2p)[240]	2.84
PBE-D4/CP-DZP[a]	2.39
DRSLL/CP-DZP[a]	0.51
CCSD(T)/6-311++G(2d,2p)[240]	2.53

[a]This work.

The binding energy trend is defined as the difference of the binding en-
ergy between Benz-Ni^{2+} and Benz-Fe^{2+}, the results are reported in Table
4.4. The PBE-D4 estimate for the binding energy difference is in much bet-
ter agreement with CCSD(T) than with other methods. MP2 overestimates
the binding energy trend by about 0.29 eV. Furthermore, the deviation in
the interaction energy between CCSD(T) and PBE-D4 is comparable to or
better than that for the hybrid functionals. Hence, the use of hybrid func-
tionals or large basis sets does not necessarily improve the quality of the
trend. DRSLL, instead, underestimates the trend by 2.02 eV compared to
CCSD(T). To understand the binding energy stabilization estimated using
PBE and DRSLL, we computed the spin density isosurfaces for both com-
plexes at PBE and DRSLL levels, shown in Fig. 4.5 and Fig. 4.6. A large
population of spin-down localized on the transition metals and a small
population in the carbon atoms confirm the donation of density from the
p orbitals to d orbitals of the transition metal, whereas a large fraction
of the spin-up population is localized in the region of CC and CH bonds.
These effects explain the overstabilization of the binding energy compared
to PostHartreeFock methods. Furthermore, dispersion energy does not
play an important role in spin localization and, therefore, the electronic
structure. In fact, PBE and DRSLL show the same spin population, and,
therefore, the spin density does not explain the trend divergence compared
to the other methods. The next section will further focus on this topic.

Dispersion Energy and the BSSE effect. We studied the interaction of
a small PAH, naphthalene, and a large one, benzocoronene, on three {010}
forsterite surfaces. The three considered forsterite surfaces are optimized
at the most stable spin configuration, singlet for the {010}-fo, quintet for
Fe-{010}, and triplet for Ni-{010}. Fig. 4.7 shows the calculated binding
energies for benzocoronene and naphthalene using PBE-D4 and its pre-
decessor PBE-D3(BJM)[243] along with non-dispersion-corrected PBE. The
latter allows us to understand how the dispersion correction affects these
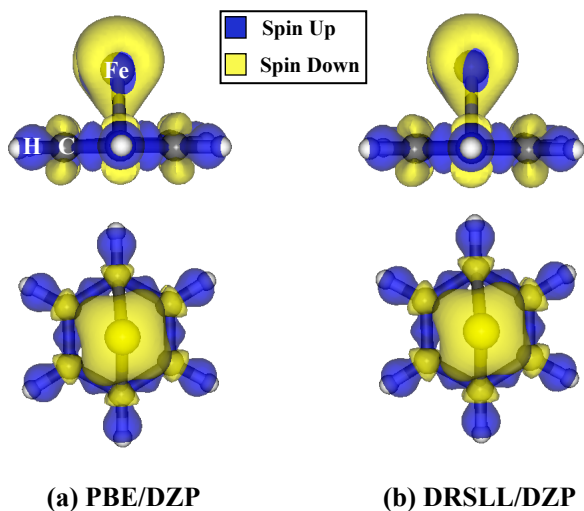
(a) PBE/DZP   **(b) DRSLL/DZP**

Figure 4.5: Side view and top view of spin density isosurface (isovalue 0.007 e/A^3) of Benz-Fe^{2+} computed in quintet state at PBE/DZP and DRSLL/DZP level. Spin population and atomic labels are reported.
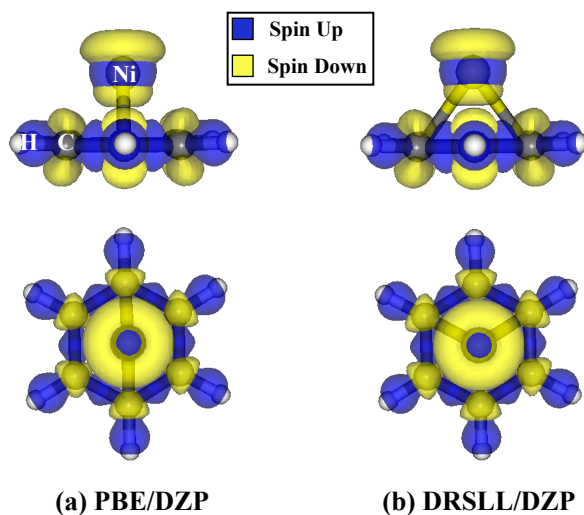
(a) PBE/DZP   **(b) DRSLL/DZP**

Figure 4.6: Side view and top view of spin density isosurface (isovalue 0.005 e/A^3) of Benz-Ni^{2+} computed in triplet state at PBE/DZP and DRSLL/DZP level. Spin population and atomic labels are reported.

systems.

Fig. 4.7 demonstrates that the trend and the absolute value of binding energies, using PBE-D4 and PBE-D3(BJM), are consistent with each

Figure 4.7: Binding energies of benzocoronene and naphthalene chemisorbed on {010}-fo (singlet state), Fe (quintet state), and Ni-{010}-fo (triplet state) surfaces using different levels of theory (PBE-D4, PBE-D3(BJM), and PBE) with the CP-DZP basis set. The order of the labels corresponds to the order of the bars. Note: Numerical values are reported in the Appendix.

other. However, the binding energies for naphthalene are higher than those for benzocoronene at the bare PBE level. This conflicts with the common assumption that larger molecules have a stronger interaction with the surface.[244] Benzocoronene has eight aromatic rings and naphthalene has only two; the high electronic delocalization of the π-system of benzocoronene must contribute significantly to its adsorption to the surface through long-range interactions. However, PBE seems to poorly describe the long-range density transfer.[244,245] The difference in energy between PBE and PBE-D4/D3(BJM) is the dispersion energy, which we calculate to be large for these aromatic systems. Therefore, it is evident that noncovalent bonds play an important role in binding PAHs on the surface through van der Waals interactions between the - system and the surface. Furthermore, including the van der Waals interaction results in a different trend in the binding energy as compared to the PBE-only calculations. Specifically, the energy trend calculated with DFT-D methods follows the order Fe > Ni > Mg. However, when DFT-D methods are not applied, the trend is Fe > Mg > Ni. Hence, it is important to use a method that can describe the dispersion interaction of PAHs on a surface well.

To test the performance of the LCAO method in comparison to the PW

Table 4.5: Dispersion-corrected binding energies (E_b), in eV, at different levels of theory using PW (see Appendix for details) and LCAO methods of naphthalene (Napht) on {010}-fo, Fe-{010}-fo and Ni-{010}-fo.

	$E_b^{PBE-D4/PW}$	$E_b^{PBE-D4/CP-DZP}$
Napht ({010}-fo)	1.31	1.14
Napht (Fe-{010}-fo)	1.55	1.46
Napht (Ni-{010}-fo)	1.15	1.17

method, we have computed the dispersion-corrected binding energies of naphthalene on {010}-fo, Fe-{010}-fo and Ni-{010}-fo using VASP,[92,200–202] as shown in Table 4.5. The LCAO method underestimates the binding energy of naphthalene on {010}-fo by about 0.17 eV, which is consistent with previous theoretical investigations by Lee *et al.*[246] that estimate a difference of about 0.25 eV between the two methods. The authors stated that this energy difference cannot be removed easily even by increasing the orbital-confining cutoff radii of the basis set. Instead, there is good agreement between the LCAO and PW methods for the case of naphthalene on Fe-{010}-fo and Ni-{010}-fo by about 0.020.09 eV, where a strong bond formation occurs between the carbon atoms and the transition-metal one. The discrepancies between LCAO and PW might be attributed to the weak interaction between naphthalene and the pristine surface, which is partially overcorrected by the counterpoise energy, whereas these differences might not be important for small systems such as benzene, in which the dispersion energy is less important.

Therefore, we have also evaluated the binding energy trend using a vdW-inclusive density functional (DRSLL) taking into account the BSSE effect. The results are summarized in Fig. 4.8. We conclude that DRSLL is not consistent with PBE-D4 in terms of absolute binding energy values since it shows a different energy trend: Ni > Fe > Mg. Finally, both PBE-D4 and DRSLL largely overestimate the binding energies, when they are not corrected for the BSSE, with respect to the counterpoise-corrected values.

Specifically, we analyzed the optimized geometries using both PBE and DRSLL functionals. Fig. 4.9 shows the Mg, Ni, and FeC distances. We noticed that DRSLL tends to provide larger Ni-C and Fe-C distances by about 0.10 Å; in contrast, this effect is not so evident for the case of MgC bonds. This is in accordance with the studies carried out by Buimaga-Iarinca *et al.*[208] that confirm the presence of a BSSE effect in combination with an overestimation of the metalC distances when vdW-DF functionals are employed to study aromatic molecules on a gold surface.

The spin density of PAHs on forsterite surfaces is reported in the Appendix and, as for the case of transition-metal complexes, it did not show any differences between DRSLL and PBE. DRSLL diverges from PBE-D4 since the dispersion energy is computed as the inclusive nonlocal dis-

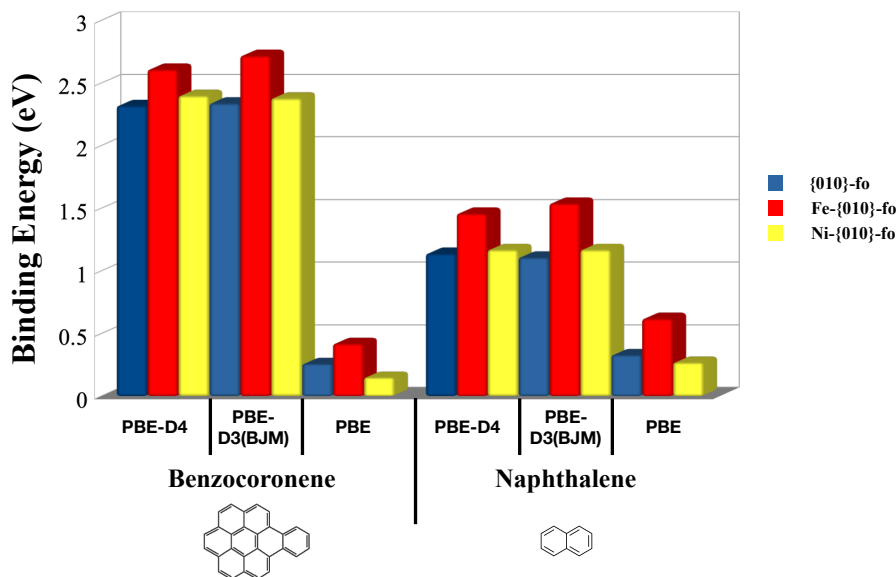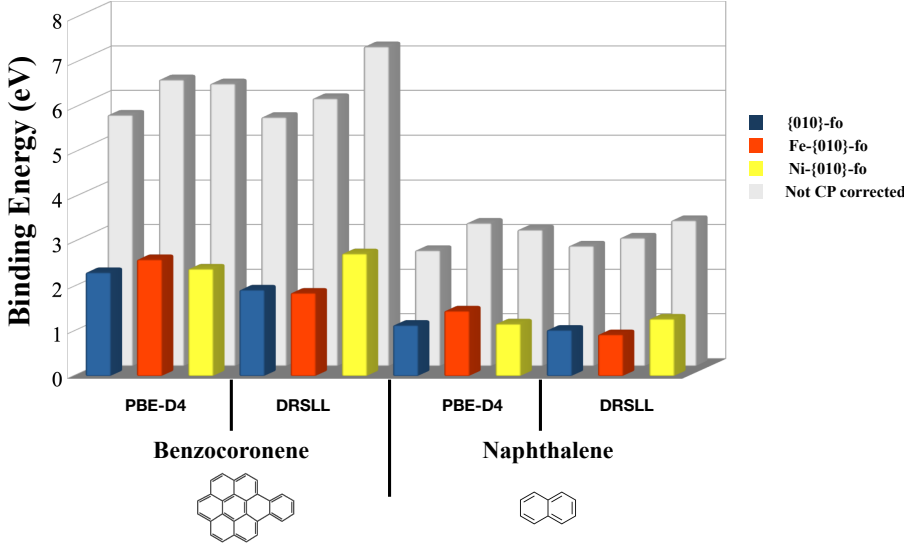**Figure 4.8:** Binding energies of benzocoronene and naphthalene chemisorbed on {010}-fo (singlet), Fe (quintet), and Ni-{010}-fo (triplet) surfaces using PBE-D4 and DRSLL with the CP-DZP basis set and with the corresponding counterpoise-noncorrected values at the back. The order of the labels of the forsterite surfaces corresponds to the order of the bars. Note: Numerical values are reported in the Appendix.

Table 4.6: Binding energy (E_b) and counterpoise-corrected binding energy (E_{CP-b}) at different level of theories. D4 dispersion energy (E_{D4}) and non-local dispersion energy (E_{nld}) calculated as the difference between the binding energy computed at the DRSLL level and revPBE ($E_{nld}^{DRSLL}=E_b^{DRSLL}-E_b^{revPBE}$) for the benzocoronene (Benzoco) adsorbed on Fe and Ni-{010}-fo. The energies are reported in eV.

	E_b^{PBE}	E_b^{revPBE}	E_{CP-b}^{PBE}	E_{CP-b}^{revPBE}	$E_{CP-b}^{revPBE-D4}$	E_{D4}^{PBE}	E_{D4}^{revPBE}	E_{nld}^{DRSLL}
Fe-{010}-fo:								
Benzoco	4.23	3.20	0.42	-0.42	3.12	2.18	3.53	2.28
Ni-{010}-fo:								
Benzoco	4.11	3.10	0.15	-0.48	3.08	2.22	3.56	3.23

persion energy (E_{nl}) at each SCF cycle, whereas PBE-D4 makes use of empirical formalism, the DFT-D4 method,[221] that has been computed a posteriori. Further differences between DRSLL and PBE-D4 are related to the exchangecorrelation energy (E_{xc}) that, for the case of DRSLL,[72] is computed at revPBE[70] level. We believe that the difference between DRSLL ($E_{xc}^{revPBE}+E_{nl}$) and PBE-D4 ($E_{xc}^{PBE}+E_{D4}^{PBE}$) is caused by the nonlocal dispersion energy and to justify this, we calculated the dispersion energy computed at the DRSLL level. We optimized the structures, for only the case in which the inversion trend is significant as for the case of benzo-

Figure 4.9: Atomic labels and optimized structures of naphthalene and benzo-coronene chemisorbed on Ni-{010}-fo (a) and (b) and Fe- {010}-fo (c) and (d). Table of carbon and metal distances ($d_{cc/mc}$) between the PAH and the surfaces using PBE and DRSLL. Note: As we are reporting only the geometric parameters and not the energy, we have not included the D3(BJM) and D4 correction (see the Theoretical Methods and Models section).

coronene, with revPBE estimating the nonlocal dispersion as the difference between the DRSLL and revPBE absolute energies as shown in Table 4.6. revPBE overcorrects the BSSE for the adsorption of benzocoronene on

both transition-metal-doped surfaces, whereas revPBE and PBE function-
als do not consistently use the counterpoise correction and exclude the
dispersion energies. However, the revPBE counterpoise correction energy
overcorrects about 1 eV more with respect to PBE, resulting in negative
binding energies. In contrast, the dispersion energies (E_{D4} and E_{nld}) for
the adsorption on the Fe-doped surface computed at DFT-D4 and DRSLL
levels are in good agreement, whereas this difference becomes larger for
the case of the Ni-doped surface. This is consistent with the binding energy
accuracy of benzene on transition-metal cation complexes at the DRSLL
level, which shows a larger agreement with the other DFT methods for
the adsorption on Fe^{2+} with respect to Ni^{2+} (Table 4.3). We also computed
the counterpoise-corrected binding energy at the revPBE-D4 level that is
consistent in the binding energy trend with PBE-D4. Therefore, the trend
inversion among the functionals observed in Fig. 4.8 is to be attributed
to the overestimation of nonlocal dispersion energy operated by DRSLL for
the case of the Ni-{010}-fo.

4.4. Conclusions

Understanding the organic inventory of regions of planet formation is
key in astrophysics. The delivery of prebiotic organic species to Earth, and
terrestrial planets in general, has direct links to the origin of life on Earth
and elsewhere in the universe. Chemistry on mineral surfaces is thought
to play an important role in astrochemistry both in molecular clouds and
protoplanetary disks as also in planetesimals, the first steps in planet
formation, but this chemistry is poorly understood. Quantum chemical
methods can play an important role in identifying chemical routes and re-
action products.[16,39,247,248] However, due to the large computational cost,
little has been done to study the chemical and physical properties of PAHs
on minerals.[218,219] In this work, we identified a DFT method that can accu-
rately compute the binding energy of aromatic molecules on a mineral sur-
face. The PBE-D4/DZP binding energies are accurate enough to be used
in astronomical gas-grain models to predict the abundance of aromatic
species in some regions of interstellar medium. We focused on the {010}
forsterite surface as the most abundant and best-studied mineral surface
composition of the rocky parts of our universe, such as submicron-sized
silicate grains, and benzene as the smallest example of aromatic species.
We conclude that to accurately describe the binding and, therefore, the
adsorption energies, London dispersion forces have to be taken into ac-
count as currently available GGA functionals cannot accurately describe
the electronic delocalization at long-range distances.

The interaction of aromatic molecules on a mineral surface in which
transition metals are present requires an accurate description of local-
ized electrons in the d and f orbitals along with an accurate description of

the electronic delocalization at long-range distances. The BSSE-corrected PBE-D4/CP-DZP using local atomic orbitals describes the binding energy of benzene on {010}-fo with the same accuracy as that of plane wave methods. We found that a full optimization using a large basis set, *e.g.*, TZP, is necessary to reduce the BSSE, whereas a TZP single-point calculation on the optimized geometry with DZP does not reduce the BSSE.

For the complexes of aromatic molecules interacting with transition-metal ions, DFT overbinds by about 1 eV with respect to CCSD(T). However, the binding energy difference between the Ni^{2+} and Fe^{2+} benzene complexes at the PBE-D4/ CP-DZP level provides results in good agreement with the binding energy trend estimated by CCSD(T), while hybrid functionals overestimate this difference.

Finally, as a test case for PBE-D4, we studied the interaction of PAHs on three different {010} forsterite surfaces: pure-Mg, single doped Fe and Ni surfaces. We found that the interaction of PAHs with the surfaces is driven by important dispersion interactions and BSSE effects that need to be taken into account for a correct description of the aromatic systems on a mineral surface. We conclude that PBE-D4 is in good agreement with the predecessor PBE-D3(BJM). We also took into account London dispersion using DRSLL as the vdW-DF functional. DRSLL estimates slightly lower binding energies than PBE-D4 if transition metals are not present on the surface.

For the case of transition metals on forsterite surfaces, DRSLL does not provide consistent trend results with respect to PBE-D4. This is caused by the nonlocal dispersion energy computed on each SCF cycle. Moreover, DRSLL tends to overestimate the carbonmetal bond distance with respect to PBE.

This study provides a robust theoretical method to describe the interaction of aromatic molecules with forsterite mineral surfaces for astronomical and planetary science applications, applicable equally well to similar systems for material science applications. We showed that indeed, our proposed method, using PBE-D4/CP-DZP, is ideally suited to model the adsorption of aromatic molecules on a silicate mineral surface. This work will provide a solid springboard necessary for future experimental and computational studies and, in the follow-up work in preparation, we will apply our proposed method to the binding and molecular structure of a sample of PAHs on various forsterite surfaces.

4.5. Appendix

Plane Wave Methods

We employed VASP code[92,200–202] to validate the bulk and the binding
energy trend, calculated with the LCAO method, along with Project Aug-
mented Wave (PAW) pseudopotentials.[90,91] The energy cut-off converged to
500 eV in order to account for the correct number of plane waves. The cho-
sen exchange-correlation functional, convergence criteria, sampling of the
Brillouin zone, etc. has been adopted as in LCAO methods (see Theoretical
Methods and Models section).

Mesh Cutoff Convergence Test

In order to choose the appropriate value of plane wave cutoff for the grid
(Mesh Cutoff), we performed a convergence binding energy test of naph-
thalene adsorbed on pristine {010} forsterite. We did not take into account
BSSE and D4 energy correction since they are not relevant for the pur-
pose of selecting the proper mesh cutoff. The convergence test, in Fig.
4.10, shows that the binding energy does not change with the increasing
of the mesh cutoff over 200 Ry.
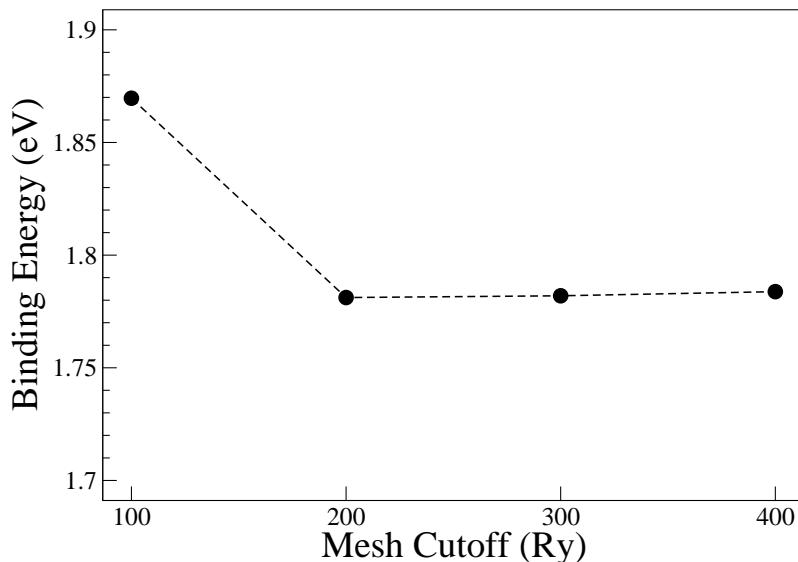
Figure 4.10: Mesh Cutoff convergence test as a function of the binding energy of the interaction of naphthalene on {010} forsterite surface. The binding energy was calculated at the PBE/BSSE-DZP level, BSSE and D4 correction were not taken into account.

PAHs on Forsterite

Table 4.7: Binding energies (E_b), reported in Fig. 4.7 of this work, at different levels of theory with counterpoise corrected basis set (CP), of the adsorption of naphthalene and benzocoronene on the Mg-pure forsterite surface ({010}-fo), single doped Fe forsterite surface (Fe-{010}-fo) and Ni (Ni-{010}-fo) one.

PAH (*PBE-D4/CP-DZP*)	$E_b^{\{010\}-fo}$ (eV)	$E_b^{Fe-\{010\}-fo}$ (eV)	$E_b^{Ni-\{010\}-fo}$ (eV)
Naphthalene	1.14	1.46	1.17
Benzocoronene	2.32	2.61	2.40
PAH (*PBE-D3(BJM)/CP-DZP*)	$E_b^{\{010\}-fo}$ (eV)	$E_b^{Fe-\{010\}-fo}$ (eV)	$E_b^{Ni-\{010\}-fo}$ (eV)
Naphthalene	1.11	1.54	1.17
Benzocoronene	2.34	2.72	2.38
PAH (*PBE/CP-DZP*)	$E_b^{\{010\}-fo}$ (eV)	$E_b^{Fe-\{010\}-fo}$ (eV)	$E_b^{Ni-\{010\}-fo}$ (eV)
Naphthalene	0.33	0.62	0.27
Benzocoronene	0.26	0.42	0.15

Table 4.8: Binding energies (E_b) of the adsorption of naphthalene and benzo-coronene on {010} forsterite surfaces reported in Fig. 4.8 of this work and mentioned in Table 4.7 at different levels of theory. Results using counterpoise corrected (CP-DZP) and non-corrected (DZP) basis sets are reported.

PAH (*DRSLL/CP-DZP*)	$E_b^{\{010\}-fo}$ (eV)	$E_b^{Fe-\{010\}-fo}$ (eV)	$E_b^{Ni-\{010\}-fo}$ (eV)
Naphthalene	1.03	0.93	1.28
Benzocoronene	1.93	1.86	2.74
PAH (*DRSLL/DZP*)	$E_b^{\{010\}-fo}$ (eV)	$E_b^{Fe-\{010\}-fo}$ (eV)	$E_b^{Ni-\{010\}-fo}$ (eV)
Naphthalene	2.69	2.87	3.26
Benzocoronene	5.57	5.99	7.15
PAH (*PBE-D4/DZP*)	$E_b^{\{010\}-fo}$ (eV)	$E_b^{Fe-\{010\}-fo}$ (eV)	$E_b^{Ni-\{010\}-fo}$ (eV)
Naphthalene	2.59	3.2	3.05
Benzocoronene	5.62	6.41	6.32

Spin Density Population

(a) Fe-{010}-fo (PBE/DZP)

(b) Ni-{010}-fo (PBE/DZP)

(c) Fe-{010}-fo (DRSLL/DZP)

(d) Ni-{010}-fo (DRSLL/DZP)
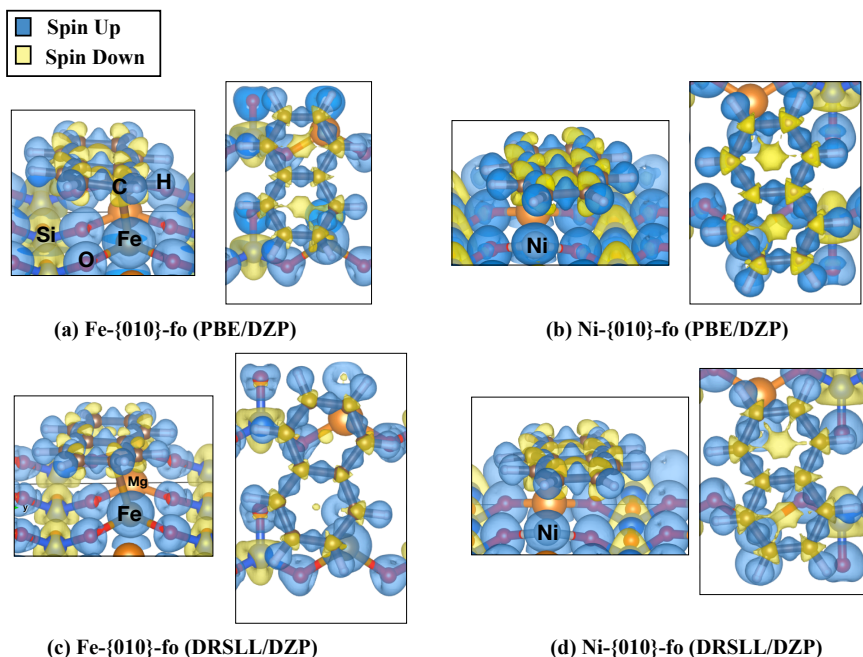
Figure 4.11: Spin density isosurfaces of naphthalene, optimized at PBE and DRSLL level, adsorbed on Fe and Ni-{010}-fo (isovalues 0.007 and 0.005 e/A^3, respectively) with the corresponding atomic and spin population labels reported.

(a) Fe-{010}-fo (PBE/DZP)

(b) Ni-{010}-fo (PBE/DZP)

(c) Fe-{010}-fo (DRSLL/DZP)

(d) Ni-{010}-fo (DRSLL/DZP)
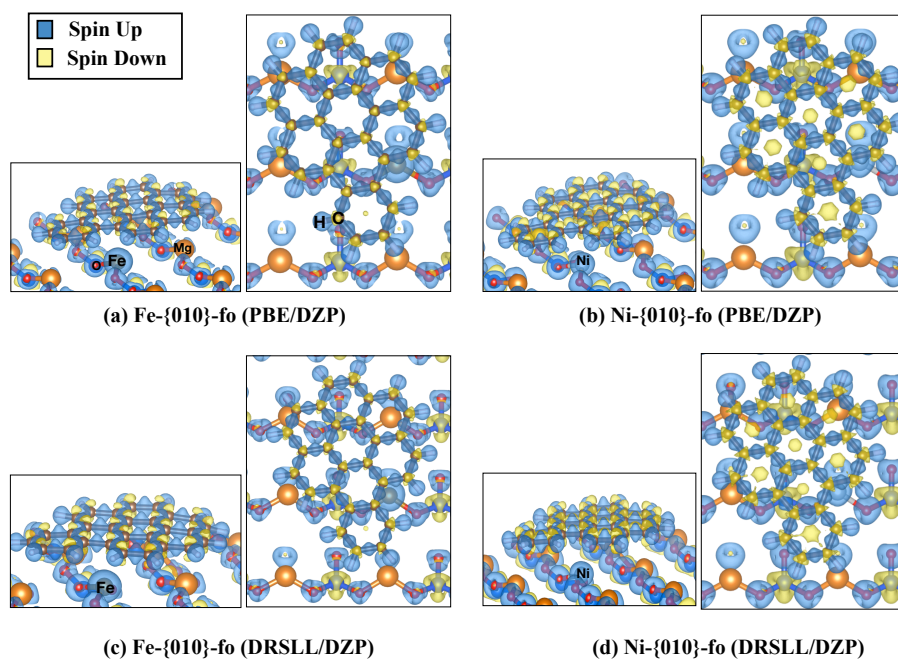
Figure 4.12: Spin density isosurfaces of benzocoronene, optimized at PBE and DRSLL level, adsorbed on Fe and Ni-{010}-fo (isovalues 0.007 and 0.005 e/A^3, respectively) with the corresponding atomic and spin population labels reported.

CHAPTER 5

ADSORPTION OF PAHS AND C_{60} ONTO FORSTERITE: C-H BOND ACTIVATION BY THE SCHOTTKY VACANCY

D. Campisi, Thanja Lamberts, Nelson Y. Dzade, Rocco Martinazzo, Inge Loes ten Kate, and Alexander G. G. M. Tielens, **2021**, submitted

Abstract. Understanding how to break catalytically the C-H bond of aromatic molecules such as polycyclic aromatic hydrocarbons (PAHs) is the first step in converting these species into a variety of organic molecules. This is currently a big challenge and subject of study in catalysis, surface science, organic chemistry, astrochemistry, and planetary science. In the latter, the study of the breakdown reaction of PAHs is important to understand their link with the prebiotic molecules of regions of star and planet formation. Moreover, forsterite is a mineral abundant on our planet and aroused interest as a cheap and safe alternative to synthetic catalysts.

In this work, we employed a periodic DFT-D4 approach to study the surface phenomena of a sample of polycyclic aromatic hydrocarbons (naphthalene, anthracene, fluoranthene, pyrene, coronene, benzocoronene) and fullerene (C_{60}) on the [010] forsterite surface and its defective surfaces for their implication in catalysis and astrochemistry. The defects modeled onto the forsterite surfaces are Fe, Ni-doped surfaces and MgO Schottky vacancy. These defects have shown higher stability when located on the surface layer of the forsterite slab model. PAHs adsorb on the pristine, Fe, and Ni-doped forsterite surfaces with geometrical structures close to planarity. The adsorption of PAHs and C_{60} on the Fe-doped forsterite surface is stronger with respect to the pristine and Ni-doped surface. On these surfaces, PAHs adsorbed with binding energies in a range between about 1 and 2.6 eV. The binding energy of PAHs adsorbed on MgO Schottky forsterite vacancy surface is in the range of about 2-3.5 eV. The binding energy is influenced by the number of contact points (orbital interactions between the carbon atoms and Mg, Fe, and Ni atoms on the surface), which depend on the PAH surface area. The larger is the area, the larger is the number of contact points.

The MgO Schottky vacancy has shown different reactivity based on the orientation of the PAH approaching the surface. Parallel adsorption on the MgO Schottky forsterite vacancy surface leads to the chemisorption of the molecule with the formation of stable covalent C-Si and C-O bonds. On the vacancy surface, anthracene has higher binding energy with respect to the other PAHs due to the presence of perfect $\widehat{COO}$ 109° and $\widehat{SiOO}$ 120° angles in agreement with sp^3 and sp^2 hybridized carbon atoms respectively, whereas the other PAHs diverge from this value. Pyrene and coronene do not form covalent bonds when adsorbed onto the MgO Schottky vacancy. Furthermore, the large surface area of coronene causes the formation of vacancy reconstruction during the adsorption process. Finally, fullerene benefits from the chemisorption on the vacancy surface due to the covalent bond formation that stabilizes the buckyball structure.

Perpendicular orientation of the PAH with respect to the vacancy surface leads to the catalytic breaking of the aromatic C-H bond via a barrierless reaction. With reaction energies between -3.2 and -5.3 eV, perpendicular adsorption is more favourable than the parallel adsorption. Spin density isosurfaces and Voronoi charge analysis show that C-H dissociation is promoted by electron donation from the vacancy to the PAH. As a result of the undercoordinated Si and O atoms, the vacancy acts as a frustrated Lewis pair catalyst. Therefore, MgO Schottky vacancy [010] forsterite surface proved to have potential catalytic activity for the activation of C-H bond breaking in aromatic molecules.

5.1. Introduction

The study of the reactivity of organic molecules as feedstock for the formation of precursors of complex molecular species is the focus of organic chemistry, material science, catalysis, astrochemistry, and planetary science.[8,115,249,250] The orbital interaction of an sp^2 carbon with an s orbital of a hydrogen atom forms a strong C-H bond with bonding energy of about 4.6 eV that we can find in aromatic species such as benzene[251] and polycyclic aromatic hydrocarbons (PAHs).[41] Shedding light on the activation of the aromatic C-H bond is the first step to understand the reactivity of inert species such as PAHs and how to use them as catalytic materials in organic synthesis.[252]

PAHs lock up about 20% of carbon in the universe, whereas 80% is locked up in other species. PAHs might be linked to other organic molecules since they can act as carbon feedstock and, therefore, studying their reactivity is also important to understand the chemical evolution of our universe.[8]

Finding a natural material that is able to activate and catalyze the C-H bond breaking of aromatic species is still a big challenge due to their high bond energy and their high stability. Synthetic and pollutant transition metal catalysts such as Wilkinson's (rhodium-based catalysts),[253] palladium,[254,255] and iridium catalysts[256] are able to break the aromatic C-H bond. However, these catalysts are harmful to human health and moreover very rare and therefore very expensive. Recently metal-free catalysts such as Frustrated Lewis Pairs[257] (FLPs), formed by a Lewis acid and bases that cannot bind together due to steric hindrances, have been studied since they can activate aromatic hydrocarbons.[258]

Mineral-bearing materials are organized periodic systems and have been considered as a cheap and safe alternative to synthetic catalysts.[259] In fact, mineral surfaces have active inorganic interfaces that can host molecular species and possibly activate them.[203] Even though minerals might act as catalysts, they cannot be regenerated during the catalytic cycle (reaction cycle in which a catalyst is partaking). They catalyze processes that are thermodynamically favourable but kinetically hindered by high energy barriers.[260]

Forsterite (Mg$_2$SiO$_4$) is one of the most abundant olivinic minerals available on Earth and in space.[46,261] Experimental studies have reported the potential catalytic role of forsterite and Fe-doped forsterite for the conversion of methanol to olefine and PAHs.[262,263] However, theoretical and mechanistic studies on the catalytic activity of forsterite are currently lacking. Only a few studies have addressed the interaction of organic species with a forsterite surface using first-principle methods.[12,218,219]

In this work, we use periodic density functional theory (DFT) along with the Grimme's D4 method[222] (DFT-D4), to study the adsorption and C-H activation of PAHs (naphthalene, anthracene, fluoranthene, pyrene,

coronene and benzocoronene) on the most stable [010] forsterite surface
([010]-fo).[12,216,217,261] In space, forsterite is a potential catalyst and, there-
fore, might be used to promote the conversion of PAHs into other organic
species. Along with the pristine [010]-fo surface, we also study defective
surfaces of [010] forsterite.[236] Specifically, we modeled the [010]-fo with
a single Mg atom replaced by a Fe atom (Fe-[010]-fo),[37,213] by a Ni atom
(Ni-[010]-fo)[12] as well as by a MgO-Schottky vacancy (V_{MgO}-[010]-fo).[264]
Defects are ubiquitous, at different concentrations, in all crystalline min-
eral structures. They are often promoted by the radiation of isotopic decay,
or by high temperatures during the crystal growth, and they are classi-
fied as bulk, planar, line, and point defects.[265] A small amount of Fe and
Ni in olivine is generally present,[236,238,239] whereas the presence of MgO-
Schottky vacancy might have been the result of the reaction of olivine with
a small amount of water.[62]

   We also include in this study the adsorption of C_{60} as this molecule is
abundant in space.[266,267] We analyze geometrical parameters and binding
energies for the adsorption of PAHs and C_{60} as well as the energy barriers
and the electronic structure associated with the C-H dissociation of PAHs
on the vacancy forsterite surface. This study is the starting point to un-
derstand the chemistry of aromatic molecules in interstellar space and on
solar system bodies as well as for the potential role of minerals as selective
catalysts for industrial applications.

5.2.   Theoretical Methods

   Forsterite and PAH Structures. In this study, we model the crystalline
non-polar [010]-fo surface ($Mg_{96}O_{192}Si_{48}$) and its defective surfaces under
dry conditions, shown in Fig. 5.1. The present theoretical models are
used to study forsterite material as an important component of interstel-
lar dust grains, asteroids, meteorites[46] as well as for its potential use as a
catalyst.[262] All models have a 19 Å x 17.94 Å x 35.20 Å ($\alpha = \beta = \gamma = 90°$)
supercell (4 x 3 x 1) with a slab thickness of 9.25 Å. The [010] slab sur-
faces were generated cutting the optimized bulk of forsterite from a prior
study[12] using METADISE code.[220] The bottom layers (layers with a thick-
ness of about 4 Å) have been constrained during the whole optimization
procedure. The presence of defects has proved to increase the reactivity
and catalytic activity of several materials.[16,60,268] Therefore, we decided
to model the defective surfaces of [010]-fo by substituting, using chemical
intuition, a transition metal (*e.g.*, Fe and Ni for this work) for an undercoor-
dinated Mg atom from the surface and optimizing the resulting slab model.
Furthermore, V_{MgO}-[010]-fo is created by removing a MgO unit from the
[010]-fo surface, again followed by a reoptimization of the slab.

   The PAHs taken into consideration in this study, are naphthalene, an-
thracene, pyrene, fluoranthene, coronene, benzocoronene and fullerene.
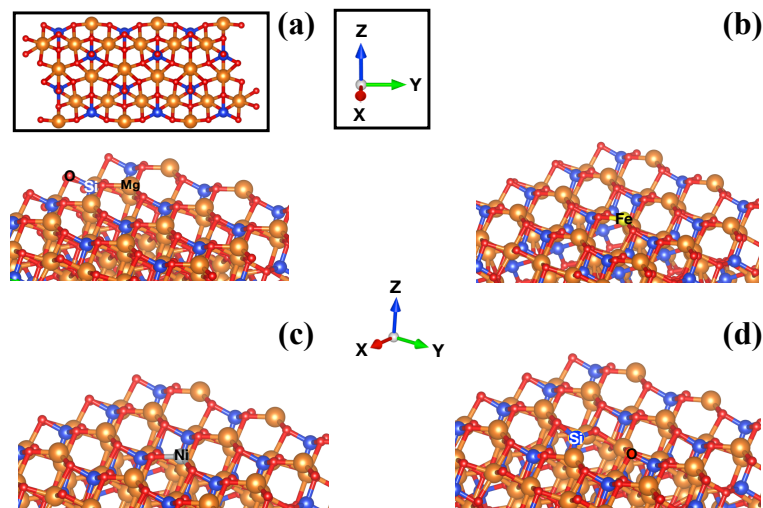
Figure 5.1: Optimized slab models of [010] forsterite at two different orientations: (a) [010]-fo, (b) Fe-[010]-fo, (c) Ni-[010]-fo and (d) V_{MgO}-[010]-fo (the location of the vacancy is indicated by the Si and O labels reported on the corresponding undercoordinated atoms). The vacuum region is located along the z axis and the atomic labels of the corresponding atoms are reported.

These species (Fig. 5.3 as well as Fig. 5.14 - 5.19 in the Appendix) are characterized by honeycomb structures of fused hexagonal carbon rings bound with hydrogen atoms on their edges. Fluoranthene is the only PAHs with a 5-membered ring. The fullerene, C_{60}, is characterized by a sperical shape (buckyball) with hexagonal and pentagonal rings bound together forming [6,6] and [5,6] ring junctions (Fig. 5.19 in the Appendix) which are bridge carbons atoms of two hexagonal rings, and hexagonal-pentagonal rings, respectively. The gas phase model of PAHs has been optimized in a cubic unit cell with sides of 15 Å.

Calculation Setup. The slab models were optimized using periodic density functional theory implemented in the SIESTA code[98] that makes use of localized atomic orbitals basis sets (LCAO). The details of the method have been described in a prior work[12] and are summarized here: We employ the Perdew, Becke, and Ernzerhof[210] (PBE) exchange-correlation functionals along with DZP basis set using core pseudopotentials and setting the radii of split valence type for the hydrogen atoms to 0.5. The counterpoise correction[100,101] (CP) is taken into account for all calculations to correct for the basis set superposition error (BSSE). We conventionally labeled the counterpoise corrected basis sets as CP-DZP, as reported in our previous work.[12] The dispersion energy is taken into ac-

count a posteriori, on the optimized geometry at PBE/DZP level, employing
Grimme's DFT-D4 code.[206,221,222] The Brillouin zone is sampled using 2 x 2
x 1 Monkhorst–Pack's[102] k-points for all surfaces with a unit cell of 18.996
Å x 17.938 Å and 1x1x1 Monkhorst–Pack's k-points for the gas phase mod-
els (reagents). The mesh cutoff is set to 200 Ry (see Appendix of chapter 4).
All calculations are run with the unrestricted formalism and convergence
is reached when the forces are lower than 0.01 eV Å^{-1}. All structures are
optimized using the limited-memory Broyden–Fletcher–Goldfarb–Shanno
(L-BFGS) algorithm.[269] An electric field along the z-axis is set to override
the resulting dipole moment along the z-axis of the slabs during the op-
timization procedure. In a prior study,[12] PBE-D4/CP-DZP was proven to
be a robust theory level to study the interaction of aromatic molecules on
mineral surfaces.

We analyzed the electronic mechanism of the vacancy surface with
the spin density isosurfaces and the charge analysis population based
on Voronoi scheme that proved to be more accurate than Mullikan and
Bader schemes.[270] These techniques allow us to define the spin-up and
spin-down population (spin density) of each atom as well as the electronic
donation and reception between the atoms (partial atomic charges). The
spin density and charge analysis have been calculated at the PBE + U
level of theory with a single point calculation using TZP on the optimized
DZP geometry with supplementary 4 x 4 x 1 Monkhorst–Pack's k-points.
The Hubbard U value, using the LDA + U method,[226] is set to 15.3 eV
to describe the strong on-site Coulomb interaction of the localized elec-
trons of the 2p orbitals of the oxygen atoms to reproduce the experimental
band-gap (8.4 eV).[227] A threshold tolerance of 10^{-2} and a tolerance pop-
ulation of $4x10^{-4}$ is selected for the LDA + U method. The radii for the
split-valence type of TZP for all atoms, excluded hydrogen, are set up to
be 0.30. The reaction barriers (*e.g.*, the characterization of a saddle point)
and the minimum energy path are calculated using the climbing-image
nudged elastic band method[271] (CI-NEB) implemented in the atomistic
simulation environment[272,273] (ASE) python module employing SIESTA as
a calculator. The minimum energy path is optimized linearly interpolating
the reagent and the product by six images. Each image can be thought
of as a representation along the reaction path with all images intercon-
nected by springs. The optimization focuses on finding the lowest energy
possible for each image, and the maximum one only for one image, while
maintaining the constraint that they are equally spaced with respect to
neighboring images. Note that after optimizing the CI-NEB path, the en-
ergies of the images represent the minimum energy path from the initial
to the final geometry. The path is optimized using the Fast Inertial Relax-
ation Engine (FIRE)[274] algorithm that provides robust results compared to
Quasi-Newton methods.[275] The spring constant is set to 0.1 eV/Å and the
six images between the reagent and the product are considered optimized
when the forces are lower than 0.025 eV/Å .

In this work, the binding energy (E_{bind}) is defined as:

$$E_{bind} = [(E_{mol} + E_{slab}) - E_{mol-slab}] \qquad (5.1)$$

E_{mol} is the energy of the optimized molecule in the gas phase, E_{slab} is the energy of the optimized forsterite slab and $E_{mol-slab}$ is the energy of the optimized adsorbed molecule on the forsterite slab. Positive binding energy values show endoergic adsorption processes.

The reaction energy (E_{react}) is defined as:

$$E_{react} = [(E_{product} - (E_{slab} + E_{mol}))] \qquad (5.2)$$

$E_{product}$ is the energy of the optimized product. For definition, E_{react} = - E_{bind}. Therefore, negative values of E_{react} shows favourable and exoergic processes.

We define contact points (C.P.) as the sum of orbital interactions between the p orbital of a carbon atom with the 3p orbital of a Mg atom, 3d orbital of Fe and Ni atoms.

The surface area of each PAHs is calculated as the sum of the area of the single hexagons and/or pentagons using the carbon backbone, *i.e.*, excluding the bound hydrogens.

5.3.   Results and Discussion

5.3.1.   Structure of the [010] Forsterite Surfaces

The [010]-fo surfaces are constituted by an orthorhombic structure with Pbnm space group and it differs from the bulk because of the presence of under-coordinated Mg atoms bound with three neighboring oxygen atoms on the external layer that faces the vacuum region.

The surface structure of [010]-fo is characterized by undercoordinated Mg atoms (M1) shown in Fig. 5.2 and fully coordinated Mg atoms (M2) located in the underlying layer. The Si (Si1) atoms on the surface are fully coordinated (tetrahedral structures). The bond distances, only for the atoms located on the surface, are reported in the table included in Fig. 5.2 and show Mg-O and Si-O distances ranging between 1.63 and 1.90 Å. Mg, O and Si atoms, on the surface, form zig-zag edges following an alternating unit scheme: -O-Si-O-Mg-O-. The Mg-O bond lengths of the under-coordinated Mg atoms on the surface (M1) are shorter than those of the octahedral Mg-O (M2-O2) with a bond distance that ranges between 2-2.16 Å. All calculated bond lengths are in agreement with the study carried out by Navarro-Ruiz *et al.*[213] using LCAO methods and by Brodholt using plane wave methods.[276]
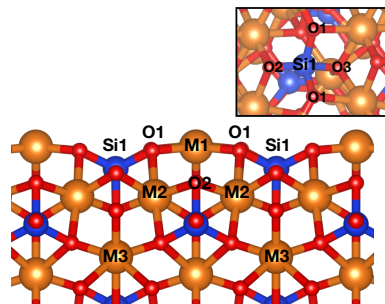
	[010]-fo (M=Mg)	Fe-[010]-fo (M=Fe)	Ni-[010]-fo (M=Ni)	V_{MgO}-[010]-fo
d(M1-O1)	1.86	1.89	1.88	
d(M1-O2)	1.90	1.96	1.93	
d(Si1-O1)	1.67	1.67	1.67	1.62
d(Si1-O2)	1.63	1.62	1.62	1.57
d(Si1-O3)	1.73	1.73	1.73	1.63
$\widehat{O1M1O1}$	123	126	120	
$\widehat{O1Si1O1}$	109	107	108	

Figure 5.2: Side-view figure that shows the labels of the atomic positions of the [010]-fo forsterite. M shows the location of an Mg, Fe, Ni atoms, or MgO vacancy. The table reports distances (d), in Angstrom (Å), and angles (⌒), in degree (°), of the atoms reported in the above figure.

We also studied the presence of point defects on the [010]-fo surface, shown in Fig. 5.1 (b). The Fe-[010]-fo surface is characterized by an undercoordinated Fe^{2+} atom bound to three oxygen atoms. When the Fe is located in the M1 site, it is more stable by 0.30 eV with respect to the M2 site and 0.22 eV with respect to the M3 site. Hence, M1 is the preferred site (Fig. 5.2). The table reported in Fig. 5.2 shows the bond distances and angles of the Fe-[010]-fo that are in close agreement with the geometrical parameters of the pristine surface.

Along with Fe-[010]-fo, we considered the presence of undercoordinated Ni as a point defect on the surface, Ni-[010]-fo (Fig. 5.1 (c)). The location of the Ni point defect in the M1 site is slightly more stable by about 0.04 and 0.01 eV compared to the M2 and M3, respectively. However, this difference is not significant considering the accuracy of the functional. [12] Once the transition metal coordinates with an aromatic molecule such as naphthalene, the Ni point defect in the M1 site is stabilized by 0.30 eV and 1.61 eV with respect to M2 and M3, respectively. The table in Fig. 5.2 shows bond distances and angles for the Ni-[010]-fo which are in close agreement with Fe-[010]-fo and [010]-fo. Overall, the presence of transition metals does not significantly change the forsterite structure compared to the pristine [010]-fo structure.

Another type of defect occurring in crystalline structures is the MgO

	Surface Area ($Å^2$)
Naphthalene	10.18
Anthracene	15.28
Fluoranthene	18.34
Pyrene	20.37
Coronene	35.64
Benzocoronene	40.73
Forsterite surfaces	340.74

Table 5.1: Surface area of PAHs and the [010] forsterite surfaces ([010]-fo, Fe-[010]-fo, Ni-[010]-fo, V_{MgO}-[010]-fo) optimized in this study. The average sizes of the hexagons and pentagons are 1.40 Å which is the distance of a single C-C bond.

Schottky defect. This defect is formed when a cation-anion pair is removed, resulting in a vacancy.[277] The energy required to form the Schottky MgO vacancy defect is about 7 eV.[62] For comparison, SiO_2 vacancies are less favorable since the formation energy is about 20 eV.[62] The presence of the Schottky MgO vacancy (V_{MgO}-[010]-fo), shown in Fig. 5.1 (d), causes an interruption of the zigzag units resulting in the formation of a SiO_3^{2-} unit and O atoms that bridge an Mg and Si atom. The absence of an Mg atom does not allow the formation of a bond between the two distant Si and O atoms on the surface. The distance between these not bound Si and O atoms, the two labeled atoms in Fig. 5.1 (d), in the vacancy is about 5.12 Å causing the formation of a cavity. The table in Fig. 5.2 shows that the Si-O distances are slightly shorter compared to the other surfaces. Instead, the O atom that lacks of a neighbour Si atom because of the vacancy (Fig. 5.1 (d)), binds with a second neighbour Si (Si1) which has a distance of 1.61 Å and 1.97 Å with the Mg located in the M2 site. Therefore, the cavity formation causes a bond length reorganization to compensate for the absence of an Mg atom. The MgO vacancy is more stable when located on the surface in the M1 site by about 2.90 and 4.94 eV with respect to the M2 and M3 sites, respectively. Hence, M1 is the most favorable site for all the three defects considered in this study.

5.3.2. Interaction of PAHs and C_{60} with [010] forsterite

Structural Analysis. Previous theoretical studies have shown that forsterite strongly binds with aromatic molecules on its surfaces.[12,218,219] Therefore, we have selected a sample of PAHs that span a range in surface area (Table 5.1) and that contain catacondensed PAHs (*e.g.*, the acenes naphthalene and anthracene), pericondensed PAHs (pyrene and coronene), and irregular PAHs (benzocoronene). In addition, we also selected the non-alternant aromatic species fluoranthene and fullerene. The skeleton structure of the mentioned PAHs is reported in Fig. 5.3.

We optimized all structures for a parallel adsorption of the molecular
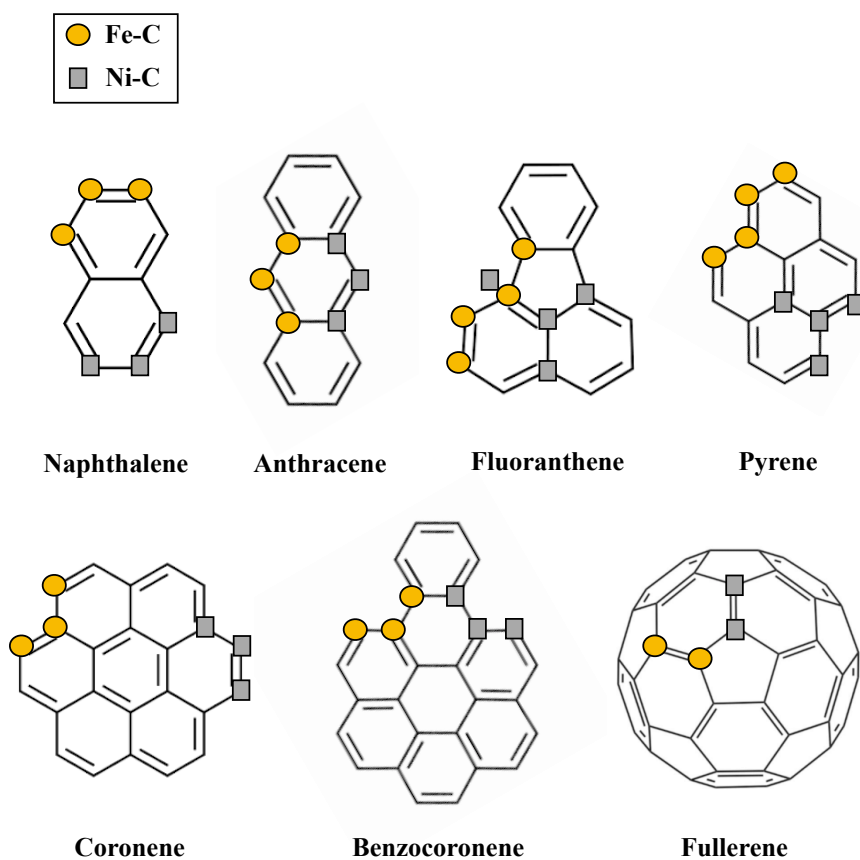
Figure 5.3: The skeleton structure of PAHs and the location of carbon-transition metal interactions less than 3 Å (see Appendix), on the PAH structure, when they adsorb on the Fe and Ni-[010]-fo. The legend shows the symbol related to C-Fe (circles) and C-Ni (squares) interactions.
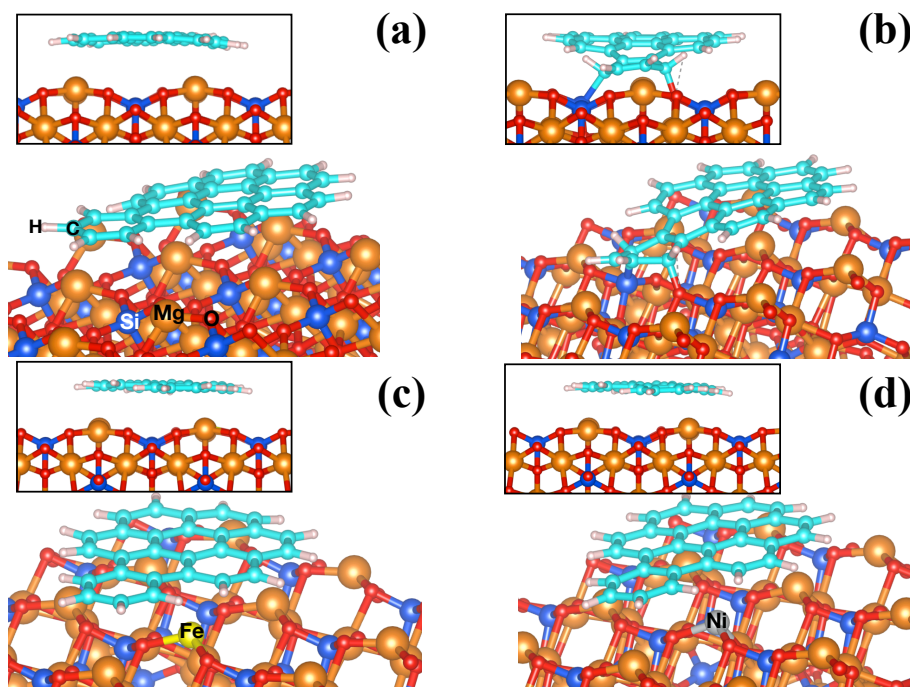
Figure 5.4: Side views using two different perspectives (second prospective in thumbnail) of the optimized geometries of benzocoronene adsorbed on (a) [010]-fo, (b) V_{MgO}-[010]-fo, (c) Fe-[010]-fo and (d) Ni-[010]-fo. Atomic labels are reported on the corresponding atoms.

plane with respect to the surface. The adsorption of PAHs on the [010] forsterite surfaces causes a slight deviation of the PAH structure from their planarity (Fig. 5.4). This is in line with the average dihedral angles of the carbon atoms of the PAH skeleton, reported in table 5.2. The average dihedral angles do not show characteristic planar structures of 180°. With the exception of pyrene, PAH adsorption on [010]-fo and Fe-[010] causes a larger deviation from planarity than for Ni-[010]-fo in which the adsorbed molecules have dihedral angles close to 180°. The average angles indicate a perfect 120° characteristic of sp^2 carbons for all PAHs with the exception of fluoranthene. The latter show larger angle deviation from 120° with respect to the other PAHs due to the presence of a 5-membered ring that causes major bending of its structure. The major flexibility due to the presence of a 5-membered ring has been identified also in other materials with PAH-like structures.[60] However, the conformational structure of PAHs on a solid surface, based on the angles and dihedral angles reported in Table 5.2, is close to the perfect planar structure that characterizes them in the gas phase. The conformational structure of the PAHs as well as the fullerene
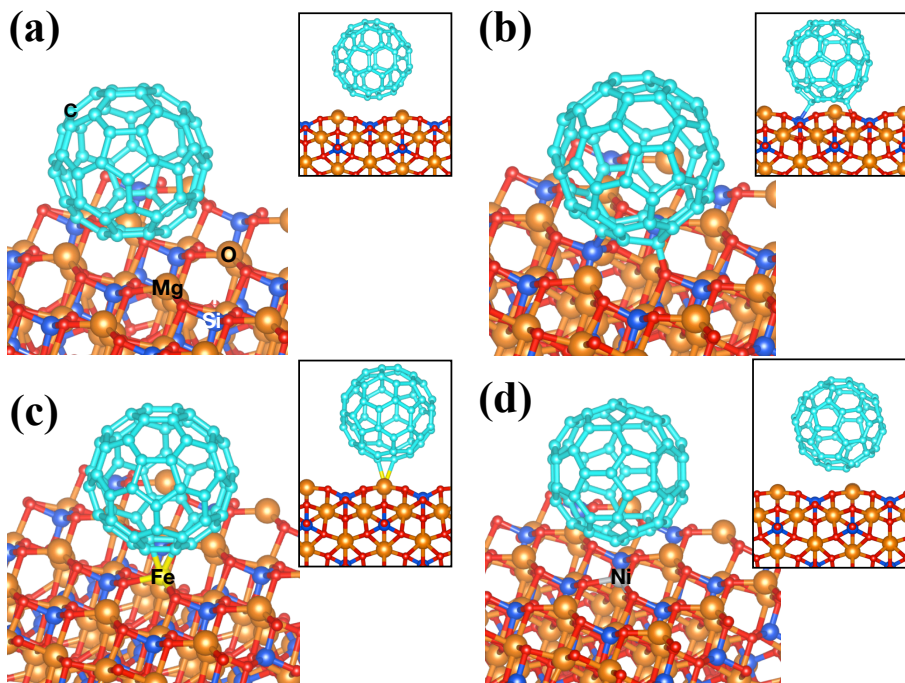
Figure 5.5: Side views using two different perspectives (second prospective in thumbnail) of the optimized geometries of fullerene adsorbed on (a) [010]-fo, (b) Fe-[010]-fo, (c) Ni-[010]-fo and (d) V_{MgO}-[010]-fo. Atomic labels are reported on the corresponding atoms.

on a solid surface, based on the angles and dihedral angles reported in Table 5.2, are very similar to those in the gas phase. Hence, the PAHs adsorbed on the surface have the 120° angles expected for planar PAHs while the fullerene (C_{60}) deviate from this by about 6° as expected for a buckyball-like structure (Fig. 5.5 (a), (c) and (d)).[278]

The larger is the surface area of the PAHs (Table 5.1), the larger is the number of the interaction of the C atoms either with an Mg or transition metal atoms (contact points), as shown in Table 5.2. Pyrene has a larger surface area with respect to fluoranthene. However, the number of contact points in pyrene is lower than fluoranthene. This is due to the more compact structure of the pyrene skeleton with respect to fluoranthene. With the exception of pyrene and fullerene, the number of Mg atoms interacting with carbon atoms at a distance less than 3 Å increases with increasing surface area of the PAH. Therefore, the larger is the surface area, the higher is the number of contact points. Distances larger than 3 Å do not present orbital interactions (see Population Analysis in the Appendix).

Interaction of PAHs and C_{60} with Doped Forsterite. Fig. 5.3 shows

Table 5.2: Geometrical parameters of PAHs adsorbed on forsterite surfaces. Reported the average distance ($\bar{d}$) in Angstrom (Å), average angles ($\overline{Ang.}$) and dihedral angles ($\overline{\Theta}$), in degree (°), number (n) of atoms (C, Mg or M) interacting with each other (*e.g.*, [nC - nMg]) and the number of contact points (C.P.) which is the sum of carbon atoms interacting either with an Mg or transition metal. M is the transition metal (*e.g.*, Fe or Ni) of the corresponding surface (*e.g.*,Fe for Fe-[010]-fo). Missing values show no interaction between the atoms. The average values are calculated from the geometrical parameters reported in the Appendix.

	$\bar{d}$(C-Mg)	$\bar{d}$(C-M)	$\overline{Ang.}$	$\overline{\Theta}$	[nC - nMg]	[nC - nM]	C.P.
Naphthalene:							
[010]-fo [12]	2.61		120.21	176.18	5 - 2		5
Fe-[010]-fo [12]	2.51	2.43	120.02	172.04	2 - 1	3 - 1	5
Ni-[010]-fo [12]	2.64	2.42	120.04	178.14	2 - 1	3 - 1	5
Anthracene:							
[010]-fo	2.65		120.82	173.06	6 - 2		6
Fe-[010]-fo	2.70	2.40	120.47	176.65	3 - 2	3 - 1	6
Ni-[010]-fo	2.73	2.41	120.38	177.05	3 - 2	3 - 1	6
Fluoranthene:							
[010]-fo	2.68		125.34	174.68	7 - 3		7
Fe-[010]-fo	2.62	2.56	125.73	176.99	3 - 2	4 - 1	7
Ni-[010]-fo	2.52	2.62	126.02	177.83	2 - 1	4 - 1	6
Pyrene:							
[010]-fo	2.72		120.79	179.15	5 - 2		5
Fe-[010]-fo	2.64	2.61	121.19	175.30	3 - 1	4 - 1	7
Ni-[010]-fo	2.66	2.50	120.86	177.64	3 - 1	4 - 1	7
Coronene:							
[010]-fo	2.73		120.92	175.63	11 - 4		11
Fe-[010]-fo	2.63	2.51	120.97	174.78	7 - 3	3 - 1	10
Ni-[010]-fo	2.68	2.46	120.80	177.90	5 - 3	3 - 1	8
Benzocoronene:							
[010]-fo [12]	2.71		120.61	176.29	11 - 4		11
Fe-[010]-fo [12]	2.66	2.47	120.46	178.90	8 - 4	3 - 1	11
Ni-[010]-fo [12]	2.67	2.48	120.43	179.18	8 - 4	3 - 1	11
Fullerene:							
[010]-fo	2.74		113.49	139.00	4 - 2		4
Fe-[010]-fo		2.10	106.82	133.63		2 - 1	2
Ni-[010]-fo	2.81	2.09	111.65	143.19	1 - 1	2 - 1	3

the preferred carbon sites of PAHs and fullerene that interact with Fe or Ni
on the surface. Naphthalene, anthracene, coronene and benzocoronene
have the same number of transition metal interactions, three interactions,
located in the edge carbons of the PAHs. Fluoranthene and pyrene have
the same number of C-Fe and C-Ni interactions since they are closer in
surface area with respect to the other PAHs. However, for fluoranthene
and pyrene, we noticed a different behavior of Ni-C interactions since the
optimization of the geometry led to a structure in which the inner carbon
of these PAHs can interact with Ni atoms at distances smaller than 3 Å (see
Geometrical Parameters in the Appendix for details). Instead, fullerene has
the same number of Fe-C and Ni-C interactions located in the [6,6] ring
junction.

On the transition metal doped surfaces (Fe and Ni-[010]-fo), PAHs do not
adsorb with the center of the π-ring as seen for benzene-cation complexes
(gas phase configuration) with the same spin configuration of the surfaces
(quintet for Fe^{2+} and triplet for Ni^{2+}).[12] The gas phase configuration shows
carbon-transition metal (C-M) bond distances of about 2.28 Å for Fe^{2+} and
2.17 Å for Ni^{2+} (values calculated from the optimized geometries reported in
a prior study[12] and in agreement with published theoretical studies of Fe-
PAH complexes in the gas-phase[279]). The PAHs on forsterite surfaces have,
as shown in Table 5.2, C-M bond distances slightly larger with respect
to the gas phase configuration. On a regular forsterite surface, the PAH
will orient itself on the surface to interact closely with as many Mg atoms
as possible. For doped surfaces, binding of PAHs is a competition of a
favorable orientation to interact with as many as possible Mg atoms and to
optimize the interaction with the transition metal. Table 5.2 summarizes
this competition, illustrating that on doped surfaces, the number of C-
Mg interactions decreases relative to the pristine surface but that this is
compensated for by the interactions with the transition metal. In general,
but not always, the number of contact points remains the same. We do
note that the difference between the Fe-C and Ni-C bond distances of the
PAHs on forsterite surfaces with respect to the gas phase configuration,
considering the optimized distance, is about 0.12-0.33 Å for Fe and 0.24-
0.45 Å for Ni. Hence, on an Fe-doped surface, PAHs can optimize the Fe-C
distance better than on a Ni-doped surface. Fullerene shows smaller (Table
5.2) C-Fe and C-Ni distances than in the PAHs, resulting in a stronger
interaction.

Interaction of PAHs and C_{60} with a Vacancy. The geometrical struc-
tures of all species adsorbed on V_{MgO}-[010]-fo are reported separately in
a table in Fig. 5.6. The vacancy has peculiar structures with respect to
the pristine and doped transition metal ones. Specifically, the adsorption
of naphthalene, anthracene, fluoranthene, benzocoronene, and fullerene
have characteristic $\widehat{O1C1C2}$ angles for the rehybridization of the C atoms
of PAHs from sp^2 to sp^3 (about 109°). The C-Si bond has a short distance,

	V_{MgO}-[010]-fo	Naph.	Anth.	Fluora.	Py.	Coro.	Benzo.	C_{60}
d(O1-Si1)	5.12	4.64	4.63	4.66	4.86	5.35	4.62	4.74
d(O1-C1)		1.46	1.45	1.47			1.46	1.44
d(Si1-C5)		1.99	2.00	2.00			2.02	1.99
d(O1-C2)					2.83	2.27		
d(Si1-C1)					2.25			
$\bar{d}$(C-Mg)			2.70	2.83	2.75	2.59	2.64	2.81
$\widehat{O1C1C2}$		111.59	109.16	111.82			112.68	111.59
$\widehat{C6C1C2}$		110.07	110.02	108.72		121.019	110.64	110.07
$\widehat{Si1C4C3}$		118.97	120.36	117.97			116.61	118.97
$\widehat{C5C4C3}$		112.05	112.03	110.57		120.21	112.06	112.05
$\overline{O1C2C3}$					121.09			
$\overline{C1C2C3}$					118.30			
$\overline{Si1C1C6}$					86.68			
$\overline{C2C1C6}$					119.58			
$\lvert\bar{\Theta}\rvert$		162.04	161.97	172.25	173.57	176.71	161.57	150.58
C.N. [O1]	2	3	3	3	2	2	3	3
C.N. [Si1]	3	4	4	4	4	4	4	4
[nC - nMg]		1 - 1	1 - 1	3 - 2	2 - 1	5 - 3	2 - 1	3 - 1

Figure 5.6: For the PAHs adsorbed on the V_{MgO}-[010]-fo surface we report: A schematic representation (naphthalene, anthracene, fluoranthene, benzocoronene, and fullerene) of the hexagonal ring chemisorbed with the undercoordinated Si and O (Figure (a)). The same as Figure (a) but for pyrene and coronene (Figure (b) and (c)). A table reporting the average distance ($\bar{d}$) and distance (d) in Angstrom (Å), angles (°) and average dihedral angles ($\lvert\bar{\Theta}\rvert$), in degree (°), coordination number (C.N.) for the specified atom and the number (n) of atoms (C and Mg) interacting with each other ($\lvert nC - nMg \rvert$) for the vacancy surface, PAHs and C_{60}. Missing values show no interaction between the atoms. The average values are calculated from the geometrical parameters reported in the Appendix.

about 1.9 Å, and the $\widehat{SiC4C3}$ angles, about 127-133°, are close to the geometrical parameters of silane complexes (about 120°).[280] Therefore the adsorption of these species on the vacancy surface causes the breaking of one aromatic ring (*i.e.*, a chemisorption process). The $\widehat{O1C1C2}$ angles, in the table in Fig. 5.6, show a perfect 109° for anthracene while the other PAHs slightly diverge from this value. Hence, the surface area of anthracene allows a perfect interaction with the vacancy. Pyrene and coronene do not show covalent bond formation. In fact, only species with a terminal aromatic ring with four hydrogen atoms (naphthalene, anthracene, fluoranthene, benzocoronene) and the six-membered ring of fullerene form covalent bonds with the undercoordinated Si and O atoms (see C. N. in the table in Fig. 5.6). This occurs due to their large structural flexibility with respect to more compact structures such as pyrene and coronene. The coordination number of O and Si increases once PAHs adsorb on the vacancy forsterite surface in line with the formation of C-O and C-Si bonds. For the case of pyrene, the molecule binds only with the Si atom, leaving the O atom with a lower coordination number (2) with respect to the adsorption of the other PAHs and C_{60}. However, the Si-C distance, for the case of pyrene, is larger by about 0.25 Å than for the other PAHs chemisorbed on the vacancy. The adsorption structure of pyrene on the vacancy is shown in Fig. 5.6 (b). All species have O-C and Si-C bond distances in good agreement with the average experimental values (1.40 and 1.87 Å).[281]

The distance of undercoordinated Si and O atoms on the vacancy structure is reduced once their coordination is completed by the chemisorption of the PAHs (see O1-Si1 distance in the table reported in Fig. 5.6). However, for the case of coronene, the distance O1-Si1 increases with respect to the non-coordinated surface. Angles and dihedral values of coronene adsorbed on the vacancy do not show the formation of C sp^3, but a quasi-planar structure in agreement with the adsorption on the pristine and transition-metal doped surfaces. The coordination number of O and Si of the vacancy, when coronene is adsorbed on it, is completed. Nevertheless, for the case of coronene adsorbed on the vacancy, there is no covalent bond formation, the vacancy enlarged its structure to accommodate the large surface area of coronene which in turn causes the formation of a Si reconstruction as shown in Fig. 5.7. The vacancy reconstruction, caused by the adsorption of coronene on the vacancy, is characterized by the formation of the Si-O bond located in the underlying surface moving the Si atom in between the surface layer and the layer below the surface, completing the coordination of the Si atom. Also, the O atom on the vacancy completes the coordination with a Si located in the underlying surface.

Due to the interaction of the PAHs with the vacancy, the number of Mg atoms interacting with C atoms is much lower with respect to the pristine and metal-doped surfaces, comparing the values between the Table 5.2 and the table reported in Fig. 5.6, respectively.
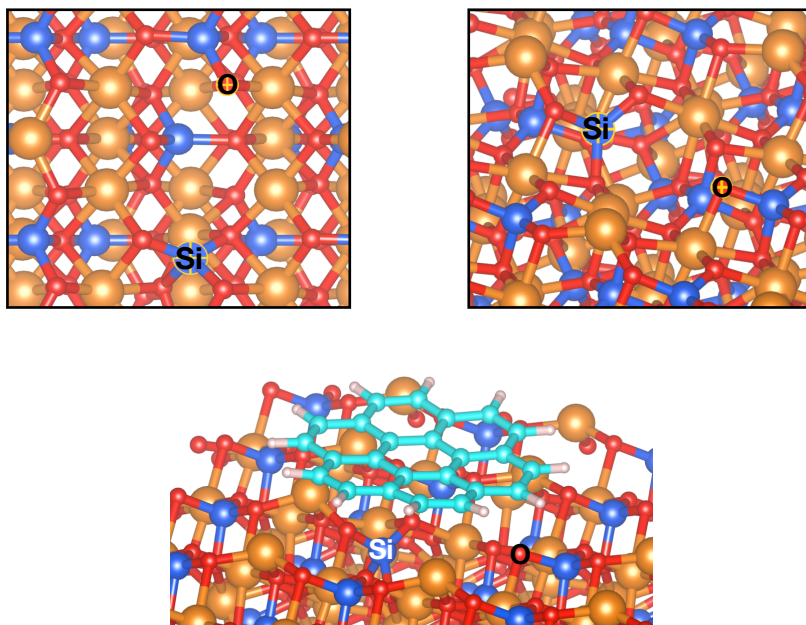
Figure 5.7: Vacancy reconstruction caused by the adsorption of coronene on V_{MgO}-[010]-fo. In thumbnail reported the close-up perspective of the reconstruction. The atomic labels on the corresponding atoms indicate the reconstructed atoms.
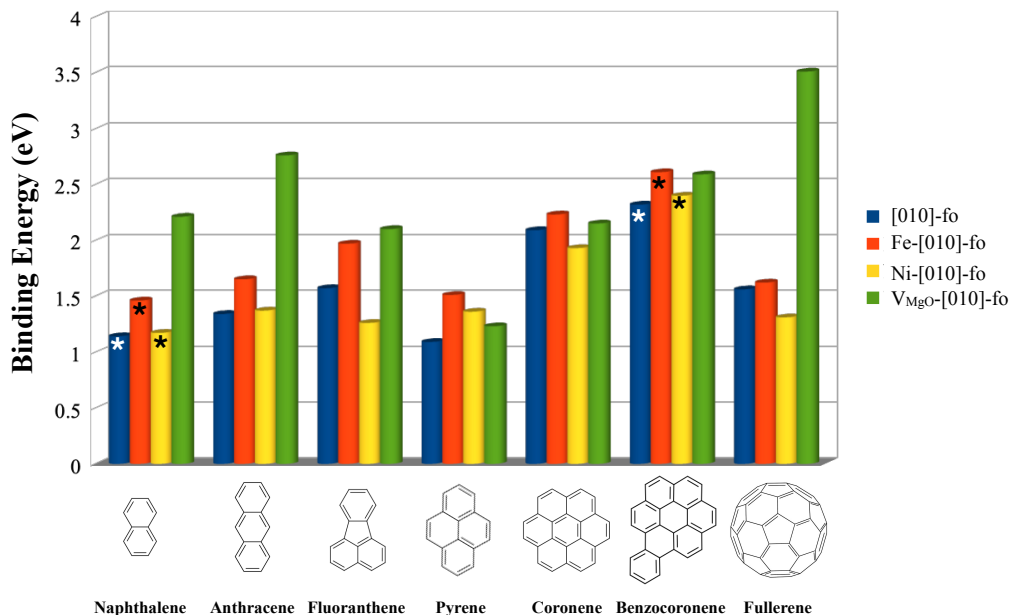
Figure 5.8: Binding energies of the adsorption of PAHs on [010] forsterite surfaces modeled in this study. The surfaces follow the order shown in the legend for all PAHs. Numerical values are reported in the Appendix. The asterisks (*) on the bars show data reported from a prior work. [12]

Binding Energy Analysis. Fig. 5.8 summarizes the binding energies for the PAHs adsorbed on the four different surfaces considered in this study. Disregarding for the moment, the interaction with the Schottky defect, there is a general trend of increasing binding energy with PAH size/surface area but pyrene forms an exception to this. Not surprisingly given its geometry, the fullerene does not adhere to this trend either. The general increase of the binding energy is to be attributed to the increasing number of contact points (see Table 5.2) that is related to the size of the surface area (see Table 5.1). We remind that the larger is the surface, the larger is the number of contact points. Excluding for now the binding energies of the vacancy surface, all PAHs are slightly more stabilized (larger binding energy) on the Fe-[010]-fo with respect to Ni-[010]-fo which is opposite to the adsorption behavior of Fe^{2+} and Ni^{2+} on benzene in the gas-phase (gas phase configuration). [12] As discussed in Structural Analysis section, this reflects subtle geometrical differences in the balance between Mg-PAH and Ni-PAH interactions. PAH adsorption on Fe-doped forsterite shows consistently higher binding energies than on the pure surface, reflecting that PAHs can optimize their interaction on this surface better than

Table 5.3: Binding energies (E_{bind}), angles ($\widehat{\ }$) of PAHs chemisorbed on V_{MgO}-[010]-fo surface.

	E_{bind} (eV)	$\widehat{O1C1C2}$	$\widehat{Si1C4C3}$
Naphthalene	2.21	111.59	118.97
Anthracene	2.76	109.16	120.36
Fluoranthene	2.10	111.82	117.97
Benzocoronene	2.59	112.68	116.61
Fullerene	3.51	111.59	118.97

Table 5.4: Binding energies (E_{bind}), at PBE-D4/CP-DZP and PBE/CP-DZP levels, and dispersion energy (D4) for the interaction of PAHs with V_{MgO}-[010]-fo surface.

	E_{bind}^{PBE-D4} (eV)	E_{bind}^{PBE} (eV)	D4 (eV)
Naphthalene	2.21	1.17	1.05
Anthracene	2.76	1.50	1.25
Fluoranthene	2.10	0.62	1.48
Pyrene	1.23	0.10	1.32
Coronene	2.15	0.55	2.15
Benzocoronene	2.59	0.35	2.30
Fullerene	3.51	1.78	1.74

on a Ni-doped surface. The binding energy trend between Fe and the pristine surface is, instead, in agreement with the gas-phase configuration.[241]

As shown in Fig. 5.8, all molecules bind strongly on the vacancy surface with binding energies larger than 2 eV. We note that anthracene has larger binding energies than naphthalene in line with the reactivity studies conducted by Bonfanti *et al.*[137] and Rasmussen *et al.*[124] Anthracene adsorbs on the vacancy surface with the formation of perfect C-Si and C-O bonds and $\widehat{O1C1C2}$ and $\widehat{Si1C4C3}$ angles of 109° and 120°, respectively. Table 5.3 shows the binding energy of PAHs and fullerene as a function of the $\widehat{O1C1C2}$ and $\widehat{Si1C4C3}$ angles (see labels in Fig. 5.6). Excluding the special case of fullerene, the binding energy of PAHs decreases as a function of the angle deviations from 109° and 120°, for $\widehat{O1C1C2}$ and $\widehat{Si1C4C3}$ respectively. Therefore, antrhacene is the PAH that benefits the most from the adsorption process on the vacancy surface. Fullerene is an exception since it benefits from the formation of covalent bonds with the O and Si atoms on the vacancy and, therefore, from the re-hybridization of the carbon atoms (from tensioned sp^2 to sp^3 carbons)[278] that break the symmetry of the icosahedral structure. Despite that benzocoronene has larger geometrical deviations than other PAHs (see angles in Table 5.3), its binding energy is closer to the anthracene one due to the higher dispersion energy (see Table 5.4). The binding energy of pyrene and coronene deviates with respect to the other PAHs due to their physisorption state (see discussion in Structural Analysis section and the table in Fig. 5.6).

The difference of binding energies between the vacancy surface and the pristine surfaces is much larger for naphthalene, anthracene, and fullerene than for the other PAHs. The smaller number of contact points for naphthalene and anthracene as compared to the other PAHs makes the contribution from the covalent bond formation on the vacancy surface relatively more important. The propensity of fullerenes for addition reactions through the carbons of the 6-membered ring facilitates covalent bond formation on the vacancy surface and results in a relatively high binding energy.

Adsorption Mechanism. In the previous section, we have seen that PAHs strongly bind on the vacancy surface with the formation of C-O and C-Si bonds. In order to evaluate the possible presence of activation barriers associated with the formation of covalent bonds (see Structural Analysis section), we have calculated the minimum energy path employing the CI-NEB approach to locate possible saddle points (transition states). Due to technical and computational difficulties in optimizing these large molecular interactions, we only have considered the adsorption of naphthalene and benzocoronene on the vacancy surface to address potential differences between small and large PAHs in the chemisorption process. For the PAH approaching the surface in parallel, the adsorption is studied for both naphthalene and benzocoronene. For a perpendicular orientation, we studied only naphthalene due to technical difficulties, see also image 1 shown in Fig. 5.9 and 5.10 respectively.

Parallel Adsorption. Fig. 5.9 shows the minimum energy path for the adsorption process of naphthalene and benzocoronene leading to the chemisorption of the carbon atoms, in para (opposite carbon sites of the hexagonal ring), forming C-Si and C-O bonds (image 8 in Fig. 5.9). Image 1 represents an optimized geometry of the PAH at a distance of about 5.6 Å from the surface. Image 8 is the optimized PAH chemisorbed on the vacancy which is the final product.

The adsorption process is barrierless and with large exoergic reaction energy of about -2.2 eV for naphthalene. We also reported the minimum energy path for benzocoronene (red curve in Fig. 5.9) to check how the path change for large surface area molecules. Benzocoronene also has large reaction energy of about -2.59 eV with a barrierless and exoergic adsorption. The benzocoronene images are lower in energy with respect to the naphthalene ones due to the larger dispersion energy with respect to naphthalene (see Table 5.4).

Perpendicular Adsorption. When the molecule is oriented perpendicularly with respect to the surface, as shown in image 1 in Fig. 5.10, the adsorption on the V_{MgO}-[010]-fo leads, during the optimization process, to the dissociation of C-H bond of the PAH. In contrast, this process on the pristine and transition metal surfaces does not lead to dissociation but only adsorption (see Fig. 5.4). On the vacancy, the optimized minimum energy path (Fig. 5.10), with the CI-NEB method, shows a barrierless and

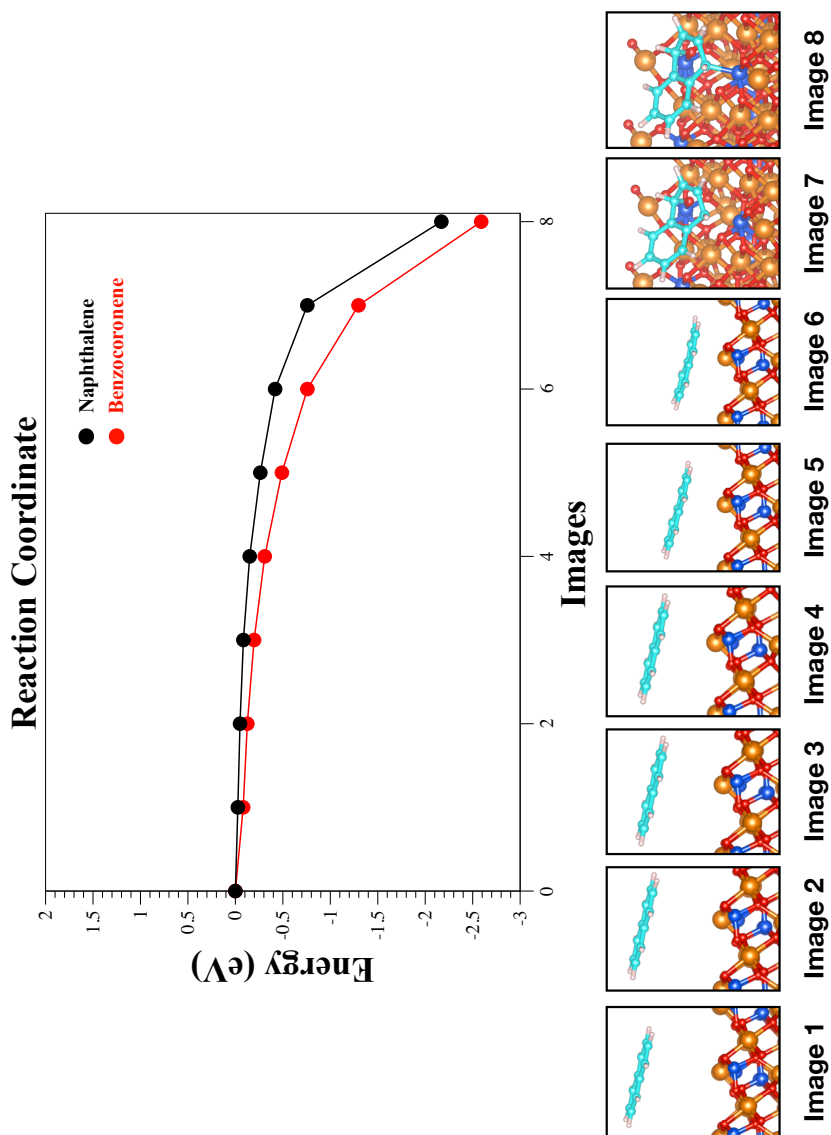**Figure 5.9:** Optimized minimum energy path of the adsorption of naphthalene (black curve) on V_{MgO}-[010]-fo. The optimized geometry, only for naphthalene, of all images is reported below the plot. Image zero is the surface and the molecule at infinite distance.

exoergic reaction of -3.5 eV. Therefore, the dissociation (perpendicular adsorption) is more favorable than the adsorption (parallel adsorption) by about -1.3 eV.

The reagent (image 1) has been optimized perpendicularly and distant about 6.5 Å with respect to the vacancy surface. Along the reaction path, the molecule approaches the surface, chemisorbing a carbon atom on the undercoordinated Si atom on the vacancy (C-Si interaction). This results in a C-Si bond length of about 2.13 Å compared to typical C-Si bond length in silane species: 1.87 Å.[281] The electron donation of the C-Si interaction causes, at the same time, the transposition of the hydrogen to the neighbor oxygen atom on the vacancy forming an O-H bond with a distance of about 0.99 Å typical for hydroxyl groups.[281] The last step implies the adsorption of the remaining carbon skeleton on the surface, as shown in image 8 on Fig. 5.10.

The spin density isosurfaces show a large population of spin-down localized on the Si atoms and spin-up localized on the O atoms of the V_{MgO}-[010]-fo surface. The Voronoi charge analysis shows a partial positive charge on the Si atom (0.897) and a partial negative charge on the O atom (-0.625). After the dissociation, the partial electronic charge is reduced to 0.625 for the Si atoms, gaining electrons, and -0.356 for the O atom, donating electrons. The Voronoi charge analysis shows a donation of the electrons from the 2p orbital of the C atom of naphthalene to the 3p orbital of the undercoordinated Si atom on the vacancy, whereas the O atom donates electron density to the proton (H) dissociated from the PAH. This behavior is similar to the catalytic effect of "Frustrated Lewis Pairs" (FLPs) that are a Lewis acid and base that are not able to bind due to geometrical hindrance. Therefore, the geometrical hindrance causes the increase of the strength of the Lewis acid and base. The simultaneous electron transfer is responsible for the cleavage of the C-H bond through a barrierless reaction promoted by an O and undercoordinated Si atoms which is similar to the electron transfer mechanism of the FLPs.[282]

Table 5.5 reports the reaction energy (dissociation energy) for all PAHs on the V_{MgO}-[010]-fo based on the two studied mechanisms (perpendicular and parallel). For the parallel adsorption, naphthalene, anthracene, and fluoranthene show comparable reaction energies, whereas both coronene and pyrene show exoergic reaction energies larger by about -0.4 eV. The exoergicity of benzocoronene is even larger (-5.25 eV) with respect to all PAHs. Anthracene has slightly lower reaction energy with respect to naphthalene and fluoranthene. This might reflect the fact that the electron density is mainly localized in the central ring of anthracene. The electron density is lower in the terminal ring (the ring bound with the surface) than the central one.[39,124,283] However, on the vacancy surface, anthracene prefers to bind with the terminal ring, not with the central one, as the latter would require major structural changes. As a result, the reaction energy of anthracene is not as large as for naphthalene and fluoranthene. The reac-
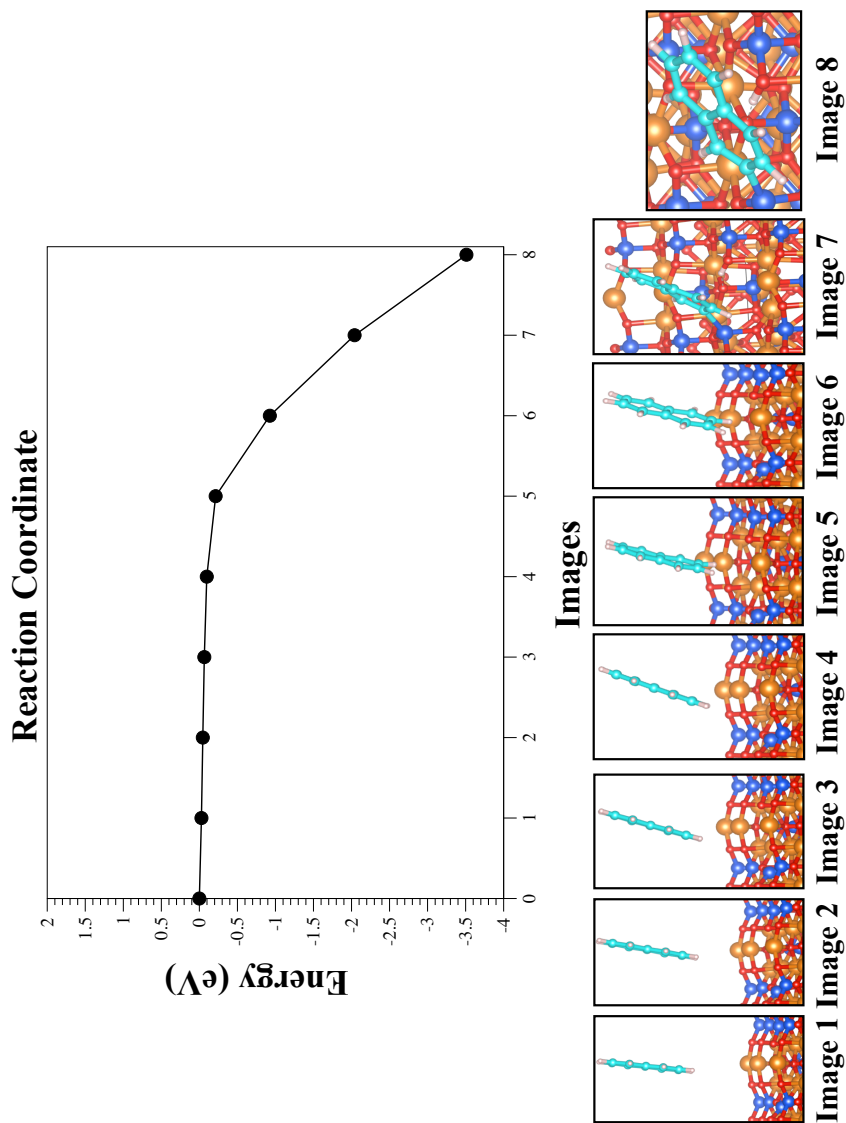
Figure 5.10: Optimized minimum energy path of the CH dissociation of naphthalene on V_{MgO}-[010]-fo. The optimized geometry of all images is reported below the plot. Image zero is the surface and the molecule at infinite distance.
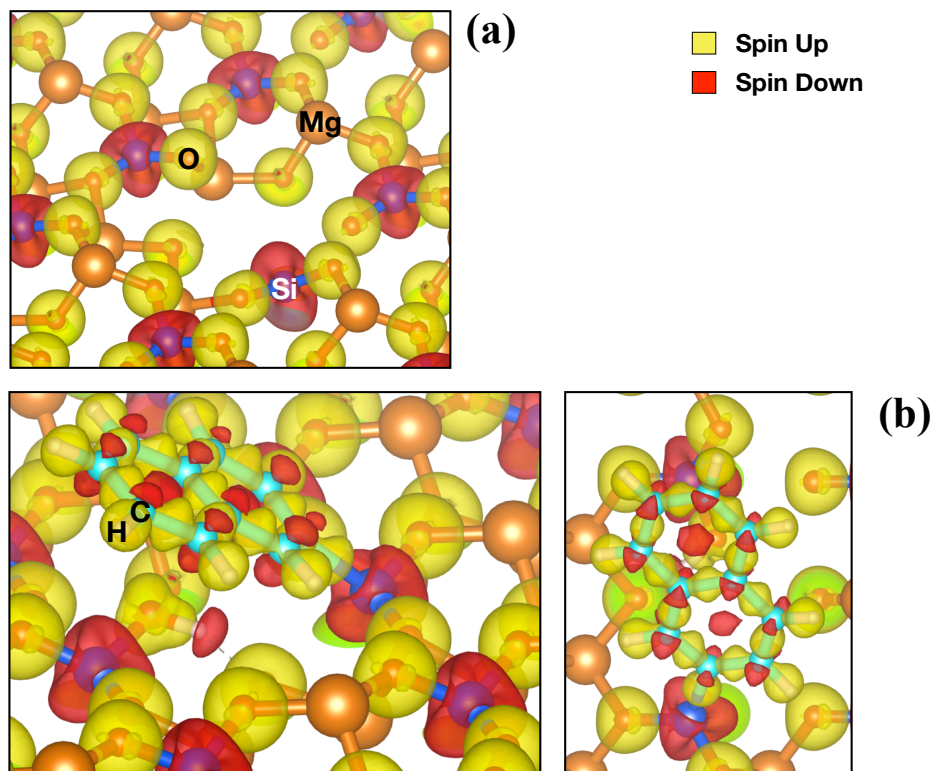
Figure 5.11: Spin density isosurface (isovalue 0.007 e/A^3) of V_{MgO}-[010]-fo (a) and the dissociation of the CH bond of naphthalene on the V_{MgO}-[010]-fo (b). Yellow density indicates spin up population and red density spin down one.

Table 5.5: Reaction energies for the adsorption of PAHs on V_{MgO}-[010]-fo through a perpendicular ($E^{\perp}_{react}$) and parallel ($E^{=}_{react}$) adsorption.

	$E^{\perp}_{react}$ (eV)	$E^{=}_{react}$ (eV)
Naphthalene	-3.51	-2.21
Antracene	-3.22	-2.76
Fluoranthene	-3.55	-2.10
Pyrene	-3.92	-1.23
Coronene	-3.92	-2.15
Benzocoronene	-5.25	-2.59

tion energy trend, for the perpendicular adsorption, is the reverse of the parallel adsorption in which anthracene is more stabilized with respect to naphthalene and fluoranthene due to the perfect geometrical fit with the vacancy surface (see discussion in Binding Energy Analysis section and Table 5.3)

The C-H dissociation trough a perpendicular adsorption mechanism is more energetically favourable and, therefore, more likely to happen with respect to the parallel adsorption (Table 5.5). Based on the Bell–Evans–Polanyi principle,[138,139] higher reaction energies are associated with low energy barriers and, therefore due to the large exoergicity, we would expect a barrierless process also for anthracene, fluoranthene, pyrene and coronene.

5.4. Astrochemical and Cosmochemical Implications

The study of the interaction of silicate minerals with PAHs in star forming regions is important since it may relate to the organic composition of comets and asteroids. The latter locks up a variety of organic molecules including the prebiotic building blocks of life as well as PAHs.[46] During the phase of the formation of a star, silicate dust grains surrounding the protostar coagulate to form planetesimals and cometesimals that eventually will lead to planet formation. Therefore, the cometary and asteroidal composition locks up valuable information about the processes that form molecules in space.[8,46]

In this study, we focused on crystalline forsterite as the main component of silicate grains, asteroids, and meteorites.[44,284] Silicate minerals in protoplanetary disks and the solar system often have a crystalline nature as revealed by observations of dust disks around young stellar objects, comets and asteroids.[35] In the ISM, silicates have strong infrared Si-O stretching mode and O-Si-O bending mode absorption features around 9.7 μm and 18 μm, respectively.[285] While IR observations reveal that interstellar silicate grains lack large scale order,[286] X-ray absorption studies reveal short scale crystalline structures.[287] Possibly, interstellar silicates are polycrystalline and, in that case, their adsorption behavior would be well described by the study presented here. However, in the ISM, there are no direct evidence of the presence of crystalline silicate and, thus, this issue is still under investigation.[44,286]

The composition of the dust, asteroids and meteorites (silicate materials) is largely dominated by silicate structures belonging to the olivine and pyroxene's families with stoichiometric formulae $Mg_{2x}Fe_{2-2x}SiO_4$ and $Mg_xFe_{1-x}SiO_3$, respectively. The composition of silicate materials in the universe is usually very rich in Mg and poor of Fe (Mg/Fe ratios less than

a few percent).[288] The trace of transition metals is embedded in forsterite as point defects,[236] distortionary rearrangement of a perfect crystal lattice, along with Mg, Si, and MgO Schottky vacancy.[217,264] Point defects might already have formed in the envelope of AGB stars or may reflect energetic processing of silicate grains in the ISM by *e.g.*, cosmic rays,[289,290] whereas thermal annealing and irradiation by the stars are the processes taking place in protoplanetary disks.[291] Molecular dynamic simulations suggest the vacancy formation has been preferentially formed around the AGB stars through O-loss or Schottky defect creation.[264]

Part of the condensed dust in the ISM is formed by PAHs along with other aromatic carbonaceous molecules due to the formation of cluster agglomerates by the π-stacking of their aromatic skeleton.[32,292] In space, PAHs are important to maintain the energy and ionization balance in some regions of the interstellar medium as well as for the production of the most important molecule in the universe, H_2.[16,39] In carbonaceous meteorites, PAHs were hypothesized to be formed by the conversion of aliphatic compounds to aromatic ones through post-Fischer-Tropsch synthesis at low temperature catalyzed by minerals at 360-400 K. However, due to the large abundance of non-alkylated PAHs with temperatures between 400-800 K, the hypothesis of PAH formation post-Fischer-Tropsch synthesis was rejected.[50] Therefore, the origin of PAHs in asteroidal settings is still to be clarified, whereas it is clear that in circumstellar regions and the ISM are the most likely sources for the formation of these aromatic compounds.[44]

The silicates found in meteorites, specifically carbonaceous chondrites, have characteristic composition of non-volatile elements, *e.g.* Fe, Ni, Mg, etc., in which the abundance is comparable to the abundance of elements observed in the Sun.[293,294]

The abundance of PAHs in the Murchinson carbonaceous meteorite is about 1.82 mmol/g with a large abundance of PAHs with four aromatic units.[53] PAHs with more than six aromatic units such as coronene ($C_{24}H_{12}$) and benzocoronene ($C_{28}H_{14}$) have not yet been identified in meteorites. The presence of fullerene in meteorites is suspected and still need further clarifications.[295] Therefore, we considered studying the interaction of coronene and a similar molecule with an extra aromatic ring (benzocoronene) along with fullerene to clarify the matter about the reason why large organic species were not yet detected.

The potential catalytic activity of forsterite and its defective surfaces, revealed by this study, provides a new view on why large PAHs might not be present in carbonaceous meteorites. The degradation of PAHs, as we saw for the CH activation on the vacancy surface, is favorable for PAHs up to 7 aromatic units. In the ISM the barrier for H-loss from PAHs, such as coronene, in the gas phase is 4.7 eV,[183] and it can be easily promoted by energetic UV-photons (about 12 eV). Astronomical models imply that photodestruction is more rapid for small PAHs than for large PAHs.[41,296] In our calculations based on the binding and reaction energies, on a solid

surface, we see the opposite trend and the dissociation rate is more fa-
vorable for large PAHs, suggesting that defects in crystalline olivine might
catalyze the dissociation of the C-H bond of PAHs in an asteroidal setting.
Therefore, this work provides the basis for future astronomical modeling
and experimental studies. In particular, the dissociation sequence of each
C-H bond of PAHs as well as the estimation of energy barriers for the pris-
tine and metal-doped surfaces needs to be clarified in future works.

5.5.   Conclusions

We employed periodic DFT-D4 to study the interaction of PAHs with the
[010] forsterite surface and its defective surfaces: Fe, Ni-doped surfaces.
Furthermore, we studied the catalytic property (CH activation) of the MgO
Schottky vacancy. We studied the adsorption of naphthalene, anthracene,
fluoranthene, pyrene, coronene, benzocoronene, and fullerene on these
four [010] forsterite surfaces. With the exception of fullerene, all species
adsorb on the surfaces maintaining angles and dihedral angles close to the
gas-phase configuration. A large surface area allows large contact points
(number of atomic interactions) with the surface. Excluding the vacancy
surface, we found that all organic species, in this study, present larger
binding energy on the Fe-[010]-fo surface with respect to Ni and pristine
surface which is the opposite behavior of benzene-cation complexes in the
gas-phase. These small differences in the binding energy for the adsorp-
tion of PAHs on pristine and transition metal surfaces are caused by differ-
ences in the number of contact points. The vacancy has shown different
behavior with respect to pristine and transition metal surfaces due to the
formation of a covalent bond with PAHs. Specifically, C-O and C-Si bonds.
Anthracene has a larger binding energy with respect to other PAHs due to
the formation of perfect $\widehat{OCC}$ and $\widehat{SiCC}$ angles of 109° and 120° charac-
teristic of silane complexes. Deviation from these angles are reflected in
the differences in binding energy of PAHs on the vacancy surface. Pyrene
and coronene physisorb on the vacancy without covalent bond formation.
For the case of coronene, the physisorption causes the reconstruction of
Si-O bonds on the vacancy. Fullerene adsorption occurs through the for-
mation of C-O and C-Si bonds on the 6-membered ring analogous to PAHs
chemisorption. The larger binding energy of the chemisorption of fullerene
on the vacancy reflects the formation of covalent bonds that break the
icosahedral symmetry of the buckyball.

We found that based on the orientation of the molecule with respect to
the vacancy surface the barrierless adsorption or the adsorption with a
barrierless CH dissociation might take place on the surface; parallel and
perpendicular to the surface, respectively. The perpendicular adsorption,
with associated CH dissociation, is energetically more favorable than the
parallel adsorption. Therefore, the vacancy has potential catalytic activity

for the dissociation of CH bond of PAHs. For the CH dissociation process, the charge analysis has shown an electron donation of the O atoms to the C atoms and electron attraction of the H to the Si atom. This causes splitting of the C-H bond and the formation of C-Si and O-H bonds on the surface. This mechanism is similar to the electron transfer mechanism of Frustrated Lewis Pairs (FLPs) catalysts.

Hence, forsterite shows potential catalytic activity for the dissociation of aromatic CH which might be used as a cheap and safe catalyst. Furthermore, the catalytic potential of forsterite might shed light on the formation of the so-called organic inventory of star-forming regions in space. This study will follow up with future studies on addressing the selectivity of the vacancy for the dissociation of the hydrogen bound with different carbon sites of the PAHs as well as clarifying the catalytic activity of the pristine surfaces and how to release the fragmented PAH strongly bound with the catalytic site.

5.6. Appendix

Binding Energies

Table 5.6: Binding energies (E_{bind}) of the adsorption of PAHs and fullerene onto [010] forsterite surfaces.

	$E_{bind}^{[010]-fo}$ (eV)	$E_{bind}^{Fe-[010]-fo}$ (eV)	$E_{bind}^{Ni-[010]-fo}$ (eV)	$E_{bind}^{V_{MgO}-[010]-fo}$ (eV)
naphthalene	1.14 [12]	1.46 [12]	1.17 [12]	2.21
anthracene	1.34	1.65	1.37	2.76
fluoranthene	1.57	1.97	1.26	2.1
pyrene	1.09	1.51	1.36	1.23
coronene	2.09	2.23	1.93	2.15
benzocoronene	2.32 [12]	2.61 [12]	2.4 [12]	2.59
fullerene	1.56	1.62	1.31	3.51

Population Analysis

The electronic structure and the nature of chemical bonding are studied with the projected density of state (PDOS), the crystal orbital overlap (COOP), and hamilton population (COHP).[297] The theoretical level used for the PDOS, COOP, and COHP, consists of a PBE+U/TZP single-point calculation on the PBE/DZP optimized geometry (explained in detail in a previous work[12]).

Figure 5.12: PDOS, COOP, and COHP of benzocoronene adsorbed on Fe-[010]-fo at different distances from the surface (Δz=+0 Å,+1 Å,+2 Å,+3 Å) with the respective atomic legend reported. For the PDOS, the peaks down and up refer to spin down and up, respectively. For the COOP and COHP, positive values are bonding contribution and negative ones are anti-bonding contribution. The Fermi level has been shifted at 0 eV.

The binding energy analysis provides meaningful insights into understanding the strength of the adsorption of the four forsterite surfaces. However, the only binding energy analysis does not provide information on the bonding nature between the molecule and the surface. Therefore, we calculated, as test-case, the PDOS, COOP, and COHP only for the ad-

sorption of the PAH that has large binding energy when adsorbed on the forsterite surfaces: benzocoronene on Fe-[010]-fo and V_{MgO}-[010]-fo, for instance. We decided to consider the only benzocoronene in view of its large surface area (40.73 Å), and for the surface, we limit ourselves to Fe-[010]-fo and V_{MgO}-[010]-fo since those are the surfaces that show higher binding energy for most of the cases of this study. Specifically, we calculated the PDOS of benzocoronene at different distances from the surface (0, 1, 2 and 3 Å far from the surface). We reported only the valence band region since we are interested in shedding light on the binding nature of the molecular interaction with the surface. In Fig. 5.12, we report the PDOS for the benzocoronene adsorbed on the Fe-[010]-fo surface. The valence band is dominated by the electrons of the 2p orbitals of the O atoms, followed by the electrons of the 3p orbitals of the Mg atoms and 3d orbitals of the Fe atoms. When benzocoronene is interacting with the surface (Δz+0 Å), we notice an overcrowded region of small peaks belonging to orbitals of C and Fe that suggest orbital interaction. Once the molecule moves away from the surface the region of the Fermi level becomes less busy with larger gaps between the peaks of all three atoms reflecting the reduced interaction of the molecule with the surface.

The PDOS provides a good description of the electronic contribution of the atoms to the overall band structure, however, does not provide information about the bonding and antibonding nature of these electrons. Therefore, we partitioned the density of state in the bonding and antibonding contribution of the specific atoms (COOP spectra). Fig. 5.12 report the COOP spectra for the orbital interaction between Mg and C atoms as well as Fe and C atoms. The upward and downward peaks reflect bonding and anti-bonding contribution, respectively. Qualitatively, we see that the bonding contribution prevails with respect to the antibonding contribution. Once the molecule is 1 Å away from the surface (Δz+1 Å), the antibonding contribution disappears since the electron-electron repulsion is lower. Once the molecule is 2 and 3 Å away (Δz+2 Å and Δz+3 Å, respectively) from the surface there is not bonding contribution since the electronic interaction becomes weaker.

The COHP is the same as the COOP, but in this case, we partition the band energy rather than the electronic structure. Therefore, the COHP usually is the opposite of the COOP, but for simplicity, we inverted the sign of the peaks for ease of comparison to COOP. As expected, COHP has a similar trend with respect to COOP for the case of benzocoronene on Fe-[010]-fo, shown in Fig. 5.12.

For the interaction of benzocoronene with the V_{MgO}-[010]-fo, Fig. 5.13, the PDOS is dominated by the electron of the 2p orbitals of the O atoms followed by 3p orbitals of Mg, 3p orbitals of Si, in line with the PDOS bulk structure of forsterite, [12] and 2p orbitals of the C atoms. Due to the presence of three different types of interaction, it is difficult to analyze substantial variations in the PDOS at three different distances from the
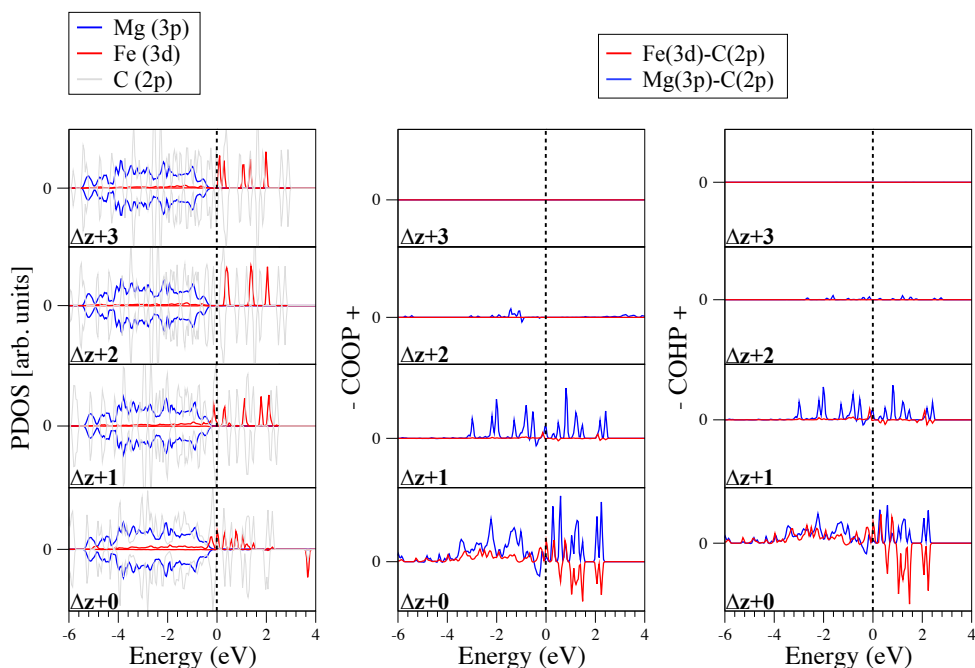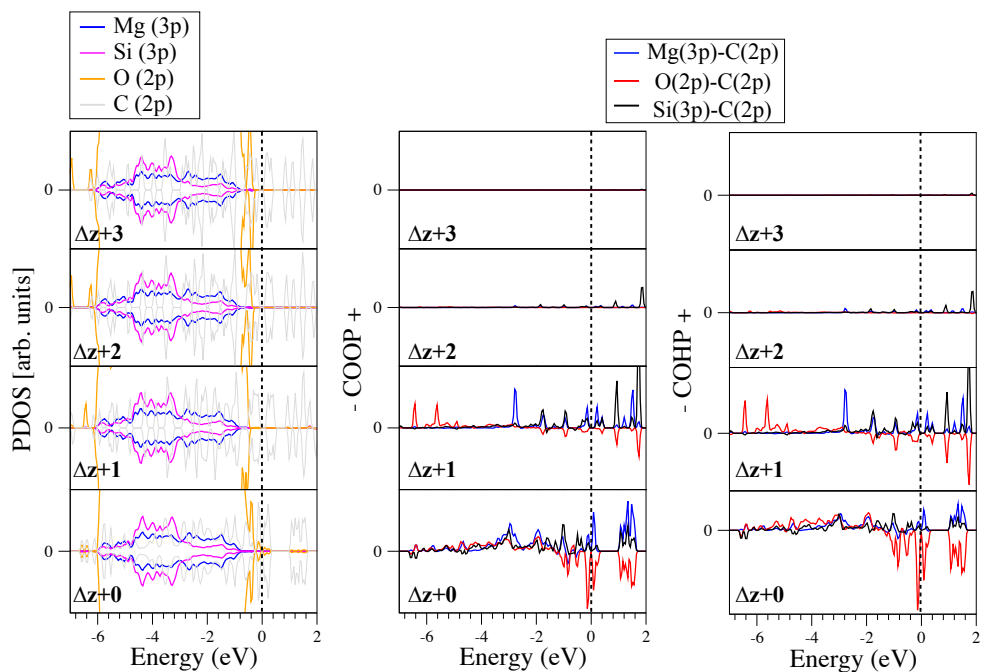
Figure 5.13: PDOS, COOP, and COHP of benzocoronene adsorbed on V_{MgO}-[010]-fo at different distances from the surface (Δz=+0 Å,+1 Å,+2 Å,+3 Å) with the respective atomic legend reported. For the PDOS, the peaks down and up refer to spin down and up, respectively. For the COOP and COHP, positive values are bonding contribution and negative ones are anti-bonding contribution. The Fermi level has been shifted at 0 eV.

surface. Instead, the COOP and COHP show non-bonding peaks as well as larger bonding peaks for the interaction of O-C orbitals. This suggests the presence of a covalent bond formation since the electron of the 2p orbitals of C atoms come close to the electrons of the 2p orbital of the O atoms repelling each other.

Geometrical Parameters

In the previous section (Population Analysis), we see that there is not orbital interaction when the molecule is 3 Å away from the surface. Therefore, we report the geometrical parameters considering only C-Mg and C-M (M is a transition metal) interactions with distances less than 3 Å.
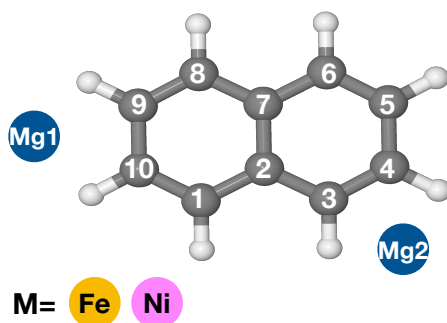
	[010]-fo	Fe-[010]-fo	Ni-[010]-fo	V_{MgO}-[010]-fo
Mg1-C9	2.73			
Mg1-C10	2.50			
Mg2-C2	2.80			
Mg2-C3	2.46	2.53		
Mg2-C4	2.59	2.50	2.44	
Mg2-C5			2.85	
M-C1		2.26	2.19	
M-C10		2.14	2.22	
M-C9		2.89	2.86	
Si-C8				1.98
O-C1				1.46
$\widehat{C4C3C2}$	120.42	120.55	119.92	120.85
$\widehat{C10C1C2}$	120.00	119.50	120.17	110.07
$\Theta(C4C3C2C1)$	173.06	179.33	179.81	-176.04
$\Theta(C10C1C2C3)$	179.30	164.75	-176.48	148.04

Figure 5.14: Schematic figure of naphthalene structure and its atomic labels interacting with Mg and transition metals atoms (Fe and Ni) on the surface. Table of bond distances (-) in Angstrom (Å), angles (⌢) and dihedral angles (Θ), in degree (°), of the interaction of naphthalene with the [010] forsterite surfaces. The missing values indicate bond distances larger than 3 Å. The geometrical parameters of this molecule adsorbed on [010]-fo, Fe-[010]-fo, and Ni-[010]-fo are calculated from the optimized geometry of prior work. [12]
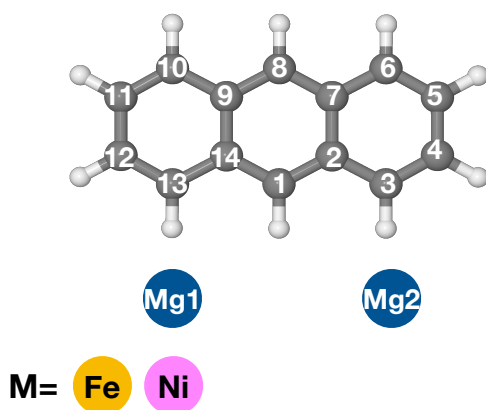
	[010]-fo	Fe-[010]-fo	Ni-[010]-fo	V_{MgO}-[010]-fo
Mg2-C2	2.63			
Mg2-C3	2.45			
Mg2-C4	2.64	2.81	2.93	
Mg2-C5				2.70
Mg1-C11		2.87	2.80	
Mg1-C12	2.75	2.43	2.46	
Mg1-C13	2.50			
Mg1-C14	2.94			
M-C14		2.65	2.58	
M-C1		2.14	2.15	
M-C2		2.42	2.51	
Si-C10				2.00
O-C13				1.46
$C12\widehat{C13}C14$	119.94	120.28	120.02	110.02
$C\widehat{14C1}C2$	121.15	121.17	121.25	121.17
$\widehat{C2C3}C4$	121.38	119.95	119.71	121.04
$\Theta(C12C13C14C1)$	-179.46	-178.41	176.72	150.19
$\Theta(C1C2C3C4)$	166.67	-174.89	-177.39	173.75

Figure 5.15: Schematic figure of anthracene structure and its atomic labels interacting with Mg and transition metals atoms (Fe and Ni) on the surface. Table of bond distances (-) in Angstrom (Å), angles (⌢) and dihedral angles (Θ), in degree (°), of the interaction of anthracene with the [010] forsterite surfaces. The missing values indicate bond distances larger than 3 Å.
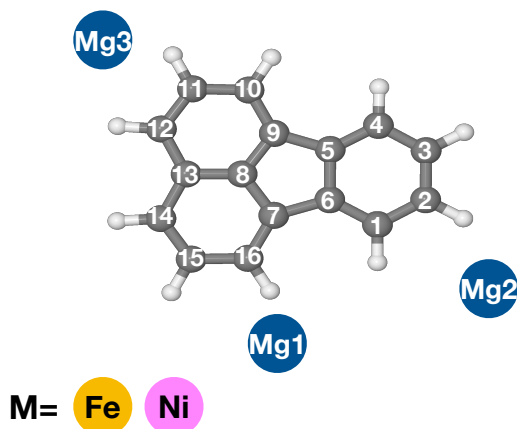
	[010]-fo	Fe-[010]-fo	Ni-[010]-fo	V$_{MgO}$-[010]-fo
Mg1-C16	2.41			
Mg1-C13				2.68
Mg1-C14				2.88
Mg1-C15	2.71			
Mg1-C7	2.71			
Mg2-C2	2.44	2.43	2.51	
Mg2-C1	2.91			
Mg2-C3	2.86	2.70	2.53	2.93
Mg3-C11	2.76	2.74		
M-C15		2.96		
M-C16		2.17		
M-C7		2.23	2.66	
M-C6		2.88		
M-C8			2.32	
M-C9			2.66	
M-C13			2.86	
Si-C1				2
O-C4				1.47
$C14\widehat{C15C}16$	122.13	122.99	122.78	123.06
$C\widehat{16C7C}6$	134.71	135.79	135.74	135.99
$C\widehat{6C1C}2$	118.24	118.46	118.58	110.57
$C14\widehat{C13C}12$	126.81	127.20	128.73	128.05
$C\widehat{13C8C}7$	124.80	124.21	124.26	125.03
$\Theta(C15C16C7C6)$	-169.04	175.58	-176.31	-179.59
$\Theta(C2C1C6C7)$	178.30	179.04	178.82	-153.39
$\Theta(C14C13C12C11)$	179.53	174.07	-176.44	178.13
$\Theta(C13C8C7C6)$	171.84	179.28	179.76	177.89

Figure 5.16: Schematic figure of fluoranthene structure and its atomic labels
interacting with Mg and transition metals atoms (Fe and Ni) on the surface. Table
of bond distances (-) in Angstrom (Å), angles (⌢) and dihedral angles (Θ), in degree
(°), of the interaction of fluoranthene with the [010] forsterite surfaces. The missing
values indicate bond distances larger than 3 Å.

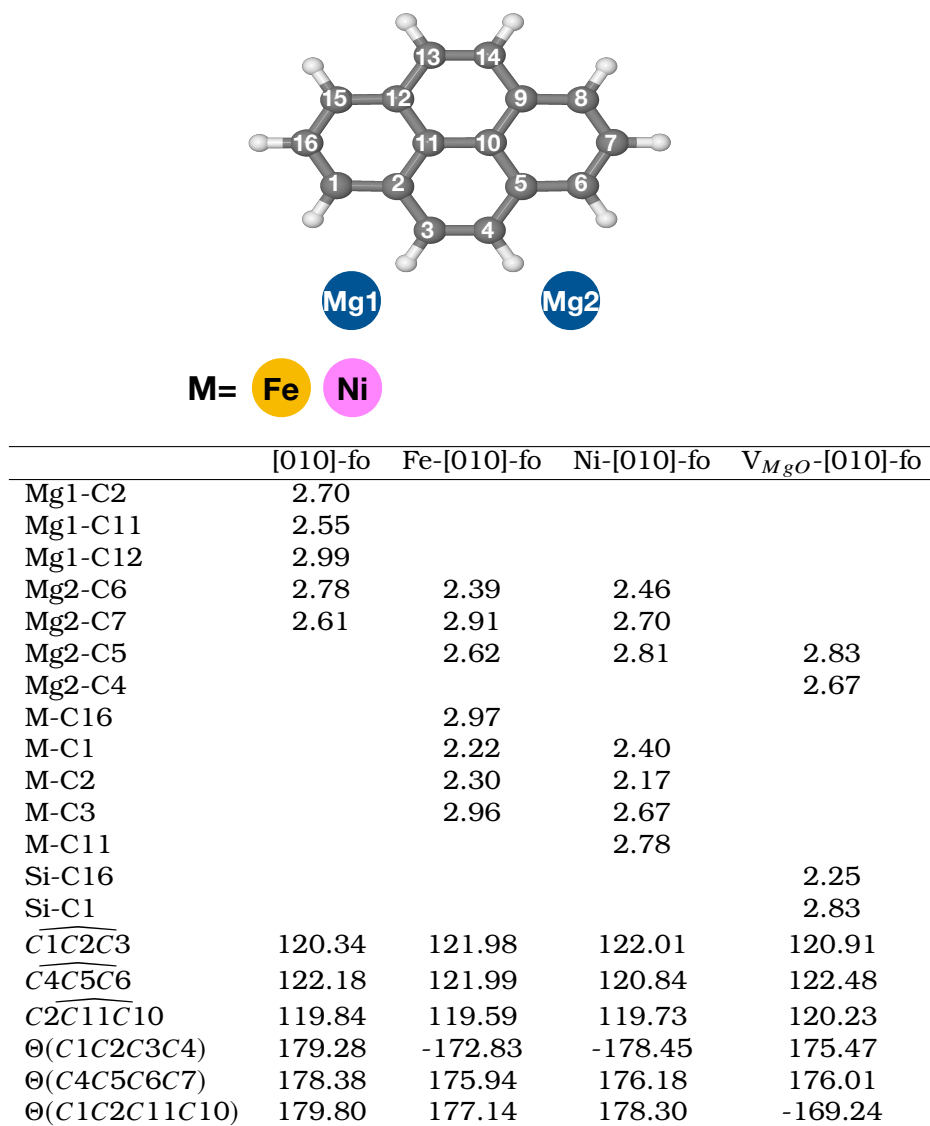|	[010]-fo	Fe-[010]-fo	Ni-[010]-fo	V_{MgO}-[010]-fo
Mg1-C2	2.70			
Mg1-C11	2.55			
Mg1-C12	2.99			
Mg2-C6	2.78	2.39	2.46	
Mg2-C7	2.61	2.91	2.70	
Mg2-C5		2.62	2.81	2.83
Mg2-C4				2.67
M-C16		2.97		
M-C1		2.22	2.40	
M-C2		2.30	2.17	
M-C3		2.96	2.67	
M-C11			2.78	
Si-C16				2.25
Si-C1				2.83
$\widehat{C1C2C3}$	120.34	121.98	122.01	120.91
$\widehat{C4C5C6}$	122.18	121.99	120.84	122.48
$\widehat{C2C11C10}$	119.84	119.59	119.73	120.23
$\Theta(C1C2C3C4)$	179.28	-172.83	-178.45	175.47
$\Theta(C4C5C6C7)$	178.38	175.94	176.18	176.01
$\Theta(C1C2C11C10)$	179.80	177.14	178.30	-169.24

Figure 5.17: Schematic figure of pyrene structure and its atomic labels interacting with Mg and transition metals atoms (Fe and Ni) on the surface. Table of bond distances (-) in Angstrom (Å), angles ($\frown$) and dihedral angles (Θ), in degree (°), of the interaction of pyrene with the [010] forsterite surfaces. The missing values indicate bond distances larger than 3 Å.

M= Fe Ni

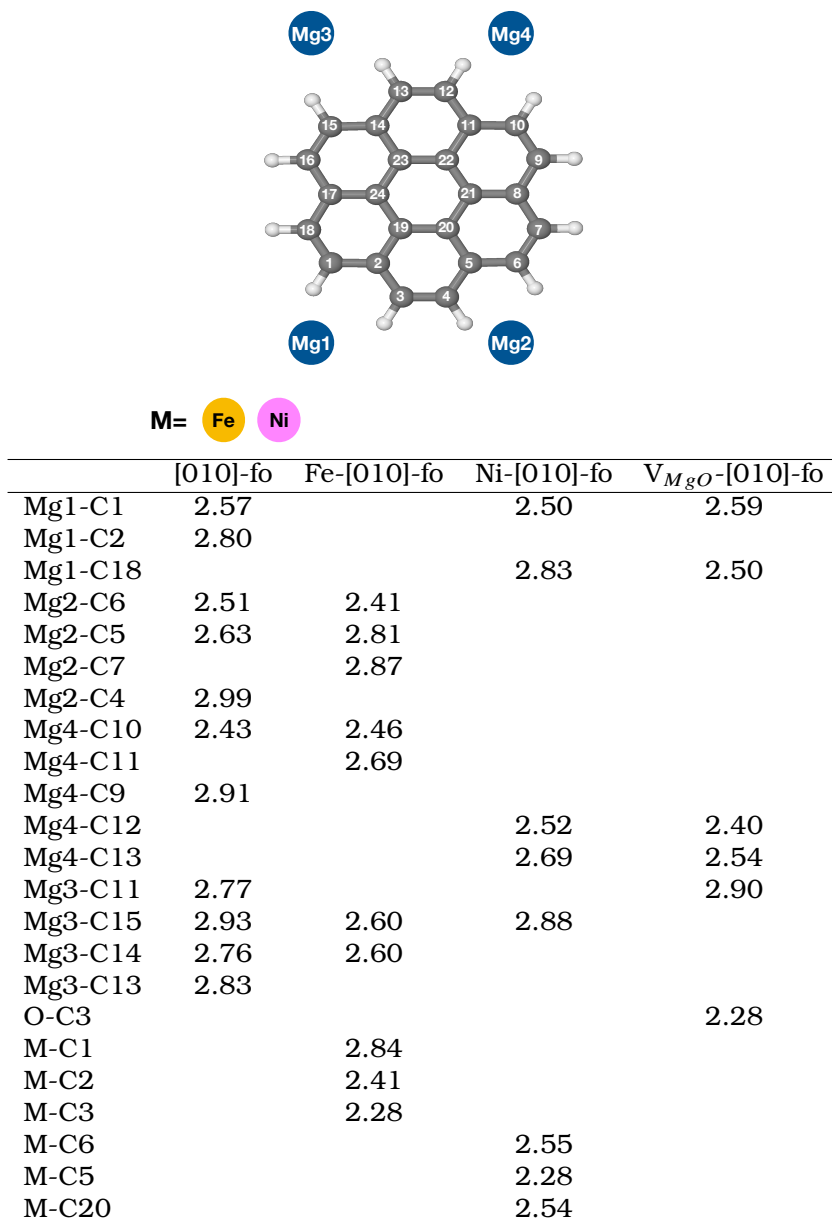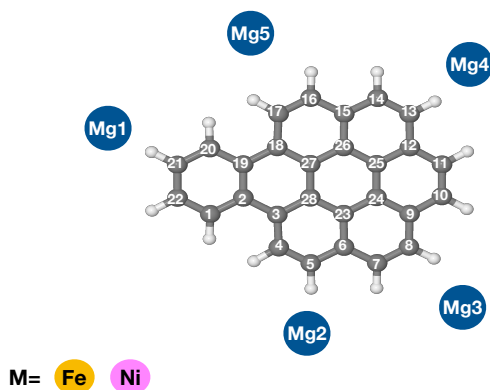|	[010]-fo	Fe-[010]-fo	Ni-[010]-fo	V_{MgO}-[010]-fo
Mg1-C1	2.57		2.50	2.59
Mg1-C2	2.80			
Mg1-C18			2.83	2.50
Mg2-C6	2.51	2.41		
Mg2-C5	2.63	2.81		
Mg2-C7		2.87		
Mg2-C4	2.99			
Mg4-C10	2.43	2.46		
Mg4-C11		2.69		
Mg4-C9	2.91			
Mg4-C12			2.52	2.40
Mg4-C13			2.69	2.54
Mg3-C11	2.77			2.90
Mg3-C15	2.93	2.60	2.88	
Mg3-C14	2.76	2.60		
Mg3-C13	2.83			
O-C3				2.28
M-C1		2.84		
M-C2		2.41		
M-C3		2.28		
M-C6			2.55	
M-C5			2.28	
M-C20			2.54	

Figure 5.18: Schematic figure of coronene structure and its atomic labels inter-
acting with Mg and transition metals atoms (Fe and Ni) on the surface. Table of
bond distances (-), in Angstrom (Å), for the interaction of coronene with the [010]
forsterite surfaces. The missing values indicate bond distances larger than 3 Å.

	[010]-fo	Fe-[010]-fo	Ni-[010]-fo	V_{MgO}-[010]-fo
$C\widehat{18C1C}2$	120.61	120.89	121	121.47
$C\widehat{5C6C}7$	121.19	121.10	120.35	120.94
$C\widehat{9C10C}11$	121.00	120.99	121.05	120.50
$C\widehat{16C15C}14$	120.88	120.63	120.86	120.96
$C\widehat{18C17C}16$	121.87	121.90	121.70	121.88
$C\widehat{17C24C}23$	119.99	120.29	119.82	119.58
$\Theta(C18C1C2C3)$	178.05	-173.03	-177.82	179.96
$\Theta(C7C6C5C4)$	173.25	170.68	-175.06	-175.68
$\Theta(C9C10C11C12)$	-170.93	-174.64	-176.72	176.45
$\Theta(C16C15C14C13)$	176.15	-178.00	-179.91	-176.78
$\Theta(C17C24C13C22)$	-179.76	177.57	-179.98	174.68

Table 5.7: Table of angles (⁀) and dihedral angles (Θ), in degree (°), of the interaction of coronene with the [010] forsterite surfaces. The atomic labels are referred to Fig. 5.18. The geometrical parameters of this molecule adsorbed on [010]-fo, Fe-[010]-fo, and Ni-[010]-fo are calculated from the optimized geometry of prior work. [12]

	[010]-fo	Fe-[010]-fo	Ni-[010]-fo	V_{MgO}-[010]-fo
$C\widehat{20C21C}22$	119.71	119.55	119.48	122.23
$C\widehat{6C5C}4$	120.91	120.80	120.58	121.35
$C\widehat{12C13C}14$	120.95	121	121	120.42
$C\widehat{17C16C}15$	120.88	120.51	120.66	120.77
$\Theta(C21C20C19C18)$	178.80	179.77	-179.28	-151.08
$\Theta(C17C16C15C14)$	174.51	-177.02	-178.34	165.39
$\Theta(C4C5C6C7)$	-175.56	-179.91	-179.92	-168.25
$\Theta(C20C19C18C17)$	-9.65	3.67	4.74	7.98
$\Theta(C1C2C3C4)$	3.87	-4.51	1.58	-1.51

Table 5.8: Table of angles (⁀) and dihedral angles (Θ), in degree (°), of the interaction of benzocoronene with the [010] forsterite surfaces. The atomic labels are referred to Fig. 5.19.

	[010]-fo	Fe-[010]-fo	Ni-[010]-fo	V_{MgO}-[010]-fo
Mg1-C21	2.59			
Mg1-C20	2.70			
Mg2-C5	2.50			
Mg2-C6	2.68			
Mg2-C22		2.70	2.74	
Mg3-C7		2.55	2.54	
Mg3-C8		2.53	2.55	
Mg3-C6		2.89	2.87	
Mg3-C24				2.67
Mg3-C25				2.61
Mg4-C13	2.54	2.50	2.51	
Mg4-C14		2.79	2.79	
Mg5-C15	2.91			
Mg5-C16	2.71	2.56	2.61	
Mg5-C17	2.62	2.76	2.73	
Mg5-C18	2.77			
Mg5-C15	2.91			
Mg5-C27	2.93			
M-C3		2.28	2.35	
M-C4		2.47	2.41	
M-C2		2.65	2.68	
Si-C20				2.02
O-C1				1.46

Figure 5.19: Schematic figure of benzocoronene structure and its atomic labels interacting with Mg and transition metals atoms (Fe and Ni) on the surface. Table of bond distances (-), in Angstrom (Å), for the interaction of benzocoronene with the [010] forsterite surfaces. The missing values indicate bond distances larger than 3 Å. The geometrical parameters of this molecule adsorbed on [010]-fo, Fe-[010]-fo, and Ni-[010]-fo are calculated from the optimized geometry of prior work. [12]
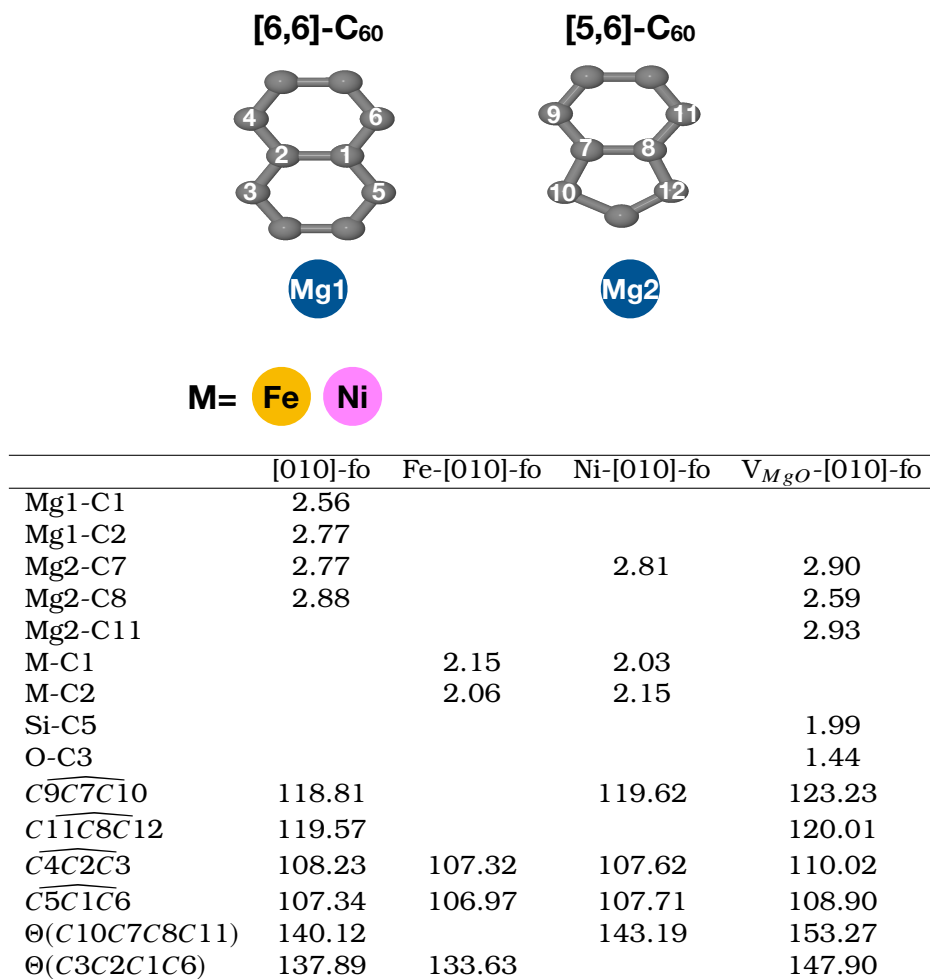
	[010]-fo	Fe-[010]-fo	Ni-[010]-fo	V_{MgO}-[010]-fo
Mg1-C1	2.56			
Mg1-C2	2.77			
Mg2-C7	2.77		2.81	2.90
Mg2-C8	2.88			2.59
Mg2-C11				2.93
M-C1		2.15	2.03	
M-C2		2.06	2.15	
Si-C5				1.99
O-C3				1.44
$\widehat{C9C7C}10$	118.81		119.62	123.23
$C1\widehat{1C8C}12$	119.57			120.01
$\widehat{C4C2C}3$	108.23	107.32	107.62	110.02
$\widehat{C5C1C}6$	107.34	106.97	107.71	108.90
$\Theta(C10C7C8C11)$	140.12		143.19	153.27
$\Theta(C3C2C1C6)$	137.89	133.63		147.90

Figure 5.20: Schematic figure of fullerene [6,6] and [6,5] ring junctions and their atomic labels interacting with Mg and transition metals atoms (Fe and Ni) on the surface. Table of bond distances (-) in Angstrom (Å), angles (⌢) and dihedral angles (Θ), in degree (°), of the interaction of fullerene with the [010] forsterite surfaces. The missing values indicate bond distances larger than 3 Å.

BIBLIOGRAPHY

[1] Usselman, M. C.; Rocke, A. J. "Chemistry". Encyclopedia Britannica, https://www.britannica.com/science/chemistry.

[2] Tielens, A. G. G. M. *Molecular Astrophysics*; Cambridge University Press, 2021.

[3] Gorbunov, D. S.; Rubakov, V. A. *Introduction to the Theory of the Early Universe*; World Scientific Publishing Company, 2011.

[4] Boxaider, G. Big Bang. 1991; http://cds.cern.ch/record/39140.

[5] Atkins, P.; Paula, J. *Atkins' physical chemistry*; Oxford University press, 2008.

[6] Tennyson, J. *Astronomical Spectroscopy: An Introduction to the Atomic and Molecular Physics of Astronomical Spectra (2ND Edition)*; 2011.

[7] Klemperer, W. *Annu. Rev. Phys. Chem* **2011**, *62*, 173–184.

[8] Tielens, A. G. G. M. *Rev. Mod. Phys.* **2013**, *85*, 1021–1081.

[9] Cuppen, H. M.; Walsh, C.; Lamberts, T.; Semenov, D.; Garrod, R. T.; Penteado, E. M.; Ioppolo, S. *Space Sci. Rev.* **2017**, *212*, 1–58.

[10] Hanefeld, U.; Lefferts, L. *Catalysis: An Integrated Textbook for Students*; WILEY-VCH Verlag GmbH Co. KGaA, Weinheim, 2008.

[11] Jensen, F. *Introduction to Computational Chemistry*; John Wiley Sons, Inc.: Hoboken, NJ, USA, 2006.

[12] Campisi, D.; Lamberts, T.; Dzade, N. Y.; Martinazzo, R.; ten Kate, I. L.; Tielens, A. G. G. M. *J. Phys. Chem. A* **2021**, *125*, 2770–2781.

[13] Pechukas, P. *Annu. Rev. Phys. Chem.* **1981**, *32*, 159–177.

[14] Tielens, A. G. G. M. *The Physics and Chemistry of the Interstellar Medium*; Cambridge University Press, 2005.

[15] Anders, E.; Hayatsu, R.; Studier, M. H. *Astrophys. J. Lett.* **1974**, *192*, L101.

[16] Campisi, D.; Candian, A. *Phys. Chem. Chem. Phys.* **2020**, *22*, 6738–6748.

[17] Rauls, E.; Hornekær, L. *Astrophys. J.* **2008**, *679*, 531–536.

[18] Ferullo, R. M.; Zubieta, C. E.; Belelli, P. G. *Phys. Chem. Chem. Phys.* **2019**, *21*, 12012–12020.

[19] Rimola, A.; Taquet, V.; Ugliengo, P.; Balucani, N.; Ceccarelli, C. *Astron. Astrophys.* **2014**, *572*, A70.

[20] Goumans, T. P. M.; Catlow, C. R. A.; Brown, W. A. *J. Chem. Phys.* **2008**, *128*, 134709.

[21] Watanabe, N.; Kouchi, A. *Astrophys. J.* **2002**, *571*, L173–L176.

[22] Shock, E. L.; Schulte, M. D. *Nature* **1990**, *343*, 728–731.

[23] Andrews, H.; Boersma, C.; Werner, M. W.; Livingston, J.; Allamandola, L. J.; Tielens, A. G. G. M. *Astrophys. J* **2015**, *807*, 99.

[24] Henning, T.; Salama, F. *Science* **1998**, *282*, 2204–2210.

[25] Allamandola, L.; Sandford, S.; Valero, G. *Icarus* **1988**, *76*, 225–252.

[26] Tielens, A. *Annu. Rev. Astron. Astrophys.* **2008**, *46*, 289–337.

[27] van Diedenhoven, B.; Peeters, E.; Van Kerckhoven, C.; Hony, S.; Hudgins, D. M.; Allamandola, L. J.; Tielens, A. G. G. M. *Astrophys. J.* **2004**, *611*, 928–939.

[28] McGuire, B. A.; Burkhardt, A. M.; Kalenskii, S.; Shingledecker, C. N.; Remijan, A. J.; Herbst, E.; McCarthy, M. C. *Science* **2018**, *359*, 202–205.

[29] Hony, S.; Van Kerckhoven, C.; Peeters, E.; Tielens, A. G. G. M.; Hudgins, D. M.; Allamandola, L. J. *Astron. Astrophys.* **2001**, *370*, 1030–1043.

[30] Zhen, J.; Castellanos, P.; Paardekooper, D. M.; Linnartz, H.; Tielens, A. G. G. M. *Astrophys. J.* **2014**, *797*, L30.

[31] Berné, O.; Tielens, A. G. G. M. *Proc. Natl. Acad. Sci. U.S.A.* **2012**, *109*, 401–406.

[32] Rapacioli, M.; Calvo, F.; Spiegelman, F.; Joblin, C.; Wales, D. J. *J. Phys. Chem. A* **2005**, *109*, 2487–2497.

[33] Wakelam, V.; Bron, E.; Cazaux, S.; Dulieu, F.; Gry, C.; Guillard, P.; Habart, E.; Hornekær, L.; Morisset, S.; Nyman, G.; Pirronello, V.; Price, S. D.; Valdivia, V.; Vidali, G.; Watanabe, N. *Mol. Astrophys.* **2017**, *9*, 1–36.

[34] Hollenbach, D. J.; Tielens, A. G. G. M. *Annu. Rev. Astron. Astrophys.* **1997**, *35*, 179–215.

[35] Draine, B. *Annu. Rev. Astron. Astrophys.* **2003**, *41*, 241–289.

[36] Navarro-Ruiz, J.; Sodupe, M.; Ugliengo, P.; Rimola, A. *Phys. Chem. Chem. Phys.* **2014**, *16*, 17447–17457.

[37] Navarro-Ruiz, J.; Ugliengo, P.; Sodupe, M.; Rimola, A. *Chem. Commun.* **2016**, *52*, 6873–6876.

[38] Ruffle, D. P.; Herbst, E. *Mon. Not. R. Astron. Soc.* **2000**, *319*, 837–850.

[39] Campisi, D.; Simonsen, F. D. S.; Thrower, J. D.; Jaganathan, R.; Hornekær, L.; Martinazzo, R.; Tielens, A. G. G. M. *Phys. Chem. Chem. Phys.* **2020**, *22*, 1557–1565.

[40] Jensen, P. A.; Leccese, M.; Simonsen, F. D. S.; Skov, A. W.; Bonfanti, M.; Thrower, J. D.; Martinazzo, R.; Hornekær, L. *Mon. Not. R. Astron. Soc.* **2019**, *486*, 5492–5498.

[41] Andrews, H.; Candian, A.; Tielens, A. G. G. M. *Astron. Astrophys.* **2016**, *595*, A23.

[42] Jones, A. P. *ESA Special Publication* **2005**, *577*, 239–244.

[43] Min, M.; Waters, L. B. F. M.; de Koter, A.; Hovenier, J. W.; Keller, L. P.; Markwick-Kemper, F. *Astron. Astrophys.* **2007**, *462*, 667–676.

[44] Brucato, J. R.; Strazzulla, G.; Baratta, G.; Colangeli, L. *Astron. Astrophys.* **2004**, *413*, 395–401.

[45] Jones, A. P.; Tielens, A. G. G. M.; Hollenbach, D. J.; McKee, C. F. *AIP Conf. Proc.* **1997**, *402*, 595–613.

[46] Ehrenfreund, P.; Charnley, S. B. *Annu. Rev. Astron. Astrophys.* **2000**, *38*, 427–483.

[47] Sephton, M. A. *Nat. Prod. Rep.* **2002**, *19*, 292–311.

[48] Aponte, J. C.; Elsila, J. E.; Glavin, D. P.; Milam, S. N.; Charnley, S. B.; Dworkin, J. P. *ACS Earth Space Chem.* **2017**, *1*, 3–13.

[49] Pizzarello, S.; Schrader, D. L.; Monroe, A. A.; Lauretta, D. S. *Proc. Natl. Acad. Sci. U.S.A* **2012**, *109*, 11949–11954.

[50] Wing, M. R.; Bada, J. L. *Orig. Life Evol. Biosph* **1991**, *21*, 375–383.

[51] Basile, B. P.; Middleditch, B. S.; Oró, J. *Org. Geochem.* **1984**, *5*, 211–216.

[52] Kalpana, M.; Babu, E.; Mani, D.; Tripathi, R.; Bhandari, N. *Planet. Space Sci.* **2021**, *198*, 105177.

[53] Huang, Y.; Aponte, J. C.; Zhao, J.; Tarozo, R.; Hallmann, C. *Earth Planet. Sci. Lett.* **2015**, *426*, 101–108.

[54] Liu, L.; Qing, M.; Wang, Y.; Chen, S. *J. Mater. Sci. Technol.* **2015**, *31*, 599–606.

[55] Brayfindley, E.; Irace, E. E.; Castro, C.; Karney, W. L. *J. Org. Chem.* **2015**, *80*, 3825–3831.

[56] Yu, H.-G.; Nyman, G. *Astrophys. J.* **2012**, *751*, 3.

[57] Stone, A. J.; Wales, D. J. *Chem. Phys. Lett.* **1986**, *128*, 501–503.

[58] Stanković, S.; Marković, S.; Gutman, I.; Sretenović, S. *J. Mol. Model.* **2010**, *16*, 1519–1527.

[59] Bollmann, W. *Crystal Defects and Crystalline Interfaces*; Springer-Verlag Berlin Heidelberg, 1970.

[60] Cortese, R.; Campisi, D.; Duca, D. *ACS Omega* **2019**, *4*, 14849–14859.

[61] Burr, P. A.; Cooper, M. W. D. *Phys. Rev. B* **2017**, *96*, 094107.

[62] Brodholt, J. P.; Refson, K. *J. Geophys. Res. Solid Earth* **2000**, *105*, 18977–18982.

[63] Marrocchi, Y.; Bekaert, D. V.; Piani, L. *Earth Planet. Sci. Lett.* **2018**, *482*, 23–32.

[64] Kohn, W.; Sham, L. J. *Phys. Rev.* **1965**, *140*, A1133–A1138.

[65] Hohenberg, P.; Kohn, W. *Phys. Rev.* **1964**, *136*, B864–B871.

[66] Blinder, S. M. *Am. J. Phys.* **1965**, *33*, 431–443.

[67] Perdew, J. P.; Schmidt, K. *AIP Conf. Proc.* **2001**, *577*, 1–20.

[68] Perdew, J. P.; Wang, Y. *Phys. Rev. B* **1992**, *45*, 13244–13249.

[69] Mattsson, A. E.; Armiento, R.; Schultz, P. A.; Mattsson, T. R. *Phys. Rev. B* **2006**, *73*, 195123.

[70] Zhang, Y.; Yang, W. *Phys. Rev. Lett.* **1998**, *80*, 890–890.

[71] Miehlich, B.; Savin, A.; Stoll, H.; Preuss, H. *Chem. Phys. Lett.* **1989**, *157*, 200–206.

[72] Dion, M.; Rydberg, H.; Schröder, E.; Langreth, D. C.; Lundqvist, B. I. *Phys. Rev. Lett.* **2004**, *92*, 246401.

[73] Klimeš, J.; Bowler, D. R.; Michaelides, A. *J. Phys. Condens. Matter* **2009**, *22*, 022201.

[74] Becke, A. D. *J. Chem. Phys.* **1993**, *98*, 5648–5652.

[75] Perdew, J. P.; Ernzerhof, M.; Burke, K. *J. Chem. Phys.* **1996**, *105*, 9982–9985.

[76] Heyd, J.; Scuseria, G. E.; Ernzerhof, M. *J. Chem. Phys.* **2006**, *124*, 219906.

[77] Zhao, Y.; Truhlar, D. G. *Theor. Chem. Account* **2008**, *120*, 215–241.

[78] Tran, F.; Blaha, P.; Schwarz, K.; Novák, P. *Phys. Rev. B* **2006**, *74*, 155108.

[79] Biczysko, M.; Bloino, J.; Puzzarini, C. *WIREs Comput. Mol. Sci.* **2018**, *8*, e1349.

[80] Check, C. E.; Gilbert, T. M. *J. Org. Chem.* **2005**, *70*, 9828–9834.

[81] Grimme, S. *Wiley Interdiscip. Rev. Comput. Mol. Sci.* **2011**, *1*, 211–228.

[82] Berland, K.; Cooper, V. R.; Lee, K.; Schröder, E.; Thonhauser, T.; Hyldgaard, P.; Lundqvist, B. I. *Rep. Prog. Phys.* **2015**, *78*, 066501.

[83] Lee, K.; Murray, E. D.; Kong, L.; Lundqvist, B. I.; Langreth, D. C. *Phys. Rev. B* **2010**, *82*, 081101.

[84] Hyldgaard, P.; Jiao, Y.; Shukla, V. *J. Phys. Condens. Matter* **2020**, *32*, 393001.

[85] Becke, A. D.; Johnson, E. R. *J. Chem. Phys.* **2005**, *123*, 154101.

[86] Frisch, M. J. et al. Gaussian 16 Revision C.01. 2016; Gaussian Inc. Wallingford CT.

[87] Aprà, E. et al. *J. Chem. Phys.* **2020**, *152*, 184102.

[88] Smith, D. G. A. et al. *J. Chem. Phys.* **2020**, *152*, 184108.

[89] Sholl, D. S.; Steckel, J. A. *Density Functional Theory A Practical Introduction*; John Wiley Sons, Ltd, 2009.

[90] Kresse, G.; Joubert, D. *Phys. Rev. B* **1999**, *59*, 1758–1775.

[91] Blöchl, P. E. *Phys. Rev. B* **1994**, *50*, 17953–17979.

[92] Kresse, G.; Furthmüller, J. *Phys. Rev. B* **1996**, *54*, 11169–11186.

[93] Giannozzi, P. et al. *J. Phys. Condens. Matter.* **2009**, *21*, 395502.

[94] Romero, A. H. et al. *J. Chem. Phys.* **2020**, *152*, 124102.

[95] Enkovaara, J. et al. *J. Phys. Condens. Matter.* **2010**, *22*, 253202.

[96] Slater, J. C.; Koster, G. F. *Phys. Rev.* **1954**, *94*, 1498–1524.

[97] Ruggiero, M. T.; Erba, A.; Orlando, R.; Korter, T. M. *Phys. Chem. Chem. Phys.* **2015**, *17*, 31023–31029.

[98] Soler, J. M.; Artacho, E.; Gale, J. D.; García, A.; Junquera, J.; Ordejón, P.; Sánchez-Portal, D. *J. Phys. Condens. Matter.* **2002**, *14*, 2745–2779.

[99] Dovesi, R.; Erba, A.; Orlando, R.; Zicovich-Wilson, C. M.; Civalleri, B.; Maschio, L.; Rérat, M.; Casassa, S.; Baima, J.; Salustro, S.; Kirtman, B. *WIREs Comput. Mol. Sci.* **2018**, *8*, e1360.

[100] Boys, S.; Bernardi, F. *Mol. Phys.* **1970**, *19*, 553–566.

[101] Sordo, J. A.; Chin, S.; Sordo, T. L. *Theor. Chem. Acc.* **1988**, *74*, 101–110.

[102] Monkhorst, H. J.; Pack, J. D. *Phys. Rev. B* **1976**, *13*, 5188–5192.

[103] Pham, H. Q.; Hermes, M. R.; Gagliardi, L. *J. Chem. Theory Comput.* **2020**, *16*, 130–140.

[104] Bisbo, M. K.; Hammer, B. *Phys. Rev. Lett.* **2020**, *124*, 086102.

[105] Candian, A.; Zhen, J.; Tielens, A. G. G. M. *Phys. Today* **2018**, *71*, 38–43.

[106] Berné, O.; Fuente, A.; Pantin, E.; Bujarrabal, V.; Baruteau, C.; Pilleri, P.; Habart, E.; Ménard, F.; Cernicharo, J.; Tielens, A. G. G. M.; Joblin, C. *Astron. Astrophys.* **2015**, *578*, L8.

[107] Beshore, E.; Lauretta, D.; Boynton, W.; Shinohara, C.; Sutter, B.; Everett, D.; Gal-Edd, J.; Mink, R.; Moreau, M.; Dworkin, J. *2015 IEEE Aerospace Conference* **2015**, 1–14.

[108] Levison, H.; Olkin, C.; Noll, K.; Marchi, S. *European Planetary Science Congress* **2017**, EPSC2017–963.

[109] Bauschlicher, Jr., C. W. *Astrophys. J.* **1998**, *509*, L125–L127.

[110] Thrower, J.; Jørgensen, B.; Friis, E.; Baouche, S.; Menella, V.; Luntz, A.; Andersen, M.; Hammer, B.; Hornekær, L. *Astrophys. J.* **2012**, *750*, 1–6.

[111] Menella, V.; Hornekær, L.; Thrower, J.; Accolla, M. *Astrophys. J. Lett.* **2012**, *745*, 1–5.

[112] Boschman, L.; Cazaux, S.; Spaans, S.; Hoekstra, M. R.; Schlathölter, T. *Astron. Astrophys.* **2015**, *579*, 1–11.

[113] Samanta, S. K.; Singh, O. V.; Jain, R. K. *Trends Biotechnol.* **2002**, *20*, 243–248.

[114] Jacinto, M. J.; Santos, O. H. C. F.; Landers, R.; Kiyohara, P. K.; Rossi, L. M. *Appl. Catal. B.* **2009**, *90*, 688–692.

[115] Segawa, Y.; Stephan, D. W. *Chem. Commun.* **2012**, *48*, 11963–11965.

[116] Scanlon, L. G.; Balbuena, P. B.; Zhang, Y.; Sandi, G.; Back, C. K.; Feld, W. A.; Mack, J.; Rottmayer, M. A.; Riepenhoff, J. L. *J. Phys. Chem. B* **2006**, *110*, 7688–7694.

[117] Knipp, D.; Street, R. A.; Völkel, A.; Ho, J. *J. Appl. Phys.* **2003**, *93*, 347–355.

[118] Anthony, J. E. *Chem. Rev.* **2006**, *106*, 5028–5048.

[119] Samorí, P.; Severin, N.; Simpson, C. D.; Müllen, K.; Rabe, J. P. *J. Am. Chem. Soc.* **2002**, *124*, 9454–9457.

[120] Pisula, W.; Feng, X.; Müllen, K. *Chem. Mater.* **2011**, *23*, 554–567.

[121] Bettinger, H. F.; Tönshoff, C. *Chem. Rec.* **2015**, *15*, 364–369.

[122] Salama, F.; Bakes, E. L. O.; Allamandola, L. J.; Tielens, A. G. G. M. *Astrophys. J.* **1996**, *458*, 621–636.

[123] Candian, A.; Sarre, P. J. *Mon. Notices Royal Astron. Soc.* **2015**, *448*, 2960–2970.

[124] Rasmussen, J. A. *J. Phys. Chem. A* **2013**, *117*, 4279–4285.

[125] Joblin, C.; Tielens, A. G. G. M.; Thrower, J. D.; Nilsson, L.; Jørgensen, B.; Baouche, S.; Balog, R.; Luntz, A. C.; Stensgaard, I.; Rauls, E.; Hornekær, L. *EAS Publications Series* **2011**, *46*, 453–460.

[126] Habart, E.; Boulanger, F.; Verstraete, L.; Walmsley, C. M.; Pineau des Forêts, G. *Astron. Astrophys.* **2004**, *414*, 531–544.

[127] Skov, A. L.; Thrower, J. D.; Hornekær, L. *Faraday Discuss.* **2014**, *168*, 223–234.

[128] Rasmussen, J. A.; Henkelman, G.; Hammer, B. *J. Chem. Phys.* **2011**, *134*, 164703.

[129] Cazaux, S.; Boschman, L.; Rougeau, N.; Reitsma, G.; Hoekstra, R.; Teillet-Billy, D.; Morisset, S.; Spaans, M.; Schlathölter, T. *Sci. Rep.* **2016**, *6*, 1–7.

[130] Tschersich, K. *J. Appl. Phys.* **2000**, *87*, 2565–2573.

[131] Frisch, M. J. et al. Gaussian 16, Revision A.03, Gaussian, Inc., Wallingford CT, 2016.

[132] Jensen, F. *J. Chem. Theory Comput.* **2014**, *10*, 1074–1085.

[133] Schlegel, H. B. *J. Comput. Chem.* **1982**, *3*, 214–218.

[134] Simon, S.; Duran, M.; Dannenberg, J. J. *J. Chem. Phys.* **1996**, *105*, 11024–11031.

[135] Schaftenaar, G.; Vlieg, E.; Vriend, G. *J. Comput.-Aided Mol. Des.* **2017**, *31*, 789–800.

[136] Schaftenaar, G.; Noordik, J. H. *J. Comput.-Aided Mol. Des.* **2000**, *14*, 123–134.

[137] Bonfanti, M.; Casolo, S.; Tantardini, G. F.; Ponti, A.; Martinazzo, R. *J. Chem. Phys.* **2011**, *135*, 164701.

[138] Bell, R. P. *Proc. R. Soc. Lond. A.* **1936**, *154*, 414–429.

[139] Evans, M. G.; Polanyi, M. *Trans. Faraday Soc.* **1938**, *34*, 11–24.

[140] Jurchescu, O. D.; Baas, J.; Palstra, T. T. *Appl. Phys. Lett.* **2004**, *84*, 3061–3063.

[141] De Angelis, F.; Gaspari, M.; Procopio, A.; Cuda, G.; Di Fabrizio, E. *Chem. Phys. Lett.* **2009**, *468*, 193–196.

[142] Roberson, L. B.; Kowalik, J.; Tolbert, L. M.; Kloc, C.; Zeis, R.; Chi, X.; Fleming, R.; Wilkins, C. *J. Am. Chem. Soc.* **2005**, *127*, 3069–3075.

[143] Klærke, B.; Toker, Y.; Rahbek, D. B.; Hornekær, L.; Andersen, L. H. *Astron. Astrophys.* **2013**, *549*, 1–9.

[144] Sánchez-Sánchez, C.; Ignacio Martínez, J. I.; del Arbol, N. R.; Ruffieux, P.; Roman Fasel, R.; López, M. F.; de Andres, P. L.; Martín-Gago, j. A. *J. Am. Chem. Soc.* **2019**, *141*, 3550–3557.

[145] Ricca, A.; Bakes, E. L. O.; Bauschlicher, Jr., C. W. *Astrophys. J* **2007**, *659*, 858–861.

[146] Hollenbach, D. J.; Tielens, A. G. G. M. *Rev. Mod. Phys.* **1999**, *71*, 173–230.

[147] Castellanos, P.; Candian, A.; Zhen, J.; Linnartz, H.; Tielens, A. G. G. M. *Astron. Astrophys* **2018**, *616*, A166.

[148] Montillaud, J.; Joblin, C.; Toublanc, D. *Astron. Astrophys.* **2013**, *552*, A15.

[149] Page, V. L.; Snow, T. P.; Bierbaum, V. M. *Astrophys. J.* **2009**, *704*, 274–280.

[150] Boersma, C.; Bregman, J.; Allamandola, L. J. *Astrophys. J.* **2018**, *858*, 67.

[151] Pety, J.; Teyssier, D.; Fossé, D.; Gerin, M.; Roueff, E.; Abergel, A.; Habart, E.; Cernicharo, J. *Astron. Astrophys.* **2005**, *435*, 885–899.

[152] Foley, N.; Cazaux, S.; Egorov, D.; Boschman, L. M. P. V.; Hoekstra, R.; Schlathölter, T. *Mon. Notices Royal Astron. Soc.* **2018**, *479*, 649–656.

[153] Castellanos, P.; Candian, A.; Andrews, H.; Tielens, A. G. G. M. *Astron. Astrophys.* **2018**, *616*, A167.

[154] Bettinger, H. F. *J. Phys. Chem. B* **2005**, *109*, 6922–6924.

[155] Pokropivny, V. V.; Ivanovskii, A. L. *Russ. Chem. Rev.* **2008**, *77*, 837–873.

[156] Rodrigues, J. N. B.; Goncalves, P.; Rodrigues, N. F. G.; Ribeiro, R. M.; Lopes dos Santos, J. M. B.; Peres, N. M. R. *Phys. Rev. B* **2011**, *84*, 155435.

[157] Ma, J.; Alfé, D.; Michaelides, A.; Wang, E. *Phys. Rev. B* **2009**, *80*, 033407.

[158] Eggen, B. R.; Heggie, M. I.; Jungnickel, G.; Latham, C. D.; Jones, R.; Briddon, P. R. *Sci.* **1996**, *272*, 87–90.

[159] Qi, X.; Guo, X.; Zheng, C. *App. Surf. Sci.* **2012**, *259*, 195–200.

[160] Duplock, E. J.; Scheffler, M.; Lindan, P. J. D. *Phys. Rev. Lett.* **2004**, *92*, 225502.

[161] Nascimento, A. J. M.; Nunes, R. W. *Nanotechnology* **2013**, *24*, 435707.

[162] Yu, H.; Nyman, G. *Astrophys. J.* **2012**, *751*, 1–7.

[163] Oettl, S.; Huber, S. E.; Kimeswenger, S.; Probst, M. *Astron. Astrophys.* **2014**, *568*, 1–8.

[164] Yamanaka, S.; Kawakami, T.; Nagao, H.; Yamaguchi, K. *Chem. Phys. Lett.* **1994**, *231*, 25–33.

[165] Letardi, S.; Celino, M.; Cleri, F.; Rosato, V. *Surf. Sci.* **2002**, *496*, 33–38.

[166] Sebree, J. A.; Kislov, V. V.; Mebel, A. M.; Zwier, T. S. *J. Phys. Chem. A* **2010**, *114*, 6255–6262.

[167] Denis, P. A.; Iribarne, F. *J Mol.Struc.: THEOCHEM* **2009**, *907*, 93 – 103.

[168] Mardirossian, N.; Head-Gordon, M. *J. Chem. Theory Comput.* **2016**, *12*, 4303–4325.

[169] Bonfanti, M.; Martinazzo, R.; Tantardini, G. F.; Ponti, A. *J. Phys. Chem. C* **2007**, *111*, 5825–5829.

[170] Hornekær, L.; Šljivančanin, Z.; Xu, W.; Otero, R.; Rauls, E.; Stensgaard, I.; Lægsgaard, E.; Hammer, B.; Besenbacher, F. *Phys. Rev. Lett.* **2006**, *96*, 156104.

[171] Petucci, J.; Semone, S.; LeBlond, C.; Karimi, M.; Vidali, G. *J. Chem. Phys.* **2018**, *149*, 014702.

[172] Ricca, A.; Bauschlicher, C. W.; Jr,; Allamandola, L. J. *Astrophys. J.* **2011**, *729*, 94.

[173] Frenklach, M. *Phys. Chem. Chem. Phys* **2002**, *4*, 2028–2037.

[174] Cherchneff, I. *EAS Publ. Ser.* **2011**, *46*, 177–189.

[175] Baer, T.; Mayer, P. M. *J. Am. Soc. Mass Spectrom.* **1997**, *8*, 103–115.

[176] Zewail, A. H. *Femtochemistry: Ultrafast Dynamics of the Chemical Bond*; pp 3–22.

[177] Postma, J. *Interaction Dynamics in Collisions of Ions with Molecules and Clusters*. Ph.D. thesis, Rijksuniversiteit Groningen, 2011.

[178] Huber, S. E.; Mauracher, A.; Probst, M. *AIP Adv.* **2013**, *3*, 122104.

[179] Vala, M.; Szczepanski, J.; Oomens, J.; Steill, J. D. *J. Am. Chem. Soc.* **2009**, *131*, 5784–5791.

[180] Szczepanski, J.; Oomens, J.; Steill, J. D.; Vala, M. T. *Astrophys. J.* **2011**, *727*, 12.

[181] Pilleri, P.; Joblin, C.; Boulanger, F.; Onaka, T. *Astron. Astrophys.* **2015**, *577*, A16.

[182] Trinquier, G.; Simon, A.; Rapacioli, M.; Gadéa, F. X. *Molecular Astrophysics* **2017**, *7*, 27–36.

[183] Wiersma, S. D.; Candian, A.; Bakker, J. M.; Martens, J.; Berden, G.; Oomens, J.; Buma, W. J.; Petrignani, A. *Astron. Astrophys.* **2020**, *635*, A9.

[184] Bauschlicher, C. W.; Ricca, A.; Boersma, C.; Allamandola, L. J. *Astrophys. J., Suppl. Ser.* **2018**, *234*, 32.

[185] Sephton, M. In *Treatise on Geochemistry (Second Edition)*, second edition ed.; Holland, H. D., Turekian, K. K., Eds.; Elsevier: Oxford, 2014; pp 1–31.

[186] Sánchez, M.; Ruette, F. *Chem. Phys. Lett.* **2020**, *738*, 136913.

[187] Bohme, D. K. *Chem. Rev.* **1992**, *92*, 1487–1508.

[188] Ehrenfreund, P.; Rasmussen, S.; Cleaves, J.; Chen, L. *Astrobiology* **2006**, *6*, 490–520.

[189] Watanabe, N.; Kouchi, A. *Prog. Surf. Sci.* **2008**, *83*, 439–489.

[190] Fedoseev, G.; Cuppen, H. M.; Ioppolo, S.; Lamberts, T.; Linnartz, H. *Mon. Not. R. Astron. Soc.* **2015**, *448*, 1288–1297.

[191] Chuang, K. J.; Fedoseev, G.; Qasim, D.; Ioppolo, S.; van Dishoeck, E. F.; Linnartz, H. *Mon. Not. R. Astron. Soc.* **2017**, *467*, 2552–2565.

[192] Álvarez Barcia, S.; Russ, P.; Kästner, J.; Lamberts, T. *Mon. Not. R. Astron. Soc.* **2018**, *479*, 2007–2015.

[193] Butscher, T.; Duvernay, F.; Danger, G.; Torro, R.; Lucas, G.; Carissan, Y.; Hagebaum-Reignier, D.; Chiavassa, T. *Mon. Not. R. Astron. Soc.* **2019**, *486*, 1953–1963.

[194] Cherchneff, I.; Barker, J. R.; Tielens, A. G. G. M. *Astrophys. J.* **1992**, *401*, 269.

[195] Frenklach, M.; Feigelson, E. D. *Astrophys. J.* **1989**, *341*, 372.

[196] Joblin, C.; Tielens, A.; Cherchneff, I. *EAS Publ. Ser.* **2011**, *46*, 177–189.

[197] Bernstein, M. P.; Elsila, J. E.; Dworkin, J. P.; Sandford, S. A.; Alla-
mandola, L. J.; Zare, R. N. *Astrophys. J.* **2002**, *576*, 1115–1120.

[198] Cook, A. M.; Ricca, A.; Mattioda, A. L.; Bouwman, J.; Roser, J.;
Linnartz, H.; Bregman, J.; Allamandola, L. J. *Astrophys. J.* **2015**,
799, 14.

[199] Brittain, D. R. B.; Lin, C. Y.; Gilbert, A. T. B.; Izgorodina, E. I.; Gill, P.
M. W.; Coote, M. L. *Phys. Chem. Chem. Phys.* **2009**, *11*, 1138–1142.

[200] Kresse, G.; Hafner, J. *Phys. Rev. B* **1993**, *47*, 558–561.

[201] Kresse, G.; Hafner, J. *Phys. Rev. B* **1994**, *49*, 14251–14269.

[202] Kresse, G.; Furthmüller, J. *Comput. Mater. Sci.* **1996**, *6*, 15–50.

[203] Rimola, A.; Sodupe, M.; Ugliengo, P. *Life (Basel, Switzerland)* **2019**,
9, 10.

[204] Salvador, P.; Paizs, B.; Duran, M.; Suhai, S. *J. Comput. Chem.* **2001**,
22, 765–786.

[205] Grimme, S.; Antony, J.; Ehrlich, S.; Krieg, H. *J. Chem. Phys.* **2010**,
132, 154104.

[206] Caldeweyher, E.; Ehlert, S.; Hansen, A.; Neugebauer, H.; Spicher, S.;
Bannwarth, C.; Grimme, S. *J. Chem. Phys.* **2019**, *150*, 154122.

[207] Hamada, I. *Phys. Rev. B* **2014**, *89*, 121103.

[208] Buimaga-Iarinca, L.; Morari, C. *Theor. Chem. Acc.* **2014**, *133*, 1502.

[209] Demichelis, R.; Bruno, M.; Massaro, F. R.; Prencipe, M.;
De La Pierre, M.; Nestola, F. *J. Comput. Chem.* **2015**, *36*, 1439–1445.

[210] Perdew, J. P.; Burke, K.; Ernzerhof, M. *Phys. Rev. Lett.* **1996**, *77*,
3865–3868.

[211] Garrod, R. T.; Widicus Weaver, S. L. *Chemical Reviews* **2013**, *113*,
8939–8960.

[212] Suhasaria, T.; Thrower, J. D.; Zacharias, H. *Mon. Not. R. Astron. Soc.*
2017, *472*, 389–399.

[213] Navarro-Ruiz, J.; Ugliengo, P.; Rimola, A.; Sodupe, M. *J. Phys. Chem.
A* **2014**, *118*, 5866–5875.

[214] Becker, L.; Glavin, D. P.; Bada, J. L. *Geochim. Cosmochim. Acta* **1997**,
61, 475–481.

[215] de Leeuw, N. H.; Parker, S. C.; Catlow, C. R. A.; Price, G. D. *Phys.
Chem. Miner.* **2000**, *27*, 332–341.

[216] Watson, G. W.; Oliver, P. M.; Parker, S. C. *Phys. Chem. Miner.* **1997**, *25*, 70–78.

[217] de Leeuw, N. H. *J. Phys. Chem. B* **2001**, *105*, 9747–9754.

[218] Rimola, A.; Trigo-Rodríguez, J. M.; Martins, Z. *Phys. Chem. Chem. Phys.* **2017**, *19*, 18217–18231.

[219] Asaduzzaman, A.; Zega, T.; Laref, S.; Runge, K.; Deymier, P.; Muralidharan, K. *Earth Planet. Sci. Lett.* **2014**, *408*, 355–361.

[220] Watson, G. W.; Kelsey, E. T.; de Leeuw, N. H.; Harris, D. J.; Parker, S. C. *J. Chem. Soc., Faraday Trans.* **1996**, *92*, 433–438.

[221] Caldeweyher, E.; Bannwarth, C.; Grimme, S. *J. Chem. Phys.* **2017**, *147*, 034112.

[222] Caldeweyher, E.; Mewes, J.-M.; Ehlert, S.; Grimme, S. *Phys. Chem. Chem. Phys.* **2020**, *22*, 8499–8512.

[223] Grimme, S.; Ehrlich, S.; Goerigk, L. *J. Comput. Chem.* **2011**, *32*, 1456–1465.

[224] Smith, D. G. A.; Burns, L. A.; Patkowski, K.; Sherrill, C. D. *J. Phys. Chem. Lett.* **2016**, *7*, 2197–2203.

[225] Risthaus, T.; Grimme, S. *J. Chem. Theory Comput.* **2013**, *9*, 1580–1591.

[226] Dudarev, S. L.; Botton, G. A.; Savrasov, S. Y.; Humphreys, C. J.; Sutton, A. P. *Phys. Rev. B* **1998**, *57*, 1505–1509.

[227] Shankland, T. J. *Science* **1968**, *161*, 51–53.

[228] Smyth, J. R.; Hazen, R. M. *Am. Mineral.* **1973**, *58*, 588–593.

[229] Morin, F. J.; Oliver, J. R.; Housley, R. M. *Phys. Rev. B* **1979**, *19*, 2886–2894.

[230] Nitsan, U.; Shankland, T. J. *Geophys. J. Int.* **1976**, *45*, 59–87.

[231] Guan, S.-H.; Zhang, X.-J.; Liu, Z.-P. *J. Phys. Chem. C* **2016**, *120*, 25110–25116.

[232] Kirfel, A.; Lippmann, T.; Blaha, P.; Schwarz, K.; Cox, D. F.; Rosso, K. M.; Gibbs, G. V. *Phys. Chem. Miner.* **2005**, *32*, 301–313.

[233] Bruno, M.; Massaro, F. R.; Prencipe, M.; Demichelis, R.; De La Pierre, M.; Nestola, F. *J. Phys. Chem. C* **2014**, *118*, 2498–2506.

[234] Geng, M.; Jónsson, H. *J. Phys. Chem. C* **2019**, *123*, 464–472.

[235] Garcia-Gil, S.; Teillet-Billy, D.; Rougeau, N.; Sidis, V. *J. Phys. Chem. C* **2013**, *117*, 12612–12621.

[236] Fei, H.; Katsura, T. *Phys. Chem. Miner.* **2016**, *43*, 119–126.

[237] Weinbruch, S.; Palme, H.; Spettel, B. *Meteorit. Planet. Sci.* **2000**, *35*, 161–171.

[238] Palme, H.; Lodders, K.; Jones, A. In *Treatise on Geochemistry (Second Edition)*, second edition ed.; Holland, H. D., Turekian, K. K., Eds.; Elsevier: Oxford, 2014; pp 15–36.

[239] Westphal, A. J. et al. *Science* **2014**, *345*, 786–791.

[240] Demircan, C. A.; Bozkaya, U. *J. Phys. Chem. A* **2017**, *121*, 6500–6509.

[241] Kolakkandy, S.; Pratihar, S.; Aquino, A. J. A.; Wang, H.; Hase, W. L. *J. Phys. Chem. A* **2014**, *118*, 9500–9511.

[242] Kulik, H. J. *J. Chem. Phys.* **2015**, *142*, 240901.

[243] Schröder, H.; Creon, A.; Schwabe, T. *J. Chem. Theory Comput.* **2015**, *11*, 3163–3170.

[244] Dang, Y.; Liu, Y.; Feng, X.; Chen, X.; Yang, C. *Appl. Surf. Sci.* **2019**, *486*, 137–143.

[245] Ehrlich, S.; Moellmann, J.; Grimme, S. *Acc. Chem. Res.* **2013**, *46*, 916–926.

[246] Lee, K.; Yu, J.; Morikawa, Y. *Phys. Rev. B* **2007**, *75*, 045402.

[247] Langhoff, S. R. *J. Phys. Chem.* **1996**, *100*, 2819–2841.

[248] Mackie, C. J.; Candian, A.; Huang, X.; Maltseva, E.; Petrignani, A.; Oomens, J.; Buma, W. J.; Lee, T. J.; Tielens, A. G. G. M. *Phys. Chem. Chem. Phys.* **2018**, *20*, 1189–1197.

[249] Parshall, G. W. *Science* **1980**, *208*, 1221–1224.

[250] Nakao, Y.; Kashihara, N.; Kanyiva, K. S.; Hiyama, T. *J. Am. Chem. Soc.* **2008**, *130*, 16170–16171.

[251] Davico, G. E.; Bierbaum, V. M.; DePuy, C. H.; Ellison, G. B.; Squires, R. R. *J. Am. Chem. Soc.* **1995**, *117*, 2590–2599.

[252] Arndtsen, B. A.; Bergman, R. G.; Mobley, T. A.; Peterson, T. H. *Acc. Chem. Res.* **1995**, *28*, 154–162.

[253] Thalji, R. K.; Ahrendt, K. A.; Bergman, R. G.; Ellman, J. A. *J. Am. Chem. Soc.* **2001**, *123*, 9692–9693.

[254] Jia, C.; Piao, D.; Oyamada, J.; Lu, W.; Kitamura, T.; Fujiwara, Y. *Science* **2000**, *287*, 1992–1995.

[255] Gorelsky, S. I. *Coord. Chem. Rev.* **2013**, *257*, 153–164.

[256] Cho, J.-Y.; Tse, M. K.; Holmes, D.; Maleczka, R. E.; Smith, M. R. *Science* **2002**, *295*, 305–308.

[257] Stephan, D.; Erker, G. *Angew. Chem. Int. Ed.* **2010**, *49*, 46–76.

[258] Légaré, M.-A.; Courtemanche, M.-A.; Rochette, É.; Fontaine, F.-G. *Science* **2015**, *349*, 513–516.

[259] Abu El-Rub, Z.; Bramer, E. A.; Brem, G. *Ind. Eng. Chem. Res.* **2004**, *43*, 6911–6919.

[260] James Cleaves II, H.; Michalkova Scott, A.; Hill, F. C.; Leszczynski, J.; Sahai, N.; Hazen, R. *Chem. Soc. Rev.* **2012**, *41*, 5502–5525.

[261] Zamirri, L.; Corno, M.; Rimola, A.; Ugliengo, P. *ACS Earth Space Chem.* **2017**, *1*, 384–398.

[262] Li, Q.; Dai, W.; Liu, B.; Sarre, P.; Xie, M.; Cheung, A.-C. *Mol. Astrophys.* **2018**, *13*, 22–29.

[263] Ferrante, R.; Moore, M.; Nuth, J.; Smith, T. *Icarus* **2000**, *145*, 297–300.

[264] Quadery, A. H.; Pacheco, S.; Au, A.; Rizzacasa, N.; Nichols, J.; Le, T.; Glasscock, C.; Schelling, P. K. *J. Geophys. Res. Planets* **2015**, *120*, 643–661.

[265] Schwartz, K.; Lang, M. In *Encyclopedia of Geochemistry: A Comprehensive Reference Source on the Chemistry of the Earth*; White, W. M., Ed.; Springer International Publishing: Cham, 2016; pp 1–5.

[266] Cami, J. *Proc. Int. Astron. Union.* **2013**, *9*, 370–374.

[267] Maier, J. P.; Campbell, E. K. *Angew. Chem. Int. Ed.* **2017**, *56*, 4920–4929.

[268] Radzig, V. In *Physico-Chemical Phenomena in Thin Films and at Solid Surfaces*; Trakhtenberg, L. I., Lin, S. H., Ilegbusi, O. J., Eds.; Thin Films and Nanostructures; Academic Press, 2007; Vol. 34; pp 231–345.

[269] Liu, D. C.; Nocedal, J. *Math. Program.* **1989**, *45*, 503–528.

[270] Fonseca Guerra, C.; Handgraaf, J.-W.; Baerends, E. J.; Bickelhaupt, F. M. *J. Comput. Chem.* **2004**, *25*, 189–210.

[271] Henkelman, G.; Uberuaga, B. P.; Jónsson, H. *J. Chem. Phys.* **2000**, *113*, 9901–9904.

[272] Larsen, A. H. et al. *J. Phys. Condens. Matter* **2017**, *29*, 273002.

[273] Bahn, S. R.; Jacobsen, K. W. *Comput. Sci. Eng.* **2002**, *4*, 56–66.

[274] Bitzek, E.; Koskinen, P.; Gähler, F.; Moseler, M.; Gumbsch, P. *Phys. Rev. Lett.* **2006**, *97*, 170201.

[275] Garrido Torres, J. A.; Jennings, P. C.; Hansen, M. H.; Boes, J. R.; Bligaard, T. *Phys. Rev. Lett.* **2019**, *122*, 156001.

[276] Brodholt, J. *Am. Mineral.* **1997**, *82*, 1049–1053.

[277] Stoneham, A. M. *Contemporary Physics* **1979**, *20*, 535–545.

[278] Rodríguez-Fortea, A.; Irle, S.; Poblet, J. M. *WIREs Comput. Mol. Sci.* **2011**, *1*, 350–367.

[279] Simon, A.; Joblin, C. *J. Phys. Chem. A* **2007**, *111*, 9745–9755.

[280] Schwieger, S.; Wagner, C.; Bruhn, C.; Schmidt, H.; Steinborn, D. *Z. Anorg. Allg. Chem.* **2005**, *631*, 2696–2704.

[281] Russell D. Johnson III, *NIST Computational Chemistry Comparison and Benchmark Database*, NIST Standard Reference Database Number 101, Release 21. 2020.

[282] Rokob, T. A.; Bakó, I.; Stirling, A.; Hamza, A.; Pápai, I. *J. Am. Chem. Soc.* **2013**, *135*, 4425–4437.

[283] Fukui, K.; Yonezawa, T.; Shingu, H. *J. Chem. Phys.* **1952**, *20*, 722–725.

[284] Reddy, V.; Dunn, T. L.; Thomas, C. A.; Moskovitz, N. A.; Burbine, T. H. *Asteroids IV*; 2015; pp 43–63.

[285] Draine, B. T. *Interstellar extinction in the infrared. Infrared Spectroscopy in Astronomy.* 1989; p 93.

[286] Kemper, F.; Vriend, W. J.; Tielens, A. G. G. M. *Astrophys. J.* **2004**, *609*, 826–837.

[287] Zeegers, S. T.; Costantini, E.; Rogantini, D.; de Vries, C. P.; Mutschke, H.; Mohr, P.; de Groot, F.; Tielens, A. G. G. M. *Astron. Astrophys.* **2019**, *627*, A16.

[288] Molster, F.; Kemper, C. *Space Sci. Rev.* **2005**, *119*, 3–28.

[289] Bringa, E. M.; Kucheyev, S. O.; Loeffler, M. J.; Baragiola, R. A.; Tielens, A. G. G. M.; Dai, Z. R.; Graham, G.; Bajt, S.; Bradley, J. P.; Dukes, C. A.; Felter, T. E.; Torres, D. F.; van Breugel, W. *Astrophys. J.* **2007**, *662*, 372–378.

[290] Carrez, P.; Demyk, K.; Cordier, P.; Gengembre, L.; Grimblot, J.; D'hendecourt, L.; Jones, A. P.; Leroux, H. *Meteorit. Planet. Sci.* **2002**, *37*, 1599–1614.

[291] Henning, T. *Annu. Rev. Astron. Astrophys.* **2010**, *48*, 21–46.

[292] Rapacioli, M.; Joblin, C.; Boissel, P. *Astron. Astrophys.* **2005**, *429*, 193–204.

[293] Lodders, K. *Astrophys. J.* **2003**, *591*, 1220–1247.

[294] Anders, E.; Grevesse, N. *Geochim. Cosmochim. Acta* **1989**, *53*, 197–214.

[295] Hammond, M. R.; Zare, R. N. *Geochim. Cosmochim. Acta* **2008**, *72*, 5521–5529.

[296] Allain, T.; Leach, S.; Sedlmayr, E. *Astron. Astrophys.* **1996**, *305*, 602.

[297] Hughbanks, T.; Hoffmann, R. *J. Am. Chem. Soc.* **1983**, *105*, 3528–3537.

Ons heelal lijkt een donkere en lege ruimte. Het heelal is echter de omgeving van een verscheidenheid aan moleculen die bijdragen aan de vorming van sterrenstelsels, zonnestelsels en planeten. Moleculen die bestaan uit een koolstofskelet dat eruitziet als een honingraat (zeshoek) met waterstofatomen aan hun randen worden polycyclische aromatische koolwaterstoffen" (namelijk paks) genoemd. Paks zijn alom vertegenwoordigd in het heelal (een voorbeeld van paks worden getoond in Fig. 5.21) en slaan een belangrijk deel van het atoom koolstof (ongeveer 20 %) op. Daarnaast helpen paks om het fysische en chemische evenwicht in bepaalde delen van het heelal te bewaren. Paks worden waarschijnlijk gevormd in de omgeving van koolstofrijke sterren. Echter, toekomstig waarnemingen, experimenteel, en theoretisch onderzoek zijn nodig om paks volledig te begrijpen.

Het bestuderen van hoe moleculen reageren in het heelal is onmisbaar om belangrijke fysische en chemische processen te begrijpen, evenals hoe leven is ontstaan. De veronderstelde routes voor de vorming van organische moleculen in de ruimte zijn onderverdeeld in onderop en bovenaf benaderingen. De onderop chemie bestaat uit het bouwen van ingewikkelde moleculen beginnend met een klein molecuul of een atoom, welke een groter molecuul vormen. De bovenaf benadering bestaat uit het vormen van ingewikkelde moleculen die grote moleculen opsplitsen in kleinere. Het afbraakproces kan plaatsvinden door energetische processen zoals straling.

Ons heelal is een genadeloze omgeving waarin buitengewone fysieke omstandigheden chemische processen kunnen belemmeren.

Sommige moleculen en vaste materialen (bv. mineralen) zijn in staat om de energie van een chemische reactie te verlagen, een stof die de energie van een chemische reactie beïnvloedt wordt een katalysator genoemd en de bijbehorende chemische reactie wordt katalyse genoemd. Van paks is bekend dat ze moleculaire oppervlakken bieden (proces 1 in Fig. 5.21) waarop kleine atomen, zoals de veel voorkomende waterstofatomen, elkaar
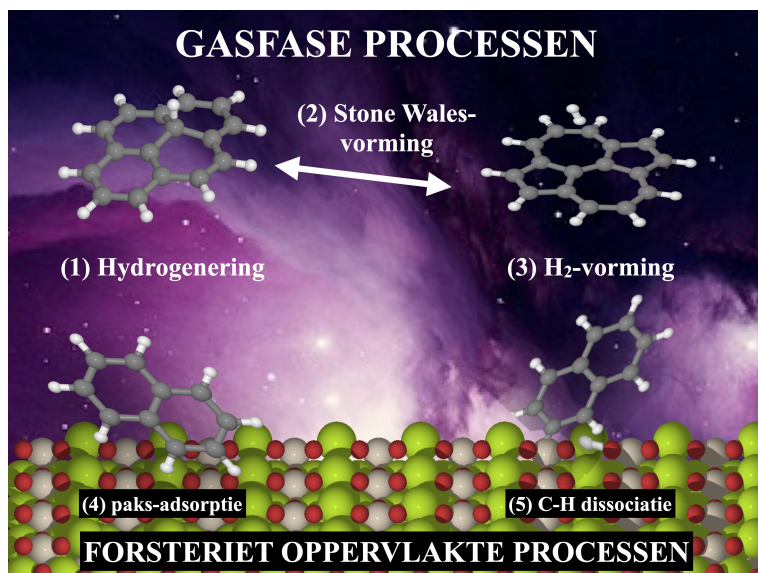
Figuur 5.21: Schema van de chemische processen die in dit proefschrift worden bestudeerd: chemische reacties die optreden in de gasfase, van 1 tot 3, en op het forsterietoppervlak van 4 tot 5.

kunnen tegenkomen en reageren tot waterstofmoleculen (proces 3 in Fig. 5.21). Zonder de aanwezigheid van paks of stofkorrels wordt de vorming van waterstofmoleculen ernstig belemmerd. Paks zijn betere katalysatoren dan stofkorrels en kunnen daardoor efficienter waterstof vormen. In sommige gebieden van het interstellair medium (ism) (nl. de materie en energie tussen de sterren), zoals de zogenaamde foto-dissociatiegebieden, staat de aanwezigheid van sterke stralingsvelden de vorming van moleculen helemaal niet toe.

Het is nog steeds niet duidelijk hoe moleculen worden geadsorbeerd op minerale korrels in de ism en hoe ze vervolgens in het zonnestelsel worden afgeleverd en daarom wordt dit nog onderzocht. We vinden paks samen met andere moleculen zoals aminozuren (de bouwstenen van het leven) in meteorieten in ons zonnestelsel. Waarschijnlijk slaan meteorieten verschillende organische moleculen op, welke mogelijk in het vroege stadium van ons zonnestelsel zijn gevormd. De kernvragen van astrochemie en kosmochemie houden verband met het begrijpen van de rol van moleculen in het heelal en de vorming van de voorraad van organische moleculen in het zonnestelsel. En in het bijzonder, hoe het atoom koolstof opgesloten in paks kan worden gekoppeld aan de diverse organische moleculen die in meteorieten zijn gevonden.

Dit proefschrift heeft tot doel het katalytische proces te begrijpen dat

leidt tot de vorming van waterstofmoleculen in het ism (proces 3 in Fig. 5.21) en de afbraak van paks in asteroïde omgevingen (proces 5 in Fig. 5.21). Dit is bereikt met behulp van dichtheidsfunctionaaltheorie (dft), een kwantumchemische methode die het mogelijk maakt om grote organische moleculen te modelleren en hun reactiviteit te voorspellen. **Hoofdstuk 2** en **3** van dit proefschrift hebben tot doel het katalytische proces dat leidt tot waterstofmoleculenvorming te begrijpen. Gevolgd door **hoofdstuk 4** en **5**, welke zich richten op de nauwkeurigheid van kwantumchemische methoden om de interactie van paks en forsteriet, en de chemische processen die optreden op forsterietoppervlakken.

Paks en Waterstofmoleculen

Ik bestudeerde, met behulp van kwantumchemische methoden, de hydrogeneringsvolgorde die leidt tot de vorming van volledig gehydrogeneerd pentaceen, een lineaire pak. Dit is om de aanwezigheid van verschillende gehydrogeneerde pentaceen (pentaceen met verschillende aantallen extra waterstofatomen aan hun oppervlak) te verklaren die in de experimenten werden gevonden (**hoofdstuk 2**). In **hoofdstuk 3** heb ik het mechanisme bestudeerd dat leidt tot de vorming van Stone-Walespyreen (processen 1-3 in Fig. 5.21), een pak met twee zeven- en vijfhoeken. Specifiek kan een waterstof atoom de energie verminderen die nodig is voor de vorming van de Stone-Wales, die op zijn beurt de vorming van waterstofmoleculen kan katalyseren.

Paks en het Forsterietmineraal

In **hoofdstuk 4** heb ik de dft-methoden getest om de interactie van organische moleculen op forsteriet te bestuderen. Ik ontdekte dat de nieuwe dft-D4-benadering, die rekening houdt met de lange-afstandsinteracties tussen het molecuul en het oppervlak, kan worden gebruikt om paks nauwkeurig te modelleren op een silicaatmineraaloppervlak zoals forsteriet (nl. een magnesiumsilicaat) met een lage rekenkracht. In het laatste hoofdstuk (**hoofdstuk 5**), heb ik met behulp van de dft-methoden die zijn getest in **hoofdstuk 4**, de adsorptie van een set paks op het imperfecte forsterietoppervlak onderzocht (proces 5 in Fig. 5.21). In het bijzonder heb ik een imperfect forsterietoppervlak gemodelleerd met de aanwezigheid van een ijzeratoom of een nikkelatoom dat een magnesiumatoom vervangt. Verder heb ik het zogenaamde Schottky-gebrek onderzocht dat wordt gevormd door het ontbreken van aangrenzend magnesium en een zuurstofatoom (een gat in het oppervlak). Het Schottky-gat blijkt een hoge katalytische activiteit te hebben voor een barrièreloze verbreking van de koolstof-waterstofbinding van paks (proces 5 in Fig. 5.21).

Toekomstige Onderzoeken

Toekomstige ontwikkeling van kwantumchemische methoden, experimentele studies, en observaties met de lancering van de James Webb Space Telescope zullen het verband tussen paks en de zogenaamde ingewikkelde organische moleculen in het zonnestelsel ophelderen.

Our universe seems a dark and empty space. However, the universe is the habitat of a variety of molecules that contribute to forming galaxies, solar systems, and planets. Molecules ubiquitous in the universe are called "Polycyclic Aromatic Hydrocarbons" (namely PAHs). They are molecules formed by a carbon skeleton that looks like a honeycomb (hexagonal rings) with hydrogens attached to their edges (examples of PAHs are shown in Fig. 5.22). PAHs lock up an important fraction of the elemental carbon (about 20%) in the universe and they help to maintain the physical and chemical balance in certain regions of the universe. PAHs are, amongst others, formed in the surrounding of a carbon-rich star. However, future observational, experimental, and theoretical investigations are necessary to fully understand their formation.

Studying how molecules react in the universe is indispensable to understand important physical and chemical processes as well as how life emerged. The hypothesized pathways to the formation of organic molecules in space are divided into bottom-up and top-down approaches. The bottom-up chemistry consists of building complex molecules starting from a small molecule or an atom forming a bigger one. The top-down approach consists of forming complex molecules breaking down big structures into smaller ones. The breaking down process might occur through energetic processes such as radiation.

Our universe is a hostile environment in which extreme physical conditions might impede chemical processes.

Molecules, as well as solid materials such as minerals, are capable to reduces the energy required to form molecular species, and such type of process is called catalysis, and catalysts are the atomic, molecular, or solid entities responsible for this process. PAHs are known to offer molecular surfaces (process 1 in Fig. 5.22) on which small atoms, such as the most abundant atomic hydrogen, can meet and react forming molecular
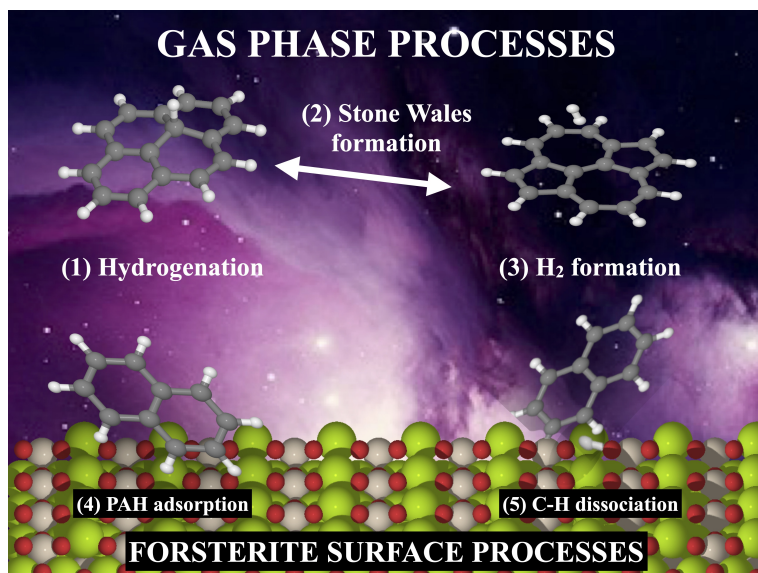
Figure 5.22: Scheme of the chemical processes studied in this thesis: chemical reactions occurring in the gas-phase, from 1 to 3, and on forsterite surface from 4 to 5.

hydrogen (process 3 in Fig. 5.22). This process is in general impeded without the presence of PAHs or dust grains. In some regions of the interstellar medium (the medium between the stars) such as the so-called photo-dissociation regions, the presence of strong radiation fields does not allow the formation of molecular entities. However, PAHs can catalyze the molecular hydrogen formation (process 3 in Fig. 5.22) more efficiently with respect to other surfaces such as dust grains.

It is still not clear how molecules are adsorbed on mineral grains in the interstellar medium and how they are delivered into the solar system and, thus, this is still under investigation. We find PAHs along with other molecular species such as amino acids (the building blocks of life) in the solar system and specifically in meteorites. Hence, meteorites lock up different organic species that might have been formed in the early stage of our solar system. The key questions of astrochemistry and cosmochemistry are related to shedding light on the role of molecules in the universe and the formation of the so-called organic inventory of the solar system. Specifically, how the elemental carbon locked in PAHs might be linked to the diverse organic species found in meteorites.

This thesis aims to understand the catalytic process that leads to the formation of molecular hydrogen in the interstellar medium (process 3 in Fig. 5.22) and the breakdown of PAHs in asteroidal settings (process 5

in Fig. 5.22). This has been achieved using density functional theory (DFT) which is a quantum chemical method allowing to model large organic molecules and predict their reactivity. **Chapter 2** and **3** of this thesis aim to understand the catalytic process that leads to molecular hydrogen formation. **Chapter 4** and **5** focus on the accuracy of quantum chemistry methods to model the interaction of PAHs and forsterite as well as the chemical processes occurring on forsterite surfaces.

PAHs and Molecular Hydrogen

I studied, using quantum chemical methods, the hydrogenation sequence that leads to the formation of fully hydrogenated pentacene, a linear PAH. This is to explain the presence of several hydrogenated pentacenes (pentacenes with different numbers of extra hydrogens attached to their surfaces) found in the experiments (**Chapter 2**). In **Chapter 3**, I studied the mechanism that leads to the formation of Stone-Wales pyrene (processes 1-3 in Fig. 5.22), a PAH with two heptagons and pentagons. Specifically, an atomic hydrogen can reduce the energy necessary to the formation of the Stone Wales which in turn can catalyze the formation of molecular hydrogen.

PAHs and the Forsterite Mineral

In **Chapter 4**, I tested the DFT methods in order to study the interaction of organic molecules on forsterite. I found that the new DFT-D4 approach which takes into consideration the long range interactions between the molecule and the surface can be used to accurately model PAHs on a silicate mineral surface such as forsterite (a magnesium silicate) using a low computational power. In the last chapter (**chapter 5**), using the DFT methods tested in **chapter 4**, I investigated the adsorption of a set of PAHs on the forsterite surface (process 5 in Fig. 5.22) and forsterite defective surfaces. Specifically, I modeled a defective forsterite surface with the presence of an iron and another one with nickel replacing a magnesium atom. Furthermore, I investigated the so-called Schottky defect which is formed by the lack of adjacent magnesium and an oxygen atom (a vacancy surface). The Schottky vacancy shows to have high catalytic activity for a barrierless breaking of the carbon-hydrogen bond of PAHs (process 5 in Fig. 5.22).

Future Investigations

Future development of quantum chemical methods as well as experimental studies and observation with the launch of the James Webb Space Telescope will clarify the link between PAHs and the so-called complex organic molecules found in the solar system.

RIEPILOGO

Il nostro universo sembra uno spazio buio e vuoto, tuttavia, è l'habitat di una varietà di molecole che cooperano tra loro per formare galassie, sistemi solari e pianeti. Gli "Idrocarburi Policiclici Aromatici" (chiamati IPA) sono molecole onnipresenti nell'universo e sono formate da uno scheletro di carbonio dalle sembianze di un nido d'ape (anelli esagonali) con idrogeni legati ai loro bordi (degli esempi di IPA sono mostrati in Fig. 5.23). Gli IPA racchiudono un'importante frazione (circa il 20%) del carbonio elementare nell'universo e aiutano a mantenere il suo equilibrio fisico e chimico. Gli IPA si formano nei dintorni di una stella ricca di carbonio. Tuttavia, sono necessarie future indagini osservative, sperimentali e teoriche per comprendere appieno la loro formazione.

Studiare come le molecole reagiscono e si differenziano nell'universo è indispensabile per comprendere importanti processi fisici e chimici, nonché come è emersa la vita. I percorsi ipotizzati per la formazione di molecole organiche nello spazio sono divisi in approcci dal basso verso l'alto (bottom-up) e dall'alto verso il basso (top-down). La chimica bottom-up consiste nel costruire molecole complesse partendo da una piccola molecola o da un atomo che ne forma una più grande. L'approccio top-down consiste nel formare molecole complesse scomponendo grandi molecole in molecole più piccole. Il processo di rottura potrebbe avvenire attraverso processi energetici come la radiazione.

Il nostro universo è un ambiente ostile in cui condizioni fisiche estreme potrebbero impedire i processi chimici. Le molecole, così come i materiali solidi come i minerali, sono in grado di ridurre l'energia necessaria per formare specie molecolari e questo tipo di processo è chiamato catalisi, mentre i catalizzatori sono le entità atomiche, molecolari o solide responsabili di questo processo. È noto che gli IPA offrono superfici molecolari (processo 1 in Fig. 5.23) su cui piccoli atomi, come l'idrogeno che è l'atomo più abbondante nell'universo, possono incontrarsi e reagire formando
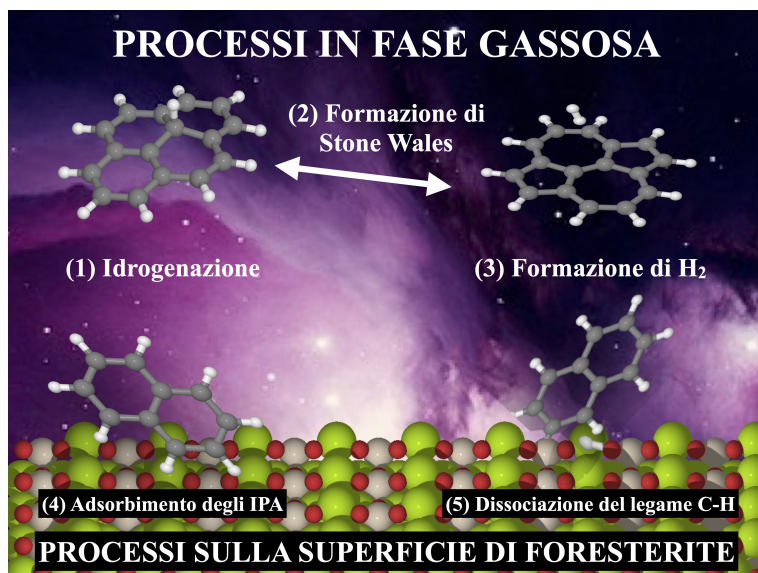
189

Figura 5.23: Schema dei processi chimici studiati in questa tesi: reazioni chimiche che avvengono in fase gassosa, da 1 a 3, e sulla superficie di forsterite da 4 a 5.

idrogeno molecolare (processo 3 in Fig. 5.23). Questo processo è generalmente impedito senza la presenza di IPA o grani di polvere. In alcune regioni del mezzo interstellare (il mezzo tra le stelle), come le cosiddette regioni di foto-dissociazione, la presenza di forti campi di radiazione non consente la formazione di entità molecolari. Tuttavia, gli IPA possono catalizzare la formazione di idrogeno molecolare (processo 3 in Fig. 5.23) in modo più efficiente rispetto ad altre superfici come i granelli di polvere.

Non è ancora chiaro come le molecole vengano adsorbite sui grani di minerali nel mezzo interstellare e come vengano trasportate nel sistema solare. Di conseguenza, questo processo è ancora oggetto di indagine. Troviamo gli IPA insieme ad altre specie molecolari come gli amminoacidi (i mattoni della vita) nel sistema solare e in particolare nei meteoriti. Quindi, i meteoriti contengono diverse specie organiche che potrebbero essersi formate nella fase iniziale del nostro sistema solare. I punti chiave dell'astrochimica e della cosmochimica riguardano il ruolo delle molecole nell'universo e la formazione del cosiddetto inventario organico del sistema solare. In particolare, il carbonio contenuto nelle diverse specie organiche trovate nei meteoriti potrebbe derivare dal carbonio elementare contenuto negli IPA.

Questa tesi mira a comprendere il processo catalitico che porta alla formazione di idrogeno molecolare nel mezzo interstellare (processo 3 in Fig. 5.23) e la scomposizione degli IPA in ambienti asteroidali (processo 5 in

Fig. 5.23). Ciò è stato ottenuto utilizzando la teoria del funzionale della densità (DFT), che è un metodo quantomeccanico che consente di modellizzare grandi molecole organiche e prevederne la reattività. I Capitoli 2 e 3 di questa tesi mirano a comprendere il processo catalitico che porta alla formazione dell'idrogeno molecolare, mentre i capitoli 4 e 5 si concentrano sull'accuratezza dei metodi quantomeccanici per modellizzare l'interazione di IPA con la forsterite e i processi chimici che si verificano sulla superficie di forsterite.

Gli IPA e l'Idrogeno Molecolare

Ho studiato, utilizzando metodi quantomeccanici, la sequenza di idrogenazione che porta alla formazione del pentacene completamente idrogenato (un IPA lineare). Questo per spiegare la presenza di diverse specie di pentacene idrogenati (pentaceni con un diverso numero di extra idrogeni legati sulle loro superfici) trovati in studi sperimentali (Capitolo 2). Nel Capitolo 3, ho studiato il meccanismo che porta alla formazione del difetto di Stone-Wales nel pirene (processi 1-3 in Fig. 5.23), un IPA con due ettagoni e due pentagoni. Nello specifico, un idrogeno atomico può ridurre l'energia necessaria alla formazione dello Stone Wales che a sua volta può catalizzare la formazione di idrogeno molecolare.

Gli IPA e il Minerale di Forsterite

Nel Capitolo 4, ho testato i metodi DFT per studiare l'interazione delle molecole organiche sulla forsterite. Ho scoperto che il nuovo approccio DFT-D4, che prende in considerazione le interazioni a lungo raggio tra la molecola e la superficie, può essere utilizzato per modellizzare accuratamente gli IPA su una superficie minerale di silicato come la forsterite (un silicato di magnesio) utilizzando una bassa potenza di calcolo. Nell'ultimo capitolo (capitolo 5), utilizzando i metodi DFT testati nel capitolo 4, ho studiato l'adsorbimento di un insieme di IPA sulla superficie della forsterite (processo 5 in Fig. 5.23) e le sue superfici difettose: una superficie con la presenza di un ferro e un'altra con nichel che sostituiscono un atomo di magnesio, oltre a una superficie vacante, chiamata difetto di Schottky, per la mancanza di magnesio e un atomo di ossigeno adiacente. Il difetto di Schottky mostra di avere un'elevata attività catalitica per la scissione, senza barriere, del legame carbonio-idrogeno degli IPA (processo 5 in Fig. 5.23).

Studi Futuri

Lo sviluppo futuro di metodi della chimica quantistica, nonché studi sperimentali e osservazionali, come il lancio del telescopio James Webb,

chiarirà il legame tra gli IPA e le cosiddette molecole organiche complesse presenti nel sistema solare.

First Author

1. **D. Campisi***, T. Lamberts, N. Y. Dzade, R. Martinazzo, I. L. ten Kate, A. G. G. M. Tielens, *Interaction of Aromatic Molecules with Forsterite: Accuracy of the Periodic DFT-D4 Method*, **Journal of Physical Chemistry A 2021**, *125*, 13, 2770-2781. DOI: https://doi.org/10.1021/acs.jpca.1c02326

2. **D. Campisi*** and A. Candian*, *Do Defects in PAHs Promote Catalytic Activity in Space? Stone–Wales Pyrene as a Test Case*, **Physical Chemistry Chemical Physics 2020**, *22*, 6738-6748. DOI: https://doi.org/10.1039/C9CP06523G

3. **D. Campisi***, F. D. S. Simonsen, J. D. Thrower, R. Jaganathan, L. Hornekær, R. Martinazzo and A. G. G. M. Tielens*, *Superhydrogenation of Pentacene: the Reactivity of Zigzag-Edges*, **Physical Chemistry Chemical Physics 2020**, *22*, 1557-1565. DOI: https://doi.org/10.1039/C9CP05440E

Contributed Author

1. R. Cortese, **D. Campisi**, A. Prestianni and D. Duca*, *Alkane Dehydrogenation on Defective BN Quasi-Molecular Nanoflakes: DFT Studies*, **Molecular Catalysis 2020**, *493*, 110891. DOI: https://doi.org/10.1016/j.mcat.2020.110891

---

*Corresponding Author

2. R. Cortese, **D. Campisi** and D. Duca[*], *Hydrogen Arrangements on Defective Quasi-Molecular BN Fragments*, **ACS omega 2019**, *4*, 14849-14859. DOI: https://doi.org/10.1021/acsomega.9b01445

In Preparation/Submitted

1. **D. Campisi**[*], N. Y. Dzade, R. Martinazzo, I. L. ten Kate, T. Lamberts and A. G. G. M. Tielens, *Adsorption of PAHs and C_{60} onto Forsterite: C-H Bond Activation by the Schottky Vacancy*

2. **D. Campisi**[*], W. Dononelli, B. Hammer and A. G. G. M. Tielens, *Finding the stable location of a MgO vacancy in Forsterite (Mg_2SiO_4) using global optimization with first principles energy expressions*

---

[*]Corresponding Author

CURRICULUM VITAE

I was born on one of the hottest Saturdays of summer in Italy, specifically, on the 14th of June 1986 in Palermo (Sicily). My mom was a chemical expert in a clinical analysis lab and she infused me her love for organic chemistry. On top of this, I have been always fascinated by computers and programming. My first computer was a commodore 64 in which I learned the basics of BASIC code. Later on, in middle school, my teacher, Graziella Solina, introduced me to science and math. So I decided to be enrolled in scientific high school (Liceo Scientifico) in which my teacher Elvira Piccione mentored me and inspired me to love chemistry and astronomy.

After high school, I felt lost and I was dealing with some personal and family issues that led me to be enrolled initially in a geology bachelor course which I left after one year and a half since I did not feel that was a path to follow. Later on, when I was about 24, I decided to be enrolled in a chemistry bachelor course (Laurea Triennale) at Palermo University. The chemistry bachelor course in Italy was too focused on the experimental aspect of chemistry. On top of this, the faculty members discouraged students from undertaking internships based on research but rather they pushed them to consider analytical chemistry careers in the industry. This made me realized that I did not want to be a lab mouse but rather I was curious about researching and discovering. Hence, I did an internship in the national research council (CNR) and I carried out an experimental thesis in organic chemistry.

I have not been happy with my bachelor's course and I was reluctant to proceed with a master's course in chemistry since I needed a more open-minded environment that allows exploring different disciplines. However, I knew that I wanted to have a PhD, and being enrolled in the chemistry master course (Laurea Magistrale) at Palermo University was a smart choice. Here, I have been introduced to theoretical chemistry, spectroscopy, and catalysis — three disciplines that I completely fell in love with. So, I deci-

ded to carry out a thesis in computational chemistry applied to catalysis in Dario Duca's group, co-supervised by Remedios Cortese. Furthermore, they introduced me to astrochemistry and the idea of catalysis in space. I got my master with the top grade and I started to search for PhD positions.

When I found advertised several positions in astrochemistry within a Marie Curie network called EUROPAH, I decided to apply without second thoughts. So, I have been introduced to my co-supervisor, Inge Loes ten Kate, and my promotor, Xander Tielens, and they decided to accept me as PhD candidate at Leiden University as well as one of the Early Stage Researcher (ESR) of the Marie Curie ITN-EUROPAH network.

During the first EUROPAH training event at Aarhus University, which I attended in the second week of my PhD, I have been asked to run small calculations in support of the final poster. Here, I gave a good impression to Liv Hornekær (Aarhus University) who asked me to collaborate with her and with Rocco Martinazzo (Milan Universe). This collaboration gave birth to the results of chapter 2 of this thesis. In my first two years, I have been in contact with Alessandra Candian (my office mate) who mentored me and collaborated with me in chapter 3 of this thesis.

The first part of my PhD thesis has been focused on the interstellar medium and gas-phase processes. However, I wanted to explore also solar system and this resulted in my final two chapters with the collaboration of Rocco Martinazzo, Thanja Lamberts who has become officially my co-supervisor, Nelson Dzade at Cardiff University, and Inge Loes ten Kate. Furthermore, during the time spent in the EUROPAH network, I had the privilege to get broad training thanks to several organized workshops, conferences, and outreach activities. I also have been seconded to Milan University for four months in which I received training on periodic calculations. I spent a month in Bristol, UK, to develop an outreach project that gave birth to a pop-up shop. I have been part of the Social Organizing Committee (SOC) of the "PAH Research: Theory, Experiments in an Astronomical context" conference organized by EUROPAH's ESRs. Finally, I have been seconded to Aarhus University in Bjørk Hammer's group in which I received training on machine learning. Unfortunately, my secondment has been interrupted by the COVID-19 pandemic which led me to continue remotely. Finally, I will be appointed, this fall (2021), as a post-doc in Laura Gagliardi's theoretical chemistry group at Chicago University. I will work on applying and developing quantum chemical methods based on wave function methods that will be tested on the forsterite models studied in this thesis as well as on actinide chemistry.

ACKNOWLEDGMENTS

In four years of my PhD, I have met many brilliant and inspiring people. I am afraid that I might forget to acknowledge some of them. Hence, if your name is not in this acknowledgment, I thank you because somehow you provided an indirect contribution to finalize this thesis. Every person I met during my PhD helped me to grow as a scientist.

First of all, I would like to thank Alessandra Candian for supporting, inspiring, and mentoring me in the first two years of my PhD. I thank her for teaching me, not just how to do research, but also the political aspect of academia.

A special thank goes to the EuroPAH network for this beautiful experience. I am so grateful to have had this privilege. Hence, I would like to thank Liv Hornekær, Andrew Cassidy, and John Thrower for the collaborations and training that helped me develop as a scientist. I thank all EuroPAH ESRs (Early Stage Researchers): Gabi, Lindsey, Juliana, Shreyak, Martin, Sanjana, Evgeny, Georgios, Rushdi, Yaolin, Lorenzo, Laurène, Zeyuan, Rijutha, and Frederik (even though he is not an ESR, we always considered him as part of the group). From Aarhus University, I would also like to thank Bjørk Hammer for hosting me during my secondment and Wilke Dononelli for supervising my machine learning calculations.

I would like to thank all current members and past members of the interstellar medium group (the pizza meeting!) of which I have been in charge for three years: Andrew, Pedro, Kimberly, Cornelia, Marina, Morgan, Claudia, Sascha, Andrew, Pablo, Lizette, Raymond, Jordy, Ümit, Kevin and my office mates Cameron and Morgan.

I acknowledge the astrobiology group in Utrecht: Claudia, Nina, Eloi, and Alexandra as well as Helen King and the former members Vincent, Arjen, Kateryna, and Lucas. Thanks also to Nelson Dzade for his support and teachings as well as Mariëtte Wolthers, Sergio Ruiz Hernandez, and Nora de Leeuw for their input on chapter 4 and 5.

I thank Jordy for being my science buddy and forcing me to study hard every day due to his daily scientific questions.

Now, a special thank goes to Michał Bulak, a friend, colleague, and ESR fellow that was a witness of this journey and for his unconditional support and love (proverbs 17:17, "A friend loves at all times, and a brother is born for adversity").

I thank Folkert as well as Marina for supporting and advising me during a hard time in this pandemic and for correcting the dutch version of the summary of this thesis.

A big thank goes to Marta for designing the amazing cover of this thesis.

I thank all the secretaries: Monica and Marjan for the daily pleasant chat and support as well as Susan and Alexandra. I would like to thank also Els and Evelijn for helping me with the EuroPAH budget. A double thank goes to Evelijn for helping me when I was in Aarhus during the corona outbreak.

I would like to thank Gabriella for helping me to finalize the non-scientific part of this thesis as well as for the pleasant Italian chats.

I thank Dilovan for the friendly coffee break chats (pre-pandemic) in my office and for helping me to finalize my propositions.

Now, I would like to mention all the people that did not directly contributed to this thesis and I met in Leiden during this journey. I thank all my friends and colleagues: Anna, Fraser, Kirsty, Marta, Danna, Lammim, Martijn (Oei), Martijn (van Gelder), Jeroen, Alex, Patrick, Bas, Mantas, Dieuwertje, Omar, Margot, Gwén, Lydia, Pooneh, Erik, Roland, Frits, Stijn, Sarah, Helgi, Sandra, Benoit, Matus and the new PhD students (I wish I could have had more time to know you better) Roi, Elina, Tara, Niccolò, Joshua, Pranjal and Julia.

A special shazam goes to Turgay (he knows what this means) for his unmanageable sense of humor and support.

I would like to mention the people that contributed and helped me to keep going with my hobbies alongside science. I thank Anniek that pushed me to restart a hobby and passion that I stopped 12 years ago. Another special thank goes to my former band members, colleagues and friends (Dario and the Monkeys). Specifically, Łukasz (the sad monkey) for your unconditional friendship, helping me with the final steps of this thesis and trusting me with an honor of being a witness at your wedding. I am so grateful to have met you, you are the real star of this band. Hiddo (the happy monkey), thanks for your friendship and for being the happy light of this band. I thank my new band (Dario and the Guinea Pigs) specifically Alice and Evgenii (Chaikin) who helped me improve my vocal cords and supported me with some music during the lockdown. Evgenii thanks also for all the pleasant chats and friendship outside the music.

I would like to thank Carla Murineddu and the modern dance group at USC Leiden, this is a wonderful initiative that all universities should have (mens sana in corpore sano).

Finally, I acknowledge my supervisors A.G.G.M. Tielens, I.L. ten Kate, and T. Lamberts for their support and fruitful discussions.

Ringraziamenti

Ringrazio me stesso per essermi permesso tutto questo. Ringrazio la mia famiglia, in particolare, mio padre e mia madre che hanno creduto in me e supportato in questo cammino.

Ringrazio Roberta per il suo so/supporto.

Ringrazio Valeria Amaro, la prima persona italiana che conobbi a Leiden, per le risate, la sua amicizia e i nostri battibecchi scientifici.

Un ringraziamento speciale a Rocco Martinazzo per il suo supporto teorico e i suoi insegnamenti. Ringrazio anche Mirko Leccese per la sua amicizia e lo scambio di opinioni, via whatsapp, che mi ha aiutato ad aggiornare le mie conoscienze di chimica teorica.

Ringrazio Dario Duca e Remedios Cortese per il loro supporto scientifico e i loro consigli.

Ringrazio Elvira Piccione per avermi permesso di tenere un seminario al mio vecchio liceo. E' stata una grande emozione ritornare, ma dall'altro lato del banco.

Uno speciale ringraziamento a Clarissa Arvizzigno per la sua amicizia, il suo supporto morale e per avere controllato la versione italiana del riepilogo di questa tesi.